Setup and operation of a multi-ion clock based on linear In$^+$/Yb$^+$ crystals
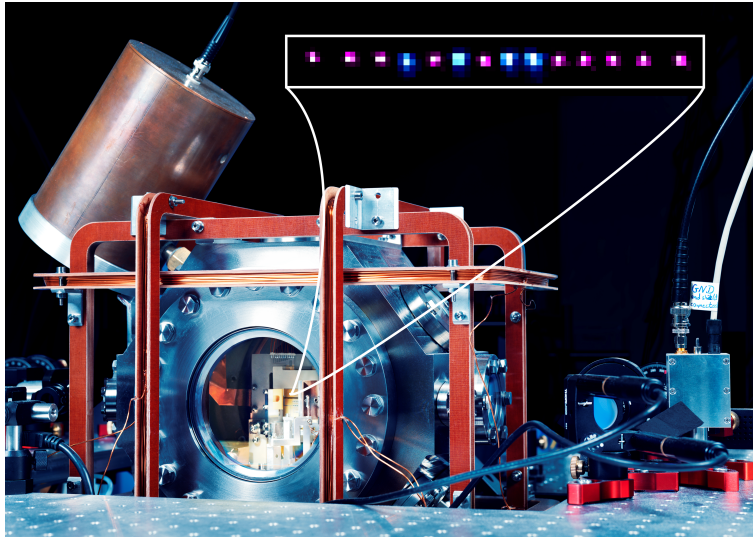
M.Sc. Tabea Nordmann

geboren am 20. Januar 1993 in Georgsmarienhütte

2023

Zusammenfassung

Die aktuell genausten optischen Atomuhren basieren auf gefangenen und lasergekühlten Atomen oder Ionen. Dabei wird ein schmalbandiger Laser auf einen geeigneten elektronischen Übergang im Atom oder Ion stabilisiert und so Frequenzmessungen mit relativen systematischen Unsicherheiten bis $\approx 1 \times 10^{-18}$ realisiert. Während Neutralatomuhren viele tausend Atome gleichzeitig nutzen und somit ein gutes Signal-zu-Rausch-Verhältnis haben, basiert die Mehrzahl der heutigen Ionenuhren auf der Verwendung eines einzelnen Ions, das manchmal mit einem oder zwei weiteren Ionen einer anderen Spezies sympathetisch gekühlt wird. Die exzellente Kontrolle über die Umgebungsbedingungen und die äußeren Einflüsse auf die Energieniveaues des einzelnen Uhrenions sind eine große Stärke dieses Ansatzes. Die lange Mittelungszeit von einigen Wochen um eine systematische Unsicherheit von 10^{-18} statistisch aufzulösen ist jedoch ein großer Nachteil, insbesondere für Anwendungen außerhalb des Labors. Aus diesem Grund wird im Forschungsfeld der optischen Ionenuhren aktuell mit verschiedenen Ansätzen an einer Verbesserung der Instabilität geforscht.

Die Motivation dieser Arbeit ist, durch die Verwendung von Ionenketten mit mehreren Uhren-Ionen das Signal-zu-Rausch-Verhältnis zu erhöhen und gleichzeitig die exzellente Kontrolle auch für ein Vielteilchensystem zu bewahren. Die Ionenketten bestehen aus $^{115}\mathrm{In}^+$ Uhren-Ionen, die sympathetisch mit $^{172}\mathrm{Yb}^+$ Ionen gekühlt werden. Gegenstand dieser Arbeit ist die Entwicklung eines experimentellen Aufbaus, der geringe systematische Unsicherheiten und eine simultane nach Ionen aufgelöste Zustandsdetektion beider Spezies ermöglicht, sowie der Betrieb einer Multi-Ionen-Uhr. Das umfasst die Charakterisierung der mit der Ionenfalle verbundenen sytematischen Unsicherheiten und die Optimierung des sympathetischen Kühlens.

Das vorgestellte Indiumionenuhr befindet sich am deutschen nationalen Metrologieinstitut, Physikalisch-Technische Bundesanstalt (PTB), in Braunschweig. Im April 2022 war die Indiumionenuhr an einer internationalen Messkampagne zu Frequenzvergleichen von optischen Uhren (European Metrology project 18SIB05 ROCIT[1]) beteiligt. Nach Abschluss der noch andauernden Auswertung werden daraus zahlreiche bisher unbekannte Frequenzverhältnisse resultieren. Mit der Inbetriebnahme ist die Indiumionenuhr als drittes optisches Frequenznormal mit einer systematischen Unsicherheit im niedrigen 10^{-18}-Bereich an der PTB ein wichtiger Bestandteil der Forschungsinfrastruktur für optische Uhren an der PTB und im internationalen Netzwerk der nächsten Jahre.

———

[1]Robust optical clocks for international timescales, http://empir.npl.co.uk/rocit/

Abstract

Today's most accurate optical atomic clocks are based on trapped and laser cooled atoms or ions. Here, a narrow band laser is stabilized to a suitable electronic transition in the atom or ion, realizing frequency measurements with relative systematic uncertainties up to $\approx 1 \times 10^{-18}$. While neutral atom clocks use many thousands of atoms simultaneously and thus have a good signal-to-noise ratio, the majority of current ion clocks are based on the use of a single ion, sometimes sympathetically cooled with one or two other ions of a different species. The excellent control over the environmental conditions and the external influences on the energy levels of the individual clock ion are a major strength of this approach. However, the long averaging time of several weeks to statistically resolve a systematic uncertainty of 10^{-18} is a major drawback, especially for applications outside the laboratory. For this reason, different approaches are currently being pursued to improve instability in the field of optical ion clocks.

The motivation of this work is to increase the signal-to-noise ratio by using ion chains with multiple clock ions while maintaining excellent control in this step from a single ion to a many-body system. The ion chains consist of $^{115}\text{In}^+$ clock ions, sympathetically cooled with $^{172}\text{Yb}^+$ ions. The subject of this work is the development of the experimental setup which allows low systematic uncertainties and simultaneous ion-resolved state detection of both species, as well as the operation of a multi-ion clock. This includes the characterization of the systematic uncertainties associated with the ion trap and the optimization of sympathetic cooling.

The presented indium ion clock is located at the German national metrology institute, Physikalisch-Technische Bundesanstalt (PTB), in Braunschweig. In April 2022, the indium ion clock was involved in an international measurement campaign of frequency ratios of optical clocks (European Metrology project 18SIB05 ROCIT[2]). After completion of the ongoing evaluation, this will result in various previously unknown frequency ratios. With the commissioning, the indium ion clock, as the third optical frequency standard with a systematic uncertainty in the low 10^{-18} range at PTB, is an important part of the optical clock research infrastructure at PTB and in the international network of optical clocks in the years to come.

—

Keywords: Multi-ion clock, optical frequency standard, Coulomb crystals, sympathetic cooling, precision spectroscopy

---

[2]Robust optical clocks for international timescales, http://empir.npl.co.uk/rocit/

Contents

Contents

1. Introduction

The measurement of time has always been important and continuously evolved, giving rise to many inventions. Precise timing is essential for our technologically highly developed and digital world, which is based on overall synchronization. Examples include the global navigation satellite system (GNSS), telecommunication, energy distribution or international economic and financial transactions.

To measure time, a periodic process is counted. Until the middle of the 20th century this process has been the earth rotation. With the invention of clocks based on quartz crystals in the 1930s and 1940s, it was observed that the Earth's rotation frequency fluctuates [1]. Since 1967, the SI second is defined as the duration of 9 192 631 770 periods of the radiation corresponding to the microwave transition between two hyperfine states of the ground state of the ^{133}Cs atom [2]. The idea to use atoms for time measurements originates from James Clerk Maxwell in 1870 [3] and is still the most reproducible reference known to mankind. Since the definition in 1967, Cs atom clocks improved, with technological advances such as the invention of the laser [4, 5] and associated cooling techniques [6–9]. Nowadays they approach a fractional uncertainty of 1×10^{-16} [10]. The development of highly stable lasers [11] and the invention of the optical frequency comb [12] paved the way to use clock transitions in the optical domain, with a five orders of magnitude higher frequency and significantly lower frequency uncertainties.

One realization of optical clocks, that nowadays reach systematic uncertainties in the 10^{-18} regime, are neutral atom lattice clocks where 1000s of atoms are probed simultaneously, offering a high signal-to-noise ratio [13–17]. Another approach is the localization of a single ion in a Paul trap, where it can be isolated well from environmental perturbations, resulting in systematic frequency uncertainties reaching even below 10^{-18} for the best reported value at the time of writing [18]. A limitation of this approach is the binary information obtained from the single particle, leading to a low signal-to-noise ratio. Averaging times of around 13 days are required to resolve the best reported single-ion systematic uncertainty [18] with the best realized single-ion statistical uncertainty [19]. Shortening of the averaging time to reach a fixed systematic uncertainty by a factor N can be achieved with simultaneous interrogation of N ions, which can be stored as a Coulomb crystal [20]. The challenge is to maintain the excellent control of systematic shifts for an extended crystal, which requires precise engineering of the ion trap and high control of the many-body system. A precision ion trap developed at PTB [21, 22], provides the prerequisites for a multi-ion clock with systematic uncertainties in the 10^{-19} range [23]. On long term the segmentation of the trap allows cascaded clock schemes in one experimental setup to improve stability, while maintaining the low systematic uncertainty demonstrated in linear ion crystals.

1. Introduction

Investigations for multi-ion clocks based on large 3-dimensional crystals either involve cancellation schemes for systematic shifts [24–26] or their focus is mainly on stability to build so called ensemble or cascaded clocks [27–29]. For example, a 3-dimensional crystal can be used to prestabilize the clock laser and enable longer, up to lifetime-limited, interrogation in a separate, high-accuracy atomic reference. With ion ensembles, one can apply other techniques to lower the instability, e.g., by using entanglement [30–35].

Improved instabilities, and accordingly reduced averaging times, of these highly accurate clocks increase their application potential. Systematic uncertainties of 10^{-18} allow to resolve height differences with $1\,cm$ precision based on the relativistic time dilation caused by the gravitational potential of the earth. In the interdisciplinary field of chronometric leveling, the red-shift measured between two precise clocks at different heights can be used to measure the height difference without a direct line of sight, e.g. via a large distance fiber-link [36–40]. Here, transportable optical clocks are particularly interesting [16, 41, 42]. The outstanding low systematic uncertainty of optical clocks also makes them suitable for testing theories beyond the boundaries of our present understanding of the fundamental laws of physics and measure e.g. temporal or spatial variations of fundamentals constants or violations of Einstein's equivalence principle [43–48].

Further approaches to realize optical clocks are based on the interrogation of a transition in the nucleus of an ion [49–52] or an electronic transition in a highly charged ion [53–55]. Both systems provide high sensitivity for the search of changes in the fundamental constants [56–58]. Trapping neutral atoms in optical tweezer arrays instead of optical lattices is another approach to increase the control in large atom ensembles [59].

The two orders of magnitude improvement in the systematic uncertainty of optical clocks compared to the current definition of the SI second from 1967 leads to plans for a redefinition [60, 61]. Two of the considered options would be a basis of several frequency ratios between clocks of different species or a single species [62]. In any case, optical clocks must prove their reliability, which requires different realizations that are repeatedly tested against each other. With the redefinition of several other SI units in 2019 and the conceptual change to define all SI units based on natural constants [63], the relevance of the SI second even increased as it is involved in the definition of the other SI units.

The aim of this thesis is the setup and operation of an optical clock based on the simultaneous interrogation of multiple $^{115}\text{In}^+$ ions, which are sympathetically cooled with $^{172}\text{Yb}^+$ ions in a linear Coulomb crystal.

The thesis is structured as followed: Chapter 2 reviews the theoretical concept of optical clocks, the properties of the clock species $^{115}\text{In}^+$, the basics of ion trapping in Paul traps and interaction between trapped particles and laser light. Additionally, the theoretical foundation of systematic frequency shifts are given and possible ion candidates with regard to multi-ion based clock operation are discussed. The experimental setup optimized for accurate multi-ion operation is presented in chapter 3 and includes the description of the bichromatic detection system for simultaneous ion resolved state detection of $^{115}\text{In}^+$ and $^{172}\text{Yb}^+$ ions. In chapter 4,

the ion trap is characterized and a trap-related uncertainty budget for a multi-ion In^+ clock with a crystal length of $400\,\mu m$ is derived. The control of dual-species linear crystals is the content of chapter 5. This includes an experimental search of the suitable range of the Mathieu q parameter for stable linear In^+/Yb^+ crystals and a systematic analysis of the influence of the crystal composition and permutation on the efficiency of sympathetic cooling. Based on those results, methods to reliably reorder dual-species crystals are investigated experimentally. With consideration of the findings from the previous chapters, spectroscopy of the $^1S_0 \leftrightarrow {}^3P_1$ and $^1S_0 \leftrightarrow {}^3P_0$ transitions in $^{115}In^+$ ions has been performed and the results are presented in chapter 6. Besides the results on the first transition, used for state detection and possibly in future second-stage cooling, the focus is set on clock spectroscopy of In^+ ions. The instability reached in the first operation of a single In^+ ion clock, which is sympathetically cooled with Yb^+ ions, is presented and also includes an extension to up to 4 In^+ ions. Chapter 7 summarizes all results and discusses next steps and improvements to extend the multi-ion operation.

2. Theoretical basis for ion optical clocks

2.1. Optical clocks

2.1.1. Principle

Time is typically measured by counting cycles of a periodic process. The periodic process is the oscillation of the local oscillator (LO). In an optical clock, this is a laser whose frequency is kept at a known reference value by means of feedback from an electronic transition between two internal states of an atom. Without external disturbances, the transition frequency between the two energy levels is identical for all atoms of the same isotope. In an optical clock, these disturbances are kept as low as possible and must be known exactly so that the frequency is reproducible.
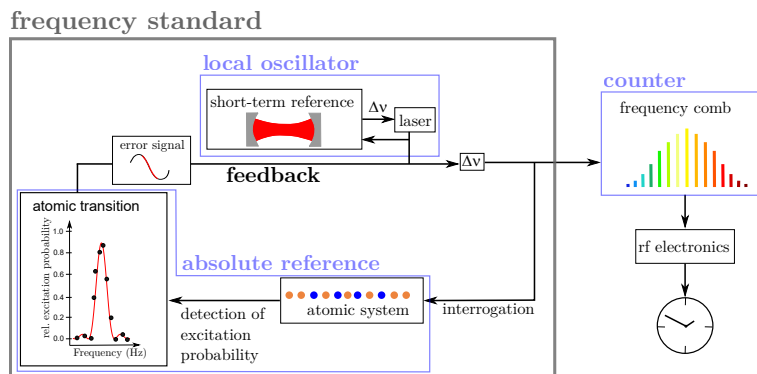
Figure 2.1.: *Constituents of an optical frequency standard (grey box) and its implementation in an optical atomic clock.*

Figure 2.1 schematically shows the constituents for the measurement of time in an optical clock. A frequency standard is a laser (local oscillator) stabilized to an atomic reference transition frequency (absolute reference). The laser frequency signal ($\approx 10^{15}\,\text{Hz}$) is converted to the rf domain ($\approx 10^{8}\,\text{Hz}$) by means of a frequency comb [12, 64, 65] (counter) to enable the use of electronics to count the periodic process. Because the interrogation of the atomic system and the determination of the transition frequency is orders of magnitude slower than the transition frequency and has a low signal-to-noise ratio (SNR), a flywheel oscillator is used to pre-stabilize the clock laser. A short-term frequency reference, typically an optical cavity, provides continuous feedback to the clock laser and the combined system is the so called local oscillator (LO).

2. Theoretical basis for ion optical clocks

The performance of a frequency standard is characterized by its instability and inaccuracy. The instability is the statistical contribution to the frequency uncertainty, which is a function of the averaging time τ. On short time scales, the instability of a frequency standard is dominated by the local oscillator, while on long time scales it is determined by the error signal derived from the interrogation of the atomic transition. The best published instability of an ion-based frequency standard known to the author at the time of writing this is $1.0 \times 10^{-15} \, (\tau/\text{s})^{-1/2}$ [66]. Details on the fundamental limit and the theoretical scaling of the instability with the number of interrogated particles are described in section 2.1.2. Experimental results on the instability of this frequency standard are presented in section 6. The systematic deviation from the unperturbed transition frequency is described by the inaccuracy of the frequency standard. Its value is estimated from all relevant influences, such as external fields, motional excitation or collisions with other particles. While known frequency shifts can be accounted for, the inaccuracy is still limited by the uncertainties of these corrections. More details about the systematic frequency shifts in an optical clock are discussed in section 2.4. At the time of writing, the lowest published fractional systematic uncertainty of a frequency standard based on ions is 9.4×10^{-19} [18]. In terms of inaccuracy, work presented in this thesis is the characterization of the trap related contribution for a linear ion crystal with a length of $300 \, \mu$m, presented in section 4. A comprehensive overview about optical clocks is given in [67].

2.1.2. Instability of a multi-ion frequency standard

Instability is usually quantified using the Allan deviation [68]:

$$\sigma_{\text{y}}(\tau) = \sqrt{\frac{1}{2} \langle (\bar{y}_2 - \bar{y}_1)^2 \rangle},$$

(2.1)

where the term in the angled brackets describes the mean value of the difference of two successive frequency measurement results $\bar{y}_i$, that have both been averaged over the duration τ. More details can be found in [69].
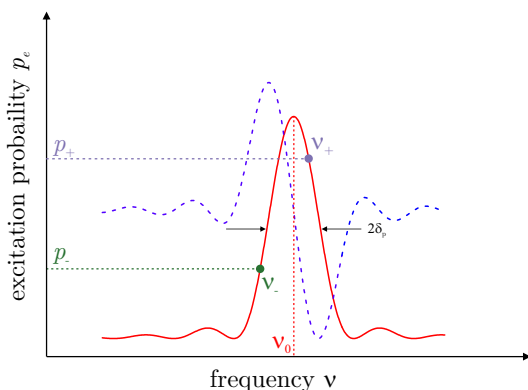
Figure 2.2.: *Error signal generation from Rabi interrogation. The excitation probability p_e is probed at two points left (ν_-) and right (ν_+) of the center frequency ν_0 with a detuning $\delta_p = (\nu_+ - \nu_-)/2$. The red line shows the Rabi lineshape and the dashed blue line its first-order derivative, which is relevant for the error signal sensitivity.*

The fundamental limit of the achievable instability in an optical clock based on a single ion arises in the determination of the error signal that is applied to steer the frequency of

the LO. The detuning from the resonance frequency between the ground state $|g\rangle$ and the excited state $|e\rangle$ is deduced from the transition probability between these states after applying a single pulse, in case of the Rabi scheme, or from the phase evolution of a superposition $(|g\rangle + \exp(i\phi)|e\rangle)/\sqrt{2}$, in case of the Ramsey scheme [70]. The error signal is derived from the difference in the excitation probability probed at two different detunings around the resonance (Rabi) or with different relative phase shifts (Ramsey). In this work, only the Rabi scheme is used and therefore all following derivations are limited to that case. Figure 2.2 illustrates the generation of the error signal $E(\nu)$ for Rabi interrogation. The excitation probability is probed at two points left (ν_-) and right (ν_+) of the center frequency ν_0 with a detuning $\delta_p = (\nu_+ - \nu_-)/2$. The most sensitive error signal can be generated around half the maximum excitation probability ($2\delta_p = \text{FWHM}$), since there the Rabi lineshape is the steepest, as indicated by the first-order derivative (dashed blue line) in Fig. 2.2. The error signal is defined as

$$E(\nu) = (p_+(\nu) - p_-(\nu))N_{\text{ions}}\frac{N_{\text{cycles}}}{2}. \tag{2.2}$$

N_{ions} and N_{cycles} are the number of interrogated ions and the total number of measurements on both probe points before the frequency correction is applied. The uncertainty of the frequency determination is given by the ratio of the uncertainty of the population measurements and the error signal slope:

$$\sigma_\nu = \frac{\sigma_p}{|\partial E/\partial \nu|}. \tag{2.3}$$

Close to resonance it is assumed that $\sigma_{p+} \approx \sigma_{p-} \approx \sigma_p$. State detection to decide whether the ions are in $|g\rangle$ or $|e\rangle$ is performed with the electron shelving technique [71] on a comparatively fast cycling transition and thus the signal from a single excitation on the clock transition is amplified with a large number of photons scattered by ions in $|g\rangle$. This method reduces technical uncertainties due to state detection to a negligible level.

Instead the uncertainty σ_p is limited by the quantum projection noise (QPN) [72], which is a fundamental limit and caused by the fact that every single interrogation yields only one bit of information by projecting the internal state of the ion onto the two states $|g\rangle$ and $|e\rangle$. Therefore, the uncertainty of multiple measurements follows a binomial distribution and yields $\sigma_p = \sqrt{N_{\text{cycles}}N_{\text{ions}}p(1-p)}$ for N_{cycles} interrogations of N_{ions} independent ions.

The QPN limited frequency uncertainty is then

$$\sigma_y = \frac{\sigma_\nu}{\nu} = \frac{\sqrt{N_{\text{cycles}} N_{\text{ions}} p(1-p)}}{\nu|\partial E/\partial \nu|} = \frac{1}{\kappa}\frac{\Delta\nu}{\nu}\frac{1}{\sqrt{N_{\text{ions}}}}\sqrt{\frac{t_{\text{c}}}{\tau}}, \tag{2.4}$$

here $\Delta\nu$ is the clock transition FWHM, τ the total time, $t_{\text{c}} = \tau/N_{\text{cycles}}$ is the duration of a single interrogation, and κ is a numerical factor of order unity that depends on details of the interrogation scheme. More details on the fundamental limit of the achievable instability in an optical clock based on a single ion are discussed in [73–75]. Depending on the operating regime, QPN can be surpassed by collective effects, such as entanglement of clock ions [30–35]

2. Theoretical basis for ion optical clocks

or cascaded interrogation schemes [27, 28].

QPN limited parallel interrogation of N_{ions} independent ions shortens the averaging time τ to reach a fixed instability by a factor $1/N_{\text{ions}}$ compared to the interrogation of a single ion. Figure 2.3 illustrates the best reported single-ion instability [19] and the achievable improvement by interrogating 10 and 100 ions with the same instability simultaneously. The averaging time to reach the best reported single-ion systematic uncertainty [18] is 13 d for a single ion, 31 h for 10 ions and 3 h for 100 ions which illustrates the potential of a multi-ion clock.
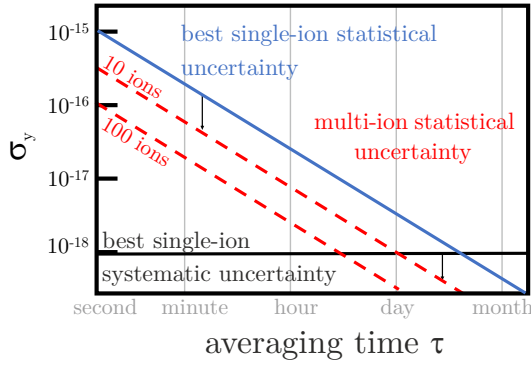
Figure 2.3.: *Achievable instability improvement by the parallel interrogation of 10 and 100 ions, assuming the best reported single-ion instability [19]. To resolve the best reported single-ion systematic uncertainty [18], an averaging time of 13 d is required for a single ion and 3 h for the parallel interrogation of 100 ions.*

In a lifetime limited measurement and because the uncertainty of the state detection σ_p is negligible, probing at δ_p (see Fig. 2.2), where the sensitivity $|\partial E/\partial \nu|$ is highest, is the optimal choice. As long as the interrogation is Fourier-limited, $|\partial E/\partial \nu|$ increases linearly with t_c. Reducing N_{cycles} in a given interval τ only scales σ_ν with $\sqrt{t_c} = \sqrt{N_{\text{cycles}}/\tau}$. The excited state lifetime ultimately limits the interrogation time.

The instability of a frequency ratio measurement of two frequencies ν_1 and ν_2 with their individual fractional frequency instabilities σ_{y,ν_1} and σ_{y,ν_2} is given by

$$\sigma_{\text{y},\nu_1/\nu_2} = \sqrt{\sigma_{y,\nu_1}^2 + \sigma_{y,\nu_2}^2}. \tag{2.5}$$

2.1.3. $^{115}\text{In}^+$ as a frequency standard

$^{115}\text{In}^+$ has several properties that make it a suitable candidate for a frequency standard. A simplified term scheme of $^{115}\text{In}^+$ is shown in Fig. 2.4, the hyperfine structure splitting resulting from the nuclear spin $I = 9/2$ is omitted for clarity.

Singly charged ions in group 13 feature a narrow $^1\text{S}_0 \leftrightarrow {}^3\text{P}_0$ transition with vanishing angular momentum of both states and have been suggested as frequency standards. This includes aluminium [76] indium [77] and thallium [78]. The $^1\text{S}_0 \leftrightarrow {}^3\text{P}_0$ transition is highly forbidden by angular momentum selection rules. However, hyperfine interaction couples the $^3\text{P}_0$ state to the $^3\text{P}_1$ and $^1\text{P}_1$ states with the same F quantum number [77]. The coupling strength increases with increasing mass, consequently the lifetime of the $^3\text{P}_0$ state decreases.

Figure 2.4.: *Simplified $^{115}In^+$ term scheme, showing all relevant transitions. The hyperfine structure is omitted for clarity. The narrow $^1S_0 \leftrightarrow {}^3P_0$ transition is used for clock spectroscopy and the $^1S_0 \leftrightarrow {}^3P_1$ transition for direct state detection.*
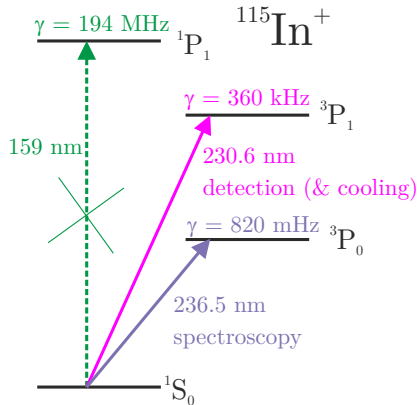
In ^{115}In$^+$, the $^1S_0 \leftrightarrow {}^3P_0$ transition is still reasonably narrow (0.82 Hz [79]) and the $^1S_0 \leftrightarrow {}^3P_1$ transition sufficiently wide (360 kHz [77]) for direct state detection via electron shelving [71]. This facilitates the simultaneous state detection for multiple ions. More complex detection strategies are needed for e.g. for ^{27}Al$^+$ [80–82] where both transitions have a longer lifetime and direct state detection on the $^1S_0 \leftrightarrow {}^3P_1$ transition is not feasible. While the shorter lifetimes in ^{115}In$^+$ are advantageous in terms of direct state detection the comparably small lifetime (195(8) ms [79]) of the excited clock state limits the ultimately achievable instability. State of the art clock lasers would even allow longer interrogation times, so that measures like entanglement of clock ions [30–35] or correlation spectroscopy [83], used to overcome the limits imposed by the local oscillator for long lived excited states, are not effective to improve the instability in ^{115}In$^+$.

All group 13 ions have a small differential static polarizability, which is the difference of the static electric-dipole polarizabilities between the two clock states [84] and results in a low sensitivity to the AC Stark effect by the clock laser or room temperature black-body radiation [85]. In ^{27}Al$^+$, the two polarizabilities are almost identical, resulting in the smallest sensitivity to the above effects. The described admixtures to the excited clock state $^3P_0$ lead to a modified g factor and a nonzero but very small electric quadrupole moment Θ of the group 13 ions compared to other candidates for frequency standards ($\Theta(^3P_0, {}^{115}In^+) = -1.6(3) \times 10^{-5} ea_0^2$ [86], where e is the elementary charge and a_0 the Bohr radius). This makes them highly suitable for frequency standards based on multiple ions where large static electric field gradients from the neighboring ions are present.

Another advantage of ^{115}In$^+$ is its high mass, which leads to a comparably low time dilation shift and its low second-order sensitivity to magnetic fields [79]. The clock transition wavelength of 236.5 nm can be generated as the fourth harmonic of an Nd:YAG laser at 946 nm and thus benefits from the high intrinsic frequency stability of a solid state laser. In addition to direct state detection, the $^1S_0 \leftrightarrow {}^3P_1$ transition at 230.6 nm offers the option of direct cooling [77], but the narrow linewidth only allows low cooling rates. An alternative for fast cooling would be the $^1S_0 \leftrightarrow {}^1P_1$ electric dipole transition (194 MHz), but its wavelength is in the vacuum-UV regime and presents a technical challenge [87] and not feasible with current laser technology. Sympathetic cooling of ^{115}In$^+$ with ^{172}Yb$^+$ ions has been proposed

in [20] and is applied in this work. ^{172}Yb$^+$ offers a favorable mass ratio [88] and has a convenient level scheme due to the lack of a nuclear spin. All relevant transitions are accessible with diode lasers and ^{172}Yb$^+$ features a narrow transition involving one state with a large g-factor, which can be used to in-situ precisely characterize the systematic shifts resulting for ^{115}In$^+$. The fluorescence of the Doppler cooling light can be used to detect excess micromotion (see section 2.4.1 and section 4.2). In principle this detection can even be done without additional dead time, during the cooling phases of the clock sequence. The efficiency of sympathetic cooling in linear dual species crystals on the example of ^{115}In$^+$/^{172}Yb$^+$ is analyzed in section 5.2. A second cooling stage on the ^{1}S$_0 \leftrightarrow$ ^{3}P$_1$ transition in ^{115}In$^+$ could be implemented after Doppler cooling. For single ions and two-ion ^{115}In$^+$ crystals, temperatures below $100\,\mu$K have been demonstrated [89].

The expected systematic frequency uncertainties of a multi-ion clock based on a linear ^{115}In$^+$/^{172}Yb$^+$ crystal are analyzed in [90].

2.2. Trapping ions in a linear rf Paul trap

This section is a brief summary about the concept of ion trapping in rf Paul traps. More comprehensive descriptions can be found in text books [91, 92]. In section 2.2.1 the mode spectrum for trapping linear dual-species crystals is derived.

The creation of a purely static electric potential of the form

$$\varphi(u_1, u_2, u_3) = \frac{U_{\text{dc}}}{2}(c_1 u_1^2 + c_2 u_2^2 + c_3 u_3^2) \tag{2.6}$$

to confine a charged particle in all three dimension is not possible according to the Earnshaw's theorem [93]. The Laplace equation $\Delta \phi = 0$ results in the condition $c_1 + c_2 + c_3 = 0$ for a charge-free region, which leads to a repulsive potential in at least one direction. To realize three dimensional confinement, a time dependent potential $\varphi_{\text{rf}}(u_1, u_2, u_3, t)$ is used in Paul traps [94, 95]. Typically, the oscillation frequency Ω_{rf} is in the rf range. To confine linear ion crystals, a linear geometry of the Paul trap is favorable. Here, rf confinement is only used in the radial plane along u_1 and u_2 and the Laplace equation is fulfilled by setting $c_2 = \text{-}c_1$ and $c_3 = 0$. In Fig. 2.5, the radial plane of a linear Paul trap is shown schematically.
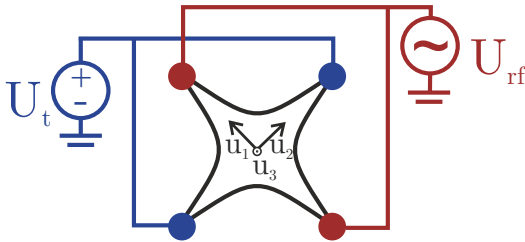
Figure 2.5.: *Schematic drawing of the radial plane in a linear Paul trap. The rf signal is applied asymmetric and the constant voltage U_{t} introduces an anisotropy between the directions u_1 and u_2.*

Close to the center, the potential can be approximated by

$$\varphi_{\mathrm{rad}} = (\kappa_{\mathrm{rf}} U_{\mathrm{rf}} \cos(\Omega_{\mathrm{rf}} t) - \kappa_{\mathrm{dc}} U_{\mathrm{t}}) \frac{u_1^2 - u_2^2}{2d}, \tag{2.7}$$

where d is the distance between the electrodes and the trap center. The factors κ are geometric constants of order unity. The constant voltage $U_{\mathrm{t}} \approx 10^{-3} \times U_{\mathrm{rf}}$ serves to introduce an anisotropy between u_1 and u_2. The linear crystal is aligned along the axial direction, where the rf field vanishes and harmonic confinement with the trap frequency ω_{ax} is created by a static electric field. In the original Paul trap design, hyperbolic shaped electrodes are used because they result in an almost purely harmonic potential over a large region. The associated limited optical access for laser beams and fluorescence detection can be improved by using other geometries. Here a chip based trap design, introduced in section 3.1 and described in detail in [22], is used. The shape of the electrodes is significantly different than the hyperbolic shape but close to the trap center the electric potential can be approximated by Eq. 2.7.

The equation of motion for a single particle with the mass m and the charge e is given by (e.g.[92])

$$\ddot{u}_i + (a_i + 2q_i cos(\Omega_{\mathrm{rf}} t)) \frac{\Omega_{\mathrm{rf}}^2}{4} u_i = \frac{eE_{\mathrm{dc,i}}}{m} \text{ with } i \in \{1, 2, 3\} \tag{2.8}$$

with the substitution of the dimensionless parameters

$$q_1 = -q_2 = \frac{2e\kappa_{\mathrm{rf}} U_{\mathrm{rf}}}{md^2\Omega_{\mathrm{rf}}^2}, \quad q_3 = 0, \tag{2.9}$$

$$a_{1,2} = -\frac{2\omega_{\mathrm{ax}}^2}{\Omega_{\mathrm{rf}}^2} \pm \frac{4e\kappa_{\mathrm{dc}} U_{\mathrm{t}}}{md^2\Omega_{\mathrm{rf}}^2} = a_{\mathrm{ax}} \pm a_{\mathrm{stat}} \text{ and } a_3 = \frac{4\omega_{\mathrm{ax}}^2}{\Omega_{\mathrm{rf}}^2}. \tag{2.10}$$

The term $\frac{eE_{\mathrm{dc,i}}}{m}$ describes the influence of an undesired external stray electric field E_{dc} which is described below.

Calculations of ion trajectories reveal that confinement is achieved within several stability regions in the a_i- and q_i-parameter space. More details can be found in [92]. The trap used in this work is operated in the lowest region of stability where $|a_i|, |q_i| \ll 1$ and the ion trajectory, described by Eq. 2.8, can be approximated by

$$u_i(t) = (u_{0,i} + u_{1,i} \cos(\omega_i t)) \left(1 + \frac{q_i}{2} \cos(\Omega_{\mathrm{rf}} t + \varphi_i)\right) \tag{2.11}$$

$$\text{with } \omega_i = \frac{\Omega_{\mathrm{rf}}}{2} \sqrt{a_i + \frac{q_i^2}{2}} \ i \in \{1, 2\}. \tag{2.12}$$

$u_{0,i}$ describes a possible static shift of the ion, caused by a static external field. The ion motion has two contributions, one is a harmonic oscillation at ω_i, called secular motion, the second is a fast rf driven oscillation with the frequency Ω_{rf}, referred to as micromotion. The micromotion can be separated in two constituents again: the term with the amplitude $\propto u_{1,i} \cos(\omega_i t)$ is connected to the ion oscillation around the trap center due to the secular motion and

2. Theoretical basis for ion optical clocks

is called intrinsic micromotion (IMM). The secular motion never vanishes completely and so the ion is periodically exposed to the rf field, but the amplitude of this motion can be reduced by cooling. The second micromotion component $\propto u_{0,i}$ is called excess micromotion (EMM) and occurs due to a residual rf field $\vec{E}_{\mathrm{rf}}$ at the potential minimum. It can be caused by a residual static electric field $\vec{E}_{\mathrm{dc}}$ or a phase shift between the rf electrodes (more details about possible phase shifts can be found in [22]). If the EMM is caused by a static electric field it can be minimized by the application of electric fields via the trap electrodes. The procedure for the compensation and the measurement of EMM is described in section 4.2.

For many considerations micromotion can be neglected because its amplitude is a factor $q_i/2$ smaller than the amplitude of the secular motion which can then be approximated by the motion of the ion in a harmonic potential. This so called ponderomotive potential or pseudo-potential describes the effect of the rf potential φ_{rf} averaged over the time of one rf period. Neglecting all dc contributions, the ponderomotive potential is given by

$$V_{\mathrm{p,rf}}(u_1, u_2, u_3) = \frac{e|\nabla\varphi_{\mathrm{rf}}(u_1, u_2, u_3)|^2}{4m\Omega_{\mathrm{rf}}^2} = \frac{e|\vec{E}_{\mathrm{rf}}(u_1, u_2, u_3)|^2}{4m\Omega_{\mathrm{rf}}^2}, \tag{2.13}$$

where $\vec{E}_{\mathrm{rf}} = -\nabla\varphi_{\mathrm{rf}}$ is the electric field corresponding to the rf potential. The ponderomotive potential $V_{\mathrm{p,rf}}$ is mass dependent and decreases with increasing ion mass m. The static electric field confinement is mass independent.

Even for the operation of the trap in the lowest region of stability where $|a_i|$, $|q_i| \ll 1$ a decreasing stability with increasing $|q_i|$ can be observed for larger Coulomb crystals as they are more sensitive to deviations from the quadratic potential. In section 5, the stability of a linear mixed $\mathrm{In}^+/\mathrm{Yb}^+$ crystal is analyzed for different radial trap potentials. The potential is classified in terms of the Mathieu q parameter of the radial trap frequency ω_{rad} of a single In^+ ion. The Mathieu q parameter corresponding to the two radial trap frequencies ω_i of a single ion can be obtained from rearranging Eq. 2.12 which results in:

$$q = \sqrt{\frac{8\,\omega_i^2}{\Omega_{\mathrm{rf}}^2} - 2a_i} \;\; i \in \{1, 2\}. \tag{2.14}$$

Here $a_i = a_{\mathrm{ax}} \pm a_{\mathrm{stat}}$ is the static E-field contribution to the radial potential consisting of an axial contribution a_{ax} and the field for the radial frequency splitting a_{stat}. The component a_{ax} can be calculated from the axial trap frequency ω_{ax} (see Eq. 2.9) and a_{stat} can be deduced from the two radial trap frequencies via

$$a_{\mathrm{stat}} = \frac{2}{\Omega_{\mathrm{rf}}^2}\left(\omega_1^2 - \omega_2^2\right) \tag{2.15}$$

with $\omega_1 < \omega_2$.

2.2.1. Motional spectra of linear dual-species crystals

With the linear ion trap in this work, large numbers of ions can be trapped simultaneously. When applying laser cooling, the kinetic energy of the individual ions typically becomes

small in comparison to the Coulomb energy and the ions form a crystalline structure, so called Coulomb crystals [96, 97]. The aspect ratio of the trap potential along the three trap axes determines if the crystal is 1-,2- or 3-dimensional. In the following, only the 1-dimensional linear ion Coulomb crystal is considered, where the N ions form a chain along the axial trap direction $z = u_3$, where micromotion is reduced to a minimum.

The Coulomb interaction between the ions modifies the effective trapping potential. The axial equilibrium positions can be found by minimizing the potential energy

$$V_{ax} = \sum_{i=1}^{N} \frac{1}{2} m_i \omega_{ax}^2 z_i^2 + \frac{1}{2} \sum_{i,j=1,i\neq j}^{N} \frac{e^2}{4\pi\varepsilon_0} \frac{1}{|z_i - z_j|}. \tag{2.16}$$

The motion of an N-ion Coulomb crystal can be described in terms of its N eigenmodes per dimension if the oscillation of the ions around their equilibrium positions is small. The derivation of the mode spectrum can be found in several publications [98–100]. The most general treatment, followed here, is for an arbitrary arrangement of ions with different masses, presented in [98].

Assuming small displacements of the ions from their equilibrium positions ($z_{0,i}$: $z_i(t) = z_{0,i} + q_i(t)$) allows to approximate the potential in Eq. 2.16 by a second-order Taylor expansion around the equilibrium positions to

$$V \approx \frac{1}{2} \sum_{i,j=1}^{N} q_i q_j \left[\frac{\partial^2 V}{\partial z_i \partial z_j} \right]_0 = \frac{1}{2} \sum_{i,j=1}^{N} q_i q_j V_{ij} \tag{2.17}$$

with

$$V_{ij} = \begin{cases} m_i \omega_{ax,i}^2 + \sum_{k=1,k\neq i}^{N} \frac{e^2}{2\pi\varepsilon_0} |z_{0,i} - z_{0,k}|^{-3} & \text{for} \quad i = j \\ \\ -\frac{e^2}{2\pi\varepsilon_0} |z_{0,i} - z_{0,j}|^{-3} & \text{for} \quad i \neq j. \end{cases} \tag{2.18}$$

The same approach with a displacement perpendicular to the axis can be used for the radial directions. For a linear chain $x_{0,i} = y_{0,i} = 0$ which leads to

$$V_{ij} = \begin{cases} m_i \omega_{rad,i}^2 - \sum_{k=1,k\neq i}^{N} \frac{e^2}{4\pi\varepsilon_0} |z_{0,i} - z_{0,k}|^{-3} & \text{for} \quad i = j \\ \\ \frac{e^2}{4\pi\varepsilon_0} |z_{0,i} - z_{0,j}|^{-3} & \text{for} \quad i \neq j. \end{cases} \tag{2.19}$$

Two important differences exist between the radial and the axial case. $m_i \omega_{ax,i}^2$ is caused by a static electric field in linear trap and thus only depends on the charge. Contrary the corresponding rf confinement term, has a mass dependency ($\propto m_i^{-1}$). This results in different values of $m_i \omega_{rad,i}^2$ for the individual ions in a mixed-species crystal. The second difference is that the Coulomb interaction reduces the total potential in the radial potential and increases it in the axial potential, which reflects that a radial displacement of an ion increases the

2. Theoretical basis for ion optical clocks

distance to all neighboring ions.

The eigenvectors β_α with $\alpha = 1 \dots N$ of V define the normal modes of motion

$$\sum_{j=1}^{N} V_{ij}\beta_{\alpha,j} = \lambda_\alpha m_i \beta_{\alpha,i} \; , \tag{2.20}$$

where the mode eigenfrequencies $\omega_\alpha = \sqrt{\lambda_\alpha}$ have to be real values for stable confinement.

In case of a linear crystal consisting of single species, there is a center of mass mode (COM mode) for each dimension in which all ions oscillate in phase at the single-ion trap frequency. Because of the different sign of the Coulomb term in Eq. 2.19 and Eq. 2.18 the COM mode is the lowest frequency mode in the axial direction and the mode with the highest frequency in the radial directions.

Figure 2.6 shows the example of a mode spectrum of a linear 10 In^+/4 Yb^+ crystal. The axial modes (black) split across a large frequency range while the radial modes (pink and blue) arrange into two blocks. The low frequency block (in blue) corresponds to radial modes where mostly the Yb^+ ions oscillate while the high frequency block (in pink) is associated with radial modes with high motional contribution of In^+ ions. The splitting of the radial modes illustrates the effect of the mass dependency of the $m_i\omega_{\mathrm{rad},i}^2$ term in Eq. 2.19. The frequency splitting strongly depends on the aspect ratio of the trap potential, the mass difference of the two species and the permutation of the crystal.
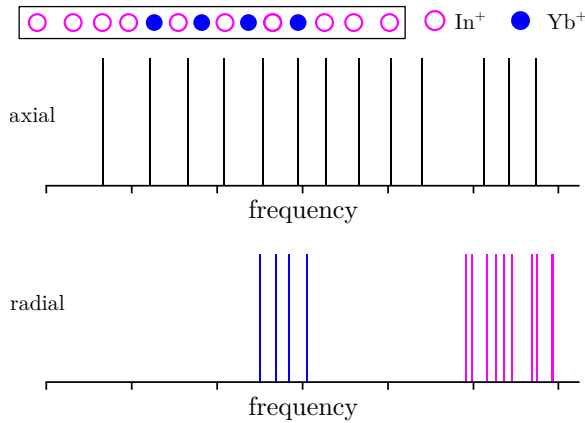
Figure 2.6.: *Motional mode spectrum of a linear 10 In^+/4 Yb^+ crystal. The crystal permutation is shown in the inset. The axial modes (black) split across a large frequency range. In the radial blue (pink) modes mostly the Yb^+ (In^+) ions oscillate.*

A given set of ion displacements can be expressed as a set of normal mode excitations by a transformation into the $\{\beta_\alpha\}$ basis

$$\pi_\alpha = \sum_{i=1}^{N} \beta_{\alpha,i} q_i = \sqrt{\frac{\hbar}{2\omega_\alpha}} \left(\hat{a}_\alpha + \hat{a}_\alpha^\dagger \right) \; , \tag{2.21}$$

where in the second step, the annihilation operator $\hat{a}_\alpha$ of the mode has been introduced. The eigenvectors β_α are mutually orthogonal, if all ions have identical masses. Due to the

mass dependence of the energy corresponding to a given displacement, this is not true for mixed-species crystals. In that case, a set of orthogonal eigenvectors β'_α can be realized by defining mass-weighted displacements $q'_i = \sqrt{m_i}q_i$ and replacing $V_{i,j}$ by $V'_{i,j} = V_{i,j}/\sqrt{m_i m_j}$ [98].

2.3. Interaction of trapped particles with laser light

In the previous sections, the trapped ions have been treated as classical point particles with the mass m and the charge e. However, the interaction of laser light with the strong confined ions allows the observation and control of quantum properties. The internal and external degrees of freedom can be characterized and controlled. This section provides a brief summary about the interaction of laser light with trapped particles and follows the summary given in [101, 102]. More detailed descriptions can be found, e.g., in [9, 103].

For simplicity the discussion is restricted to one dimension and a purely harmonic trap potential with secular frequency ω_{sec} and an effective two-level system with the internal ground state $|g\rangle$ and excited state $|e\rangle$ which are separated by the energy difference $\hbar\omega_0$. The interacting laser field is a traveling wave single mode laser with the wave vector $\vec{k}$ pointing along the x-axis and the frequency ω_L which is tuned close to the transition frequency ω_0. The laser electric field is described by $E(t) = E_0 \cos(\omega_{\mathrm{L}}t + k_x \hat{x})$. Setting the internal and external ground state energies to 0 results in the description of the system by the hamiltonian $\hat{H}$ that consists of the hamiltonian $\hat{H}_0$ determined by the ion and the trap and the interaction hamiltonian $\hat{H}_{\mathrm{i}}$

$$\hat{H} = \hat{H}_0 + \hat{H}_i \tag{2.22}$$

$$\hat{H}_0 = \hat{H}_{\mathrm{ion}} + \hat{H}_{\mathrm{trap}} = \hbar\omega_0|e\rangle\langle e| + \hbar\omega_{\mathrm{sec}}\hat{a}^\dagger\hat{a} \ , \tag{2.23}$$

$$\hat{H}_{\mathrm{i}} = \frac{1}{2}\hbar\Omega_0\left(|e\rangle\langle g| + |g\rangle\langle e|\right)\left(e^{i(\omega_{\mathrm{L}}t + k_x\hat{x})} + e^{-i(\omega_{\mathrm{L}}t + k_x\hat{x})}\right) \ . \tag{2.24}$$

Here, $\hat{a}$ is the harmonic oscillator annihilation operator, $k_x = (2\pi/\lambda)$ the x component of the wave vector of the single mode laser and $\Omega_0 \propto E_0$ the free ion Rabi frequency that is defined by the coupling strength of the laser ion-interaction and contains the details of the electronic transition. Transforming to the interaction picture with respect to $\hat{H}_0$ and neglecting terms which oscillate at $2\omega_0$ leads to

$$\hat{H}' = e^{i\hat{H}_0 t/\hbar}\hat{H}_i e^{-i\hat{H}_0 t/\hbar} = \frac{1}{2}\hbar\Omega_0 \times e^{i\omega_{\mathrm{sec}}t\hat{a}^\dagger\hat{a}}\left(|e\rangle\langle g|e^{-i(\Delta t - k_x\hat{x})} + |g\rangle\langle e|e^{i(\Delta t - k_x\hat{x})}\right)e^{-i\omega_{\mathrm{sec}}t\hat{a}^\dagger\hat{a}} \ , \tag{2.25}$$

with $\Delta = \omega_{\mathrm{L}} - \omega_0$. The matrix element for the transition from $|g\rangle$ to $|e\rangle$ with a simultaneous change in the motional quantum number for $|n\rangle$ to $|n'\rangle$ is

$$\langle n', e|\hat{H}'|n, g\rangle = \frac{1}{2}\hbar\Omega_0\left\langle n'\left|e^{ik_x\hat{x}}\right|n\right\rangle e^{i[\Delta + (n'-n)\omega_{\mathrm{sec}}]t} \ . \tag{2.26}$$

2. Theoretical basis for ion optical clocks

The resonance is shifted by the difference in motional energy $\hbar\omega_{\text{sec}}(n' - n)$ to fulfill energy conservation as the exponential term shows and effectively energy is transferred from the electronic transition $|g\rangle \to |e\rangle$ to the motional transition $|n\rangle \to |n'\rangle$. The relative strength of the transition is defined by the matrix element $\langle n'|e^{ik_x\hat{x}}|n\rangle$. Transitions with $n' = n$ are named carrier transitions, and transitions with $n' > n$ and $n' < n$ are referred to as blue sideband transitions (BSBs) and red sideband transitions (RSBs), respectively. Sideband transitions with $\Delta n = |n - n'| = 1, 2, ..., n$ are called 1st order, 2nd order, or n-th order transitions.

The Lamb-Dicke parameter η [104] relates the extension of the motional ground state wave function x_0 along x to the laser frequency ω_L and is defined as

$$\eta = k_x x_0 = k\sqrt{\frac{\hbar}{2m\omega_{\text{sec}}}} = \sqrt{\frac{\omega_{\text{r}}}{\omega_{\text{sec}}}} \ . \tag{2.27}$$

The ratio of the photon recoil frequency ω_r to the single phonon frequency ω_{sec} can be expressed as η^2. If there is an angle θ between the wave vector $\vec{k}$ and the considered principal trap axis, η reduces by a factor $\cos\theta$. With the expression of the position operator $\hat{x}$ in terms of $\hat{a}$, the ground state wavefunction spread x_0 as $\hat{x} = x_0(\hat{a} + \hat{a}^\dagger)$ and the Lamb-Dicke parameter η the matrix element $\langle n'|e^{ik_x\hat{x}}|n\rangle$ can be evaluated [9]:

$$\mu_{n,n'} = \langle n'|e^{ik_x x_0(a+a^\dagger)}|n\rangle = \langle n'|e^{i\eta(a+a^\dagger)}|n\rangle = e^{-\frac{1}{2}\eta^2}\sqrt{\frac{n_<!}{(n_< + \Delta n)!}}(i\eta)^{\Delta n}L_{n_<}^{\Delta n}\left(\eta^2\right) \ , \tag{2.28}$$

where $n_<$ is the lesser of the two values and $L_n^\alpha(x)$ is a generalized Laguerre polynomial.

The expression in Eq. 2.28 is simplified in the so called Lamb-Dicke regime where

$$\eta^2(2n + 1) \ll 1 \ , \tag{2.29}$$

the exponential in Eq. 2.28 can be replaced by a 1st-order approximation in $\eta(\hat{a} + \hat{a}^\dagger)$ and sideband transitions of order $|\Delta n| > 1$ can be neglected. This is an important regime for spectroscopy, since under this condition, the 1st-order Doppler effect on the carrier transition can be neglected as the trap absorbs the recoil energy of photons that are emitted by the ion [105].

The derivation can be extended to multiple motional modes. Each mode introduces new sidebands and an additional factor μ which reduces the transition strength. For Coulomb crystals, the Lamb-Dicke parameter of mode α for ion i can be calculated from the quantities derived in section 2.2.1 as [98]:

$$\eta_{\alpha,i} = k\beta'_{\alpha,i}\sqrt{\frac{\hbar}{2m_i\omega_\alpha}}\cos(\theta), \tag{2.30}$$

where θ is the angle between $\vec{k}$ and the trap principal axis of the mode. When a thermal ensemble is probed, the resulting distribution of Rabi frequencies, caused by the distribution of the Lamb-Dicke parameters of the modes $\eta_{\alpha,i}$, leads to a loss of contrast due to the dephasing of the Rabi oscillations. Since the carrier transition is affected as well, every mode

with a projection onto $\vec{k}$ contributes to this effect. If N modes contribute, the excited state population after a pulse of length t is

$$p_e = \sum_{n_1,\ldots,n_N=0}^{\infty} \left(\prod_{\alpha=1}^{N} P_\alpha(n_\alpha) \right) \sin^2 \left(\Omega_0^{(\text{int})} t \prod_{\alpha=1}^{N} \mu_{n_\alpha,n_\alpha'} \right), \qquad (2.31)$$

where $P_\alpha(n_\alpha)$ is the thermal occupation of state n_α. This is also known as the Debye-Waller effect [106].

The experimental results on the spectroscopy of the narrow $^1S_0 \leftrightarrow {}^3P_0$ transition in ^{115}In$^+$ at $236.5\,$nm, presented in section 6.2, contain Rabi frequency scans and Rabi oscillations, where the the excited state population (excitation probability) p_e is probed with a laser with the frequency ω_L. The generalized Rabi frequency, given in Eq. 2.32, describes the Rabi frequency in dependence of the free ion Rabi frequency Ω_0 and the detuning $\delta = \omega_L\text{-}\omega_0$ between the laser frequency and the atomic resonance frequency ω_0:

$$\Omega = \sqrt{\delta^2 + \Omega_0^2} = \sqrt{(\omega_L - \omega_0)^2 + \Omega_0^2}. \qquad (2.32)$$

The pure state Ψ of a two level system consisting of the electronic ground state $|g\rangle$ and the excited state $|e\rangle$ is described by the superposition [107]

$$\Psi(t) = c_g(t) \exp(-i\frac{\omega_0 t}{2})|g\rangle + c_e(t) \exp(i\frac{\omega_0 t}{2})|e\rangle. \qquad (2.33)$$

The amplitudes c_g and c_e of the ground and excited state are normalized to $|c_g(t)|^2 + |c_e(t)|^2 = 1$. When the ion is initially in the electronic ground state, $c_g(0) = 1$ and $c_e(0) = 0$, the excited-state population is given by

$$p_e(t) = |c_e(t)^2| = \frac{\Omega_0^2}{\Omega^2} \sin^2(\frac{1}{2}\Omega t) = \frac{\Omega_0^2}{\Omega_0^2 + \Delta^2} \sin^2(\frac{t}{2}\sqrt{\Omega_0^2 + \Delta^2}). \qquad (2.34)$$

For a π-pulse, defined by the interaction time $t = \tau_p = \pi/\Omega$, the population in the excited state $|e\rangle$ is maximized. Full state transfer with $p_e(\nu) = p_{e,\text{max}}$ only occurs on resonance, where $\delta = 0$. In theory $p_{e,\text{max}} = 1$, if the interaction time τ_p is much shorter than the excited state lifetime τ. For interaction times $\tau_p \leq \frac{\pi}{\Omega} \ll \tau$ the observed lineshape $p_e(\nu)$ when scanning the laser frequency over the resonance is depicted in Fig. 2.2. It incorporates the sinc-function sidelobes and a full width at half maximum of FWHM $\approx 0.9/\tau_p$ [69]. The derivation of an error signal from this Rabi lineshape to lock an ultra-stable laser to the atomic resonance, is described in section 2.1.2. Different line broadening effects can broaden the observed lineshape, as described, e.g., in [69] .

For the interaction between a laser and the trapped particle, two regimes need to be differentiated that depend on the ratio between the transition linewidth Γ that is addressed with the laser and the strength of the confinement of the trap described by the secular frequency ω_{sec}. The two regimes are illustrated in Fig. 2.7 (a) and (b). In the weak binding regime (a) $\Gamma > \omega_{\text{sec}}$ and the transition is broader than the spacing $\hbar\omega_{\text{sec}}$ of the equidistant energy levels

2. Theoretical basis for ion optical clocks

of the harmonic oscillator. Thus the laser can excite all of the resonances whose transition frequencies fall inside the resonance curve. The second regime, called strong binding regime, has been assumed for the derivation above. For $\Gamma < \omega_{\text{sec}}$ (b) the individual resonances are resolved and called motional sidebands, as described before. Therefore this regime is also called resolved-sideband regime. In this regime, the laser can be tuned to certain sidebands and selectively drive transitions between the corresponding vibrational states. For the control of trapped particles, transitions in both regimes are important.
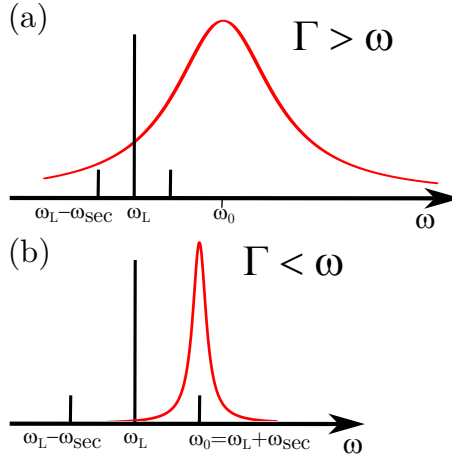
Figure 2.7.: *Illustration of the weak (a) and strong (b) binding regimes. The atomic resonance with the width Γ is displayed by the Lorentz curve. The relative absorption probabilities of the laser and its sidebands are indicated by the vertical lines. The frequencies are shown in the reference frame of the ion.*

2.3.1. Sympathetic Doppler cooling of linear dual-species crystals

This section only briefly explains the principal of Doppler cooling. More detailed descriptions can be found, e.g., in [69, 101, 108, 109]. The focus of this section is on the calculation of the efficiency of sympathetic Doppler cooling in linear dual-species Coulomb crystals. This sets the theoretical basis for the calculations presented in section 5.2, where the dependency between the efficiency of sympathetic cooling and the crystal composition and exact arrangement of the ions, called the permutation, is analyzed systematically.

For Doppler cooling, the ions are irradiated with laser light that drives a broad transition, fulfilling the condition $\Gamma > \omega_{\text{sec}}$ of the weak binding regime (compare section 2.3). The frequency of the laser has to be red detuned by $\Delta = \omega_{\text{L}} - \omega < 0$ from the resonance, this means the frequency of the laser is smaller than the resonance frequency. The absorption spectrum is given by a Lorentzian shape. With every absorption, the ion gets a momentum kick $\Delta p = \hbar k$ in the direction of the incoming wave with the wavevector $\vec{k}$. Due to the Doppler effect the probability to absorb a red detuned photon is higher when the ion is traveling towards the laser beam. The subsequent spontaneous emission of photons is isotropic such that on average no momentum is transferred. On average this leads in effective cooling of the ion in the trap. For an ion trapped in a 3-dimensional harmonic potential, a single red detuned laser beam with projections onto all three principal axes of the trap potential is sufficient to cool the ion in all three dimensions. The oscillating movement of the ion ensures

that a projection of the wave vector $\vec{k}$ is antiparallel to the ion half of the time. A balance is established between the cooling rate and the heating rate due to spontaneous emission. The Doppler temperature T_{D} is the lowest achievable temperature with Doppler cooling and is given by the following expression in case of the optimal detuning $\Delta = \text{-}\Gamma/2$:

$$T_{\mathrm{D}} = \frac{\hbar\Gamma}{2k_{\mathrm{B}}}. \tag{2.35}$$

The recoils of the spontaneously emitted photons cause Brownian motion and limit the achievable temperature. The Doppler limit assumes equal projections of the cooling beam onto all three cooled motional mode directions. Energies below the Doppler limit in one direction can be realized by reducing the angle between the laser beam and the movement of this mode, but this increases the temperature in the other mode [110].

As the Doppler temperature T_{D} is directly proportional to the linewidth Γ, there is a trade-off between minimum temperature and high photon scattering rate and thereby fast cooling.

The Doppler temperature for the $^2S_{1/2} \leftrightarrow {}^2P_{1/2}$ cooling transition in ^{172}Yb$^+$ at $370\,$nm with $\Gamma = 2\pi \times 19.6\,$MHz is $T_{\mathrm{D}} = 0.47\,$mK.

Large micromotion amplitudes can influence the efficiency of Doppler cooling because of micromotion sidebands in the absorption spectrum at $\omega_0 \pm \Omega_{\mathrm{rf}}$. Then a laser with detuning $|\Delta| < \Omega_{\mathrm{rf}}$ is blue detuned to his sideband and correspondingly the ion will be heated. This can be avoided by carefully minimizing EMM.

Starting from here linear dual-species ion crystals are considered in which one species is Doppler cooled. The Coulomb interaction between the ions couples the motion, as described in section 2.2.1. Thus applying Doppler cooling to one species will lead to cooling of the other species as well. The efficiency of this process depends on the mode structure of the crystal. Efficient cooling can be realized for modes with large motional contribution of the cooling ions while the energy transfer and therefore cooling is poor in a mode in which the motion is dominated by the second species [98]. The mass-ratio dependence of the efficiency of sympathetic cooling in dual-species 2-ion crystals has been investigated in detail [88, 100, 111]. The calculations of the efficiency of sympathetic Doppler cooling in longer linear dual-species Coulomb crystals presented in section 5.2 are based on the following derivations.

Following [101], the cooling transition scattering rate as a function of ion velocity $\vec{v}$ is linearized:

$$\Gamma_{\mathrm{sc}}(\mathrm{v}) \approx \Gamma_{\mathrm{sc},0} \left(1 + \vec{\rho} \cdot \vec{v}\right), \tag{2.36}$$

where the direction of the friction coefficient $\vec{\rho}$ is parallel to the $\vec{k}$ vector of the cooling laser.

The velocity component $v_{i,\alpha}$ for ion i with mass m_i in mode α of a Coulomb crystal can be related to the mode excitation π_α via the eigenvector component $\beta'_{i\alpha}$ [98] in mass-weighted

2. Theoretical basis for ion optical clocks

coordinates (see section 2.2.1):

$$v_{i,\alpha} = \frac{\beta'_{i,\alpha}}{\sqrt{m_i}} \dot{\pi}_\alpha \tag{2.37}$$

In this linear model, the temperature of each mode is described by the differential equation

$$\dot{T}_\alpha = c_{0,\alpha} - c_{1,\alpha} T_\alpha \ , \tag{2.38}$$

where $c_{0,\alpha}$ contains the heating rates due to spontaneous emission, recoil and fluctuating external electric fields, while $c_{1,\alpha}$ describes cooling due to photon absorption. The temperature thus exponentially approaches its equilibrium value $T_{\text{eq},\alpha} = c_{1,\alpha}/c_{0,\alpha}$, at a rate determined by

$$c_{1,\alpha} = \frac{k_B \Gamma_{\text{sc},0} \hbar k \rho}{m_{\text{cool}}} \cos(\theta_\alpha) C_\alpha \ , \tag{2.39}$$

$$\text{with } C_\alpha = \sum_{i=1}^{N_{\text{cool}}} \beta'^2_{\alpha,i} \ . \tag{2.40}$$

Here, θ_α describes the angle between $\vec{k}$ and the principal axis of mode α. The sum C_α in Eq. 2.40 quantifies the participation of cooling ions in mode α and thus scales the cooling rate independently of laser parameters or atomic properties, except for the mass ratio between the species. Due to the normalization of $\vec{\beta}'_\alpha$, $C_\alpha = 1$ for all modes in a crystal consisting entirely of cooling ions. As a reference for the values of C_α, cooling on the 370 nm $^2\text{S}_{1/2} \leftrightarrow {}^2\text{P}_{1/2}$ transition in Yb$^+$ with $\Gamma = 2\pi \times 19.6$ MHz is considered, where a saturation parameter $s = 2$ and $\theta_\alpha = 0$ are assumed, which leads to an $1/e$ time of

$$t_{\text{cool},\alpha} = \frac{1}{c_{1,\alpha}} \approx \frac{38\,\mu\text{s}}{C_\alpha} \ . \tag{2.41}$$

The equilibrium temperatures are independent of C_α as long as external heating is negligible. The saturation parameter s is defined as

$$s = \frac{I}{I_{\text{sat}}}, \tag{2.42}$$

with the intensity I and the saturation intensity I_{sat}.

All presented calculations of C_α in section 5.2 are based on ^{172}Yb$^+$ as the cooling ion and ^{115}In$^+$ as the sympathetically cooled spectroscopy ion. The results can be transferred to ^{40}Ca$^+$/^{27}Al$^+$ crystals, since the mass ratios are very similar.

2.3.2. Resolved sideband cooling

To cool the ion to the motional ground state, Doppler cooling described in section 2.3.1 is usually not sufficient. In this work, cooling to the ground state has only been used to determine the external heating rate of the ion trap. The most common implementation of cooling

to the motional ground state is resolved sideband cooling [7], for which cooling a transition in the strong binding regime, fulfilling the condition $\Gamma < \omega_{\text{sec}}$ (see Se. 2.3), is required. In this regime, the individual motional sidebands can be resolved and addressed. To cool a mode the laser frequency is set to a red sideband. With each excitation, the motional quantum number is reduced by one. In the Lamb-Dicke regime, the motional state is not affected by the subsequent emitted photon. Thus every cycle of absorption and spontaneous emission reduces the motional quantum number by one until the ion reaches the ground state.

The cooling rate of sideband cooling is much lower than for Doppler cooling because of the narrower transition. This problem can be circumvented by artificially broadening the transition via a short lived auxiliary state $|a\rangle$. After each excitation to $|e\rangle$, a laser tuned to the transition $|e\rangle \rightarrow |a\rangle$ excites the ion to the auxiliary state from which the ion rapidly decays to the ground state. This process effectively shortens the lifetime of the excited state and thereby increases the cooling rate. Repumping can either be implemented in a pulsed or continuous fashion. In this work, the continuous process is implemented: The two transitions $|g\rangle \rightarrow |e\rangle$ and $|e\rangle \rightarrow |a\rangle$ are driven simultaneously which leads to an effective two-level system with a dressed excited state $|e'\rangle$ and a tunable decay rate Γ' [112]. The advantage of this method over the pulsed scheme is that only one long sideband cooling pulse is required to cool the ion to the ground state. In addition, the tuning of Γ' allows to adjust the cooling rate and the finally achievable mean phonon number $\bar{n}$. The intensity and the frequency of the auxiliary laser have to be controlled precisely.

The lowest achievable mean phonon number after resolved sideband cooling is approximated by [9, 108]

$$\bar{n} \approx \frac{\Gamma^2}{\omega_{\text{sec}}^2} \approx \frac{\Gamma'^2}{\omega_{\text{sec}}^2}. \tag{2.43}$$

Here, Γ is the decay rate of the excited state $|e\rangle$ and therefore $\Gamma = \Gamma'$ in case of continuous sideband cooling. Off-resonant excitation of the carrier transition with subsequent decay on the blue sideband and off-resonant excitation of the blue sideband followed by decay on the carrier transition are the dominant heating processes. The probability of the heating processes depends of the effective linewidth of the transition to the excited state. Thus the tuned effective linewidth is a trade-off between cooling rate and lowest achievable $\bar{n}$.

This work employs continuous sideband cooling of a single ^{172}Yb$^+$ ion via the ^{2}S$_{1/2} \leftrightarrow ^2D_{5/2}$ quadrupole transition at 411 nm. The excited state lifetime is shortened via the ^{2}D$_{5/2} \leftrightarrow ^2P_{3/2}$ transition at 1650 nm.

2.4. Systematic frequency shifts

In this section, the most dominant sources of systematic frequency shifts for frequency standards based on trapped ions are explained briefly. For the determination of the unperturbed

2. Theoretical basis for ion optical clocks

transition frequency or the evaluation of frequency ratios measured between different frequency standards, those shifts need to be measured and corresponding corrections need to be applied. More details about the different sources of frequency shifts be be found, e.g., in [67].

The focus of this section is on the trap-related shifts, as those are the major contributions in the most accurate reported ion based frequency standards [18, 19]. In addition section 4 presents the characterization of the frequency shifts related to the ion trap for a linear multi-ion In^+/Yb^+ crystal.

2.4.1. Motional frequency shifts

Several motional frequency shifts exist in an ion trap. If the optical path length between the laser source and ion trap is stabilized, the first-order Doppler shift, which scales with the average velocity $\langle v \rangle/c$ of the ions along the laser direction, is usually suppressed. As the linewidth of the clock transition is much smaller than the secular frequency ω_{sec} and the trap drive frequency Ω_{rf}, both components of motion induce resolved sidebands and do not result in a first-order Doppler shift on the carrier transition. Nevertheless, they lead to a relativistic time dilation shift, also called second-order Doppler shift,

$$\left\langle \frac{\Delta \nu_{D2,th}}{\nu} \right\rangle = -\frac{\langle v^2 \rangle}{2c^2} = -\frac{\langle E_{kin} \rangle}{mc^2} \,, \tag{2.44}$$

which is given by the ratio between the mean kinetic energy $\langle E_{kin} \rangle$ and the rest energy. According to Eq. 2.44, the shift is independent of the atomic transition, but only depends on the speed of the ion. Thus a heavier ion has a smaller second-order Doppler shift for a given kinetic energy.

Influence of the secular motion and the ion heating rate
For a thermal state of temperature T, the secular motion kinetic energy of a mode is given by $\frac{1}{2}k_B T$. The intrinsic micromotion (IMM) also depends on the secular motion amplitude as explained in section 2.2. Under the assumption that the static potential is negligible for the radial trapping potential ($|a| \ll q^2$), the second-order Doppler shift $\frac{\Delta \nu_{D2,th}}{\nu}$ for i resulting from the secular motion in a linear mixed-species crystal can be expressed as [90]

$$\left\langle \frac{\Delta \nu_{D2,th}}{\nu} \right\rangle_i = -\sum_\alpha \frac{k_B T_\alpha}{2c^2} \frac{\beta_{\alpha,i}'^2}{m_i} \left(1 + \frac{\omega_i^2}{\omega_\alpha^2} + \frac{\omega_i^2}{\Omega_{rf}^2} \right). \tag{2.45}$$

Here, ω_i is the secular frequency of the COM mode of species i for pure rf confinement, thus ($a_i = 0$ in Eq. 2.12).

As long as the external heating rate of the ions in the trap is sufficiently low, the temperature of the ions and thus $\left\langle \frac{\Delta \nu_{D2,th}}{\nu} \right\rangle_i$ are independent of the used ion trap. But the heating rate can lead to a significant temperature increase of the ions during the probe pulse or require constant cooling during the probe pulse. The former leads to an increased temperature uncertainty and accordingly to an increased uncertainty of the second-order Doppler shift

$\left\langle \frac{\Delta\nu_{\mathrm{D2,th}}}{\nu} \right\rangle_i$. The cooling light in case of constant cooling during the probe pulse might induce an ac Stark-shift.

Electric field noise can excite the secular motion and thus heat the ions. The relation between the heating rate $\dot{\bar{n}}$ (in the unit phonons/s) of a single ion and the power spectral density S_E of the electric field noise is given by [113]

$$\dot{\bar{n}} = \frac{e^2}{4m\hbar\omega_{\mathrm{sec}}} S_E(\omega_{\mathrm{sec}}) \tag{2.46}$$

if micromotion is neglected. The origin of the external heating rate $\dot{\bar{n}}$ is discussed in section 4.3.2, where measurements of $\dot{\bar{n}}$ and the resulting influence on the second-order Doppler shift are also characterized for the used ion trap.

Because the distance between the ions and the electrodes are large, compared to the extension of a linear chain, the fields responsible for heating are assumed to be uniform across the crystal. The heating rates of higher-order modes α in linear mixed-species crystals can be calculated according to [100]

$$\dot{\bar{n}}_\alpha = \left(\sum_i \frac{\beta'_{\alpha,i}}{\sqrt{m_i}} \right)^2 \frac{e^2}{4\hbar\omega_\alpha} S_E(\omega_\alpha) = \left(\sum_i \frac{\beta'_{\alpha,i}}{\sqrt{m_i}} \right)^2 \dot{\bar{n}}_{\mathrm{meas}}(\omega_\alpha) \cdot m_{\mathrm{meas}}. \tag{2.47}$$

Here ω_α are the eigenmode frequencies and $\beta'_{\alpha,i}$ the eigenvector components of ion i for mode α in mass-weighted space, as introduced in section 2.2.1. The eigenvectors are normalized which means $\sum_i \beta'^2_{\alpha,i} = 1$. $\beta'_{\alpha,i}$ can have both signs, so that the contributions of different ions in the sum in Eq. 2.47 compensate for most modes and only the COM modes heat significantly. The power spectral density $S_E(\omega_\alpha)$ at the eigenmode frequencies ω_α can be obtained from single ion heating rate measurements $\dot{\bar{n}}_{\mathrm{meas}}$ and extrapolated to ω_α with a power law relation [114], which is given in section 4.3.2. m_{meas} is the mass of the single ion species which was used for the determination of $\dot{\bar{n}}_{\mathrm{meas}}$.

$\dot{\bar{n}}_\alpha$ results in a temporal increase of the second-order Doppler shift of

$$\frac{\partial}{\partial t}\left(\frac{\Delta\nu_{\mathrm{D2,th}}}{\nu} \right) = -\sum_\alpha \frac{\dot{\bar{n}}_\alpha \hbar\omega_\alpha}{2c^2} \frac{\beta'^2_{\alpha,i}}{m_i} \left(1 + \frac{\omega_i^2}{\omega_\alpha^2} + \frac{\omega_i^2}{\Omega_{\mathrm{rf}}^2} \right). \tag{2.48}$$

Influence of EMM

The mean kinetic energy due to EMM is given by

$$\langle E_{\mathrm{kin,EMM}} \rangle = \frac{m}{2} \langle v_{\mathrm{EMM}}^2 \rangle = \frac{1}{m} \left(\frac{e}{2\Omega_{\mathrm{rf}}} \right)^2 \langle E_{\mathrm{rf}} \rangle^2, \tag{2.49}$$

which results in a fractional second-order Doppler shift of [115]

$$\left\langle \frac{\Delta\nu_{\mathrm{D2,EMM}}}{\nu} \right\rangle = -\frac{\langle E_{\mathrm{kin,EMM}} \rangle}{mc^2} = -\left(\frac{e}{2cm\Omega_{\mathrm{rf}}} \right)^2 \langle E_{\mathrm{rf}}^2 \rangle,$$
$$\text{with } \langle E_{\mathrm{rf}}^2 \rangle = \sum_{i=x,y,z} \langle E_{\mathrm{rf,i}}^2 \rangle. \tag{2.50}$$

23

2. Theoretical basis for ion optical clocks

$E_{\mathrm{rf,i}}$ are the rf electric field components along the three directions. Measurements of the residual rf electric field components $E_{\mathrm{rf,i}}$ and the derived second-order Doppler shifts are presented in section 4.7.

2.4.2. Electromagnetic field induced frequency shifts

External electromagnetic fields shift the energy levels of the clock transition via the Stark and Zeeman effects.

Light field induced ac Stark shift
Off-resonant laser radiation present during the clock probe pulse shifts the energy levels of the clock transition. For this reason, all other lasers are switched off during clock interrogation. The beams are blocked with mechanical shutters to ensure that absolutely no light that possibly leaks trough an acousto-optic modulator (AOM) irradiates the ions during the clock pulse.

Also the probe laser itself can induce an ac Stark shift. For In$^+$, this shift is at the level of 1×10^{-22} and thus negligible [116].

rf field induced ac Stark shift
The trap rf field not only induces a second-order Doppler shift, but also an ac Stark shift $\Delta \nu_S$ (Eq. 2.51): Because the trap drive frequency Ω_{rf} is far detuned from the strongly allowed electronic transitions coupling to the clock states, it depends only on the differential static polarizability of the clock states $\Delta\alpha_{\mathrm{stat}} = (3.3 \pm 0.3) \times 10^{-41}$ Jm^2/V^2 [85] and the dynamic polarizability can be neglected.

$$
\left\langle \frac{\Delta \nu_S}{\nu} \right\rangle = \frac{\Delta \alpha_{\mathrm{stat}}}{h\,\nu} \frac{\langle E_{\mathrm{rf}}^2 \rangle}{2} = \left\langle \frac{\Delta \nu_{\mathrm{S,EMM}}}{\nu} \right\rangle + \left\langle \frac{\Delta \nu_{\mathrm{S,th}}}{\nu} \right\rangle
$$
$$
= \frac{\Delta \alpha_{\mathrm{stat}}}{h\,\nu} \frac{|E_{\mathrm{rf,EMM}}|^2}{4} + \left\langle \frac{\Delta \nu_{\mathrm{S,th}}}{\nu} \right\rangle \tag{2.51}
$$

$\langle E_{\mathrm{rf}}^2 \rangle$ is the time averaged squared rf field amplitude seen by the ions, which has a contribution from excess micromotion and from the secular motion. If the effect of the dc trap fields on the radial trapping frequency is neglected ($|a| \ll q^2$) the ac Stark shift $\frac{\Delta \nu_{\mathrm{S,th}}}{\nu}$ for species i resulting from the secular motion in a linear mixed-species crystal can be calculated via [90]

$$
\left\langle \frac{\Delta \nu_{\mathrm{S,th}}}{\nu} \right\rangle_i = -\frac{\Delta\alpha_{\mathrm{stat}}}{h\nu_0} \frac{m_i}{2e^2} \sum_\alpha \beta_{\alpha,i}'^2 k_B T_\alpha \omega_i^2 \left(\frac{\Omega_{\mathrm{rf}}^2}{\omega_\alpha^2} + \frac{\omega_\alpha^2}{\Omega_{\mathrm{rf}}^2} + 6 \right). \tag{2.52}
$$

Blackbody radiation shift
The blackbody radiation (BBR) emitted by the environment of the ion leads to a significant ac Stark shift at room temperature. The peak wavelength of the BBR spectrum at $300\,\mathrm{K}$ is at $\lambda_{\mathrm{BBR,300\,K}} = 9.7\,\mu\mathrm{m}$, which is far away from allowed dipole transitions involving the clock energy levels of ^{115}In$^+$. For this reason, the BBR shift is well described by a static approximation [84], which scales with the differential static polarizability $\Delta\alpha_{\mathrm{stat}}$ of the two

clock levels and results in

$$\frac{\Delta \nu_{\text{BBR}}}{\nu} = -\frac{1}{2h\nu} \langle E^2(T) \rangle \Delta\alpha_{\text{stat}} \cdot (1 + \eta) \left(\frac{T_{\text{ions}}}{300\,\text{K}} \right)^4 . \tag{2.53}$$

Here, $\langle E^2(T) \rangle = (831.9\text{V/m})^2$ is the mean-squared electric field and h the Planck constant. The dynamical correction for In$^+$ $\eta_{\text{In}} < 10^{-4}$ describes the deviation from the static approximation. The differential static polarizability for In$^+$ $\Delta\alpha_{\text{stat}} = (3.3 \pm 0.3) \times 10^{-41}\,\text{Jm}^2/\text{V}^2$[85] is only known from theoretical calculations so far and its uncertainty presently dominates the uncertainty of the ac Stark shift induced by BBR. $\Delta\alpha_{\text{stat}}$ could be measured more precisely by observing the IR laser-induced light shift of an IR laser with well-known intensity, which could be calibrated by its effect on an Yb$^+$ ion.

The other contribution that dominates the uncertainty of the ac Stark shift in many clocks is the uncertainty of the temperature induced by the BBR field at the position of the ion. The BBR field at the ion position is mostly determined by the ion trap temperature. The temperature distribution in this trap has been characterized very precisely using temperature measurements and an FEM model, and allows a temperature estimate at the position of the ion with an uncertainty in the range of a few 100 mK [117]. The details of the determination of the trap-related uncertainty contribution to the BBR-induced ac Stark shift are described in section 4.4.

Zeeman shift
The interaction of external magnetic fields with the magnetic moments of the clock states leads to a Zeeman shift. The first-order Zeeman sensitivity for ^{115}In$^+$ ions is small compared to other clock species, because of the small g-factors of the clock states. The first-order Zeeman shift is given by

$$\Delta\nu_{\text{B1}} = \frac{\mu_{\text{B}} B}{h} \left(g_{|e\rangle} m_{\text{F},|e\rangle} - g_{|g\rangle} m_{\text{F},|g\rangle} \right) . \tag{2.54}$$

Here μ_{B} is the Bohr magneton, g are the g-factors of the ground and excited clock state and m_{F} are the considered Zeeman sublevels of the two states. In this work the $m_{F,g} = +9/2 \rightarrow m_{F,e} = +9/2$ and $m_{F,g} = \text{-}9/2 \rightarrow m_{F,e} = \text{-}9/2$ Zeeman components are used to lock the ultrastable laser to the atomic resonance. The two transitions are probed alternately to average out the first-order Zeeman shift as explained in section 6.2.1. With $g(^1S_0) = \text{-}6.6647 \times 10^{-4}$ [118] and $g(^3P_0) = \text{-}6.87(5) \times 10^{-4}$ [79] the resulting Zeeman shift for the used Zeeman components is

$$\Delta\nu_{\text{B1}} = B \cdot 20.19\,\text{kHz/mT}. \tag{2.55}$$

For the operation of a multi-ion clock, besides temporal fluctuations of the magnetic field, also spacial gradients have to be sufficiently small. In section 3.5 the expected magnetic field gradients and resulting Zeeman broadening originating from the magnetic fields coils are estimated.

2. Theoretical basis for ion optical clocks

Furthermore, the second-order Zeeman shift has to be characterized which is given by

$$\Delta\nu_{\mathrm{B2}} = \beta\langle B^2\rangle \tag{2.56}$$

and is proportional to the time-averaged squared magnetic field $\langle B^2\rangle$. With $\beta = 4.1\,\mathrm{Hz/mT^2}$ the clock transition in In$^+$ ions has a low sensitivity to this shift [20, 67]. Typically alternating trap currents have the largest contribution to $\langle B^2\rangle$ and FEM calculations with $\Omega_{\mathrm{rf}}/2\pi = 26\,\mathrm{MHz}$ and $U_{\mathrm{rf}} = 1.5\,\mathrm{kV}$ result in $B_{\mathrm{rms}}^2 = 1.3\times10^{-12}\,\mathrm{T^2}$ for this trap[1]. The resulting fractional frequency shift for In$^+$ would be 4×10^{-21}. Operation at low trap drive currents and a large ion-electrode distances help to reduce this shift. The second-order Zeeman shift can be corrected by the magnetic field measured via the first-order Zeeman shift. Currently, the uncertainties of the g-factors limit the uncertainty of this correction.

Electric quadrupole shift

Within a Coulomb crystal, the charges of the neighboring ions establish electric-field gradients which shift the energy levels of the clock states by coupling to their electric quadrupole moments. The interaction is described by the Hamiltonian [119]

$$H_{E2} = \nabla E^{(2)}\Theta^{(2)}\,, \tag{2.57}$$

with the second-rank field gradient tensor $\nabla E^{(2)}$, evaluated at the position of the ion. $\Theta^{(2)}$ is the electric quadrupole moment tensor of the excited clock state. Ideally, clock transitions with a vanishing quadrupole moment in first-order are selected for multi-ion clocks. This is given for ^{115}In$^+$ because the $^1S_0$ and $^3P_0$ state are rotationally symmetric ($J = 0$). But the state mixing of the $^3P_0$ state with the $^3P_1$ and $^1P_1$ states (see section 2.1.3) leads to a small non-vanishing quadrupole moment of the excited clock state, as shown in higher order calculations [86]. Because of this, the quadrupole shift cannot be neglected. In [90], the quadrupole shift of a 13-ion chain including 10 In$^+$ ions is calculated to be on the order of 1×10^{-19}, but the shift highly depends on the axial confinement and corresponding distances between the ions. Several techniques have been proposed that lead to a cancellation of the quadrupole shift [120] and are discussed in section 2.5.

Static electric fields within the ion trap, are compensated by micromotion measurements. In linear ion traps, an electric field gradient is used to provide axial confinement. The magnitude of this gradient can be determined by measurements of the axial trap frequency.

2.4.3. Other frequency shifts

Apart from the already discussed sources for frequency shifts, there are various other possible sources, which are not discussed in detail in this work. In the following, the frequency shift originating from collisions between the trapped ions and background gas particles is explained briefly.

---

[1] private communication with M. Doležal, Czech Metrology Institute

Collisions between the cold trapped ions and room temperature background gas particles can have multiple consequences. They can transfer enough energy to the ions to swap positions or even melt the crystal completely. In clocks based on mixed-species crystals, almost all of those collisions can be detected and their influence be removed by discarding the respective clock cycles. Most critical for an atomic clock are the weaker collisions, that do not transfer enough energy to change the order of the ions and are not detected by the current methods employed in this work, but can lead to frequency shifts.

Collisions are classified into two types. Langevin collisions, where the scattering parameter is below a critical value, and glancing collisions, where the scattering parameter is above this value. In Langevin collisions, the ion polarizes the room temperature neutral atom and directs it onto a spiral orbit around the ion such that the particles collide and apart from momentum transfer the internal states of the ion are shifted. In glancing collisions, the motion of the ion is altered by momentum transfer, but the internal states are not affected. Whether a collision can lead to rearrangement of the ion chain depends on the energy transferred by the collision compared to the threshold for rearrangement. The trap potential determines the threshold for rearrangement, but the dependence is small compared to the span of energy transferred by collisions [121]. Collisions that do not cause rearrangement of the crystal can thus be Langevin collisions as well as glancing collisions with too low energy transfer.

In the experiment, the collision rate of the collisions that lead to reordering of the ion chain ("swap" collision) can be measured and is referred to as the collision rate Γ_{swap} in this work. There are models that allow to determine the rate of collisions $\Gamma_{\text{non}-\text{swap}}$ that do not lead to reordering ("non-swap" collisions) from Γ_{swap} and also to deduce the resulting frequency shift [121–124]. The collision rate is especially important for multi-ion clocks, as the collision rate not only depends on the background gas pressure but also scales with the ion number as each ion increases the cross section for interactions with the background gas particles. The not detectable ("non-swap") collisions and the resulting frequency shift are not discussed in this work but the rate of the detectable ("swap") collisions is measured and presented in section 3.2.3. Apart from the consequences already discussed, collisions can also lead to the formation of molecular ions. This aspect is also the subject of section 3.2.3.

2.5. Possible ion candidates for a multi-ion clock

This section gives an overview about some possible ion candidates for a multi-ion clock. Their relevant properties in terms of multi-ion operation are summarized in Table 2.1. Some species are intrinsically insensitive, others are suitable for compensatory strategies. The discussion focuses on systematic frequency shifts and not on the instability, which is addressed in section 2.1.2.

Among the most critical for the extension from single ion to multi-ion operation is the electric quadrupole shift which scales with the differential quadrupole moment Θ. As described in section 2.4.2, the neighboring ions lead to strong electric field gradients which shift

2. Theoretical basis for ion optical clocks

Table 2.1.: *Properties of some possible multi-ion clock candidates*

species	I	$\Theta(e)$ (ea_0^2)	$g(g)$ (μ_B)	$g(e)$ (μ_B)	Δa_{stat} $(10^{-41}\,\mathrm{Jm^2/V^2})$	τ
^{115}**In**$^+$	9/2	-1.6(3)×10^{-5}	-6.6647×10^{-4}	-9.87(5)×10^{-4}	3.3(3)	195(8) ms
$^1S_0(F=9/2)\to{}^3P_0(F=9/2)$		[86]	[118]	[79]	[85]	[79]
^{27}**Al**$^+$	5/2	-1.7(6)×10^{-6}	-7.9248(14)×10^{-4}	-1.97686(21)×10^{-3}	0.702(94)	20.6(14) s
$^1S_0(F=5/2)\to{}^3P_0(F=5/2)$		[86]	[125]	[125]	[18]	[125]
^{40}**Ca**$^+$	0	1.83(1)	2.00225664(9)	1.2003340(3)	-72.677(21)	1176(11) ms
$^2S_{1/2}\to{}^2D_{5/2}$		[126]	[127]	[128]	[129]	[130]
^{88}**Sr**$^+$	0	2.6(3)	2	6/5	-47.938(71)	390.8(16) ms
$^2S_{1/2}\to{}^2D_{5/2}$		[131]			[132]	[133]
^{171}**Yb**$^+$ (E2)	1/2	1.95(1)	2	0.59930(9)	69(14)	53 ms
$^2S_{1/2}(F=0)\to{}^2D_{3/2}(F=2)$		[134]		[135]	[136]	[137]
^{171}**Yb**$^+$ (E3)	1/2	-0.0297(5)	2	1.143	8.88(16)	1.58(8) years
$^2S_{1/2}(F=0)\to{}^2F_{7/2}(F=3)$		[134]		[138]	[19]	[139]
^{176}**Lu**$^+$ (M1)	7	0.63862(74)	2.435047(16)×10^{-4}	0.0771662506(33) (F=6)	0.059(4)	172 h
				0.0084282619(46) (F=7)		
				0.061920729(29) (F=8)		
$^1S_0(F=7)\to{}^3D_1$		[140]	[141]	[141]	[142]	[143]
^{176}**Lu**$^+$ (E2)	7	0.8602(14)	2.435047(16)×10^{-4}		-1.17(9)	17.3 s
$^1S_0(F=7)\to{}^3D_2$		[140]	[141]		[142]	[144]

the energy levels. Furthermore, for shifts like the Zeeman shift, spatial gradients need to be considered when a spatially extended crystal is used. For species with a negative differential static polarizability Δa_{stat} operation at the magic trap drive frequency can cancel the EMM-induced second-order Doppler shift with the ac Stark shift [115]. Otherwise, the rf field induced EMM has to be low and as homogeneous as possible over the extension of the crystal and requires precise engineering of the ion trap. Important is also the efficiency of cooling of the entire motional spectrum to low temperatures. The efficiency of sympathetic cooling in linear crystals is analyzed in section 5.2.

Comparing the values of the typical clock candidates in Table 2.1 reveals that none of them fulfills all desired properties. For some multi-ion relevant shifts, cancellation techniques exist which are described in the following.

^{115}In$^+$ and ^{27}Al$^+$ have very promising properties for the use in linear crystals, but the positive Δa_{stat} prevents the described cancellation and thus EMM would induced large second-order Doppler shifts in 2D or 3D crystals. The properties of ^{115}In$^+$ and in general group 13 ions are discussed in section 2.1.3. Regarding ^{27}Al$^+$, the inaccessibility of direct state detection, solved by the implementation of quantum logic spectroscopy for a single ^{27}Al$^+$ ion [80], imposes a challenge for the extension to multiple ions. Recently scalable quantum logic

spectroscopy with a technique not requiring ground-state cooling or individual ion addressing has been demonstrated [145].

The E3 transition in ^{171}Yb$^+$ is also interesting for the application in a linear crystal and Θ is still reasonably small. A challenge is the large light field induced ac Stark shift due to the required high intensity of the probe laser, which also applies to other highly forbidden transitions, e.g., M1 transition in ^{176}Lu$^+$, but is most critical for ^{171}Yb$^+$. For a single ion this is greatly suppressed with the technique of hyper-Ramsey spectroscopy [146, 147] but in extended crystals spatial intensity variations can significantly complicate the suppression. A homogeneous intensity distribution is generally desirable for all species to avoid different Rabi frequencies in the crystal.

For the elimination of the quadrupole shift, several techniques have been successfully demonstrated. One possibility is averaging over three mutually orthogonal magnetic field directions [119], but this requires precise alignment of the magnetic fields. Averaging over all six Zeeman components has been demonstrated in ^{88}Sr$^+$ which also cancels the tensor Stark shift, but sets high demands on the magnetic field stability [148–150]. Another option is averaging over transitions to multiple hyperfine levels when $I \geq J$ to cancel the quadrupole shift and dominant Zeeman effects, thereby creating an effective $J = 0$ level [151]. If applied to multiple ions, the averaged signal suffers from inhomogneous broadening which can be suppressed by aligning the magnetic field at an angle of $1/cos(1/\sqrt{3}) \approx 54.7°$ to the trap axis, as demonstrated in ^{176}Lu$^+$ for three ions and interrogation times on the order of 10 seconds [120]. In ^{171}Yb$^+$, the suppression of the electric quadrupole shift by more than two orders of magnitude has been demonstrated via a continuous rotation of the magnetic field during the free evolution phase of a Ramsey interrogation [134].

Cancellation of the quadrupole shift, insensitivity to magnetic field fluctuations and suppression of inhomogeneous broadening has also been realized with the use of dynamical decoupling to create robust dressed states [25, 126, 152]. In ^{40}Ca$^+$ and ^{88}Sr$^+$, the technique makes use of the uniform spacing between Zeeman sublevels [26, 153]. Transferring the atomic coherence between hyperfine states during Ramsey interrogation, thereby effectively implementing hyperfine averaging in one interrogation sequence, has been realized with three ^{176}Lu$^+$ ions and can also be interpreted as a form of dynamical decoupling [154].

The species with a negative $\Delta\, a_{\text{stat}}$ are not only interesting for linear crystals but due to the possibility of canceling the EMM-induced second-order Doppler shift also for clocks based on 2D- or 3D-crystals [24]. With the demonstrated schemes for dynamical decoupling, a linewidth on the order of 1 Hz in a spherical 400 ion ^{40}Ca$^+$ crystal is realizable according to [25]. Here, the focus is not to achieve the best systematic uncertainty in these crystals, but to significantly improve the stability and use them for example in cascaded clock schemes [27–29] to phase stabilize a probe laser for a single ion clock, thereby allowing near-lifetime-limited probe times and correspondingly reduced statistical uncertainties. Also applications not requiring ultimate accuracy but high stability could profit from this approach. Apart from the mentioned species in Table 2.1, also ^{138}Ba$^+$ [155] features a negative $\Delta\, a_{\text{stat}}$. Another interesting species in the frame of large 3D-Coulomb crystal clocks is Sn^{2+} as proposed

2. Theoretical basis for ion optical clocks

in [156]. It features a $^1S_0 \rightarrow {}^3P_0$ clock transition between two highly insensitive states with zero electronic and total angular momentum ($I = J = F = 0$) and negative $\Delta\, a_{\text{stat}}$ and has several stable isotopes with different excited state lifetimes between 1 s and several thousand years. Apart from the described clock transition, Sn^{2+} has laser-accessible transitions for direct cooling and state detection. In contrast to the other species suggested for 3D Coulomb crystals, a systematic uncertainty in the sub-10^{-19} regime is estimated [156].

3. Experimental setup

This chapter describes the main components of the experimental apparatus, including the ion trap (section 3.1), the vacuum system (section 3.2), the lasers (section 3.3), the atomic ovens and ablation targets (section 3.4), the magnetic field coils (section 3.5), the bichromatic detection system (section 3.6) and the control software (section 3.7).

3.1. The ion trap
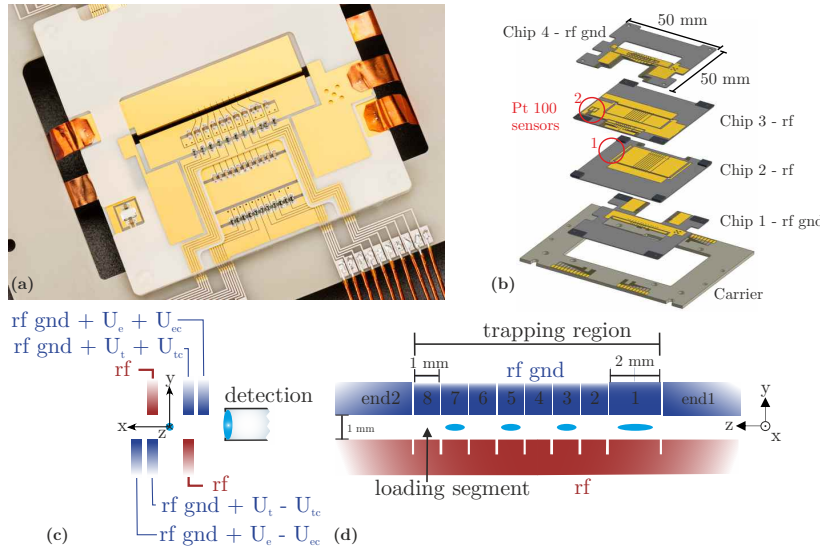
Figure 3.1.: *Linear ion trap array. (a) Photograph of the trap, showing the onboard low-pass filters and one Pt100 sensor. The ions are trapped in the black slit. (b) Exploded view of the trap stack consisting of four gold-coated AlN chips and a thick AlN support board. The temperature of the trap is monitored with two calibrated Pt100 sensors (red circles) [modified from [23]]. (c) Drawing of the radial plane, showing the rf quadrupole and compensation electrodes. (d) Drawing of the side view. The trap consists of one 2 mm-long and seven 1 mm-long segments of which the leftmost (segment 8) is used for loading.*

The segmented linear ion trap is formed by four stacked aluminum nitride (AlN) chips, as shown in Figs. 3.1 (a) and (b). The $380\,\mu$m-thick chips are sputtered with $4\,\mu$m of gold. Manufacturing tolerances below $10\,\mu$m have been achieved with laser cutting and structuring with a pulsed UV ns-laser. The distance between the central chips 2 and 3, carrying the rf voltage (see Fig.3.1 (c)), is $1\,$mm, resulting in an ion-to-electrode distance of $\approx 0.7\,$mm. The inner and outer chips are separated by $0.127\,$mm. In-situ determination of the trap

3. Experimental setup

temperature (described in section 4.4) is enabled by two calibrated Pt100 sensors which are soldered to the central chips. All materials including the SMD parts and Pt100 sensors are non-magnetic. The chip stack is glued to a 1.5 mm-thick AlN carrier. Attention was paid to good thermal contact with the vacuum chamber to efficiently dissipate the heat generated in the trap. The carrier is screwed to AlN feet which are attached to an aluminium bread-board which is in contact to the vacuum chamber. At the contact interfaces, thin sheets of Indium are placed to reduce the thermal resistance. The trap features 8 segments, as shown in Fig.3.1 (d), and allows to trap ions in every segment. The ions are loaded in segment 8 and transferred to another segment, mostly segment 1 and 2, to perform spectroscopy. The longest segment 1 has the largest section with a small micromotion component in the axial direction (compare section 4.2.2), and the segments with the largest distance from the loading segment are best protected from contamination from the atomic ovens.

The design of the trap is optimized for minimal amplitudes of the axial rf field on the trap axis z to keep the second-order Doppler shift due to axial micromotion as low as possible and for low rf induced heating and efficient heat removal. More details about the design optimization, the choice of materials and the manufacturing process can be found in [20–22, 117, 157]. The characterization of an identical trap is presented in [22, 90].

3.1.1. rf voltage drive

To supply the confining high rf voltage to the ion trap, a helical resonator is used. It is used for voltage enhancement and to match the impedance between the rf voltage source (+ amplifier) and the ion trap, keeping the required power for a given voltage at minimum and avoiding dissipation of rf power.

The resonator-trap system can be modeled as an LCR-circuit, where the trap voltage equals the voltage across the capacitor. Its resonance frequency ν_{res} can be estimated with the given formula

$$\nu_{\text{res}} = \frac{1}{2\pi\sqrt{L_c C}} \tag{3.1}$$

where L_c is the inductance of the coil and C the combined capacitance of the trap, the coil and the electrical connections. With the knowledge of the capacitance C, the coil inductance required to achieve a given resonance frequency ν_{res} can be calculated. The Q-factor of the circuit is given by

$$Q = \frac{1}{R}\sqrt{\frac{L}{C}} \tag{3.2}$$

where R is the resistance of the LCR-circuit.

A helical resonator with a small bandwidth and a high Q factor filters out the power at unwanted frequencies, hence reducing motional heating of the ions. An empirical study of the unloaded resonance frequency and the Q-factor of a helical resonator has been performed by Macalpine and Schildknecht [158] and design rules for high Q-factor resonators have been

derived which are also the basis for the resonators used in this work. The resonance frequency and Q factor of the combined resonator-trap-circuit will be significantly lower than those of the unloaded resonator. Siverns et al. describe the loaded helical resonator with a lumped element equivalent circuit model and predict the resonant frequency and the Q factor [159]. They present a design guide how to construct a helical resonator with a high Q factor, where they take into account all relevant resistances, capacitances and inductances of the system, including connecting wires and solder joints. To achieve a high loaded Q factor the load capacitance, load resistance, contact resistance and resonator resistance have to be small while its advantageous to have a large coil inductance. The resonator should be made from highly conductive material and the connection to the ion trap should be as short as possible.

However, the model of Siverns et al. and the experimentally realized resonance frequencies and Q factors in this work do not agree. Their model predicts a too low resonance frequency and a Q factor far outside of the optimal regime for the present geometries, while the experimentally determined Q factors are reaching up to 700.

An almost perfect prediction of the two characteristic properties is achieved with the modified model from Deng et al. [160]. Siverns et al. treat the equivalence capacitance C_e of the helical resonator as a parallel connection, i.e. as a simple sum, of the helical coil self capacitance C_c and the capacitance between the helical coil and the surrounding shield C_s. This approach neglects the inter-coupling effect of C_c and C_s. Deng et al. use the following expression to calculate the equivalence capacitance of the helical resonator with N winding turns:

$$C_e = C_N = \frac{1}{\frac{1}{C_{N-1}} + \frac{1}{C_{c0}}} + C_{s0}, N > 1 \qquad (3.3)$$

Here C_{c0} is the self-capacitance of one turn of the helical coil, C_{s0} is the capacitance between one turn of the helical coil wire and the surrounding shield and N is the number of winding turns. For more details, see [160]. Considering this modification the expressions for the resonance frequency ν_{res} and the Q factor change from 3.1 and 3.2 to

$$\nu_{\text{res}} = \frac{1}{2\pi\sqrt{(C_e + C_t + C_w)L_c}} \text{ and} \qquad (3.4)$$

$$Q = \frac{1}{R}\sqrt{\frac{L_c}{C_e + C_t + C_w}}, \qquad (3.5)$$

where C_t is the trap capacitance and C_w the contribution from wires.

In this work, three differently sized helical resonators (A-C) with resonance frequencies between $16.37\,\text{MHz}$ and $28.33\,\text{MHz}$ have been used: two larger ones with almost the same dimensions and a smaller one that is made to fit inside the mu-metal shield that will be installed around the setup. Drawings of all three resonators are shown on the left of Fig. 3.2 (a)-(c) and the relevant dimensions are listed in table 3.1.
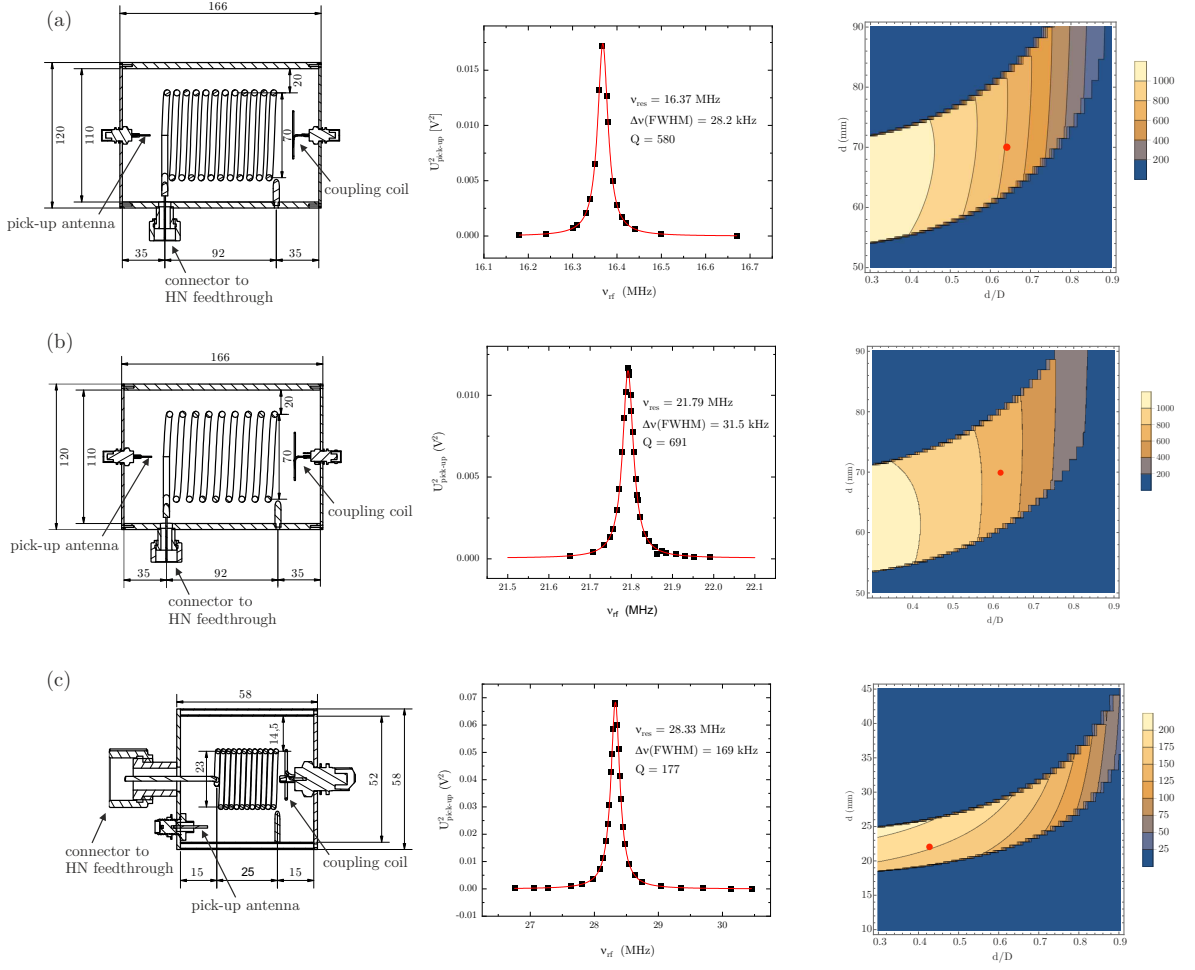
3. Experimental setup

Figure 3.2.: *Helical resonators.* (a) $\Omega_{\mathrm{rf}} = 2\pi \times 16.37\,\mathrm{MHz}$ (b) $\Omega_{\mathrm{rf}} = 2\pi \times 21.79\,\mathrm{MHz}$ (c) $\Omega_{\mathrm{rf}} = 2\pi \times 28.33\,\mathrm{MHz}$. *Drawings of the resonators (left), measurements of the resonance frequencies (center) and results of the simulated Q factors according to [160] (right). The red dots mark the present dimensions and show that they are centrally located in the stable range.*

The rf signal from the amplifier is coupled into the resonator via a single turn coupling coil which is soldered into a BNC connector, thereby decoupling the resonator from the resistive output impedance of the amplifier. The physical properties of the coupling coil, mainly the distance between the lid and the main coil, are used to match the impedance of the resonant circuit containing the ion trap and the rf amplifier until the back reflected power is below $2\,\%$ (measured with a bidirectional coupler[1]). The main coil is connected to the ion trap with a HN connection (3/4"-20 UNEF). The lid close to the HN connector features a small pick-up antenna (a wire soldered into a BNC connector) which picks up a small fraction of the rf voltage $U_{\mathrm{rf}} = k \cdot U_{\mathrm{pick-up}}$ and is used to monitor the voltage going to the ion trap. The

---

[1]Mini circuits: ZFBDC20-61 HP-S+

Table 3.1.: *Dimensions of the helical resonators A-C. The resonance frequencies are 16.37 MHz (A), 21.79 MHz (B) and 28.33 MHz (C).*

	shield length B (mm)	inner shield diameter D (mm)	length of coil b (mm)	diameter of coil d (mm)	number of windings N	wire diameter d_0 (mm)
A	162	110	92	70	12	5
B	162	113	92	70	9	5
C	55	52	28	22	12	1.5

calibration factor k is determined by matching the measured pick-up voltage $U_{\mathrm{pick-up}}$ and the measured trap frequencies to the results of a trap potential simulation that is described in [22]. Details on the trap frequency measurements and the calculation with trap potential simulator can be found in Sec, 4.1. The pick-up antenna and the coupling coil are made with silver wire, everything else is pure copper.

The center column of Fig. 3.2 shows measurements of the frequency ν versus the squared pick-up voltage $U_{\mathrm{pick-up}}$ for each resonator. The red lines are Lorentzian fits from whose width $\Delta\nu$ and center frequency the resonance frequency ν_{res} and the Q factor (Q=$\nu_{\mathrm{res}}/\Delta\nu$) can be derived. The Q factors simulated according to Deng et al. [160] of the three resonators are shown on the right in Fig. 3.2 (a)-(c). The Q factors are calculated in dependence of the coil diameter d and the coil to shield diameter ratio d/D, the red point indicates the Q factor for the dimensions of the respective resonator. The assumed trap and wire capacitance C_t and C_w are 14 pF and 0.00001 pF. The resistance of the system has been adapted in each case to match the measured Q factor. Apart from the resonators, the setup is identical which means that differences in the resistance can only arise from the resonator itself. The resistance increases with decreasing wire diameter d_0, furthermore the quality of the solder joints and the resistivity of the used copper can differ between the resonators. The latter two can not be distinguished from this comparison, therefore the resistance of the solder joints is used to get agreement between experiment and simulation. Table 3.2 summarizes for all resonators the measured resonance frequency ν_{res} and Q factor, the simulated resonance frequency $\nu_{\mathrm{res,simu}}$ and resistance of the solder joints R_{solder} to get agreement between experiment and simulation and the calibration factor k.

All three measured and simulated resonance frequencies agree well and the quality factors of the two larger resonators A and B are relatively high. The quality factor of the small resonator C suffers from the size restrictions on the shield diameter D and the shield length B which are limited to 52 mm and 55 mm, leaving little room for the variation of the coil size (b and d) and the wire diameter d_0. Furthermore, the wire diameter d_0 in resonator C is 1.5 mm compared to 5 mm wire used for the other two. The reduced diameter gives rise to an increase in resistance due to the smaller cross section and furthermore the 1.5 mm coil is significantly more flexible than the 5 mm coil. This flexibility might also reduce the Q factor. The resistance R_{solder} of resonator B is a factor 3 smaller compared to resonator A and almost a factor 14 smaller compared to resonator C. Assuming the same resistance of

3. Experimental setup

Table 3.2.: *Overview about the specifications of the three helical resonators A-C. Listed are the measured resonance frequencies ν_{res} and Q factors and the simulated resonance frequencies $\nu_{\text{res,simu}}$ and resistances R_{solder} as well as the calibration factor k between the rf voltage U_{rf} and the pick-up voltage $U_{\text{pick-up}}$.*

	ν_{res} (MHz)	Q factor	$\nu_{\text{res,simu}}$ (MHz)	R_{solder} (Ω)	k
A	16.37	580	16.19	0.025	2157
B	21.79	691	21.46	0.0074	3163
C	28.33	177	28.29	0.1	1502

the solder joints for all three resonators reveals the same Q factor within 15 % deviation, so the small outer dimensions and the thin wire do not account directly for the small Q factor. Note that the larger coil flexibility and its effect on the Q factor are not taken into account in the simulation. A resonator of dimensions C with higher Q thus seems possible, but further tests are required.

3.1.2. dc voltages

Figure 3.1 (c) shows the voltages that are provided for all trap segments including the two end segments. The symmetrically applied voltages U_{t} and U_{e} are used for the axial confinement of the ions and for squeezing of the radial trap potential to control the orientation of the two principle axes. The asymmetrically applied voltages U_{tc} and U_{ec} enable radial shifting of the total potential minimum to minimize radial micromotion in case of stray electric fields.

The dc voltage supply used in this apparatus is built analogously to the one described in [22], both of them are extensions to more trap segments of the version presented in [157]. The only difference is the use of SMD components instead of through-hole parts. Three computer-controlled analogue output modules[2] mounted in a single chassis[3] provide the voltages $\tilde{U}_{\text{t}}$, $\tilde{U}_{\text{tc}}$, $\tilde{U}_{\text{e}}$ and $\tilde{U}_{\text{ec}}$. The connection between the chassis and the host PC is established via an USB galvanic isolator and the chassis is powered by a floating linear power supply to avoid ground loops. A self-built analogue circuit, described in [22], takes the voltages from the analogue output modules as input signal to generate the four voltages for the individual trap electrodes according to the following equations:

$$U_{\text{t+}} = 1.2\tilde{U}_{\text{t}} + 0.25\tilde{U}_{\text{tc}} = U_{\text{t}} + U_{\text{tc}},$$
$$U_{\text{t-}} = 1.2\tilde{U}_{\text{t}} - 0.25\tilde{U}_{\text{tc}} = U_{\text{t}} - U_{\text{tc}},$$
$$U_{\text{e+}} = 1.2\tilde{U}_{\text{e}} + 1.2\tilde{U}_{\text{ec}} = U_{\text{e}} + U_{\text{ec}},$$
$$U_{\text{e-}} = 1.2\tilde{U}_{\text{e}} - 1.2\tilde{U}_{\text{ec}} = U_{\text{e}} - U_{\text{ec}},$$

---

[2]NI 9264, 16 channels, ± 10 V, 16-Bit resolution
[3]NI cDAQ 9174

With the scaling factors the resolution of the electric field generated by $\tilde{U}_{\text{tc}}$ and the voltage range of the other three voltages is increased.

For typical trap parameters used for clock spectroscopy in this work ($\Omega_{\text{rf}}/2\pi = 21.79\,\text{MHz}$ and $\omega_{\text{rad}}/2\pi \approx 820\,\text{kHz}$), a change of $1\,\text{mV}$ of U_{tc} corresponds to a dc field of $0.92\,\text{V m}^{-1}$ corresponding to a shift of the ion position causing a change of the rf field amplitude of $E_{\text{rf}} = 35.1\,\text{V m}^{-1}$ or respectively to a fractional second-order Doppler shift of -1.3×10^{-19} for $^{115}\text{In}^{+}$. These figures show that the voltage resolution needs to be sufficiently high and the voltages stable over long times. Figure 3.3 (a) shows the stability of one $U_{\text{t+}}$ voltage measured with a precise multimeter[4] over $600\,\text{s}$. The voltage drift is within an error band of approximately $\pm 50\,\mu\text{V}$, so the dc voltage supply has a suitable resolution for the minimization of micromotion and does not contribute significantly to the second-order Doppler-shift.
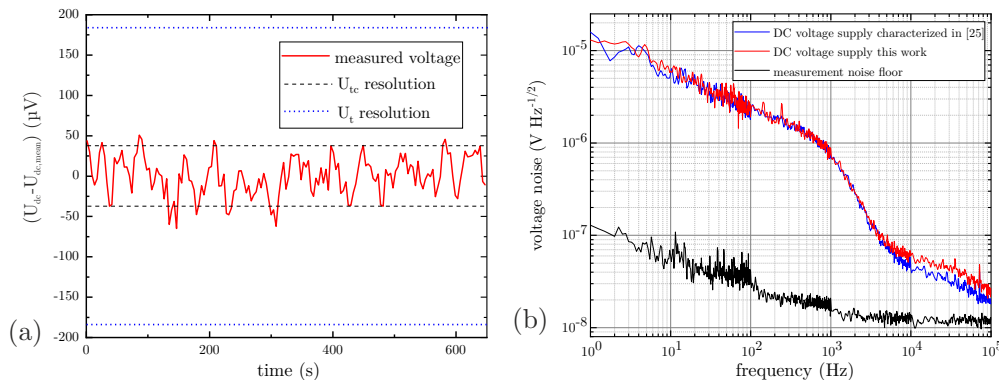

Figure 3.3.: *Characterization of the dc voltage supply. (a) Stability of one dc voltage ($U_{\text{t+}}$) provided by the self built analogue circuit and measured with a precise multimeter. The voltage remains stable within approximately $\pm 50\,\mu V$. The dashed lines indicate the voltage resolution for U_{t} and U_{tc}. (b) Measurement of the dc voltage noise of the voltage supply used in this work (red) and the one characterized in [22] (blue). The instrument noise of the used spectrum analyzer with shorted input is shown in black.*

In addition to providing the required voltages with sufficient resolution and stability, the dc power supply should suppress voltage noise at the trap frequency ω_{sec}. This will otherwise contribute to the ion heating rate. To suppress noise the analogue circuit features second-order low pass filters with cut off frequencies around $1\,\text{kHz}$. Furthermore, each trap segment has another low pass filter with a cut off frequency of $113\,\text{Hz}$ placed directly on the trap chips (as can be seen in figure 3.1 (a)). Figure 3.3 (b) shows the voltage noise spectrum measured at the output of the self-built analogue circuit for the supply used in this work and the one characterized in [22] as well as the measurement noise floor of the FFT instrument. In both supplies the second-order low pass filter suppresses the noise above $1\,\text{kHz}$ efficiently. The instrument noise is limiting the measurements for frequencies above $10\,\text{kHz}$. The two voltage supplies exhibit very similar noise characteristics, the one used in this work being slightly worse at high frequencies. However, the resulting ion heating rate is not higher in this setup

---

[4]Agilent, 34401A, 6 1/2 digit multimeter

3. Experimental setup

(see Fig. 4.16). The noise arriving at the location of the ions will be even lower as shown in Fig.3.3 (c), because of the additional on-board low pass filters.

3.2. Vacuum system

3.2.1. Geometry and components

For the design of the customized vacuum chamber, emphasis was placed on achieving a low background pressure, good thermal heat sinking and laser access from various directions as well as on the use of non-magnetic materials. A drawing of the vacuum system is shown in Fig.3.4. On the octahedral chamber, eight windows are mounted pairwise in the horizontal plane and allow laser beams to pass along the trap axis (z) as well as under an angle of $\Theta = (21 \pm 2)\,^\circ$ to the z axis. For efficient fluorescence detection, a re-entrant viewport with a diameter of $100\,\mathrm{mm}$ is placed perpendicularly to the trap axis with a distance of $24\,\mathrm{mm}$ between the vacuum window and the trap center. Facing the re-entrant viewport, the system features a window with a diameter of $80\,\mathrm{mm}$ allowing future single ion addressing. The 3-dimensional laser access is completed by windows on the top and bottom of the chamber to allow vertical laser beams to pass perpendicularly through the horizontal plane of the ion trap. One more window is placed on one upper sidewall of the chamber to provide direct view on the ablation target. All windows have an anti reflection coating in the ultraviolet (UV) range that was optimized for $230.6\,\mathrm{nm}$, $369.5\,\mathrm{nm}$ (for both R<1%) and $411\,\mathrm{nm}$ (R<2%).
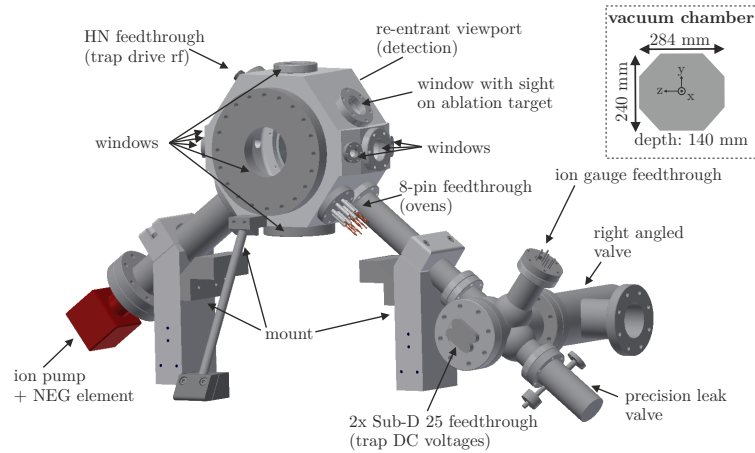

Figure 3.4.: *Drawing of the vacuum system showing all components and the outer dimensions of the octahedral chamber.*

Two electrical feedthroughs are placed on the chamber body: an 8 pin high current feedthrough providing the connection for the atomic ovens and a coaxial high voltage feedthrough (HN-type) coupling the rf voltage from the helical resonator to the trap. Via a DN40 sized tube, the chamber is connected via a cross to an ion gauge, two multipin feedthroughs (Sub-D 25) for connecting the dc voltages and Pt100 sensors of the trap, a precision leak valve for a controlled inlet of gases and to a right angled all-metal valve that can be connected to a

turbo molecular pump for initial pumping. The vacuum is maintained by a non-evaporable getter combination ion pump[5] featuring a nominal pumping speed of $200 \, l/s$ for hydrogen and oxygen and $6 \, l/s$ for argon and that is connected to the chamber via a DN63 sized tube on the opposite site of the chamber. A sheet of copper is blocking the direct sight between pump and ion trap to protect the trap from material deposition during getter (re)activation. The chamber, the viewports, the 8-pin feedthrough and the two tubes are made from titanium grade 5. Most other parts are machined from non-magnetic stainless steel (LN316). The chamber is mounted on the optical table with two brackets that enclose the tubes. A third support prevents swinging in the remaining direction. The bottom of the chamber features four counterbores inside the vacuum which are used to mount a baseplate that fits the rounding of the chamber.[6] A small breadboard, carrying the ion trap and the atomic ovens, is screwed to the baseplate. To ensure a high thermal conductivity both parts are made from aluminium and a piece of thin Indium foil is placed between all contact surfaces. With this construction, the ion trap is placed in the center of the chamber in all three dimensions.

The fully assembled system, including the trap, was baked out at $\approx 120\,°$ for 24 days. A second bake out at a temperature of $\approx 130\,°$ was done for 13 days two years later after the chamber had been opened for minor adjustments, and the resulting background pressure measured with the ion gauge is $3 \times 10^{-10} \, mbar$. Considering the theoretically expected reduction of the conductance arising from the small diameter tube between main chamber and the ion gauge the background pressure at the ion position is $\approx 3 \times 10^{-11} \, mbar$.

3.2.2. Used in-vacuum materials

All materials inside the chamber are non-magnetic and low outgassing. The materials used for the trap are described in section 3.1. For the further interior the following materials have been used: oxygen-free high conductivity copper (OHFC), aluminium EN AW 5083 (also known as C250), titanium grade 5, tantalum, macor and gold. The outgassing rate of three test samples consisting of milled titanium grade 5, milled aluminium EN AW 5083 and milled and additionally electropolished aluminium EN AW 5083, all machined in the main workshop at PTB, have been measured via accumulation measurements by the company VACOM GmbH. The result is summarized in Table 3.3 and the measurement principle is explained in detail in [161].

For the two aluminium EN AW 5083 test samples, the dominant gas is H_2. The test sample that is only milled has an outgassing rate that is more than an order of magnitude lower than that of the sample that was additionally electropolished. The additionally electropolished sample looks much rougher to the eye, so more gas particles probably adsorb in the pores of the surface. All in-vacuum aluminium parts have therefore only been milled. For the titanium grade 5 test sample, the dominant gas has the atomic mass unit (a.m.u.) 28, so

---

[5]NEXTorr D200-5

[6]Apart from the four counterbores at the bottom the chamber features eight more counterbores at the inside, four at the wall of each large viewport. These are partly used to keep dc cables at their position, others are still free to use.

3. Experimental setup

Table 3.3.: *Outgassing rate q for three test samples. The analysis has been done at two atomic mass units (a.m.u.): for H_2 and for gases with the a.m.u. 28 which could be CO, C_2H_4 or N_2. The measurements have been performed by the company VACOM GmbH.*

	q_{H2} $(\mathrm{mbar \cdot l \cdot s^{-1} \cdot cm^{-2}})$	$q_{a.m.u.28}$ $(\mathrm{mbar \cdot l \cdot s^{-1} \cdot cm^{-2}})$
background	$1.71 \cdot 10^{-15}$	$8.55 \cdot 10^{-16}$
Al EN AW 5083 milled	$9.28 \cdot 10^{-15}$	$4.27 \cdot 10^{-15}$
Al EN AW 5083 milled + electropolished	$3.87 \cdot 10^{-13}$	$1.78 \cdot 10^{-13}$
Ti grade 5 milled		$<3.57 \cdot 10^{-16}$

it could be CO, C_2H_4 or N_2, but the measured outgassing rate is a factor 2 lower than the background measurement and therefore cannot be determined. The reason for this is that titanium can chemically bind residual gases and thus reduce the background pressure. This effect is exploited in titanium sublimation pumps. All titanium in-vacuum components are also milled.

3.2.3. Collision rate and molecule formation

Collisions between the cold trapped ions and room temperature background gas particles can have multiple consequences, one of them being shifts of the internal electronic state levels and thus frequency shifts, as described in section 2.4.3. These cannot be detected directly with the methods employed in this work.

Collisions can transfer enough energy to the ions to swap positions or even melt the crystal completely. The formation of molecular ions consisting of the two collision partners is also possible. The three last-mentioned consequences can be detected by status monitoring of the crystal, as described below, and a rate of the collisions that lead to rearrangement of the ion chain ("swap" collisions) can be deduced and is referred to as the collision rate Γ_{swap} in the following. Based on Γ_{swap}, the rate of collisions leading to frequency shifts, and thus the contribution to the systematic uncertainty of the clock, can be estimated, as described in section 2.4.3.

Even though less critical, the "swap" collisions with the rate Γ_{swap} influence clock operation. If the crystal melts, the clock sequence is interrupted and measures to re-cool the crystal are taken, for example strong cooling pulses or frequency chirps. If a molecular ion is formed, the former ion is no longer fulfilling its role because the cooling or clock laser is not able to address the charged particle any longer. A rearrangement of the permutation of the ions in mixed-species crystals indicates that a high-impact collision happened and the last frequency update from the clock interrogation should be discarded. Either the clock continues with the new ion arrangement, or a reordering sequence is triggered before clock

operation is continued (see section 5.3). In both cases, the duty cycle and the stability of the clock are affected by the collisions at rate Γ_{swap}. For the clock operation described in this work, the dual-species ion crystals are reordered to a specific permutation whenever they deviate. The collision rate depends on the background gas pressure and scales with the ion number, as each ion increases the cross section for interactions with the background gas particles.

To measure the collision rate Γ_{swap}, the status of a linear mixed In^+/Yb^+ crystal or a Yb^+ crystal containing at least one molecular ion (YbX^+) is detected with the EMCCD camera by placing regions of interest (ROIs) above all ion positions in the Yb^+ image of the linear chain. Threshold detection determines the Yb^+ ion positions and thus the permutation. With this method, the collision induced permutation changes are detected and Γ_{meas} is derived as the ratio of the detected permutation changes and the measurement time. In order to calculate the collision rate Γ_{swap} from Γ_{meas}, a correction factor has to be used which takes into account the probability that the ions can end up in an indistinguishable arrangement from the one before and thus the event is not detected. To compare Γ_{swap} of different crystals, the collision rate $\Gamma_{\text{swap,ion}}$ is used in the following, which can be calculated via

$$\Gamma_{\text{swap,ion}} = \frac{\Gamma_{\text{swap}}}{N} = \frac{N!}{N(N! - N_{\text{dark}}!N_{\text{bright}}!)}\Gamma_{\text{meas}}. \tag{3.6}$$

Here, N is the total number of ions, N_{dark} is the number of dark ions (this can be either In^+ or YbX^+ molecules) and N_{bright} is the number of Yb^+ ions.

Table 3.4 summarizes measurements of the collision rate $\Gamma_{\text{swap,ion}}$ for mixed In^+/Yb^+ and Yb^+/YbX^+ crystals with ion compositions between 5 and 16 ions. The radial secular frequency f_{rad} for all measurements is about $610\,\text{kHz}$ (for a single Yb^+ ion) and the axial trap frequency f_{ax} has been adapted between $\approx 90\text{-}150\,\text{kHz}$ allowing the crystals to form a linear chain. As described in section 2.4.3, the potential only slightly affects the threshold for re-arrangement, so it can be assumed that the small variation in the axial frequency does not cause any significant change in the proportion of collisions leading to reordering of the crystal.

The data presented has been measured in two different ways, but they do not affect the resulting $\Gamma_{\text{swap,ion}}$. Most measurements of the mixed crystals have been carried out by re-ordering the crystal into a specific permutation after each change (see section 5.3 for more details) and then evaluating the time to the next deviating permutation. For the remaining measurements and those of the Yb^+/YbX^+ crystals, the permutation changes were simply detected as described before and no reordering has taken place in between (marked with * in Table 3.4).

The values of $\Gamma_{\text{swap,ion}}$ for the different crystals are measurement time weighted aver-ages of several measurements each. The collision rate $\Gamma_{\text{swap,ion}}$ for the mixed crystals is between $0.0024\,\text{s}^{-1}\,\text{ion}^{-1}$ and $0.0035\,\text{s}^{-1}\,\text{ion}^{-1}$ and shows fluctuations larger than the purely statistical uncertainty. A possible reason is thermally induced shifting of the ion position on the camera with respect to the ROI positions in some longer measurements, which

Table 3.4.: *Collision rate* $\Gamma_{\text{swap,ion}}$*, corresponding to collisions that lead to a rearrangement of the ion chain, for various compositions of mixed* In^+/Yb^+ *and* Yb^+/YbX^+ *ion crystals. The radial secular frequency* f_{rad} *for all measurements is about 610 kHz (for a single* Yb^+ *ion) and the axial trap frequency has been adapted between* $\approx 90\text{-}150 \text{ kHz}$ *allowing the crystals to form a linear chain.* * *marks measurements that have been recorded without reordering the crystal to a specific permutation.*

composition	$\Omega_{\text{rf}}/2\pi$ (MHz)	$\Gamma_{\text{swap,ion}}$ ($\text{s}^{-1}\,\text{ion}^{-1}$)
2 In$^+$ 3 Yb$^+$	16.34	0.0035 ± 0.0002
3 In$^+$ 2 Yb$^+$	16.34	0.0030 ± 0.0004
3 In$^+$ 3 Yb$^+$	16.34	0.0032 ± 0.0003
3 In$^+$ 5 Yb$^+$	16.34	0.0026 ± 0.0002
4 In$^+$ 3 Yb$^+$	16.34	0.0036 ± 0.0002
4 In$^+$ 5 Yb$^+$	16.34	0.0029 ± 0.0003
5 In$^+$ 4 Yb$^+$	21.79	0.0027 ± 0.0002
5 In$^+$ 5 Yb$^+$	16.34	0.0031 ± 0.0004
5 In$^+$ 5 Yb$^+$	21.79	0.0024 ± 0.0004
8 In$^+$ 3 Yb$^+$	16.34	0.0032 ± 0.0003
10 In$^+$ 4 Yb$^+$	16.34	0.0031 ± 0.0002
10 In$^+$ 6 Yb$^+$	16.34	0.0027 ± 0.0002
1 In$^+$ 1 Yb$^+$*	16.34	0.0028 ± 0.0004
1 In$^+$ 1 Yb$^+$*	21.79	0.0027 ± 0.0004
3-4 In$^+$ 1 Yb$^+$*	21.79	0.0029 ± 0.0007
7-10 ions (both species)*	21.79	0.0029 ± 0.0002
weighted average In$^+$/Yb$^+$ crystals	16.34	0.0031 ± 0.0003
weighted average In$^+$/Yb$^+$ crystals	21.79	0.0027 ± 0.0001
weighted average In$^+$/Yb$^+$ crystals	16.34/21.79	0.0029 ± 0.0003
5 Yb$^+$/YbX$^+$*	21.79	0.0030 ± 0.0004
9 Yb$^+$/YbX$^+$*	21.79	0.0024 ± 0.0002
3 Yb$^+$/YbX$^+$*	21.79	0.0026 ± 0.0007
weighted average Yb$^+$/YbX$^+$ crystals	21.79	0.0026 ± 0.0003

may have led to unconsidered detection errors. The process of ion loading can be excluded as a reason for higher collision rates, since the collision rate is already stable after 5 min. To summarize the data, measurement time weighted averages for the two rf drive frequencies are given which are $\bar{\Gamma}_{\mathrm{swap,ion}}(16.34\,\mathrm{MHz}) = (0.0031 \pm 0.0003)\,\mathrm{s}^{-1}\,\mathrm{ion}^{-1}$ for 16.34 MHz and $\bar{\Gamma}_{\mathrm{swap,ion}}(21.79\,\mathrm{MHz}) = (0.0027 \pm 0.0001)\,\mathrm{s}^{-1}\,\mathrm{ion}^{-1}$ for 21.79 MHz and thus agree within their uncertainties. Accordingly, there is no indication that Γ_{swap} depends on the rf-drive frequency. The combined weighted average mixed crystal collision rate is $\bar{\Gamma}_{\mathrm{swap,ion}} = (0.0029 \pm 0.0003)\,\mathrm{s}^{-1}\,\mathrm{ion}^{-1}$ which in also in agreement with the $\mathrm{Yb}^+/\mathrm{YbX}^+$ ion crystal collision rate $\Gamma_{\mathrm{swap,ion}} = (0.0026 \pm 0.0003)\,\mathrm{s}^{-1}\,\mathrm{ion}^{-1}$.

The collision rate Γ_{swap} is our most precise measure to compare background pressures in the ultra-high vacuum regime between different setups. A second setup with the identical ion trap features a comparable collision rate $\bar{\Gamma}_{\mathrm{swap,ion}}$. In that setup, the ion gauge is close to the pump and in the one described here it is far away from the ions and the pump. There is almost an order of magnitude between the indicated pressures on the ion gauges. Since the collision rates match, it can be assumed that the pressure at the ions is comparable and in this setup lower than the 3×10^{-10} mbar indicated by the ion gauge. This comparison is consistent with the theoretical estimate in section 3.2 that the small diameter tube between the main chamber and ion gauge results in an increased background pressure of one order of magnitude at the ion gauge.

Collisions that lead to the formation of molecules are less frequent than the ones leading to rearrangements of the crystals. Often one can work with the In^+ ions in a crystal without the occurrence of a molecule for 1-2 days, but a more rigorous evaluation could be performed with raw data from clock comparisons. If an In^+ ion turns into a molecule, it sometimes dissociates again within a few minutes but on other occasions it takes hours or does not dissociate again. Secular frequency measurements with the molecular ions would bring insight on the mass and thereby structure of the formed molecules and help to find strategies to selectively dissociate the In^+ molecules. YbH^+, which is most likely to from when the Yb^+ ion is in the $^2\mathrm{F}_{7/2}$ state, can be dissociated with the Doppler cooling laser of Yb^+ [162]. We observe molecules that the Yb^+ cooling laser at a wavelength of 370 nm cannot dissociate, but the In^+ detection laser at 230.6 nm can. Since water is typically responsible for much of the residual pressure in the chamber, we suspect YbOH^+. Important for the successful dissociation of Yb^+ molecules is the immediate irradiation with the UV lasers. The assumption is that with progressing time the molecules bind more and more particles and dissociation becomes more difficult. Conditional 230.6 nm (detection laser for In^+) pulses are implemented in all automated measurements when fewer Yb^+ ions than expected are observed. If the detected number of Yb^+ ions deviates by more than one or two ions from the expectation, decrystallization is assumed and frequency ramps on the cooling laser are applied as mitigation. With these two measures $\mathrm{In}^+/\mathrm{Yb}^+$ crystals of around 15 ions can be used for several days without ion loss.

3. Experimental setup

3.2.4. Temperature sensors for monitoring BBR

Seven Pt100 temperature sensors are glued with silver epoxy to the positions on the vacuum chamber indicated in Fig.3.5. Together with the Pt100 sensors integrated into the trap, this allows monitoring of the thermal environment seen by the trapped ions and the derivation of the associated BBR shift. The resistances of all Pt100 sensors can automatically be read out with a multimeter[7] featuring 4-wire measurements for multiple channels. The sensors are labeled according to the number of the channel of the multi-channel card they are connected to.
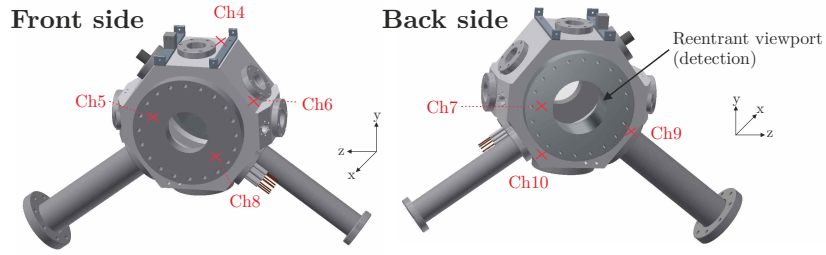
Figure 3.5.: *Location of the seven temperature sensors glued to the vacuum chamber. The sensors are labeled with Ch4 to Ch10 according to the number of the channel they are connected to. Sensors Ch4, Ch5, Ch6 and Ch8 are placed on the front side facing the laboratory and sensors Ch7, Ch9 and Ch10 one the back side facing the detection setup.*

The vendor of the Pt100 sensors specifies the temperature uncertainty with $\pm 1\,\mathrm{K}$. To reduce the uncertainty, the seven sensors were calibrated as described in appendix A.1 before being glued to the chamber. Since the temperature of the vacuum chamber is always close to room temperature a simple linear relation between the temperature T and the resistance R is sufficient and the temperature of the sensors can be calculated with

$$T(R) = \frac{R - R_0}{3.85 \cdot 10^{-3} K^{-1} \cdot R_0} + T_{\mathrm{off}}. \tag{3.7}$$

Here, $R_0 = 100\,\Omega$ and T_{off} is the offset determined from the calibration described in appendix A.1. Table 3.5 lists the offset T_{off} for all sensors. The calibration has resulted in a reduction of the uncertainty to $200\,\mathrm{mK}$.

In the horizontal plane, the In$^+$ detection laser ($230.6\,\mathrm{nm}$) and the Yb$^+$ repumper lasers cross the trap in the axial direction. The cooling and detection laser for Yb$^+$ is applied with two beams (H1 and H2), both having an angle $\Theta = 21\,^\circ$ to the trap axis. H1 and H2 are movable across all segments via motorized mirrors. Along the direction of H2 a helper beam with a detuning of -85 MHz with respect to the other cooling beams is aligned to the loading segment only. More details on the setup of the breadboard delivering the horizontal beams are given in Fig.A.6 in the appendix A.2. The vertical cooling beam for Yb$^+$ ($370\,\mathrm{nm}$ V) and the spectroscopy lasers for In$^+$ ($236\,\mathrm{nm}$) and Yb$^+$ ($411\,\mathrm{nm}$) propagate vertically through the trap.hey can be moved across all trapping segments as well which is described in Fig. A.7.

---

[7]Keithley 2700

Table 3.5.: *Temperature offset correction* T_{off} *for the Pt100 sensors Ch3 to Ch10 glued to the chamber, determined from a simple calibration. Sensor Ch3 is currently not in use.*

| Sensor	T_{off} [mK]
Ch3	-400
Ch4	-321
Ch5	-511
Ch6	-304
Ch7	-375
Ch8	-273
Ch9	-308
Ch10	-378

3.3. Laser setup and beam geometry

3.3.1. Beam geometry and waists

To decouple the pointing to the ion from the laser setups, all laser are transferred to the chamber with fibers, all of the Yb^+ laser fibers are polarization maintaining. The orientation of the lasers accessing the chamber with the ion trap is shown in Fig. 3.6. The description of all lasers follows in section 3.3.2 and 3.3.3. The beams except for the photoionization lasers (399 nm and 410 nm) can be moved across all trapping segments.

Figure 3.6.: *Orientation of all lasers entering the vacuum chamber. Apart from lasers than propagate either axially or vertically through the trap the chamber features small viewports that allow lasers to pass in the horizontal plane of the trap at an angle* $\Theta = 21°$ *to the trap axis. For clock spectroscopy the magnetic field is oriented along the trap axis (z).*
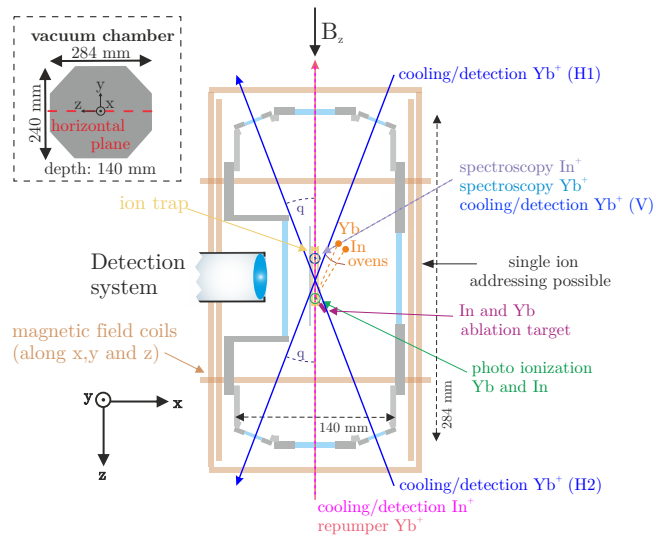
3. Experimental setup

The beam radius of all beams was either measured with a camera or determined by a saturation intensity measurement. For some beams both methods have been used. Table 3.6 lists the radii ω_{ion} of all beams at the position of the ion and (where determined) the saturation power. The beam shape of the 236 nm beam has only been measured for the collimated beam behind the outcoupler of the fiber and the effect of the focusing and the cylindrical lens has been calculated. More details on the beam shape can be found in the appendix A.2.

Table 3.6.: *Beam radii ω_{ion} at the position of the ion for all laser beams. The radii ($1/e^2$) have either been deduced from measurements with a camera or from saturation power measurements. *For the 236 nm laser, the beam radius is inferred from measurements of the collimated beam and the effect of the focusing and the cylindrical lens has been calculated.*

beam	ω_{ion} (camera) (μm)	ω_{ion} (saturation) (μm)	saturation power (μW)
230 nm (axial)		90±10	0.50±0.05
236 nm (vertical)*	estimated (radial): 55±20 elongated to ≈ 100 (axial) (see A.2)		
H1-370 nm (21 °)	60±10	55±1	7.2±0.2
H2-370 nm (21 °)		47±1	5.2±0.2
V-370 nm (vertical)	100±20	93±3	20.8±1.1
411 nm (vertical)	75±20		
410 nm (vertical)	134±15		
399 nm (vertical)	122±15		
639 nm (axial)	99±20		
935 nm (axial)	107±20		
1650 nm (axial)	135±20		

3.3.2. Yb$^+$ lasers

The term scheme of ^{172}Yb$^+$ ions is illustrated in Fig. 3.7. ^{172}Yb$^+$ has a vanishing nuclear spin, hence no hyperfine structure, which results in a relatively low number of transitions that need to be addressed. The relevant transitions are accessible with diode lasers.

For Doppler cooling, ion imaging and state detection via electron shelving [71], the electric dipole transition $^2S_{1/2} \leftrightarrow {}^2P_{1/2}$ at 370 nm with a linewidth of $2\pi \times 19.6$ MHz [163] is used. Furthermore this transition is used for the second step of the isotope selective photoioniza-
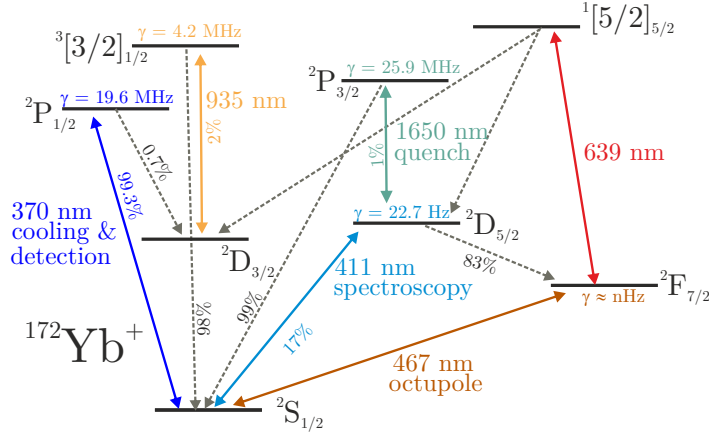
Figure 3.7.: $^{172}Yb^+$ *term scheme showing all used transitions and the natural linewidths and branching ratios of the excites states. The values are taken from the Appendix of [102] and references therein.*

tion of neutral Indium and Ytterbium ions as described in section 3.4.2. Two repumpers are needed to maintain a closed cooling cycle. Population from the $^2P_{1/2}$ state decays with a probability of 0.7 % to the $^2D_{3/2}$ state and is brought back to the cooling cycle via a laser at 935 nm that connects to the $^3[3/2]_{1/2}$ state. In addition, collision with background gas particles can populate the long lived $^2F_{7/2}$ state, which can be cleared out with a 639 nm laser via the $^1[5/2]_{5/2}$ state. This clear out is more effective if an additional laser at 1650 nm driving the $^2D_{5/2} \leftrightarrow {}^2P_{3/2}$ transition is applied simultaneously because this prevents cycling transitions [102]. The narrow quadrupole transition $^2S_{1/2} \leftrightarrow {}^2D_{5/2}$ at 411 nm with a linewidth of $2\pi \times 22.7$ Hz is used for resolved sideband spectroscopy and ground state cooling in combination with the 1650 nm laser which quenches the quadrupole transition [112]. The electric octupole transition $^2S_{1/2} \leftrightarrow {}^2F_{7/2}$ at 467 nm with a linewidth corresponding to a lifetime of 1.6 years [139] is not used in this work but the coating of the detection lenses and vacuum viewports allow its use.

Doppler cooling laser at 370 nm

An optically amplified and frequency doubled external cavity diode laser (ECDL)[8] generates the Doppler cooling light. The output power of about 40 mW is shared with a second setup and transferred to the experiment table with a large mode area (LMA) fiber[9]. The cooling light is sent to the ions from three directions, as shown in Fig. 3.6: two beams in den horizontal plane of the trap with an angle of 21° to the trap axis (H1 and H2) and one beam perpendicular to the trap axis along the vertical direction (V). In the loading segment of the trap, an additional "helper" beam with a detuning of -85 MHz to the other three beams is available along the H2 direction. The H1, H2 and V beams are movable across all segments of the trap via motorized mirror mounts or translations stages. Monitor photodiodes capture a fraction of each of the beams so that a software control loop can adjust and stabilize the

---

[8]Toptica: TA-SHG pro
[9]NKT photonics: LMA-PM-10

3. Experimental setup

power of the beams via acousto-optic modulators (AOM) in the 370 nm laser setup shown in Fig.A.8 in the appendix A.2. The beams can be switched off independently with mechanical shutters placed in front of each fiber guiding the beams from the 370 nm setup to the ion trap. The beam H2 is mainly used for optical pumping of the ions to the ground state Zeeman level with m_j=-1/2 (see section 4.14), which requires pure σ- polarization. This is generated by cleaning the polarization first with a polarizing beam splitter (PBS) followed by a motorized quarter-wave plate enabling subsequently switching from linear to circular polarization. A separate AOM is used to control the optical pumping pulses independently from the cooling pulses. The setup also allows an alternative configuration of the cooling beams in the horizontal plane: one with an angle of 45 ° to the trap axis and one along the trap axis. The 45 ° beam, which would have equal projection on all trap axis, would enter the chamber through the reentrant viewport. The detection system already includes a mirror to couple this beam into the chamber, the axial beam would be coupled through the same fiber as the repumping lasers, introduced in the next paragraph.

Repumping lasers
The three repumping lasers at 639 nm, 935 nm and 1650 nm are also shared with the second setup. All three beams are guided to the ion trap with a shared LMA fiber[10] and propagate along trap axis. Polarization maintaining fibers transfer all three lasers individually to an aluminium enclosed optical breadboard in which they are overlapped with dichroic beamsplitters after the shape of each beam is adapted to the mode field diameter of the LMA fiber. The optical setup contains AOMs for the 639 nm and 1650 nm laser to be able to switch them individually during sequences. A drawing of the overlapping setup is shown in Fig. A.9 in the appendix A.2. In addition to the repumpers, an additional 370 nm cooling beam can be included and is set up but currently not in use. The overall coupling efficiency through the enclosed breadboard and the LMA is between 60 % and 82 % depending on the wavelength and stated for the individual beams in Fig. A.9. The setup is placed in an electronics rack. More details on the setup of the box and the beam shaping are given in [164].

The LMA fiber guides the overlapped beams to the chamber, where a self-designed achromatic outcoupler consisting of four lenses, mounted in a mirror mount featuring translation and tilting in two dimensions each, directly focuses all beam to the position of the ions. Details about the setup of the outcoupler and the coating of the lenses are given in the appendix A.2 and in [164].

411 nm laser
The 411 nm laser used for resolved sideband spectroscopy consists of an ECDL at 822 nm which is stabilized to a 12 cm long cavity made from ultra low expansion (ULE) glass. The light is amplified by an injection-locked laser diode and frequency doubled to 411 nm. The whole system is described in detail in [102, 165]. The laser system is shared with a second setup and a double-pass AOM is used to control the laser frequency and to switch the laser during the sequence. A drawing of the setup is shown in Fig.A.11 in the appendix A.2. On the experiment table, the 411 nm beam is overlapped with the vertical 370 nm cooling

---

[10]NKT photonics: LMA-PM-10

laser beam. A polarizing beam splitter and a motorized half-wave plate ensure polarization cleaning and adjustment.

399 nm laser

The 399 nm laser based on a direct 399 nm diode is used for isotope-selective photoionization of neutral Ytterbium atoms[157]. It excites the atoms to the $4f^{14}6s6p\ {}^1P_1$ state and then a 370 nm photon from the cooling light excites the atom beyond the ionization threshold. The 399 nm laser is overlapped with the photoionization laser for the Indium atoms (see drawing in Fig. A.10 in appendix A.2) and transferred to the experiment table with a joined fiber. To avoid Doppler shifts, the two photoionization lasers propagate perpendicular to the atomic beams thus vertically through the loading segment of the trap.

3.3.3. In$^+$ lasers

A simplified term scheme and explanation of the relevant transitions has already been given in section 2.1.3. Here follows a brief summary of the technical details about the lasers.

Clock laser

The clock laser is a quasi-three level solid state Nd:YAG laser at 946 nm which was built in a collaboration with the Institute of Laser Physics in Novosibirsk. It is stabilized to 30 cm ULE cavity with fused silica mirrors operating at at room temperature and reaches a fractional frequency instability $\sigma_y = 1.1 \times 10^{-16}$ at 1 s. The thermal noise limit is 1×10^{-16}[166]. The lock is realized with the Pound-Drever-Hall (PDH) technique and the locking electronics are fully digital and an automatic re-lock is implemented. The ultra stable laser is sent to a frequency comb via a 160 m long PM fiber with a stabilized optical path and can be transfer locked to a cryogenic silicon cavity at 1542 nm with a fractional frequency instability $\sigma_y = 4 \times 10^{-17}$ at 1 s and drift rate of $\approx 120\,\mu$Hz/s [167]. More details about the setup and the noise contributions of the ultra-stable laser can be found in Didier et al. [168].

The system features a tapered amplifier (TA) providing 1.12 W at 946 nm at a current of 3 A. The frequency of the clock laser is controlled with a double-pass AOM. A small fraction of the light is sent through a path-length stabilized fiber to a frequency comb, which connects the clock laser to the time infrastructure at PTB. The main portion of the light is sent through an LMA fiber[11] to the experiment table. There follows another AOM that allows fast frequency switching between the different locking points of the clock sequence (compare Fig. 2.2). Next the frequency is quadrupled using a commercial fourth harmonic generation (FHG) system[12]. The system is typically operated at an output power of ≈ 3 mW, but is able to deliver up to ≈ 19 mW at 236.5 nm for an input power of 450 mW. For intensity stabilization and switching during the clock sequence a single-pass AOM at 265.5 nm is used. The setup after the FHG is shown in Fig.A.7 in the appendix A.2. With this setup, virtual $m = 0$ frequency light is sent to the frequency comb.

---

[11]NKT photonics: LMA-PM-15
[12]Toptica: FHG PRO

3. Experimental setup

Detection and cooling laser

The detection laser is an ECDL lasing at 922 nm which is stabilized to a 30 cm ULE cavity with fused silica mirrors and PDH locking technique as well and reaches a fractional frequency instability $\sigma_y = 3 \times 10^{-15}$ at 1 s. Due to the larger transition linewidth, the requirements on the stability are lower and less effort was put in the thermal shielding and the isolation of the system from vibrations and the cavity mirrors are not customized for high reflectivity at 922 nm. The light from the ECDL is amplified with a TA and frequency quadrupled with two self-built bow tie-type SHGs. The first SHG from 922 nm $\rightarrow$ 461 nm uses a periodically poled potassium titanyl phosphate (PPKTP) crystal. After the first doubling stage, the light is sent through a PM fiber to the second SHG based on a beta-barium borate (BBO) crystal, converting 461 nm $\rightarrow$ 230.5 nm. For the SHG locks, the Hansch-Couillaud technique is used. All cavities of the system feature an automatic re-lock for robust operation. As in the clock laser system, a double-pass AOM in the infrared is used for frequency control and a single-pass AOM in the UV for fast switching. A detailed description of the laser, the ULE-cavity and the two SHG cavities is given in [169]. Details about the re-locks will be published elsewhere. After the single-pass AOM, the UV light is coupled into a self-built fiber, described in the next paragraph, which guides the light to the ions. The setup of the beam path leading to the ions is depicted in Fig.A.6 in the appendix A.2.

Deep UV fibers

In both In$^+$ laser setups, self-built fibers guide the light from behind the single-pass AOM to the ions. With this the input-side setup is decoupled from the pointing to the ions and even more importantly the mode after the SHG output is cleaned. Otherwise the UV light focused to the ions could charge the trap and lead to varying electric fields at the ion position. At low wavelengths fused silica fibers show solarization [170, 171], leading to color centers which prevent transmission through the fiber [172, 173]. With hydrogen loading and curing the photonic crystal fibers at high UV intensities the color centers can be shifted to other spectral ranges [170] making the solarization-resistant at the curing wavelength. The fibers used in this setup are commercial available LMA fibers[13] and have been hydrogen loaded an UV cured according to a modification of the recipes of Y. Comlombe [174] and D. Slichter [175], which is described in detail in [169]. Both fibers have a transmission of $\approx 10\,\%$.

3.3.4. Wavemeter laser stabilization

Those lasers without a stabilization to an ultra-stable cavity all address transitions with widths of several 10 MHz, either naturally or because of saturation broadening. For their stabilization, a slow feedback to prevent frequency drifts is sufficient. These lasers are referenced to a wavemeter[14] with a mechanical 8-channel switch. The highly stable 822 nm laser [102, 165] is used to automatically calibrate the wavemeter every 10 min. With a software PI control, all other lasers (except the ultra-stable In$^+$ lasers) are tuned to the desired wavelength. For the Doppler cooling laser of Yb$^+$ at 739 nm, the stabilization to the wavemeter leads to an instability of about 1 MHz within 10 min. More details can be found in [102]. The

---

[13]NKT photonics: LMA-10-UV
[14]HighFinesse: Angstrom WS 8-2, sensitivity range: 330 nm-1180 nm

temperature sensitivity of the wavemeter increases with rising wavelength difference to the calibration wavelength of 822 nm and is 39 MHz/K for the 639 nm laser. With a linewidth of about 10 MHz and laboratory temperature variations of around 1 K over a day, several daily setpoint adjustments would be required. For this reason, a temperature stabilization has been set up. The wavemeter and the fiber switch are put into an aluminium box, which has a styrodur shell and is equipped with a Pt1000 temperature sensor and four 22 Ω heating resistors. A PI loop with a microcontroller[15] controls the resistors. On average, the temperature inside the box changes over less than 10 mK within a few hours which allows a constant setpoint for all laboratory conditions.

3.4. Loading - Atomic ovens and ablation target

3.4.1. Atomic ovens and ablation target

Figure 3.8 (a) shows the interior of the vacuum chamber: the ion trap, the two atomic ovens with two apertures each (close-up in (c)), the ablation target (close-up in (b)) and in-vacuum mirrors for a future path length stabilization for the clock laser. The left oven in (a) contains In and the right oven Yb.

Figure 3.8.: *Setup inside the vacuum chamber. (a) The ion trap, the atomic ovens, the ablation target and mirrors inside the chamber. (b) View on the ablation target through the window on the upper sidewall of the chamber. (c) Top view of the ovens and the two apertures.*
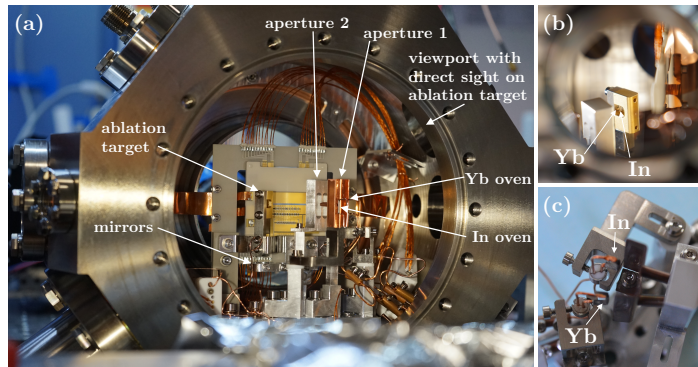
Both ovens consist of a vertical tantalum tube with a 400 μm diameter hole with spot-welded copper wires at the ends carrying the heating current. The atomic beams are collimated with an aluminium aperture having two 400 μm diameter holes limiting the atomic flux of both ovens to the loading segment (aperture 2). The copper aperture (aperture 1) with 1.5 mm diameter tubes reaching into the second aperture protects the trap from any material deposition from the ovens. For the Yb-oven, an isotope enriched sample is used while for the In-oven a natural source is used since ^{115}In has a natural abundance of more than 95 %. For the mounting of the ovens, care was taken to ensure mechanical stability and low thermal contact between the ovens and the mounts. For this reason the ovens wires are clamped inside macor surrounded by metal rings and the mounting arms are made from titanium because both materials feature a relatively low heat conductivity. The contact area is kept small with the rings only touching the holder arm at two edges and the screw touching

---

[15]Attiny84

the ovens only at one point (see Fig.3.8 (c)). The ablation target consists of a titanium holder onto which a chip of Yb and a piece of In foil have been glued, covered by a gold-coated aperture with a diameter of $400\,\mu$m. The ablation holder is mounted with a cross brace through the same holes as the trap feet. The viewport placed on the upper sidewall of the chamber provides direct view on the ablation target.
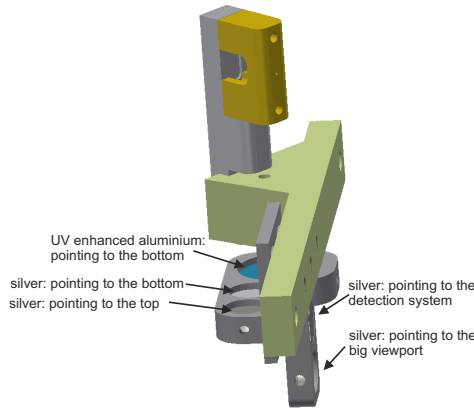

Figure 3.9.: *In-vacuum mirrors to set up a path length stabilization for the clock laser. The mirrors are screwed to the same cross bar as the ablation target which is connected to the ion trap. Two mirrors are facing the bottom, one the top, one the detection system and one the front viewport.*

The mirrors indicated in Fig.3.8 (a) and drawn in detail in Fig. 3.9 are mounted on the same cross bar as the ablation target pointing in the vertical and horizontal direction and can be used for a future path length stabilization for the clock laser. Another mirror is positioned next to the ovens (not visible in Fig.3.8 (a)), which could be used in future to reflect a $45\,^\circ$ Yb$^+$ cooling beam out of the chamber through the large viewport.

3.4.2. Deterministic loading procedure including non-fluorescing ions

Deterministic loading of both species is currently done with the atomic ovens, but the use of the ablation targets should make the loading process more time efficient in the long run. During loading, the number of ions is detected with the EMCCD camera. The Yb$^+$ ions are cooled and detected directly, while the In$^+$ ions are only sympathetically cooled via the Yb$^+$ ions and their number is inferred from the distances between the bright Yb$^+$ ions and the trap center. This way of detecting the In$^+$ ions originates from a time where the laser light and detection optics to directly detect the In$^+$ ions were not in place and is still in use because only detecting one species during loading keeps the procedure simple. Before the loading procedure is described, the detection of the fluorescing Yb$^+$ ions and the "non-fluorescing" In$^+$ ions is explained.

Detection of fluorescing Yb$^+$ ions
The fluorescing Yb$^+$ ions are detected by the camera and counted via a routine that searches for pixels with a brightness above a given threshold. Neighboring pixels above the threshold are combined to an ion object consisting of a list of contributing pixels. The position of the ions is then calculated via a brightness-weighted sum of the pixel positions with a resolution

below the pixel size.

Detection of "non-fluorescing" In$^+$ ions

In a one-dimensional linear chain, the ion positions only depend on the axial confinement and the total number of ions n_{total}, but are independent of the ion mass. Before the number of "non-fluorescing" ions n_{dark} can be inferred from every EMCCD image, a measurement of the ion positions $\vec{p}_{\text{bright}}$ of a linear ion crystal only containing fluorescing ions is used to calibrate the crystal center and the axial secular frequency ω_{ax}, with the prior knowledge of the camera pixel size a_p and the magnification M of the imaging system. This allows to normalize the experimentally determined ion positions $\vec{p}_{\text{bright}}$ with the normalization factor [176]

$$L^3 = \frac{e^2}{4\pi\epsilon_0 m\omega_{\text{ax}}^2} \tag{3.8}$$

via

$$\tilde{\vec{p}}_{\text{bright}} = \frac{\vec{p}_{\text{bright}} a_p}{ML} \tag{3.9}$$

and to compare them to dimensionless theoretical ion positions $\vec{p}_{\text{theo}}$.

$\tilde{\vec{p}}_{\text{bright}}$ containing n_{bright} elements is compared to $\vec{p}_{\text{theo}}[i]$ with $n_{\text{bright}} \leq i \leq n_{\text{max}}$. In the following, the number x of elements of a vector is denoted by $[x]$. Each element of $\tilde{\vec{p}}_{\text{bright}}[n_{\text{bright}}]$ is assigned the index from $\vec{p}_{\text{theo}}[i]$ with the closest position. If two elements of $\tilde{\vec{p}}_{\text{bright}}[n_{\text{bright}}]$ are assigned the same index, solution i is discarded because no two ions can be at the same position in the crystal. The assigned indices of $\vec{p}_{\text{theo}}[i]$ are transferred to $\vec{p'}_{\text{theo}}[n_{\text{bright}}]$ which only contains indices corresponding to bright ion positions.

For the decision which i corresponds to the correct total ion number, the quantity

$$b(i) = \frac{|\tilde{\vec{p}}_{\text{bright}}[n_{\text{bright}}] - \vec{p'}_{\text{theo}}[n_{\text{bright}}]|^2}{n_{\text{bright}}} \tag{3.10}$$

is derived for all i. $b(i)$ corresponds to the averaged squared difference between the experimental normalized ion positions and the assigned theory positions. The smallest value of $b(i) = b_{\text{min}}$ is compared to a threshold ϵ.

For

$$b_{\text{min}} < \epsilon \tag{3.11}$$

i is taken as the total ion number $n_{\text{total}} = n_{\text{bright}} + n_{\text{dark}}$ otherwise there is no solution.

The minimum value of ϵ, when no more solution is found, depends on the ratio of the uncertainty of the ion position determination to the minimal ion distances to differentiate. With decreasing ω_{ax} the ion distances for a given number of total ions n_{total} increase which

3. Experimental setup

relaxes the demands on ϵ. The uncertainty of the ion position determination is influenced by the resolution of the detection system, but also by the chosen threshold for the fluorescing ion detection in relation to the exposure time and the intensity used to drive the fluorescing transition.

Imperfections in the detection system, for example locally varying distortions of the image can lead to a wrong determination of n_{total}. The probability for a wrong result increases with increasing n_{total} and increasing ratio $n_{\text{dark}}/n_{\text{bright}}$ and strongly depends on the permutation of the bright and dark ions.

In practice, initial tests with up to 16 ions, including up to 14 "non-fluorescing" ions, have yielded the correct total ion number n_{total}. For 16 ions, however, not all of the possible permutations of the two ion species have occurred, so that without a detailed experimental statistical investigation or an estimation of the relevant uncertainties, no precise statement can be made about the reliability of the presented method. A more detailed analysis will be published elsewhere.

Loading procedure
The loading procedure is similar for both ion species and depicted in Fig. 3.10, only the exact parameters, which are summarized in Table 3.7, differ slightly.
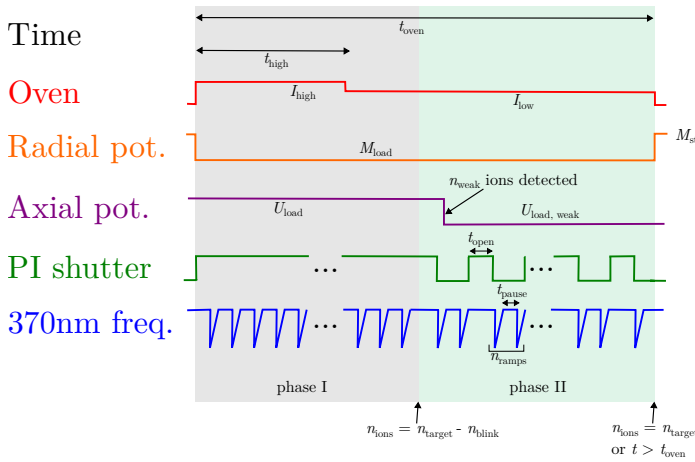
Figure 3.10.: *Deterministic loading procedure for Yb$^+$ and In$^+$ ions. The radial and axial trap potential is changed for the loading process. In phase I (gray) the photo ionization laser is applied continuously and in phase II (green) it is paused for short time periods while cooling ramps are applied to safely count the number of ions n_{ions} and stop loading at the targeted ion number n_{target}.*

The targeted number n_{target} of Yb$^+$ ions is loaded first, then the In$^+$ ions are loaded. During loading, the radial trap frequency f_{rad} is reduced to about $380\,\text{kHz}$ (Yb$^+$ COM mode) by setting the output power of the trap drive rf source to a lower value M_{load} than the standard value M_{st}. The axial confinement U_{load} is set with the U_t voltages of segment 7, 8 and end2 such that a linear crystal forms with a large enough ion spacing to clearly distinguish the ions from each other. As soon as the loaded ion number reaches n_{weak}, the axial potential is lowered to $U_{\text{load,weak}}$. For both species, the loading process is divided into two phases. In phase I, the photo ionization laser is switched on continuously and -7Γ to -$\Gamma/2$ cooling ramps on the Yb$^+$ cooling beams H1, H2 and the helper beam at -85 MHz are applied. The

Table 3.7.: *Parameters and variable names for the deterministic oven loading procedure of* Yb^+ *and* In^+ *ions.*

	parameter	value	physical meaning
oven	I_{high}	9.0 A (Yb) / 11.0 A (In)	
	I_{low}	8.9 A (Yb) / 10.8 A (In)	
	t_{oven}	420 s (Yb) / 350 s (In)	
	t_{high}	100 s (Yb) / 150 s (In)	
potential	M_{load}	-15.0 dBm (380 mVpp)	$\omega_{rad}/2\pi \approx 380$ kHz
	M_{st}	-8.9 dBm (756 mVpp)	$\omega_{rad}/2\pi \approx 820$ kHz
	U_{load}	(Ut_7, Ut_8, Ut_{end2})=(2.0, 0.2, 1.1) V	$\omega_{ax}/2\pi \approx 110$ kHz
	$U_{load,weak}$	(Ut_7, Ut_8, Ut_{end2})=(1.2, 0.2, 0.7) V	$\omega_{rad}/2\pi \approx 85$ kHz
	n_{weak}	8	
lasers	370 nm DP frequency	107.5 MHz	$-\Gamma/2$
	370 nm powers	50 μW (H1), 20 μW (H2), 3 μW (helper)	$s_{H1} = 7$, $s_{H2} = 4$
	PI power	3.9 mW (Yb)/ 2.2 mW (In)	
timing	t_{pause}	100 ms	
	t_{open}	1000 ms (Yb) / 2000 ms (In)	
	n_{ramps}	2	
	n_{blink}	2-3	

pause t_{pause} between the cooling ramps is used to update the loaded ion number with every EMCCD image. To prevent loading of more than n_{target} ions, in phase II the loading process is paused in between by switching off the photo ionization (PI) laser to safely determine the number of ions n_{ions} and prevent overshooting of n_{target} due to delayed crystallization. Simultaneously, cooling ramps are executed to support the crystallization. Phase II starts as soon as n_{ions}=n_{target}-n_{blink}. As a safety measure the loading process is aborted as soon as the maximum oven time t_{oven} is reached. For time efficient loading, the oven is heated up at a higher current I_{high} for the time t_{high} before its current is reduced to a lower current I_{low} to counteract the exponential increase of the oven temperature and the atomic flux.

During loading of the In$^+$ ions, the laser at 230 nm is switched on for dissociation of YbX$^+$ molecules that otherwise tend to form more frequently while the Indium oven is running (more details about molecule formation are given in section 3.2.3). Loading times reach from three to about eight minutes depending on the target ion number n_{target}.

3.5. Magnetic field coils & magnetic shielding

Magnetic field coils

The magnetic field at the position of ions can be controlled by three pairs of coils aligned along x, y and z in approximate Helmholtz configuration as shown in Fig. 3.11.
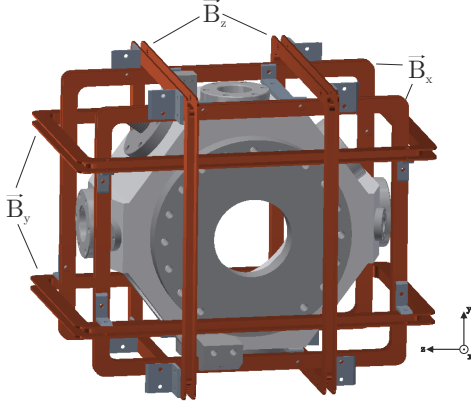

Figure 3.11.: *Three pairs of magnetic field coils in almost Helmholtz-like configuration. The current-carrying coils each generate a magnetic field along x, y or z and are mounted at right angles to each other on the chamber.*

All six coils consist of 24 windings of a 1 mm diameter lacquered copper wire. The dimensions of all three coil pairs is listed in Table 3.8. The holders are fabricated from hard fabric panels[16] and mounted to each other with right-angled aluminum connectors. The holders of the B_x coils are mounted to the top and bottom of the chamber through four counterbores each, which defines the alignment of the entire coil system to the chamber and thus to the ion trap. The current for the coils is provided by remote controlled low-noise current supplies[17]. All three coil pairs are designed to provide a magnetic field of about $300\,\mu$T at a maximal current of 2.5 A. The relation between the magnetic field B and the applied current I of the three coil is also given in Table 3.8.

Table 3.8.: *Dimensions and ratio B/I of the magnetic field and the applied current I of the magnetic field coils. The width d, length l and center-to-center distance A of the three coil pairs providing magnetic fields along the x-, y- and z-direction.*

coil pair	d (mm)	l (mm)	A (mm)	B/I (μT/A)
B_x	296	252	162	135.275
B_y	206	346	170	129.820
B_z	288	246	144	147.035

Long-term drifts of external magnetic fields are compensated with the help of the ^{2}D$_{3/2}$ $\leftrightarrow$ ^{3}[3/2]$_{1/2}$ transition at 935 nm. At zero B-field, only Δm=0 transitions are allowed so that the

[16]HGW 2082, trade name: Novotex
[17]TTi: QL355T

outer substates of the $^2D_{3/2}$ level become dark. By minimizing fluorescence during Doppler cooling, the coil currents for compensation can be found. More details about this procedure are given in in [177, 178].

The coils have been optimized for magnetic fields as homogeneous as possible, especially along the z-direction which is the direction along which the ion chain aligns. During clock spectroscopy, a magnetic field of $100\,\mu T$ is applied along the z-direction to separate the Zeeman transitions and enable optical pumping into the stretched states. As described in section 2.4.2 the Zeeman splitting of the ground and excited clock sates of $^{115}In^+$ is determined by the g-factors $g(^1S_0) = -6.6647 \times 10^{-4}$ [118] and $g(^3P_0) = -6.87(5) \times 10^{-4}$ [79]. The first-order Zeeman sensitivity of the $^1S_0(m_F=9/2, m_F=-9/2) \leftrightarrow ^3P_0(m_F=9/2, m_F=-9/2)$ transition is $20.19\,kHz/mT$, as derived in section 2.4.2. To keep inhomogeneous Zeeman broadening below the natural linewidth of $820\,mHz$, the variation of the magnetic field component ΔB_z across all ions has to be below $40.6\,nT$. This value provided an orientation for the design of the coils. In the optimal case, only the B_z coils provide a B-field component along the z-direction. Figure 3.12 shows the calculation of the variation of the magnetic field component B_z from the average $\overline{B}_z$ component along the z-direction for all three coil pairs. Apart from an optimal alignment, a displacement of $1.2\,mm$ (and $2.4\,mm$) along x and y is assumed. Conservatively, the calculations are performed for a current $I=2.5\,A$ which would result in case of optimal alignment in magnetic field components $B_x = 340\,\mu T$, $B_y = 320\,\mu T$ and $B_z = 370\,\mu T$.
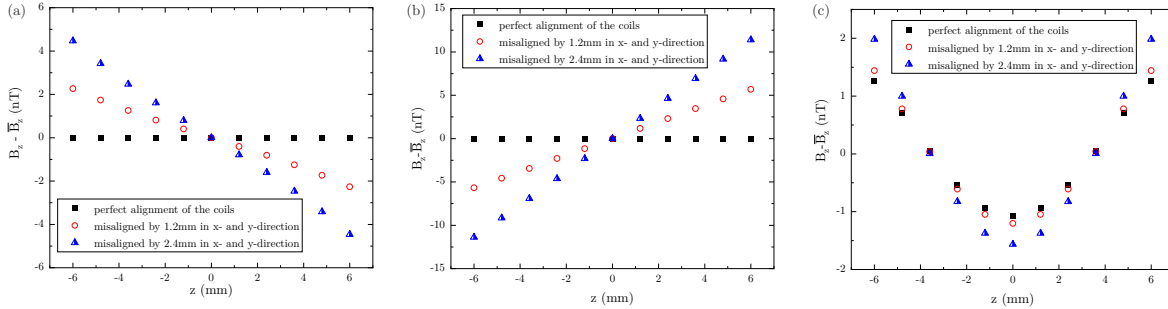

Figure 3.12.: *Calculated inhomogeneity of the magnetic field component B_z along the z direction for all three coil pairs: (a) B_x coils, (b) B_y coils and (c) B_z coils. The graphs show the difference between the magnetic field component B_z and the average $\overline{B}_z$ component along the z-direction. In addition to an optimal alignment, a displacement of both coils by $1.2\,mm$ ($2.4\,mm$) in x- and y-direction is assumed.*

Table 3.9 lists the results of $\Delta B_{z,opt}$ and $\Delta B_{z,dis}$ for a $300\,\mu m$ crystal in the center of the coils and a hypothetical crystal across the $9.7\,mm$ trapping region. Hereby $\Delta B_{z,opt}$ and $\Delta B_{z,dis}$ are the variations of the z- component for optimal alignment and a conservatively assumed displacement of $2.4\,mm$ in x- and y-direction. Apart from the results of the individual coil pairs, also the sum is listed.

The results for the $300\,\mu m$ crystal are more than an order of magnitude below the target

3. Experimental setup

Table 3.9.: *Evaluation of the expected magnetic field homogeneity of all coils along the z-direction. Listed are $\Delta B_{z,\mathrm{opt}}$ for optimal alignment and $\Delta B_{z,\mathrm{dis}}$ assuming a displacement of 2.4 mm in x- and y-direction for all three coil pairs. The evaluation is done for a 300 μm crystal in the center of all coils and a hypothetical crystal across the 9.7 mm trapping region.*

	coil pair	$\Delta B_{z,\mathrm{opt}}$ (nT)	$\Delta B_{z,\mathrm{dis}}$ (nT)
300 μm crystal	B_x coils	0	0.2
	B_y coils	0	0.58
	B_z coils	<0.14	<0.2
	sum	<0.14	<1
9.7 mm trapping region	B_x coils	0	6.83
	B_y coils	0	18.30
	B_z coils	1.79	2.57
	sum	1.79	27.7

and even for clock operation with ions across the whole trapping region, the magnetic field inhomogeneity of the sum of the B_z components would be low enough to keep the Zeeman broadening below the natural linewidth. One has to keep in mind that the calculations assume perfect winding of the coils and only consider displacements but no tilts. But the assumed conservative maximal displacement shows a larger deterioration as a realistic tilt of a single coil and is therefore used as a worst-case scenario. Because the calculations have been performed at currents providing B-fields around $300\,\mu$T, the expected variations are even lower when operating at typical B-fields of $100\,\mu$T in z-direction and the typical $2\,\mu$T and $35\,\mu$T for the compensation in the other two directions.

The calculated spatial variation of all B-field components of the three coil pairs along the z-direction can be seen in the appendix A.3.

Magnetic shielding

Magnetic field fluctuations at the position of the ions originating from the environment increase the uncertainty of the atomic clocks. To attenuate magnetic field fluctuations, a two-layer μ-metal shield is designed to fit around the vacuum chamber, the magnetic field coils and the helical resonator. Both 1.5 mm thick layers consist of a bottom and top part as shown in Fig. 3.13.

The outer bottom part rests on two angles that are connected to the chamber mounts. A thin layer of polymer prevents sliding of the shield. The layers are designed for a spacing of 1 cm, therefore the inner bottom layer is held in place by four polymer pieces which are placed in the corners in between the layers. The top parts have a slightly smaller horizontal

***Figure 3.13.:** Drawing of the setup with two-layer μ-metal shielding. The two layers have a bottom (blue) and top (green) part each. The outer bottom part is placed on two angles, that are screwed to the chamber mounts. The inner parts fit into the respective bottom parts. Cutouts ensure access for laser beams, the detection system and cables.*
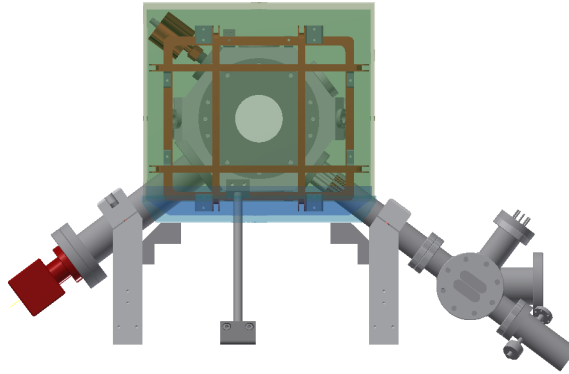
cross-section than the respective bottom parts to fit and thereby close the shield. The shield has cutouts for all laser beams, the two tubes on the left and right side of the chamber, the detection system and the cable to the helical resonator. A theoretical model, which neglects the cutouts predicts an attenuation factor of 5000. Due to the cutouts, the attenuation factor will be reduced. A comparable μ-metal shield from the same vendor exhibits an attenuation in the high 10^2 to low 10^3 regime which decreases for lower frequencies. At frequencies of only a few kHz no attenuation is noticeable. This attenuation factor is more realistic estimate for this shield, but of course the attenuation factor highly depends on the cutouts and the exact frequency.

3.6. Detection system

The content of this section is part of a publication by the author of this thesis, currently under review for publication in "Review of Scientific Instruments".

The detection system enables simultaneous imaging of the fluorescence of both ion species on a shared EMCCD camera, thereby providing spatially resolved state detection of both species for spectroscopy. Furthermore, the collection of the fluorescence of both species on individual photomultiplier tubes (PMT) is possible.

To enable a large numerical aperture NA, the vacuum system features a 6.35 mm thick reentrant viewport (as shown in Fig. 3.4). A drawing of the horizontal plane of the chamber with the reentrant viewport and the relevant dimensions for the detection system is shown in Fig.3.14. The working distance of the imaging system is 35.54 mm.

3.6.1. Specifications

The smallest possible working distance of the system is 31 mm. The spatial limitations of the reentrant viewport allow a lens diameter of 2" enabling an NA of 0.4-0.5. A field of view of $\pm150\,\mu$m is desired to image Coulomb crystals with a length around $300\,\mu$m. The
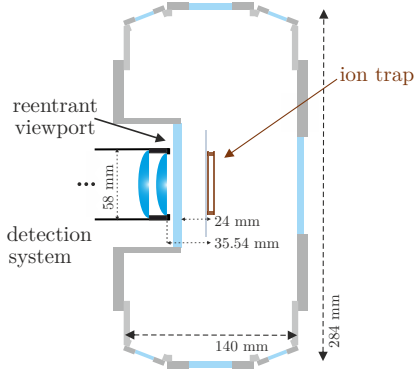
3. Experimental setup

Figure 3.14.: *Drawing of the horizontal plane of the vacuum chamber with the ion trap at its center. The detection system is placed behind the 6.35 mm thick reentrant viewport, the distance between the ions and the viewport is 24 mm and the working distance of the detection system is 35.54 mm.*

targeted magnification is between 12 and 16. The lower bound is given by the requirement to resolve the individual ions on the 16 μm sized pixels of the EMCCD camera[18]. For example, if a 20-ion chain is trapped at a radial secular frequency of $2\pi \times 1$ MHz (for Yb$^+$), then the maximum axial secular frequency at which the ions still form a linear chain is about $2\pi \times 100$ kHz (for Yb$^+$). For the lower bound of the magnification this would correspond to a distance of the innermost ions of 4.6 μm and therefore 3.5 pixels. The upper bound ensures that the full field of view is imaged on the 8 mm sized camera chip. Ideally, each ion is only imaged to a single pixel to keep the noise contribution for the read-out minimal. The targets of simultaneous imaging of both UV wavelengths and single-ion resolution are significantly more important than the noise properties, so that imaging each ion to 2×2 or 3×3 pixels is also sufficient given the minimal distance of 3.5 pixels between two ions that needs to be resolved.

The evaluation criterion for optimization of the design is the fraction of enclosed energy f_{ee} in a given radius from centroid r_c.

A diffraction limited system can be characterized by its Airy full width at half maximum (FWHM) δ_A [179, 180]:

$$\delta_A = \frac{0.51 \cdot \lambda}{NA}, \tag{3.12}$$

where λ is the wavelength of the imaging light. The fraction of the energy enclosed in the radius $r_A = \delta_A/2$ is $f_{ee}(r_A) = 0.76$.

In the following, the radius r_A is is used to classify the system via simulations of the fraction of enclosed energy f_{ee} in a given radius from centroid r_c. Since the simulations contain the magnification M, Eq. 3.12 needs to be corrected for M in order to compare the values, which results in:

$$r_A = \frac{0.51 \cdot \lambda \cdot M}{2NA}, \tag{3.13}$$

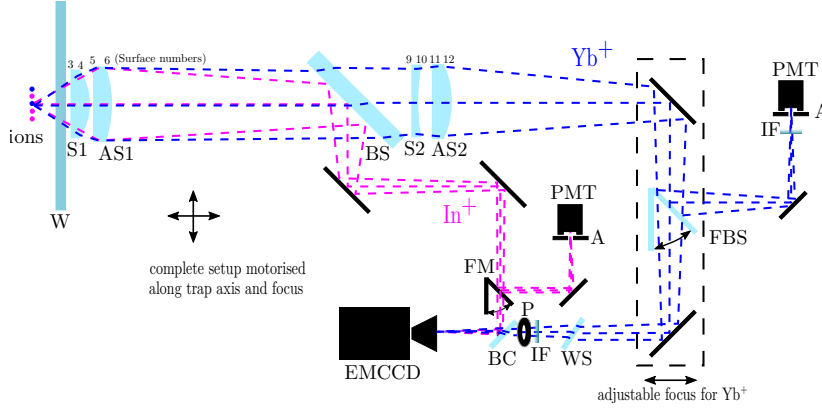---

[18] Andor, iXon Ultra 897

3.6.2. Design

Figure 3.15.: *Setup of the bichromatic detection system. The In$^+$ and Yb$^+$ fluorescence at 230.6 nm and 369.5 nm are collected by a lens doublet (S1 and AS1) and are then separated by a dichroic beamsplitter (BS). The In$^+$ fluorescence is reflected, while the Yb$^+$ fluorescence is transmitted and passes through a second lens doublet (S2 and AS2) and is guided over two mirrors to be overlapped with the In$^+$ fluorescence again and both wavelengths are simultaneously imaged onto the EMCCD camera. Abbreviations: vacuum window (W), spherical lens (S1/S2), aspherical lens (AS1/AS2), beam combiner (BC), flippable mirror/beamsplitter (FM/FBS), wedged substrate (WS), pinhole (P), slit aperture (A), interference filter (IF). The small numbers are used to label the surfaces.*

Figure 3.15 shows a schematic drawing of the imaging system. Fluorescence light of both ion species passes through the 6.35 mm thick vacuum window (W) and is collected by the first lens doublet consisting of a sphere (S1) and an asphere (AS1). The next optical element is a beam splitter (BS), which reflects the In$^+$ wavelength but transmits the Yb$^+$ wavelength (cutoff wavelength for reflectance: 245 nm). The Yb$^+$ image is then corrected by a second lens doublet consisting of a sphere (S2) and an asphere (AS2). Afterwards it is reflected by two mirrors and transmitted through a 1 ° wedged substrate (WS). With a pinhole (P), the NA for the Yb$^+$ image on the camera is reduced to ≈ 0.25. Finally, a beam combiner (BC) combines the In$^+$ and Yb$^+$ fluorescence again on the EMCCD camera. The wedged substrate compensates aberrations induced by the beamsplitter and the beamcombiner. All lenses have a anti-reflection coating optimized for both wavelengths (curved surfaces: R<2% at 230 nm and R<2.5% at 370 nm, plane surfaces of S1 and AS1: R<1% at 230 nm and R<1% at 370 nm, plane surfaces of S2 and AS2: R<0.2% at 370 nm).

The system is fully motorized: besides the motors to adjust the focus and axial position to image ions in all eight segments of the trap [90], the system provides two automated flip mirrors to send the fluorescence of both species on photomultiplier tubes (PMTs). The Yb$^+$ fluorescence is filtered by interference filters (IF) with a transmission $T = 0.9$ and a bandwidth $BW = \pm 6$ nm in front of the PMT and EMCCD each, to protect those from background stray light. For the In$^+$ beam path, no filter is needed since the coating of the substrates is only reflective for wavelengths within a 40-60 nm band around the In$^+$ intercombination line at

3. Experimental setup

230.6 nm and the PMT is solar blind[19]. The two mirrors behind the second lens doublet are mounted on a shared translations stage to adjust minor focus differences in the two beam paths individually. These two mirrors are also the only mirrors that can be tilted in two directions to control the position of the Yb^+ image on the camera independently of the In^+ image. In general, the number of degrees of freedom was kept as low as possible to achieve the best possible stability and simplest possible adjustment of the complex system. In front of both PMTs a slit aperture (A) is mounted to protect them from stray light e.g. scattered light from the trap electrodes.

With both wavelengths in the UV, the number of optical elements was kept to a minimum, therefore aspheric lenses were chosen. Because of the narrower linewidth and the lower wavelengths of the fluorescence of the In^+ compared to the Yb^+ ions, the focus for the optimization was set on lowest aberrations at 230.6 nm. For this reason, as few as possible transmittive elements are used to avoid losses in the deep UV light. Furthermore, dichroic beamsplitters are easier to realize when the longer wavelength is transmitted and the shorter reflected, respectively [181].

The first design idea was to use two biaspheric lenses instead of lens doublets, but the relative centering of two aspheric lens surfaces could not reach the necessary tolerances. Lenses with one planar surface can be machined with much higher precision.

Table 3.10.: *Surfaces as given in the Zemax lens data editor. The numbering of the surfaces is consistent with Fig. 3.15. The coefficients of the aspheric surfaces 6 are k=-3.7, A_4=1.065 × 10^{-6} and A_6=-8.995 × 10^{-10} and for surface 12 k=0.83, A_4=-3.956 × 10^{-7} and A_6=-1.714 × 10^{-10}*

Lens	Surface e	Type	Radius (mm)	Thickness (mm)	Diameter (mm)	Glass
S1	3	Sphere	Infinity	15.00	44.00	Corning 7980
S1	4	Sphere	-34.59	5.00	44.00	
AS1	5	Sphere	Infinity	15.00	50.80	Corning 7980
AS1	6	Even asphere	-57.708	95.00	50.80	
S2	9	Sphere	Infinity	5.00	48.80	Corning 7980
S2	10	Sphere	53.68	10.00	48.80	
AS2	11	Sphere	Infinity	15.00	50.80	Corning 7980
AS2	12	Even asphere	-51.60	197.825	50.80	

---

[19]CsTe cathode with sensitivity range: 160 nm-320 nm, QE = 30 % at 230nm, Hamamatsu R7154

The system was optimized for three different positions in the object plane: at $0\,\mu m$, $106\,\mu m$ and $150\,\mu m$ off the optical axis. Table 3.10 lists the result of the optimization. The numbering of the surfaces is indicated in Fig.3.15. The front surfaces of all lenses, surfaces 3, 5, 9 and 11, are plane. Surfaces 6 and 12 are aspherical and surfaces 4 and 10 are spherical. The optimized system has an $NA = 0.45$ and a magnification $M = 12$ for 230.6 nm and $NA = 0.40$ and $M = 10$ for 369.5 nm. The NA is limited by the diameter of the second lens for the 230.6 nm path and by the fourth lens for the 369.5 nm path. The beamsplitter (BS) in the 369.5 nm path will introduce aberrations, for the compensation of which the wedged substrate (WS) was introduced. These two components and the vacuum window (W) have not been considered in the tolerancing, described in section 3.6.3, as this would have exceeded the complexity of the tolerancing. In order to achieve a high collection efficiency on the PMT and a possibly aberration free image on the camera, an aperture was included on the way to the camera to reduce the NA to ≈ 0.25.

Figure 3.16 (a) shows the 2D point spread function (PSF) and the fraction of enclosed energy f_{ee} of the 230.6 nm path for the three optimization points in the image plane. Fig. 3.16 (b) illustrated the same quantities for the 369.5 nm path. It is noticeable that the imaging quality of the 369.5 nm beam path is significantly better for the off-axis positions. The on-axis PSF shows a pale vertical and horizontal stripe.
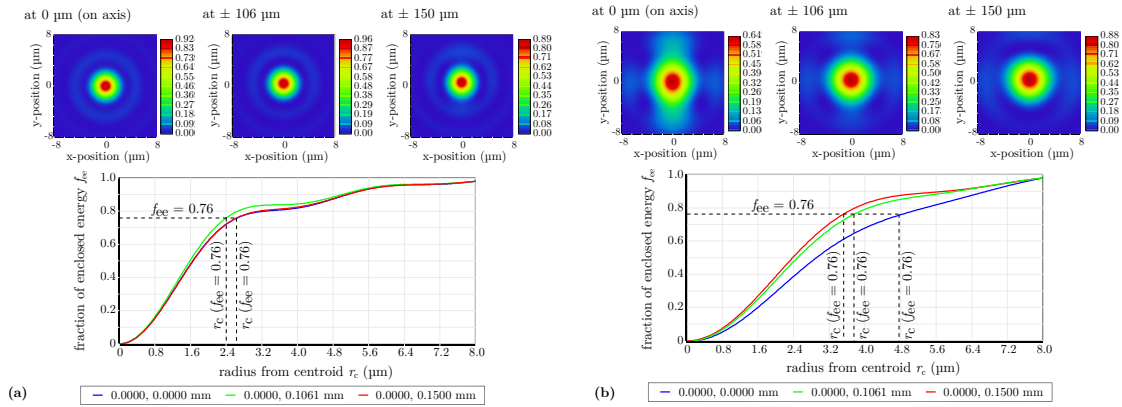
Figure 3.16.: *2D point spread function (PSF) (top) and fraction of enclosed energy f_{ee} versus the radius from centroid r_c (bottom) of the optimized 230.6 nm (a) and 369.5 nm (b) path at three positions in the object plane: $0\,\mu m$, $\pm 106\,\mu m$ and $\pm 150\,\mu m$ (off the optical axis). For the optimized systems $f_{ee}(r_c = 8\,\mu m) = 0.98$, which means that 98 % of the fluorescence is imaged on a single $16\,\mu m$ pixel for both wavelengths.*

Table 3.11 compares the radius $r_A = \delta_A/2$ at which a diffraction limited system theoretically reaches a fraction of enclosed energy $f_{ee}(r_A) = 0.76$, calculated according to Eq. 3.13, with the radius $r_{c,ideal}(f_{ee} = 0.76)$ corresponding to the simulations of the optimized system (shown in Fig. 3.16, $f_{ee} = 0.76$ and the respective values for r_c, are indicated). For both wavelengths $r_{c,ideal}(f_{ee} = 0.76)$ is a factor 1.5-2 worse than the diffraction limited $r_A(f_{ee} = 0.76)$. Diffraction limited imaging of both wavelengths could only have been achieved on the axis

point. The additional field correction to image $300\,\mu$m long crystals prevents diffraction limited imaging at the large NA without further optical components. Imaging both species to a single pixel with a size of $16\,\mu$m $\times\,16\,\mu$m is possible as the fractions of enclosed energy $f_{ee}(r_{c,ideal}=8\,\mu m)=0.98$ for both paths of the ideal system. This holds for the ideal system, since so far no tolerances are taken into account.

Table 3.11.: *Comparison of the theoretical diffraction-limited radius $r_A = \delta_A/2$ at which the fraction of enclosed energy $f_{ee}(r_A) = 0.76$ with the radius from centroid $r_{c,ideal}$ at which $f_{ee} = 0.76$ for the ideal system according to the simulations in Fig. 3.16 (a) and Fig. 3.16 (b). The field correction to image $300\,\mu$m long crystals prevents diffraction limited imaging at the large NA.*

	r_A	$r_{c,ideal}(f_{ee}=0.76)$
	(μm)	(μm)
230.6 nm	1.57	2.4-2.6
369.5 nm	2.36	3.5-4.8

3.6.3. Tolerancing

The performance of the system shown in section 3.6.2 is idealistic. The realistic performance will be lower due to manufacturing tolerances of the lens surfaces and the mounting.
The tolerancing includes tolerances for the center thickness, radii, the mounting and the surface form tolerances of the lenses, which are listed and described in the appendix A.4. All components apart from the four lenses are assumed to be perfect.

Considering all tolerances of the lenses, except the surface form tolerances, reduces the enclosed energy in worst-case to $f_{ee}(r_c=8\,\mu m)=0.8$ for the 230.6 nm path and $f_{ee}(r_c=8\,\mu m)=0.7$ for the 369.5 nm path, as shown in Fig. 3.17. Here, worst case means the worst result out of 4000 combinations of all considered tolerances. This means the expected fluorescence yield on one pixel is reduced to 80% and 70 % at 230.6 nm and 369.5 nm, respectively.

Consideration of the surface form tolerances, given in the appendix A.4, reduces the fluorescence enclosed in a radius $r_c = 8\,\mu$m by another 8 %, resulting in $f_{ee,tol}(r_{c,tol}=8\,\mu m)\approx 0.7$ and $f_{ee,tol}(r_{c,tol}=8\,\mu m)\approx 0.6$ for the 230.6 nm and 369.5 nm, respectively. As mentioned in section 3.6.2, the beamsplitter (BS) and wedged substrate (WS) in the 369.5 nm path, as well as the vacuum window (W), are not considered in the tolerancing process. However, transmitting elements exhibit a large influence on aberrations, so the actual performance will probably be worse.

Figure 3.17.: *Worst-case on-axis 2D point spread function (PSF) and fraction of enclosed energy of the 230.6 nm (a) and 369.5 nm (b) path considering the tolerances for the center thicknesses, radii, tilts and decentering of the lenses and assuming all other parts to be perfect. The 2D PSFs for the two other positions are similar to the on-axis position.*
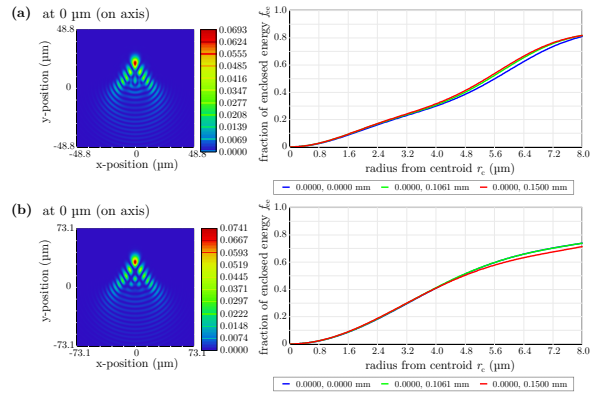
3.6.4. Mechanical mounting

The total weight of all four lenses is ≈ 160 g. For the mounting, the distance of the two lenses within one doublet and a possible tilt between the lenses are most critical. The requirement for the distance between the two doublets is lower. Both lens doublets are mounted monolithically inside a black anodized aluminum tube according to the same principle, as shown in Fig. 3.18. The distance between the two steps holding the plane surfaces is machined with a tolerance of $\pm 10\,\mu$m and a flatness of 3-4 μm, which is better than the required tolerances stated in Table A.8.

Figure 3.18.: *Mounting of the first lens doublet. The lenses are enclosed in an aluminum tube that features two two precisely machined steps that touch the plane front of the two lenses (S1 and AS1). The lenses are held in place by threaded rings (yellow).*
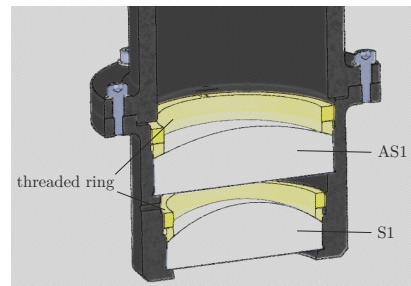
An overview of the mounting of the whole system is shown in Fig. 3.19. The number of adjustable degrees of freedom is reduced to a minimum in order to keep the complexity of the setup as low as possible. Apart from the Yb$^+$ PMT, all parts are mounted on a 300 mm×400 mm aluminum plate with a thickness of 10 mm. The two mounted lens doublets and the beam splitter (BS) are connected via a black anodized aluminum tube and mounted on a height adjustable table. Both beampaths are guided into a light tight box where the rest of the optical elements is placed. The size and the height of the slit aperture in front of the In$^+$ PMT is adjustable with a high-precision screw. For the Yb$^+$ path, the last two mirrors are placed on a shared translation stage to adjust the focus of the two beam paths individually and the wedged substrate (W) is fixed on a rotational stage. Both stages can be adjusted from outside the box. Motorized flip mirror holders[20] with a repeatability of less than 100 μrad are used to guide the fluorescence on either the PMT or the EMCCD camera

---

[20]Owis: KSHM 40-LI-MDS and KSHM 90-LI-MDS

3. Experimental setup

in case of the In$^+$ path (FM) and on both in equal proportions or only on the EMCCD in case of the Yb$^+$ path (FBS). The Yb$^+$ PMT is mounted on the wall of the small box and connected in a light-tight construction with the interference filter (IF) and the slit aperture (A). The small box is mounted on a height adjustable table. The connection between the two boxes is sealed light-tight with a bicycle tube.
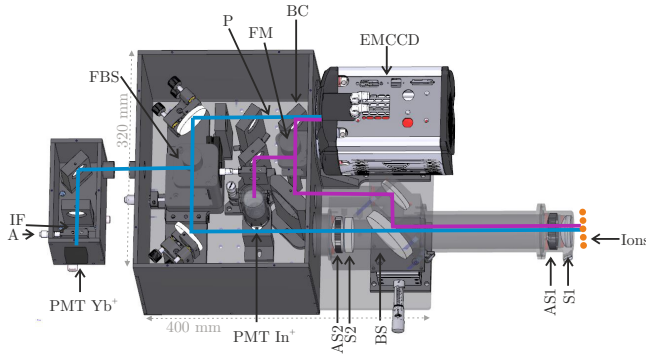

Figure 3.19.: *Mounting of all optical components. Most components are placed on an aluminum base plate inside a light-tight box. All components which require precise adjustment are equipped with fine adjustment screws. With the exception of the degrees of freedom that affect the solar-blind In$^+$ PMT, all adjustments can be made with the box closed.*

The whole system with a weight of about 25 kg is placed on a 450×600 mm carbon fiber reinforced polymer breadboard with a thickness of 50 mm. The board is connected to a self constructed motorized 2-dimensional translation stage as shown in Fig. 3.20. For the translation of the systems along the focus two translation stages are used, one is driven with a dc motor (Thorlabs: Z812B) and the other serves as support. The translation along the trap axis is similar but here two support translation stages are used. The breadboard material was selected because of its low thermal expansion and low weight combined with a relatively good stability. The grey steel cuboid placed on the breadboard next to the detection system brings the center of gravity of the system back over the rail system to allow smooth translation.
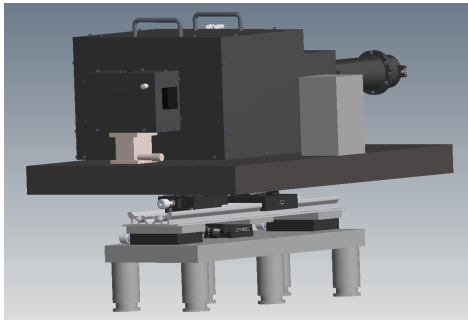

Figure 3.20.: *Translation of the imaging system. The system is mounted on a $450 \times 600 \times 50$ mm carbon breadboard which is placed on two translation stages, one of them being motorized, to adjust the focus of the system. The stages are connected via an aluminum rail to three other stages translating perpendicular to the focus to move along the trap axis, also here only one stage is motorized. The grey cuboid is a balance weight made from steel bringing the center of gravity over the rail system.*

3.6.5. Characterization

A false color EMCCD image of a linear 10 In$^+$/4 Yb$^+$ ion crystal is shown in Fig. 3.21. The size of the Yb$^+$ image is increased to match the magnification of the In$^+$ image and is rotated by 1.2° to compensate a tilt of the system. Due to their different magnifications, the two

species are imaged at slightly different positions in vertical direction to avoid overlapping In^+ and Yb^+ ion positions on the EMCCD camera.

Figure 3.21.: *EMCCD image (false color) of a linear Coulomb crystal consisting of 10 In^+ and 4 Yb^+ ions. The Yb^+ ion image is increased to the same magnification as the In^+ image and rotated by 1.2°. The simultaneous exposure time is 200 ms.*
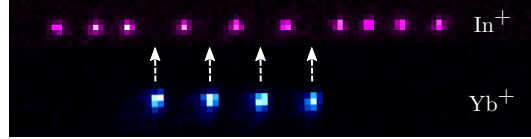
During the assembly of the system, the most critical alignment was the angle with respect to the vacuum window, because small deviations lead to distortions of the Yb^+ ion image without the pinhole reducing the NA. After alignment optimization the Yb^+ ion image still shows coma on the EMCCD camera as depicted in Fig. 3.22 (b).
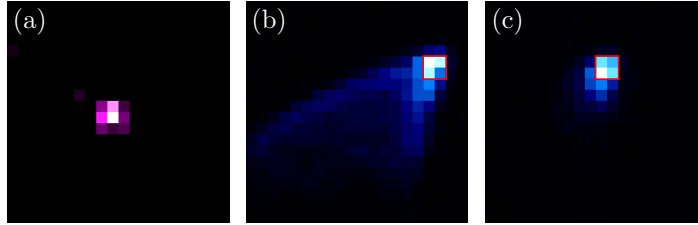
Figure 3.22.: *Single ion images: In^+ ion image (a) Yb^+ ion image with open pinhole (b) and closed pinhole (c). The pinhole cuts away edge rays that lead to the tail in (b). The fluorescence in the indicated red ROI is reduced by 5 %. The overall fluorescence summed across the shown image is reduced to one third of (b) in (c).*

With the closure of the pinhole between the wedged substrate (WS) and the beam combiner (BS) to a diameter of $\approx 6\,\mathrm{mm}$, the fluorescence in the center of the image (indicated by the red square in Fig. 3.22 (b) and (c)) is only reduced by 5 %. The resulting image is shown in Fig. 3.22 (c). The pinhole reduces the NA to ≈ 0.25, which is accompanied by a reduction of the total fluorescence to 1/3. The In^+ ion image shows no indication of coma or other aberrations (compare Fig. 3.22 (a)).

Fig. 3.23 serves to characterize the system performance at 230.6 nm quantitatively and to compare it to the simulation that considers the tolerances described in section 3.6.3 and reveals $f_{\mathrm{ee,tol}}(r_{\mathrm{c,tol}} = 8\,\mu\mathrm{m}) \approx 0.7$. A possible approach is to determine $f_{\mathrm{ee,exp}}(r_{\mathrm{c,tol}} = 8\,\mu\mathrm{m})$ from experimental images of individual In^+ ions. The large pixel size ($16\,\mu\mathrm{m} \times 16\,\mu\mathrm{m}$) of the camera with respect to the radius $r_{\mathrm{c,tol}} = 8\,\mu\mathrm{m}$ complicates this determination. If the ion is perfectly located in the center of one pixel, $r_{\mathrm{c,tol}} = 8\,\mu\mathrm{m}$ encloses this pixel and the fluorescence in this pixel can be used to calculate $f_{\mathrm{ee,exp}}(r_{\mathrm{c,tol}})$. In most cases, the ion is located such that up to four pixels fall into the range of $r_{\mathrm{c,tol}}$.

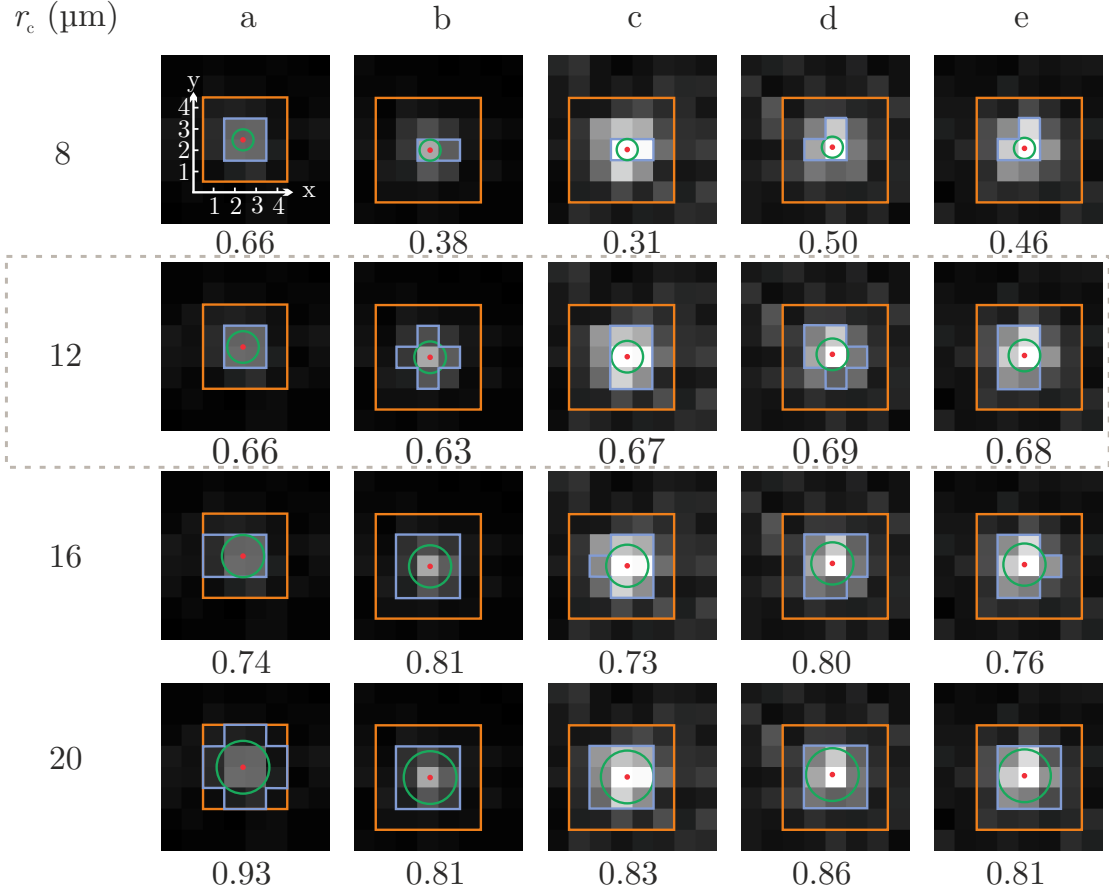**Figure 3.23.:** *Determination of the radius $r_{c,exp}$ which fulfills $f_{ee,exp} \approx 0.7$ for the 230.6 nm path. Shown are five images (a-e) of a single In^+ ion, recorded with the camera. For the images, the balance point (red point) of the ion is calculated via the gray values of the pixels in the orange ROI. The green circle around the balance point indicates r_c, which is varied between $8\,\mu m$ and $20\,\mu m$, and the blue ROI presents the area which has been used to calculate $f_{ee,exp}(r_c)$ given below each image.*

For the evaluation in Fig. 3.23, the position of the ion is determined by calculating its balance point within a region of interest (ROI). In the first line of Fig. 3.23 (for $r_c = 8\,\mu m$), five images of single In^+ ions (a-e), recorded with different saturation parameters and exposure time, are shown. The orange ROI indicates the area in which the fluorescence of the ion is collected and thus considered for the following analysis. A coordinate system (x, y) labels the pixels as indicated in the first image (a), where the start $(x = 0,\ y = 0)$ is placed in the center of one pixel. The x- and y-coordinate of the balance point are calculated by weighing the gray values with the respective x- and y-coordinates and the sum of all gray values in the orange ROI. The balance points for all images are displayed as red points. Around the balance point, a green circle with $r_c = 8\,\mu m$ is drawn in the first line of Fig. 3.23. The blue ROI shows which pixels intersect with the green circle and considered to calculate the value of $f_{ee,exp}(r_c)$ given below each image.

The position of the balance point varies for the images a-e and 2-4 pixels are taken into account to calculate $f_{\text{ee,exp}}(r_c)$, which results in values between 0.31 and 0.66 for the five images. This shows that $r_c = 8\,\mu\text{m}$ is too small to fulfill $f_{\text{ee,tol}}(r_{\text{c,tol}} = 8\,\mu\text{m}) \approx 0.7$, derived from the tolerancing of the system. To estimate the value of r_c which fulfills $f_{\text{ee,tol}} \approx 0.7$, r_c is increased to $12\,\mu\text{m}$, $16\,\mu\text{m}$ and $20\,\mu\text{m}$ in the following rows of Fig. 3.23 and the evaluation of the images a-e is repeated. The values $f_{\text{ee,exp}}(r_c = 12\,\mu\text{m})$ agree with $f_{\text{ee,tol}} \approx 0.7$. Since the blue ROI is larger than the green circle, a too large area is included in the calculation of $f_{\text{ee,exp}}$, but the pixel size does not allow for better resolution. The evaluations at $r_c = 16\,\mu\text{m}$ and $r_c = 20\,\mu\text{m}$ serve to check if r_c can be increased to $r_c > 12\,\mu\text{m}$ without reaching $f_{\text{ee,exp}} > 0.7$ for some images. For $r_c = 16\,\mu\text{m}$, all five values of $f_{\text{ee,exp}}(r_c = 16\,\mu\text{m}) > 0.7$, so for the 230.6 nm path $r_{\text{c,exp}}(f_{\text{ee,exp}} = 0.7) = (12 \pm 2)\,\mu\text{m}$ is concluded. This means that the ratio between the experimentally determined radius $r_{\text{c,exp}}$ and the radius determined from the toleranced simulation $r_{\text{c,tol}}$ for $f_{\text{ee}} = 0.7$ is $r_{\text{c,exp}}/r_{\text{c,tol}} = 1.5$.

For the 369.5 nm path with $f_{\text{ee,tol}}(r_{\text{c,tol}} = 8\,\mu\text{m}) \approx 0.6$, a detailed characterization with multiple images has been omitted because the image exhibits coma as described earlier. With the pinhole closed, typically 65% of the fluorescence are collected on 3×3 pixels which corresponds to $r_{\text{c,exp}} \approx 24\,\mu\text{m}$.

Table 3.12 summarizes relevant parameters of the imaging system for both beam paths. The theoretical detection efficiencies of the PMTs consider the collected fraction of the solid angle, the scattering rate, the scattering pattern, the transmission of the vacuum window and the lenses and the quantum efficiency specified by the vendor.

Table 3.12.: *Specifications of the detection system. The theoretical detection efficiencies for the PMTs are based on the collected fraction of the solid angle, the quantum efficiency of the PMT, the scattering rate and the transmission of the windows and lenses.*

	In$^+$ (230.6 nm)	Yb$^+$ (369.5 nm)
numerical aperture NA	0.45	0.40
		(0.25 for the camera)
measured magnification M	11.64 ± 0.03	9.98 ± 0.05
		(with FBS: 9.88 ± 0.09)
theoretically collected fraction of the solid angle $\frac{\Omega}{4\pi}$	0.067	0.042
		(0.016 for the camera)
ratio of measured/theoretical detection efficiency for PMT	0.6	0.95
$f_{\text{ee,tol}}(r_{\text{c,tol}} = 8\,\mu\text{m})$	0.7	0.6
$r_{\text{c,exp}}(f_{\text{ee,tol}})$ (μm)	12 ± 2	≈ 24
$r_{\text{c,exp}}(f_{\text{ee,tol}})/r_{\text{c,tol}}(f_{\text{ee,tol}})$	1.5	≈ 3

3. Experimental setup

While for the Yb$^+$ PMT, the achieved fluorescence yield is 0.95 of the expectation, it is only 0.6 for the In$^+$ PMT. A possible reason for the deviation could be a lower quantum efficiency as given in the datasheet of the PMT due to aging processes or larger losses in the vacuum window and mirrors than expected. For the 230.6 nm path $r_{c,exp}(f_{ee,tol} = 0.7) = (12 \pm 2)\,\mu$m, which is a factor 1.5 larger than the value $r_{c,tol} = 8\,\mu$m derived from the simulation considering the tolerances for the lenses. Important to note is that the In$^+$ image does not exhibit the coma shown in the worst-case scenario in Fig. 3.17 (a). Nevertheless $r_{c,exp}(f_{ee,tol} = 0.7)$ is larger than expected from this scenario. Most likely the deviation arises from the vacuum window, which has not been included in the tolerancing. For the 369.5 nm path only a rough estimate has been done revealing $r_{c,exp}(f_{ee,tol} = 0.6) \approx 24\,\mu$m which is ≈ 3 times larger than the value $r_{c,tol} = 8\,\mu$m derived from the simulation considering the tolerances for the four lenses.

As expected from the tolerances, the imaging of ions on a single pixel is not possible. Nevertheless, the achieved imaging quality is well suited for our purpose of simultaneous spatially-resolved state detection of Yb$^+$ and In$^+$ ions.

Figure 3.24 (a) shows clearly separated histograms for In$^+$ ion state detection with the EMCCD using a detection time of 10 ms. The fluorescence signal of a single In$^+$ ion that is sympathetically cooled with one Yb$^+$ ion, recorded with the PMT while scanning the frequency across the resonance is illustrated in Fig. 3.24 (b).
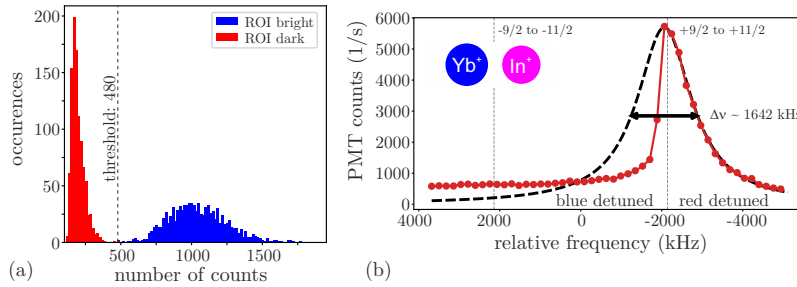

Figure 3.24.: *In$^+$ ion detection. (a) Histogram for In$^+$ state detection with the EMCCD. The detuning from resonance is -Γ/2, the detection time is 10 ms, the saturation parameter $s = 6$, 3×3 pixels have been binned to one superpixel which is read out as the region of interest (ROI). In red the dark background counts are shown and in blue the bright counts. (b) PMT recording of a frequency scan across the $+9/2 \rightarrow +11/2$ Zeeman component of the $^1S_0 \leftrightarrow {}^3P_1$ transition of a single In$^+$ ion at a saturation parameter $s = 10$. The black dashed line is a Lorentzian fit to the experimental data, which results in a linewidth $\Delta\nu = 1642\,kHz$.*

3.7. Control software

A combination of two different software systems is used for the control of the experiment.The
"Advanced Real-Time Infrastructure for Quantum Physics (ARTIQ)"[21] is an open-source
control system for quantum information experiments. It runs on its custom open-hardware
platform Sinara[22] centered around an FPGA[23]. ARTIQ consists of gate- and firmware com-
ponents on the FPGA and software on a host PC. Experimental sequences run by the FPGA
can be programmed with a python-like high-level programming language, which is compiled
and executed with nanosecond resolution. It is also possible to combine sequences run by the
FPGA with conventional python code on a computer[182]. A graphical user interface (GUI)
allows to control the experiment process and the management of datasets or the control of
connected hardware. The timing control of ARTIQ ensures that processes happen in time
allocated to them[183]. All processes that run on the FPGA (Real Time IO) are placed at
runtime on a timeline and are assigned a fixed start time. In case that it comes to a conflict
between filling the timeline and execution the FPGA terminates the further process. This
prevents the occurrence of unwanted states, that can arise unnoticed. Instructions that do
not access the same resources can be executed in parallel on the FPGA.

The second software system is the $C++$ based program "Master Control Program (MCP)"[24]
which runs on a PC.

The timing control makes it desirable to run all processes of the clock-cycle or in general
time critical spectroscopy sequences on the FPGA. The small computing power[25] is some-
times obstructive so that more complex calculations, requiring larger computation power, are
outsourced to the PC, also during the clock-cycle. Some hardware components like the ones
used to set the trap voltages can currently only be controlled via a PC. Gradually, meth-
ods are moved to the FPGA to exploit the full potential of parallel execution during clock
operation. More details about the programming of the clock-cycle can be found in [184].

---

[21]https://zenodo.org/record/51303
[22]https://github.com/sinara-hw
[23]Xilinx Artix-7 XC7A100T
[24]Developed from Prof. Kilian Singer at the university of Kassel. The program is unpublished and currently
    not publicly available.
[25]https://github.com/sinara-hw/Kasli/wiki

4. Ion trap characterization

This chapter presents measurements which characterize the ion trap, performed mainly in segment 2. It starts with measurements of the secular frequencies in dependence of the trap dc and rf voltages in section 4.1. In section 4.2 and 4.3 measurements of micromotion amplitudes and heating rates are presented. The rf induced trap heating, the resulting temperature increase at the position of the ions and the associated frequency shift are analyzed in section 4.4. Finally, in section 4.5, a trap-related uncertainty budget for the operation of a multi-ion In$^+$/Yb$^+$ clock is derived.

4.1. Secular frequencies

In this section measurements of the radial secular frequencies of a single ^{172}Yb$^+$ ion are compared to theory, as generated by an updated version of the trap potential calculator described in [22].
The trap frequencies have been measured by modulating the light intensity of the H1 cooling laser beam via the AOM with a modulation depth close to $100\,\%$. The modulation of the light intensity causes radiation pressure also to be modulated. If the modulation frequency matches to the secular frequency, the ion heats up which can be observed as blurring of its image on the EMCCD camera or a drop of fluorescence on the PMT.

Using the a-parameters $a_z(U_{\mathrm{ax}}, U_{\mathrm{t}}, U_{\mathrm{e}})$ and $a_{\mathrm{rad,i}}(U_{\mathrm{ax}}, U_{\mathrm{t}}, U_{\mathrm{e}})$ and the q-parameter $q(U_{\mathrm{rf}})$ the trap frequencies can be calculated via

$$\omega_{\mathrm{ax}} = \frac{\Omega_{\mathrm{rf}}}{2}\sqrt{a_z(U_{\mathrm{ax}}, U_{\mathrm{t}}, U_{\mathrm{e}})},$$

$$\omega_{\mathrm{rad,i}} = \frac{\Omega_{\mathrm{rf}}}{2}\sqrt{a_{\mathrm{rad,i}}(U_{\mathrm{ax}}, U_{\mathrm{t}}, U_{\mathrm{e}}) + \frac{1}{2}q^2(U_{\mathrm{rf}})}.$$

The index $i \in \{1,2\}$ represents the two orthogonal principal axes and U_{ax} are the symmetrically applied U_{t} voltages of the two neighbouring trap segments, which provide the axial confinement. For example for trap segment 2 the voltage $U_{\mathrm{ax}} = 1\,\mathrm{V}$ corresponds to $U_{\mathrm{t,seg1}} = U_{\mathrm{t,seg3}} = 1\,\mathrm{V}$. The pure ponderomotive potential is radially symmetric. A radial asymmetry is introduced by the application of the dc voltages U_{ax}, U_{t} and U_{e}. U_{t} influences the resulting potential with a factor of 2-10 stronger than the other two voltages. The potentials of the three dc voltages have a different orientation so that the trap axes can be rotated by adjusting the ratio $U_{\mathrm{e}}/U_{\mathrm{t}}$. The parameter $a_{\mathrm{rad,i}}(U_{\mathrm{ax}}, U_{\mathrm{t}}, U_{\mathrm{e}})$ can not be expressed by a sum of individual $\tilde{a}_{\mathrm{rad,i}}$ parameters, that depend alone on one of the individual voltages, due to the different orientation of their three dc potentials. Instead all resulting potentials have

4. Ion trap characterization
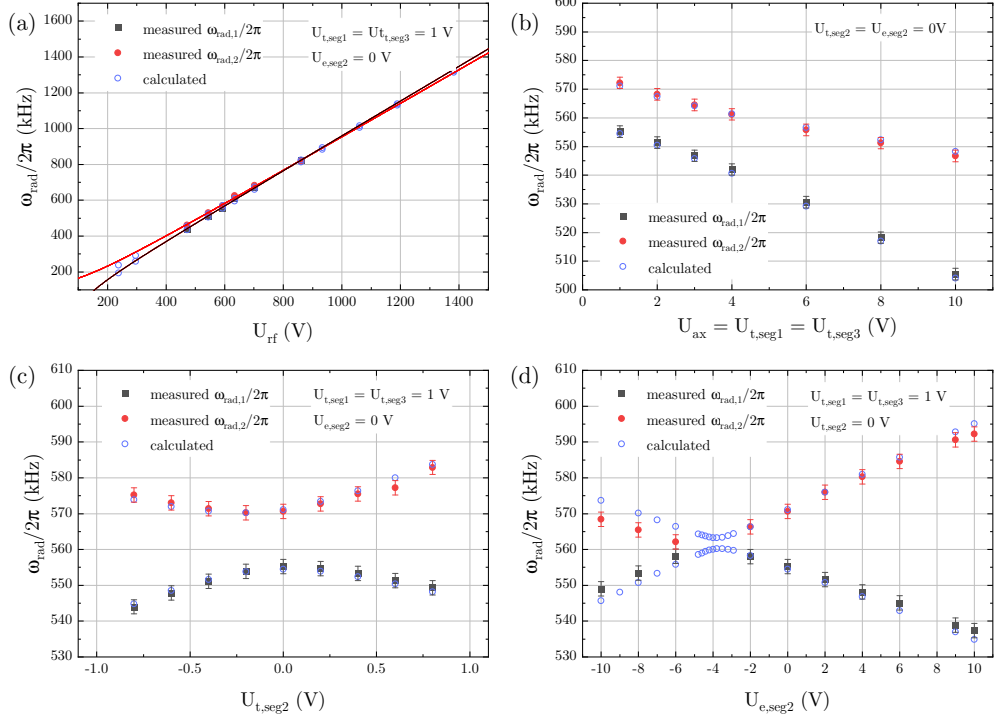
to be added to calculate the total potential.

Figure 4.1.: *Measured and calculated radial secular frequencies in segment 2 (1 mm length) for a single $^{172}Yb^+$ ion at a trap drive frequency of $\Omega_{\mathrm{rf}} = 2\pi \times 16.4\,MHz$. Where fixed, the parameters were, $U_{\mathrm{ax}} = 1\,V$, $U_{\mathrm{t,seg2}} = U_{\mathrm{e}} = 0\,V$ and $U_{\mathrm{rf}} = 593\,V$. In order to match the calculations to the data it was necessary to adjust the calculations with a constant offset voltage $U_{\mathrm{e,off}} = 2.4\,V$, which was added in the calculations for all trap segments. The uncertainty of the trap frequency measurement is $\sigma_{\omega\,\mathrm{rad}}/2\pi = 2\,kHz$.*

Figure 4.1 shows measurements and calculations of the radial trap frequencies $\omega_{\mathrm{rad,1}}$ and $\omega_{\mathrm{rad,2}}$ for a single $^{172}Yb^+$ ion trapped in segment 2 (1 mm length) at a trap drive frequency of 16.4 MHz. The trap voltages U_{rf}, U_{ax}, U_{t} and U_{e} have been varied separately to test if the calculated potential predicts each individual influence correctly. To obtain the rf voltage amplitude U_{rf} the voltage amplitude $U_{\mathrm{pick-up}}$ measured at the pick-up antenna of the helical resonator (see Fig. 3.2) has to be multiplied with the calibration factor $k = 2265$ [1]. The factor k was determined so that the experimentally measured secular frequencies match the calculations. The measured frequency splittings between the two radial frequencies for all measurements only agree if in the calculations an offset voltage $U_{\mathrm{e,off}} = 2.4\,V$ is added to U_{e} in all trap segments. An offset $U_{\mathrm{e,off}}$ with the same value is also required to match the measured and calculated trap frequencies in trap segment 1 of the identical trap characterized in [22]. There a slow change of the value over the course of a few weeks has been observed. Such a

---

[1] k is slightly different than the value given in Table 3.2 because the position of the antenna has changed between this measurement and now

drift of $U_{e,off}$ has not been observed for this setup within 2.5 years.

Measured and calculated trap frequencies agree within a few kHz in most cases. The maximum deviations of up to 10 kHz are observed for high rf voltages. If only the dc voltages are varied, the maximum differences between measured and calculated trap frequencies are 5 kHz (in case of the application of large U_e voltages). For the variation of the other voltages the agreement is within 2 kHz. The dependency of the radial frequencies on the rf voltage U_{rf} is described by Eq. 4.1 with $\tilde{q}$ being the q-parameter normalized to $U_{rf} = 1\,\mathrm{V}$ and a a constant including the contribution of the dc potential. This function has been fitted to the measured data points in Fig. 4.1 (a).

$$\omega_{rad}(U_{rf}) = \frac{\Omega_{rf}}{2}\sqrt{\frac{1}{2}\tilde{q}^2 U_{rf}^2 + a} \tag{4.1}$$

A relation between the radial frequencies and the dc voltages U_{ax}, U_t and U_e does not exist as described previously.

Figure 4.2 shows measurements and calculations of the axial trap frequency ω_{ax} of the COM mode of Yb$^+$ in segment 2 in dependence of U_{ax}, U_t and U_e at an rf drive frequency of 21.7 MHz. The axial trap frequency is only determined by the dc potential. The axial trap frequencies are not obtained via modulation of the light intensity but interred from the ion distances from EMCCD images of the crystal with the knowledge of the magnification and the size of the pixels. The imaging system magnification was originally calibrated in comparisons to axial frequency measurements via modulated laser powers.
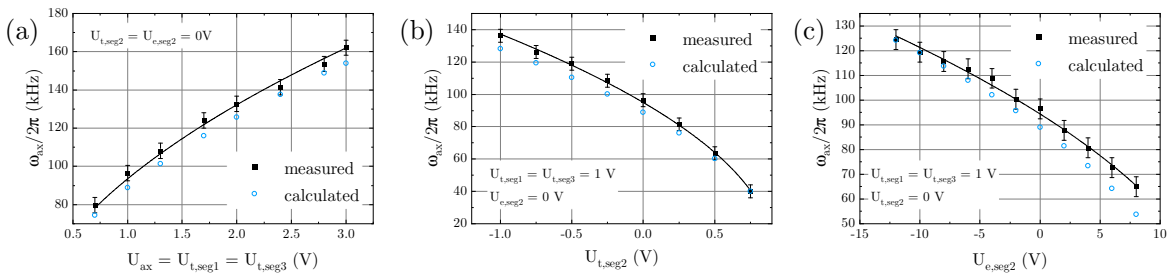
Figure 4.2.: *Measured and calculated axial secular frequencies of the COM mode of Yb$^+$ in segment 2 at a trap drive frequency of $\Omega_{rf} = 2\pi \times 21.7\,MHz$. Except for the voltage that is changed the trap voltage configuration for all measurements was $U_{ax} = 1\,V$, $U_{t,seg2} = U_e = 0\,V$ and $U_{rf} = 1138\,V$. The uncertainty of the trap frequency measurement is $\sigma_{\omega\,rad}/2\pi = 4\,kHz$.*

The relations between the axial trap frequency ω_{ax} and U_{ax}, U_t and U_e which are fitted to

4. Ion trap characterization

the experimental data are

$$\omega_{ax}(U_{ax}) = \frac{\Omega_{rf}}{2}\sqrt{\tilde{a}_{z,ax}U_{ax}} \qquad (4.2)$$

$$\omega_{ax}(U_t) = \frac{\Omega_{rf}}{2}\sqrt{\tilde{a}_{z,t}U_t + \tilde{c}_t} \qquad (4.3)$$

$$\omega_{ax}(U_e) = \frac{\Omega_{rf}}{2}\sqrt{\tilde{a}_{z,e}U_e + \tilde{c}_e}. \qquad (4.4)$$

$$(4.5)$$

The maximum deviation between measured and calculated axial trap frequencies is $10\,\mathrm{kHz}$.

To summarize, the potential calculator predicts the trap frequencies with an uncertainty of around $10\,\mathrm{kHz}$. It also estimates the orientation of the two trap axes. First tests reveal that here the agreement between experiment and calculator is better if no offset for U_e is applied in the calculations. To resolve this inconsistency further investigations are needed.

4.2. Excess micromotion

While radial micromotion can be minimized with the compensation electrodes, the excess micromotion along the trap axis cannot be compensated and the focus of the design of the ion trap was to keep its amplitude small. Low axial micromotion is especially important for the operation of a multi-ion clock. For a single ion, only one point in the segment with low micromotion amplitude is required, while for an ion crystal there must be a spatially extended region that does not necessarily exist. In section 4.2.1 the method and resolution for the measurement of excess micromotion are presented. Results on the axial micromotion component in segment 1 and 2 and the 3D-EMM in segment 2 are shown in section 4.2.2 and section 4.2.3, respectively. Changes of the dc voltage U_e and the rf voltage amplitude U_{rf} influence the micromotion component along the vertical direction, which has not been observed in the identical trap characterized in [22]. The influence and its consequences are discussed in section 4.2.4. The relations between the compensation voltages U_{tc} and U_{ec} and the resulting electric field components $E_{rf,x}$ and $E_{rf,y}$ are measured and compared to calculations in section 4.2.5.

4.2.1. Method & experimental implementation

All micromotion amplitude measurements are performed with the photon-correlation spectroscopy technique for a single Yb^+ ion. The ion fluorescence resulting from Doppler cooling on a transition with linewidth Γ shows a modulation at the trap drive frequency Ω_{rf} because of the first-order Doppler shift. The amplitude of the modulation scales with the micromotion amplitude. In case of $\Omega_{rf} \ll \Gamma$ the method has been described in detail in [115].

For this setup with trap frequencies $\Omega_{rf} \approx \Gamma$ the treatment derived in [115] is no longer valid and a more general theoretical description is required for the correct relation between the observed modulation of the fluorescence and the micromotion amplitude. A more general model has been derived and verified in [102, 185]. Here only the most important relations to

understand the following measurements are summarized.

The effect of the first-order Doppler shift due to micromotion can be described as laser phase modulation at the frequency Ω_{rf} in the reference frame of the ion:

$$E(\omega) = E_0 cos(\omega\, t + \beta cos(\Omega_{\mathrm{rf}}\mathrm{rf}t)). \tag{4.6}$$

$\beta = |\vec{k}\vec{x_0}| = \frac{|\vec{k}\vec{v_0}|}{\Omega_{\mathrm{rf}}}$ is the phase modulation index with the micromotion amplitude $\vec{x_0}$ and velocity $\vec{v_0}$ and the wave vector $\vec{k}$ of the laser. The modulation index β can be converted into the rf field amplitude $\vec{E}_{\mathrm{rf}}$, which is used within this work to quantify micromotion, via

$$|\vec{E}_{\mathrm{rf}}| = \frac{m\Omega_{\mathrm{rf}}^2}{e}|\vec{x_0}| = \frac{m\Omega_{\mathrm{rf}}}{e}|\vec{v_0}| = \frac{m\Omega_{\mathrm{rf}}^2}{ke}\beta. \tag{4.7}$$

The observed fluorescence signal S in the time domain is approximated by

$$S(t) \approx S_0 + \Delta\, S\cos(\Omega_{\mathrm{rf}}t + \varphi). \tag{4.8}$$

It is composed of a static part S_0 and a component ΔS that oscillates at Ω_{rf}. The quantity $\Delta S/S_0$ can be used to extract β or E_{rf}. For the relations $E_{\mathrm{rf}}(\Delta S/S_0)$ and $\beta(\Delta S/S_0)$ numerical simulations of the quantum mechanical master equation take into account the effect of saturation. A second-order polynomial is fitted to the simulated results to find expressions to convert $\Delta S/S_0$ to E_{rf} and β. For more details the reader is referred to [102, 185].

Figure 4.3 shows a measurement of $\Delta S/S_0$ versus the detuning Δ to find the value of highest sensitivity for a trap drive frequency $\Omega_{\mathrm{rf}} = 2\pi \times 21.73\,\mathrm{MHz}$. In addition to the measurement a theoretical simulation (see [102, 185]) is indicated which agrees with the measurement. The maximum signal is obtained at a detuning $\Delta = \text{-}1.2\,\Gamma$. For the trap drive frequency $\Omega_{\mathrm{rf}} = 2\pi \times 16.4\,\mathrm{MHz}$ the optimum is to measure at a detuning $\Delta = \text{-}1.0\,\Gamma$. The dependence of the phase φ on the detuning Δ is also described correctly by this model as presented in [102, 185].
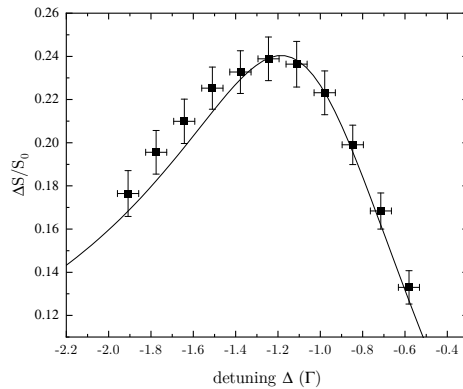

Figure 4.3.: *Dependence of the measured signal $\Delta S/S_0$ β on the detuning Δ for a trap drive frequency $\Omega_{\mathrm{rf}} = 2\pi\, 21.73\,MHz$. The solid line shows a simulation. The measurement is most sensitive at a detuning detuning $\Delta = \text{-}1.2\,\Gamma$.*

To determine the rf field amplitudes $\vec{E}_{\mathrm{rf}}$ in all three directions x, y and z, all three cooling laser beams (H1, H2 and V as introduced in Fig. 3.6) are used consecutively. Because the V

beam has no projection onto the trap axis, a strongly attenuated H1 beam is added during the V measurements to provide cooling in the axial direction. The power is actively stabilized using an AOM. The intensity is set to $I = 0.4 \times I_{\mathrm{sat}}$ as a compromise between the count rate and micromotion sensitivity. The ion fluorescence is detected with the PMT and a discriminator which produces a TTL pulse for each detected photon. The discriminator TTL signal from the PMT provides the start trigger for a time-to-digital converter (TDC). A split-off portion of the rf trap drive signal is sent through a sine-to-square converter (SSC) and used as the stop trigger for the TDC. The TDC then generates a histogram of the observed delays which resembles the time-inverted distribution of the photons within one rf period.

The resulting signal has the form of Eq. 4.8. A correction for parasitic crosstalk of the rf field on the PMT signal as described in [102, 185] can be neglected, as this effect is at the level of $\Delta\nu/\nu = 7 \cdot 10^{-23}$. A sinusoid is fitted to the data and the value $\Delta S/S_0$ is determined by its offset and amplitude. Via the second-order polynomial resulting from the numerical calculations of the system, the three rf amplitudes $E_{\mathrm{rf,H1}}$, $E_{\mathrm{rf,H2}}$ and $E_{\mathrm{rf,V}}$ are deduced, which are the projections of the rf field $\vec{E}_{\mathrm{rf}}$ onto the three laser axis. From these three values the rf amplitudes $E_{\mathrm{rf,x}}$, $E_{\mathrm{rf,x}}$ and $E_{\mathrm{rf,z}}$ along the coordinate axes defined in Fig. 3.6 can be calculated:

$$E_{\mathrm{rf,x}} = \frac{1}{2\cos(90° - \theta)}\sqrt{E_{\mathrm{rf,H1}}^2 + E_{\mathrm{rf,H2}}^2 + 2E_{\mathrm{rf,H1}}E_{\mathrm{rf,H2}}\cos(\varphi_{\mathrm{H1}} - \varphi_{\mathrm{H2}})} \tag{4.9}$$

$$E_{\mathrm{rf,y}} = E_{\mathrm{rf,V}} \tag{4.10}$$

$$E_{\mathrm{rf,z}} = \frac{1}{2\cos(\theta)}\sqrt{E_{\mathrm{rf,H1}}^2 + E_{\mathrm{rf,H2}}^2 - 2E_{\mathrm{rf,H1}}E_{\mathrm{rf,H2}}\cos(\varphi_{\mathrm{H1}} - \varphi_{\mathrm{H2}})}. \tag{4.11}$$

In the equations $\theta = 21°$ is the angle between the z-axis and the beams H1 and H2 and φ_{H1} and φ_{H2} are the phases of the EMM signal (Eq. 4.8) for the beams H1 and H2.

A major advantage of the photon-correlation method is the contained phase information, which allows a distinction between excess micromotion due to displacement and due to an rf phase shift, since the phase of the former changes by π when the ion is moved across the rf node.

The influence of individual uncertainties on the total uncertainty of the micromotion measurement have been investigated in [102, 185]. The dominant contribution is the fit error of the sine amplitude ΔS. The uncertainty is shot noise limited and can be reduced by increasing the measurement time. To measure the resolution limit, perfectly compensated micromotion has been simulated by correlation measurements with a stray light signal of the same count rate as the signal for all three beams. In Fig. 4.4, the standard deviation of 50 of these correlation measurements are shown as a function of the integration time for the three directions x, y and z. The data closely follow the relation $\sigma_{\mathrm{Erf}}(t) = \sigma_{\mathrm{Erf}}(1\mathrm{s})/\sqrt{t}$ which assumes an uncertainty limited by shot noise. With an integration time of $7.5\,\mathrm{s}$ the resolution limit is below $9.7\,\mathrm{V/m}$ for all three directions which is equivalent to $\Delta\nu/\nu = 1 \cdot 10^{-20}$ for In$^+$ ions. The difference of the resolution limit of the three directions arises from the different projections according to Eq. 4.9-4.11. In z-direction the projection percentage of all three

beams is highest which results in the best resolution limit because the effective integration time is longest.

Figure 4.4.: *Shot noise limited uncertainty of the photon-correlation method. The integration time dependent resolution limit along the directions x, y and z is measured via stray light signals of the same count rate as the signal from the ion. An integration time of $7.5\,s$ is enough to provide a resolution limit below $\Delta\nu/\nu = 1 \cdot 10^{-20}$ in all directions for In^+ ions.*
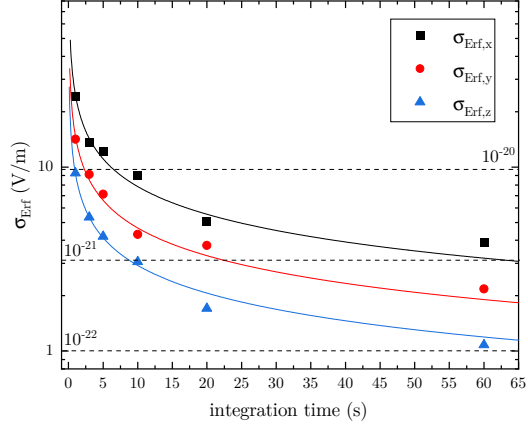
To compensate EMM, the influence of the compensation voltages U_{tc} and U_{ec} on the position of the ion in the radial plane has to be known because the ion cannot be shifted along the x- and y-direction independently. Figure 4.5 illustrates a cut through the radial plane of the trap and visualizes the voltages applied to the different trap chips. The U_{tc} voltage pushes the ion with almost equal projection in the x- and y-direction as indicated by the solid arrow. The U_{ec} voltage mainly shifts the ion in the x-direction as indicated by the dashed arrow and only has a small influence on the y-direction. The compensation algorithm first minimizes the $E_{rf,x}$ component. For this photon-correlation measurements of the H1 and H2 beam are performed and the U_{tc} voltage is varied to find the minimum of $E_{rf,x}$ according to Eq.4.9. Afterwards the $E_{rf,y}$ component is measured with beam V and the ion is shifted via the voltage U_{ec} to find the minimum for that component. Because U_{ec} also has a small influence on the $E_{rf,x}$ component this has to be corrected afterwards via U_{tc}. To position the ion exactly at the position with minimal $E_{rf,x}$ and $E_{rf,y}$, the exact projections need to be known which can be expressed as the four slopes $\Delta E_{rf,x}/\Delta U_{tc}$, $\Delta E_{rf,y}/\Delta U_{tc}$, $\Delta E_{rf,x}/\Delta U_{ec}$ and $\Delta E_{rf,y}/\Delta U_{ec}$. The values of these four slopes depend on the rf drive frequency Ω_{rf}, the two radial trap frequencies $\omega_{rad,1}$ and $\omega_{rad,2}$ and the orientation of the dc potential with respect to the x- and y-direction. Measurements of the slopes and calculations of the trap potential are presented in section 4.2.5.

4.2.2. Axial micromotion in segment 1 and 2

For the measurements of the excess micromotion along the trap axis, a single Yb^+ ion was shifted along this axis by changing the axial trap voltage. In [23] this method is compared with a measurement of micromotion on a 14-ion Coulomb crystal with an extension of $400\,\mu m$ and both methods agreed well within their combined uncertainties at the 10^{-19} level. Accordingly a single ion can be used to measure the micromotion that would be present in an ion Coulomb crystal.
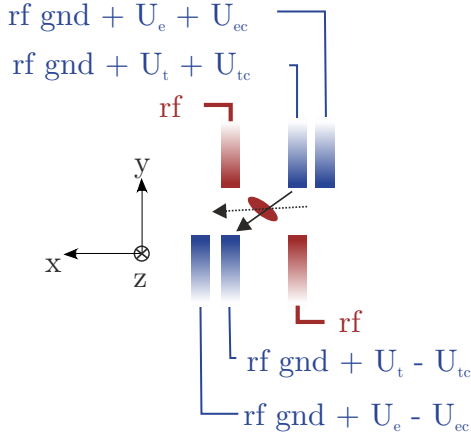
4. Ion trap characterization

Figure 4.5.: *Cut through the radial plane of the trap, visualizing the voltages applied to the different trap chips. The U_{tc} voltage pushes the ion with almost equal projection in the x- and y-direction (indicated by the solid arrow). The U_{ec} voltage mainly shifts the ion in the x-direction (dashed arrow) and only has a small influence on the y-direction. For the compensation algorithm the influence of the two voltages on the $E_{\text{rf,x}}$ and $E_{\text{rf,y}}$ need to be known precisely for the used trap potential to shift the ion exactly at the EMM minimum in the radial plane.*

The axial micromotion has been characterized in trap segment 1 and 2 for an rf voltage amplitude of $U_r f = 600\,\text{V}$ at a drive frequency of $\Omega_{\text{rf}} = 2\pi \times 16.4\,\text{MHz}$, corresponding to a radial confinement of $\approx 560\,\text{kHz}$. As the axial confinement was varied to shift the ion along the trap axis, the overall radial secular frequencies were not constant throughout the measurement. The observed $E_{\text{rf,z}}$ component is shown in Fig. 4.6. Almost over the complete length of both trap segments, (2 mm and 1 mm, respectively), the measured rf field component $E_{\text{rf,z}}$ is below $73\,\text{V/m}$ which is equivalent to a fractional frequency shift $\Delta\nu/\nu$ below $1 \cdot 10^{-18}$ for In$^+$. It is noticeable that there is no zero crossing of the $E_{\text{rf,z}}$ component in the center of the segments. The absence of those is also proven by the lack of a phase shift since the phase changes by π when the rf nodal line is crossed.
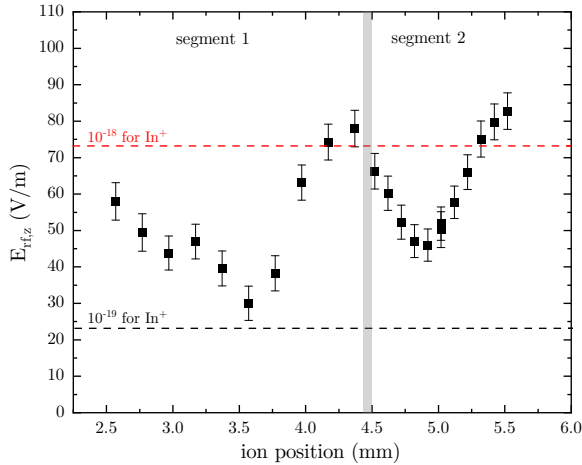
Figure 4.6.: *Measurement of the axial micromotion component $E_{\text{rf,z}}$ in the trap segments 1 and 2. The grey vertical line marks the notch between the two segments. The dashed horizontal lines indicate the limits for fractional frequency shifts of In$^+$ of $1 \cdot 10^{-18}$ and $1 \cdot 10^{-19}$, respectively. The $E_{\text{rf,z}}$ component is lowest in the center of the segments and increases towards the edges.*

Any tilt angle between the two rf electrodes (chip 2 and 3) will introduce a constant offset in the axial rf field according to finite-element-model (FEM) simulations presented in [20]. This can be a rotation around the z-axis, but the same effect appears for a rotation of one rf electrode around the y-axis of the trap [22]. In contrast to this trap, the characterization of the identical trap in [22] revealed two zero crossings and the maximum axial micromotion

amplitude in the center of segment 1.

While the trap characterized in [22] features a $100\,\mu$m long region with a fractional frequency shift of In$^+$ at the level of $1\cdot10^{-19}$ due to the zero crossing, this is not the case in this trap. But in segment 1 there is a $1\,$mm long range (in segment 2 $0.75\,$mm) where the spread of $E_{\mathrm{rf,z}} < 25\,$V/m and the uncertainty of $E_{\mathrm{rf,z}}$ is on the order $7\,$V/m. This means that even though the fractional frequency shift is in the mid 10^{-19} region the associated uncertainty is $\approx 1\text{-}2\times10^{-19}$.

4.2.3. 3D-EMM in segment 2

Figure 4.7 (a) shows the data from the axial micromotion component (shown in Fig. 4.6) and the radial micromotion components in trap segment 2. The radial micromotion along x and y has been minimized via the compensation voltages U_{tc} and U_{ec} of segment 1,2 and 3 at the axial ion position $5.02\,$mm. The same compensation voltages have been applied in the three segments. While the resulting $E_{\mathrm{rf,x}}$ and $E_{\mathrm{rf,y}}$ components are consistent with zero at this position, they increase towards the edges of the segment. For the $E_{\mathrm{rf,x}}$ component the values stay below $1\cdot10^{-19}$ for In$^+$ while for the $E_{\mathrm{rf,y}}$ component the increase is slightly higher but still well below $1\cdot10^{-18}$. Presumably, the electric field components $E_{\mathrm{rf,x}}$ and $E_{\mathrm{rf,y}}$ at the outer positions can be further reduced if the compensation voltages in segments 1 and 3 are chosen to be different from segment 2, since the gradients toward the edges are linear. The total value of the $|\vec{E_{\mathrm{rf}}}|$ vector is shown in Fig. 4.7 (b). The maximum value $|\vec{E_{\mathrm{rf}}}| = (87\pm6)\,$V/m corresponds to a time dilation shift of $(1.4\pm0.2)\times10^{-18}$. Across a $600\,\mu$m region, $|\vec{E_{\mathrm{rf}}}| < 1\times10^{-18}$. In the $400\,\mu$m region between $4.72\,$mm and $5.12\,$mm the spread of $|\vec{E_{\mathrm{rf}}}| = (8.2\pm7.7)\,$V/m so that for a Coulomb crystal trapped in this region the spread of the resulting time dilation shift is $\approx 2\times10^{-19}$, as shown in Table 4.7.
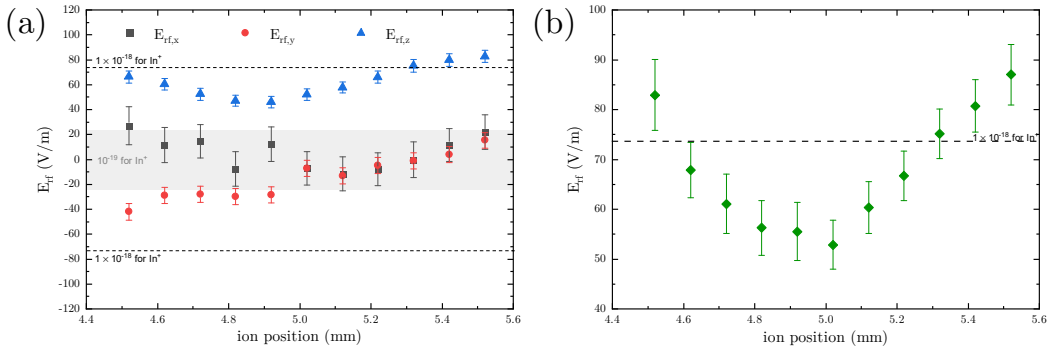

Figure 4.7.: *3-dimensional micromotion measurement along trap segment 2. (a) $E_{\mathrm{rf,z}}$ component (blue triangles, discussed in section 4.2.2) and the radial micromotion components $E_{\mathrm{rf,x}}$ (black squares) and $E_{\mathrm{rf,y}}$ (red dots). (b) Resulting total value of the $|\vec{E_{\mathrm{rf}}}|$ vector. The shaded areas indicate the resulting time dilation shifts for In$^+$.*

4. Ion trap characterization

4.2.4. Discrepancies: Influence of U_e and rf voltage amplitude dependent radial ion displacement

The EMM in the trap of this setup features some behaviors that have not been observed in the identical trap characterized in [22]. The first dependence concerns the radial components on U_e. The second dependence is a change in the $E_{rf,y}$ component depending on the applied rf amplitude U_{rf}. Both dependencies and their consequences for clock operation are described in this section.

Influence of U_e

The voltage U_e is used for controlling the orientation of the two radial principal axes and is applied symmetrically to the trap chips 1 and 4 as indicated in Fig. 3.1 (c). In contrast to the asymmetrically applied voltages U_{tc} and U_{ec} that enable radial shifting of the total potential minimum, a change in U_e should not influence the radial position of the ion as long as the voltage is really applied symmetrically.
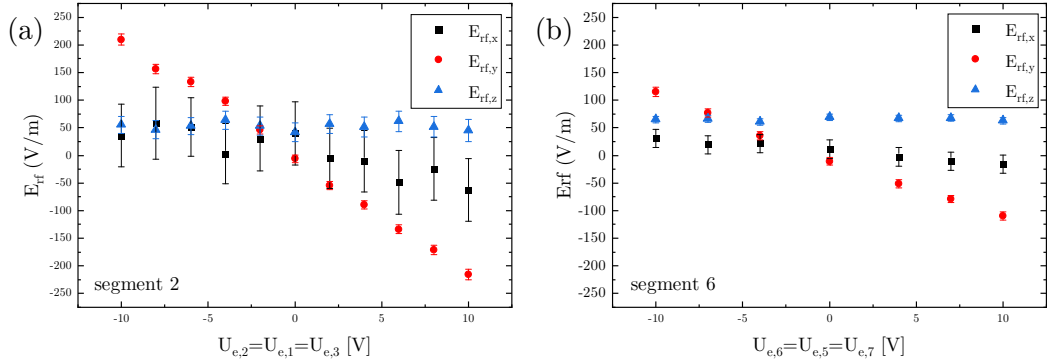
Figure 4.8.: *Influence of the voltage U_e on the $E_{rf,x}$ and $E_{rf,y}$ component in trap segment 2 (a) and 6 (b). EMM has been compensated at $U_e=0$ V in the respective and its neighboring segments. Afterwards the U_e voltage has been varied between -10 V and +10 V and the 3D EMM has been measured. In both segments the $E_{rf,y}$ components changes significantly and with a clear linear trend with the variation of the U_e voltage, but in segment 2 with almost twice the magnitude.*

Figure 4.8 (a) shows a 3D-EMM measurement of a single Yb^+ ion in the center of segment 2 where the compensation has been performed with $U_{e,2}=U_{e,1}=U_{e,3}=0$ V. Afterwards the value of the three U_e voltages has been varied between -10 V and +10 V and the 3D-EMM has been measured. Figure 4.8 (b) shows the same measurement for trap segment 6. As for the previously shown measurements of this chapter, the trap drive frequency $\Omega_{rf} = 2\pi \times 16.4\,\text{MHz}$, $\omega_{ax} \approx 150\,\text{kHz}$ and the radial trap frequencies have been $\approx 560\,\text{kHz}$, slightly varying with the applied U_e voltages. In segment 2 the $E_{rf,y}$ component shows a linear decrease from $\approx +200\,\text{V/m}$ to$\approx$ -200 V/m if U_e is varied from -10 V to +10 V. In case of segment 6 the same behavior with lower magnitude is visible. The $E_{rf,y}$ component changes from $110\,\text{V/m}$ at $U_e = $ -10 V to -110 V/m at U_e=+10 V. This linear relation can be seen in all segments, with

the difference between the two extreme values decreasing from segment 1 to segment 8.

In order to better understand the influence of U_e along the entire trapping region Fig. 4.9 shows the 3D-EMM across all segments for $U_e = +10\,$V (a) and $U_e = $-10 V (b) after previous compensation at $U_e = 0\,$V. As before, U_e is applied in the respective segment and its neighbors. The influence of U_e on the $E_{rf,x}$ and $E_{rf,y}$ component is highest in segment 1 and lowest for segment 8. For $U_e = +10\,$V the effect on the $E_{rf,y}$ component changes almost linearly from -250 V/m to -20 V/m when going from segment 1 to 8 and the effect on the $E_{rf,x}$ component linearly from -75 V/m to 60 V/m. For $U_e = $-10 V the effect on the $E_{rf,y}$ component is analogue, but interestingly, the $E_{rf,x}$ component is not affected within the measurement uncertainty. In segment 8 the application of $U_e = $-10 V has no influence.
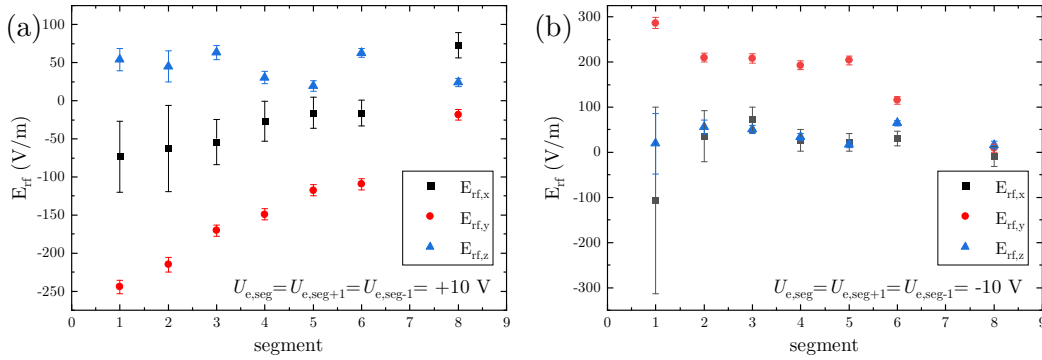
Figure 4.9.: *Influence of the voltage U_e on the $E_{rf,x}$ and $E_{rf,y}$ component across all segments. The compensation has been done at $U_e=0$ V in the respective and its neighboring segments, afterwards the U_e voltage has been changed and its influence on the 3D-EMM has been measured. Shown are the 3D-EMM measurements for $U_e = +10$ V (a) and $U_e = $-10 V (b) for all trap segments, except segment 7. The influence of U_e on the $E_{rf,x}$ and $E_{rf,y}$ component is highest in segment 1 and decreases towards segment 8.*

As described earlier, the U_e voltages are applied symmetrically, so that they should not change the radial position of the ion. This is only true if the electrodes are perfectly manufactured and aligned parallel to each other. The clear linear trend of the $E_{rf,y}$ component along the segments for the extreme values $U_e = \pm10\,$V indicates a geometric deviation. If the distance of the two compensation electrodes to the ion is not equal, this could potentially lead to the observed effect. Possibly, one or both compensation electrodes have a tilt.

Another hypothesis for the observed effect are unbalanced voltages on the two compensation electrodes due to deviations in the used components. For the dc-voltage supply used for the identical trap characterized in [22] the components, e.g., resistances have been precisely measured and hand selected to keep the variations between different pieces of the same production series below the value that was stated by the manufacturer. This hand selection was probably not done for the dc-voltage supply in this setup (see section 3.3) or larger deviations have been accepted. This could result in marginally deviating equivalent resistor values in

4. Ion trap characterization

the supply circuit of different electrodes that then lead to a slightly asymmetric application of the U_e voltages. To shift the ion to $E_{rf,y} \approx 300\,\text{V}$, as in the case of segment 1 at $U_e = \text{-}10\,\text{V}$ (compare Fig. 4.9 (b)), the actual applied voltages on the two opposing U_e electrodes (chip 1 and 4) would have to differ by $\approx 8\,\%$. This estimate is based on the EMM slopes measured in section 4.2.5. Typical manufacturing tolerances are lower. Furthermore, one would expect a random variation of the influence of the U_e voltages on the $E_{rf,y}$ component across all segments. A geometric imperfection thus seems more likely.

The shifted axial micromotion component, described in section 4.2.2, can also have its origin in a tilt angle, but between the rf electrodes (chip 1 and 2). For further analysis of the two effects, the measurements have to be compared to FEM simulations.

The influence of the U_e voltages on the radial position of the ions does not pose a problem for the clock or increases its uncertainty as long as the EMM compensation is performed at the dc voltage settings that are used for clock operation. As soon as EMM measurements and compensations are made in-situ during the clock cycle, this condition will always be given. At the moment, the clock cycle is interrupted for EMM measurements, but even here the dc potential is not changed.

rf voltage amplitude dependent radial ion displacement
The second unexpected behavior is that the U_{ec} value which zeroes the $E_{rf,y}$ component depends on the applied rf amplitude U_{rf}. A possible explanation is that the rf field of the ion trap induces charges on nearby dielectric surfaces, which dissipate at a limited rate, such that the electric field reaches a steady state. When the rf amplitude is changed, a new equilibrium is established after some time. A dc electric field which displaces the ion to cause an $E_{rf,y}$ component must be oriented along the x-direction. In that direction, the closest components are the ablation target ($\approx 14\,\text{mm}$) and the reentrant viewport ($\approx 24\,\text{mm}$), as well as the oven apertures ($\approx 24\,\text{mm}$). The ablation target was initially not grounded. After grounding, the amplitude and the time constant went down. The time constant shortened from several weeks to a about 25 minutes. Potentially, the remaining effect comes from another part after the dominant contribution of the ablation target has been removed, or the grounding is not yet sufficient.

Below, the magnitude and time constant of the effect are analyzed for rf voltage changes that are applied when operating the clock. To facilitate crystallization during ion loading, the rf voltage amplitude U_{rf} is reduced to $595\,\text{V}$ compared to $1151\,\text{V}$ applied during spectroscopy, which corresponds to a change in the radial frequency from $\omega_{rad} = 2\pi \times 820\,\text{kHz}$ to $2\pi \times 415\,\text{kHz}$ at a trap drive frequency $\Omega_{rf} = 2\pi \times 21.8\,\text{MHz}$. Figure 4.10 illustrates the effect of this voltage change on the radial micromotion components in the loading segment (segment 8). Up to the time where the measurement was started the rf amplitude was at $1151\,\text{V}$ and EMM was compensated. Then the amplitude is reduced to $595\,\text{V}$ and EMM is measured repeatedly. The radial micromotion components are expressed as E_{dc} components to clearly distinguish the described U_{rf} dependent stray field effect from the U_{rf} dependent changes in the E_{rf} field components. Note that $E_{dc,x}$ causes an $E_{rf,y}$ component and vice versa. The $E_{dc,x}$ component shows a decrease to $\approx \text{-}6\,\text{V/m}$ within $33\,\text{min}$, which corresponds

Figure 4.10.: U_{rf} dependent change of the radial micromotion components. EMM was compensated at $U_{\mathrm{rf}} = 1151\,V$, afterwards the amplitude was reduced to 595 V and set back to its original value. The $E_{\mathrm{rf,x}}$ component decreases during the phase at $U_{\mathrm{rf}} = 595\,V$ to $\approx$ -6 V/m within 33 min and relaxes back to its original value within 25 min after reversing to $U_{\mathrm{rf}} = 1151\,V$. The blue shaded area (dashed line) indicates the limit for a fractional frequency shift below 1×10^{-18} (5×10^{-18}).
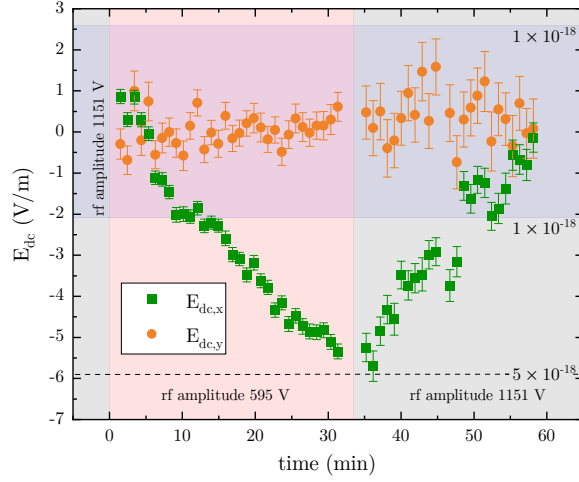
to a fractional frequency shift of $\approx 5 \times 10^{-18}$. Then the rf amplitude is set back to 1151 V and $E_{\mathrm{dc,x}}$ relaxes back to its original value within 25 min. The $E_{\mathrm{dc,y}}$ component only shows increased scatter, but no drift. The process of loading is much shorter than the course of the measurement in Fig. 4.10 and takes about 5 min, the exact duration being dependent on the ion number.

Figure 4.11.: Influence of the rf voltage amplitude change applied during ion loading. EMM has been compensated at $U_{\mathrm{rf}} = 1151\,V$ and afterwards U_{rf} was reduced to 595 V for a duration of 5 min to simulate loading (red). The blue shaded area indicates the limit for a fractional frequency shift below 1×10^{-18}.
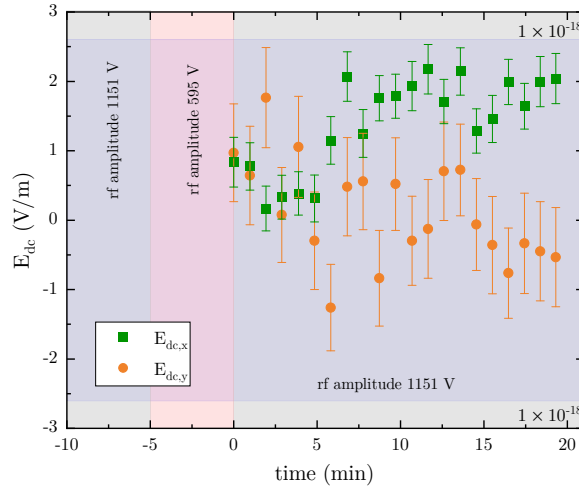
In Fig. 4.11, the effect of a 5 min long reduction of U_{rf}, comparable to the loading conditions, on the two radial micromotion components is shown. The EMM has been compensated at $U_{\mathrm{rf}} = 1151\,V$, then U_{rf} has been reduced to 595 V/m for 5 min, has been set back to 1151 V/m afterwards and measurement of the radial micromotion components has been started. Both radial micromotion components reveal a small effect of the previous U_{rf} reduction, which is below a fractional frequency shift of 1×10^{-18}.

4. Ion trap characterization

The other occasion where the rf voltage amplitude U_{rf} is changed within clock operation is during reordering of the ions (see section 5.3). Here U_{rf} is reduced to similar values but only for 158 ms so this is a negligible amount of time compared to the loading process.

4.2.5. Measurements and calculations of radial micromotion slopes

For the EMM compensation algorithm, influences of the compensation voltages U_{tc} and U_{ec} on the $E_{rf,x}$ and $E_{rf,y}$ component have to be known precisely, as described in section 4.2.1. The dependencies between the two voltages and the rf field components can be expressed in the four slopes $\Delta E_{rf,x}/\Delta U_{tc}$, $\Delta E_{rf,y}/\Delta U_{tc}$, $\Delta E_{rf,x}/\Delta U_{ec}$ and $\Delta E_{rf,y}/\Delta U_{ec}$ which depend on the rf drive frequency Ω_{rf}, the two radial trap frequencies $\omega_{rad,1}$ and $\omega_{rad,2}$ and the orientation of the dc potential with respect to the x- and y-direction. The sign of the rf field amplitude E_{rf} is defined such that changes of $-\Delta U_{tc}$ and $-\Delta U_{ec}$ shift the ions to higher $E_{rf,x}$ and $E_{rf,y}$ values.

Table 4.1 summarizes measurements and calculations of the four slopes for two different confinements in segment 2. While the fractional deviations between calculation and measurement are ≈ 0.05 for the $\Delta E_{rf,x}/\Delta U_{tc}$ and $\Delta E_{rf,y}/\Delta U_{tc}$ slopes, the fractional deviations of the $\Delta E_{rf,x}/\Delta U_{ec}$ and $\Delta E_{rf,y}/\Delta U_{ec}$ slopes are much larger, apart from one exception. As for the calculations of the axial trap frequency ω_{ax} described in section 4.1 no offset for U_e is applied, because this does not lead to a better agreement in contrast to the calculations for the radial trap frequencies ω_{rad}.

Table 4.1.: *Comparison between measured and calculated radial micromotion slopes for two different dc confinements with different orientation of the principal trap axes in trap segment 2. The rf drive frequency $\Omega_{rf} = 2\pi \times 21.7\,MHz$ and the rf voltage amplitude $U_{rf} = 1151\,V$ in both comparisons.*

EMM slope	measurement ((V/m)/V)	simulation ((V/m)/V)	fractional deviation
$\Delta E_{rf,x}/\Delta U_{tc}$	-25585 ± 321	-27040	-0.057
$\Delta E_{rf,y}/\Delta U_{tc}$	-20758 ± 234	-21740	-0.047
$\Delta E_{rf,x}/\Delta U_{ec}$	-211 ± 5	-374	-0.773
$\Delta E_{rf,y}/\Delta U_{ec}$	-3814 ± 22	-4857	-0.273

(a) The two principal axes have a projection of $\approx 60°$ and $\approx 30°$ with respect to the y-direction: $U_{t,1} = U_{t,3} = U_{t,4} = 8\,V$, $U_{t,2} = 0.05\,V$, $U_{e,1} = U_{e,2} = U_{e,3} = U_{e,4} = 0\,V$. This corresponds to $\omega_{rad,1}/2\pi \approx 800\,kHz$, $\omega_{rad,2}/2\pi \approx 820\,kHz$ and $\omega_{ax}/2\pi \approx 260\,kHz$ and is the confinement used for clock spectroscopy within this work.

EMM slope	measurement $((\text{V/m})/\text{V})$	simulation $((\text{V/m})/\text{V})$	fractional deviation
$\Delta E_{\text{rf,x}}/\Delta U_{\text{tc}}$	-27724 ± 538	-26698	0.037
$\Delta E_{\text{rf,y}}/\Delta U_{\text{tc}}$	-22792 ± 424	-24356	-0.069
$\Delta E_{\text{rf,x}}/\Delta U_{\text{ec}}$	-537 ± 11	-536	0.002
$\Delta E_{\text{rf,y}}/\Delta U_{\text{ec}}$	-3798 ± 46	-5218	-0.374

(b) *The two principal axes have a projection of $\approx 90°$ and $\approx 0°$ with respect to the y-direction: $U_{\text{t,1}} = U_{\text{t,3}} = U_{\text{t,4}} = 8\,V$, $U_{\text{t,2}} = -0.79\,V$, $U_{\text{e,1}} = U_{\text{e,2}} = U_{\text{e,3}} = U_{\text{e,4}} = -12\,V$. This corresponds to $\omega_{\text{rad,1}}/2\pi \approx 780\,kHz$, $\omega_{\text{rad,2}}/2\pi \approx 835\,kHz$ and $\omega_{\text{ax}}/2\pi \approx 260\,kHz$.*

In the following, the deviations between the measurements and calculations of the two slopes $E_{\text{rf,x}}/U_{\text{tc}}$ and $E_{\text{rf,y}}/U_{\text{tc}}$ are analyzed in more detail, because the calculated values are used for the specification of the radial displacement in the context of the reordering sequence in section 5.3 (Table 5.1). There, slopes for different radial and axial confinement are required. For this reason, the deviations are analyzed as a function of these two parameters in Fig. 4.12 and Fig. 4.13. In Fig. 4.12 (a) and (b), the $\Delta E_{\text{rf,x}}/\Delta U_{\text{tc}}$ and $\Delta E_{\text{rf,y}}/\Delta U_{\text{tc}}$ slopes are shown for different radial confinement, which is expressed as the Mathieu q_{Yb} parameter for a single Yb$^+$ ion. The dc voltages are as specified in Table 4.2a and Table 4.2b, respectively. For both dc potentials the fractional deviation between measurement and calculation are well below 0.1.
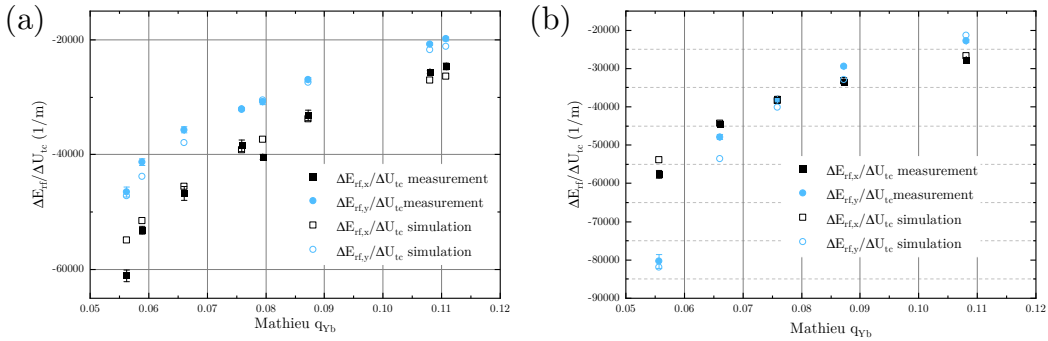

Figure 4.12.: *Comparison between measured and calculated $\Delta E_{\text{rf,x}}/\Delta U_{\text{tc}}$ and $\Delta E_{\text{rf,y}}/\Delta U_{\text{tc}}$ slopes of segment 2 in dependence on the radial confinement for the two dc potentials specified in Table 4.2a and Table 4.2b. The radial potential is expressed as the Mathieu q_{Yb} parameter for a single Yb$^+$ ion. The shown values correspond to radial trap frequencies $\omega_{\text{rad}}/2\pi$ between 360 kHz and 835 kHz. In (a) the orientation of the two principal axes have a projection of $\approx 60°$ and $\approx 30°$ with respect to the y-direction and in (b) the projections are $\approx 90°$ and $\approx 0°$. The rf rf drive frequency and rf voltage amplitude are $\Omega_{\text{rf}} = 2\pi \times 21.7\,MHz$ and $U_{\text{rf}} = 1151\,V$, respectively.*

To analyze whether the simulations predict the dependence of the two slopes on the axial

confinement correctly, a respective comparison is shown in Fig. 4.13. As expected, the axial confinement has hardly any influence on the two slopes and also here the fractional deviations between simulations and measurements are well below 0.1.
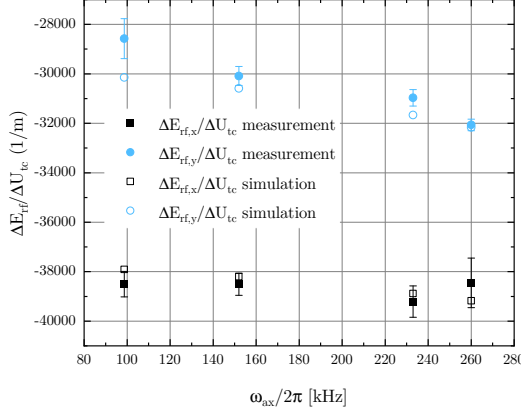

Figure 4.13.: *Comparison between measured and calculated $\Delta E_{\mathrm{rf,x}}/\Delta U_{\mathrm{tc}}$ and $\Delta E_{\mathrm{rf,y}}/\Delta U_{\mathrm{tc}}$ slopes of segment 2 for different axial confinement ω_{ax}. The rf drive frequency and the rf voltage amplitude are $\Omega_{\mathrm{rf}} = 2\pi \times 21.7\,MHz$ and $U_{\mathrm{rf}} = 810$ V, respectively, which corresponds to radial trap frequencies $\omega_{\mathrm{rad}}/2\pi$ around 570 kHz, the exact values being slightly dependent on the axial confinement. The projection of the two principal axes on the y-direction are $\approx 60°$ and $\approx 30°$.*

In summary, the simulation correctly predicts the two slopes with a fractional deviation of less than 0.1. Thus, the slopes needed for the specification of the radial displacement in chapter 5.3 can be calculated and do not have to be measured. As uncertainty 10 % of the slope is assumed there.

4.3. Heating rate

To measure the heating rate of the trap, the $^2\mathrm{S}_{1/2} \leftrightarrow {}^2\mathrm{D}_{5/2}$ quadrupole transition of a single $^{172}\mathrm{Yb}^+$ ion has been used. The ion is cooled to the motional ground state via continuous resolved sideband cooling, and after a wait time the mean phonon number is determined from the ratio of blue and red sidebands. First the spectroscopic sequence for ground state cooling is described briefly and then measurements of the heating rate are presented and compared to the identical trap characterized in [22, 114].

4.3.1. Ground state cooling sequence

An external magnetic field of $B = 65\,\mu\mathrm{T}$ is applied in the direction of H2 which leads to a Zeeman splitting of the sublevels of the ground state $^2\mathrm{S}_{1/2}$ and the excited state $^2\mathrm{D}_{5/2}$. For spectroscopy and sideband cooling, the transition $m_j = -\frac{1}{2} \leftrightarrow m_{j'} = -\frac{5}{2}$ is used which is a $\Delta m = -2$ transition and is ideally driven when the magnetic field vector $\vec{B}$, the wave vector $\vec{k}$ of the laser and the polarization $\vec{E}$ of the laser are mutually orthogonal to each other [99]. Therefore the 411 nm propagates along the y-direction and the polarization $\vec{E}$ is orthogonal to H2.

For the ground state cooling and heating rate measurements the dc potential of the trap is adjusted such that one radial trap axis is oriented vertically along the y-axis so that the

411 nm laser only interacts with one radial mode. Furthermore, the H2 beam polarization is changed from linear to circular (σ^-) polarization to enable optical pumping. The last adjustment is to take the beamsplitter of the Yb$^+$ detection beam path out of the beam via the automated flip mount to send the complete fluorescence light to the camera for most efficient detection. The experimental sequence for continuous ground state cooling and the heating rate measurement is shown in Fig. 4.14 and the individual steps are briefly explained in the following. The sequence is repeated for each parameter set 100-200 times to have enough statistics on the the ground state and excited state population.

	reference image	Doppler cooling	optical pumping	sideband cooling	repumping	wait time	spectroscopy pulse	detection image	repumping
370 nm H1, V	■	■						■	■
370 nm H2, (σ-)			■						
411 nm				RSB			■		
639 nm	■	■	■	■					■
935 nm	■	■	■	■	■			■	■
1650 nm	■	■	■	■	■				■
Length	1 ms	5 ms	0.5 ms	5 ms	0.1 ms	0 -1000 ms	0.001 - 0.4 ms	1 ms	20 ms

Figure 4.14.: *Experimental sequence for continuous sideband cooling and the heating rate measurements.*

Reference and detection image
A reference image is taken, to confirm that the ion is in the electronic ground state at the beginning of each spectroscopy cycle. All repumper lasers and the Doppler cooling laser beams H1 and V are switched on and the camera is triggered to start and stop the exposure. At the end of the spectroscopy cycle, the camera is triggered again to detect the state of the ion via the electron shelving technique[71]. In contrast to the reference image, only the Doppler cooling laser beams and the 935 nm beam is switched on. The count rate in a region of interest of typically 3×3 pixels (or 2×2 superpixels if binning of 2×2 pixels each is used) is evaluated against a fixed threshold value. All images with count rates above the threshold are considered as 'bright', which means the ion is in the ground state. Images with count rates below the threshold are counted 'dark' and the ion is in the excited state. If the reference image at the beginning of the spectroscopy cycle is 'dark', the complete cycle is discarded.

The exposure time needs to be long enough to clearly differentiate the bright and dark ions. Typically, a detection time of 1-2 ms has been used, depending on the available at 370 nm (typically $s_V \approx$ 1-2). Longer detection times are not advisable as the lifetime of the excited state is ≈ 7 ms.

Doppler cooling
For Doppler cooling the power is significantly reduced ($s_V \approx 0.1$ and $s_{H1} \approx 0.02$), compared to the reference and detection image, to achieve the low temperatures. With subsequent

4. Ion trap characterization

measurements of Rabi oscillations on the carrier transition, the powers in H1 and V have been optimized. These measurements correspond to the sequence in Fig. 4.14, with the sideband cooling, the following repuming and the wait time left out. The achieved mean phonon number and temperature can be deduced from the Rabi frequency and the contrast as described in [102]. Typically, the resulting Rabi oscillations are consistent with the assumption of Doppler temperature T_D (see Eq. 2.35).

Optical pumping

Following the Doppler cooling the ion is optically pumped to the $^2S_{1/2}(m_j = -\frac{1}{2})$ ground state with the σ^- polarized H2 beam. If the light is perfectly polarized, only the $^2S_{1/2}(m_j = +\frac{1}{2}) \leftrightarrow$ $^2P_{1/2}(m_{j'} = -\frac{1}{2})$ transition with $\Delta m = $-1 can be driven, so that on average the scattering of $\approx$ 1-2 photons should be sufficient to bring the ion in the desired $^2S_{1/2}(m_j = -\frac{1}{2})$ state, which is dark. To optimize the optical pumping, the scattering rate on the Doppler cooling transition can be minimized or the excitation on the $^2S_{1/2}(m_j = +\frac{1}{2}) \leftrightarrow {}^2D_{5/2}(m_{j'} = +\frac{5}{2})$ is suppressed. The optimization includes the rotation of the 370 nm quarter waveplate and the pointing of the magnetic field vector. The optical pumping time of 0.5 ms, that has been used so far, can significantly be reduced considering that with perfectly polarized light on average $\approx$ 1-2 photons need to be scattered.

Sideband cooling

During sideband cooling, the 411 nm laser frequency is tuned to the first red sideband (RSB) and simultaneously the 1650 nm illuminates the ion. During the 5 ms of continuous sideband cooling the ion cycles between the Zeeman states $^2S_{1/2}(m_j = -\frac{1}{2}) \leftrightarrow {}^2D_{5/2}(m_j = -\frac{5}{2}) \leftrightarrow$ $^2P_{3/2}(m_j = -\frac{3}{2})$ which is a closed cycle because of the selection rules. This scheme results in an effective two-level system, where the excited state is a so-called dressed state with a tunable decay rate Γ', as explained in section 2.3.2. The tuning is done via the Rabi frequency of the $^2D_{5/2} \leftrightarrow {}^2P_{3/2}$ transition which can be adjusted with the laser intensity at 1650 nm.

The decay rate of the dressed excited state is typically adjusted to $\Gamma' = 2\pi \times 50\text{-}80\,\text{kHz}$, which is a good compromise between cooling rate and final temperature. A separate, slightly modified experimental sequence is used for the adjustment. After optical pumping, a π-pulse ($\approx 20\,\mu\text{s}$ with $\approx 250\,\mu\text{W}$) on the $^2S_{1/2} \leftrightarrow {}^2D_{5/2}$ carrier transition is added to bring the population to the $^2D_{5/2}$ state. This is followed by a 1650 nm pulse with variable pulse length and internal state detection. The 1650 nm laser power, which is on the order of nW, is adjusted until the desired decay rate Γ' is reached.

Following the sideband cooling, a short 1650 nm repumping pulse with a length of 0.1 ms is applied to ensure that the ion returns to the $^2S_{1/2}$ ground state.

Wait time

In case of a heating rate measurement, a wait time with a variable length is introduced before the spectroscopy pulse. During that time all lasers are switched off.

Spectroscopy pulse

The spectroscopy pulse is a 411 nm pulse on the quadrupole transition which can vary either in duration, frequency or light intensity depending on the quantity to be measured. A measurement with a fixed frequency, for example on the carrier transition, and a variable pulse duration records Rabi oscillations and the Rabi frequency and the 411 nm light intensity seen by the ion can be calculated. To determine the mean phonon number $\bar{n}$ after ground state cooling (with or without a wait time) the excitation probability on the first blue and red sideband transition, I_{BSB} and I_{RSB}, are compared to each other at the same 411 nm laser intensity and pulse duration. Following [102, 113] the mean phonon number $\bar{n}$ can then be calculated according to

$$\bar{n} = \frac{1}{\frac{I_{\mathrm{BSB}}}{I_{\mathrm{RSB}}} - 1}. \tag{4.12}$$

Repumping

The last component of the spectroscopy cycle is the repumping of the state population back to the $^2\mathrm{S}_{1/2}$ ground state. During that all repumper lasers and the Doppler cooling lasers beams illuminate the ion. A conservative length of $\approx 20\,\mathrm{ms}$ has been used and the number of 'bright' reference images indicate that its length is sufficient. The critical step is that all Zeeman sublevels of the $^2\mathrm{F}_{7/2}$ state need to be depleted.

4.3.2. Measurements

Low and constant ion temperatures, that are known with low uncertainties, are desirable for precision spectroscopy in order to keep the thermal second-order Doppler shift low (see Eq. 2.45). To prevent ac Stark shifts it is advantageous to avoid cooling during the clock pulses. This requires a sufficiently low external heating rate on time scales of the interrogation.

Electric field noise can excite the secular motion and thus heat the ions. The relation between the heating rate $\dot{\bar{n}}$ (in the unit phonons/s) and the power spectral density S_E of the electric field noise, when disregarding micromotion is given in Eq. 2.46. The are multiple sources of electric field noise in the relevant frequency range, but the dominant source is suspected to be fluctuating patch potentials on the electrode surfaces, pickup of external electromagnetic noise by the electronics supplying the trap voltages and Johnson-Nyquist noise. The processes have different scaling laws, but in general heating rates decrease with larger electrode-ion distance d [113, 186], higher secular frequency [114] and lower temperature of the apparatus [187]. But even with similar experimental conditions, spreads of heating rates over several orders of magnitude are observed which are not yet fully explained [188]. A heating rate on the order of $1\,\mathrm{phonon\,s^{-1}}$ has already been demonstrated for the identical trap characterized in [22, 90] due to the relatively large value of $d \approx 0.7\,\mathrm{mm}$ and the lowpass filtering on the trap chips, which have a cutoff frequency of only $113\,\mathrm{Hz}$ leading to a suppression of electric noise at the secular frequencies by 3 to 4 orders of magnitude.

4. Ion trap characterization

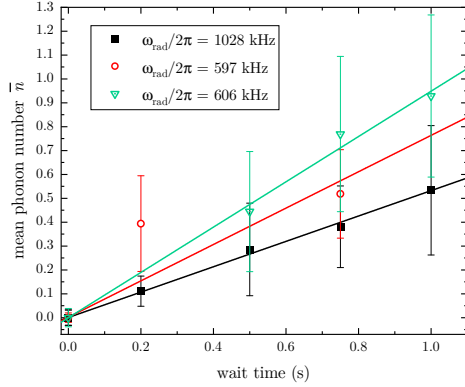**Figure 4.15.:** *Measurements of radial heating rates at different secular frequencies ω_{rad} of a single $^{172}Yb^+$ ion trapped in segment 2. The mean phonon number $\bar{n}$ is determined by comparisons of first-order red and blue sideband excitations (I_{RSB} and I_{BSB}) after variable wait times. The heating rates are deduced from linear fits.*

Figure 4.15 presents measurements of the mean phonon number $\bar{n}$ after ground state cooling and a variable wait time for different secular frequencies ω_{rad} that have been determined via the experimental sequence explained in section 4.14 with a single ^{172}Yb$^+$ ion trapped in segment 2. Linear fits to the data reveal the heating rates $\dot{\bar{n}}$ which are listed in Table 4.3, where also the respective spectral density S_E of the electric field noise calculated via Eq. 2.46 is given.

Table 4.3.: *Results of radial heating rate measurements at different secular frequencies ω_{rad}, deduced spectral densities S_E of the electric field noise and the resulting second-order Doppler shift increase in the absence of cooling for $^{115}In^+$ $\frac{\partial}{\partial t}\left(\frac{\Delta\nu_{\mathrm{D2,\dot{n}}}}{\nu}\right)$ for a single trap axis. The heating rates have been measured at different trap drive frequencies Ω_{rf}.*

$\omega_{\mathrm{rad}}/2\pi$	$\dot{\bar{n}}$	$S_E(\omega_{\mathrm{sec}})$	$\frac{\partial}{\partial t}\left(\frac{\Delta\nu_{\mathrm{D2,\dot{n}}}}{\nu}\right)$	$\Omega_{\mathrm{rf}}/2\pi$
(kHz)	(phonons s^{-1})	($10^{-14}\,(\mathrm{V/m})^2\,\mathrm{Hz}^{-1}$)	($10^{-20}\,\mathrm{s}^{-1}$)	(MHz)
597	0.76 ± 0.24	1.34 ± 0.11	-2.62 ± 0.83	16.4
606	0.95 ± 0.24	1.70 ± 0.43	-3.32 ± 0.84	28.3
1028	0.53 ± 0.15	1.61 ± 0.45	-3.14 ± 0.89	16.4

As the ions are not cooled during the clock interrogation the second-order Doppler shift due to each mode increases as described in Eq. 2.48, which can be simplified to

$$\frac{\partial}{\partial t}\left(\frac{\Delta\nu_{\mathrm{D2,\dot{n}}}}{\nu}\right) = -\frac{\dot{\bar{n}}\hbar\omega_{\mathrm{sec}}}{mc^2} \tag{4.13}$$

for a single mode in case of a single ion. This allows to estimate the influence of the here measured heating rate on the thermal second-order Doppler shift in ^{115}In$^+$. In Table 4.3, the contributions derived for a single trap axis for ^{115}In$^+$ are given which result in frequency shifts $\frac{\Delta\nu_{\mathrm{D2,\dot{n}}}}{\nu}$ on the order of $\approx 6\times10^{-21}$ in case of clock interrogation pulses with a length of 200 ms as used in this work. Therefore this contribution is negligible compared to other

frequency shifts and the low heating rate would even allow interrogation times of several seconds in species with longer excited-state lifetimes.

Figure 4.16 compares the measured heating rates to the ones of the identical trap characterized in [22, 114] (labeled as 'Yb-setup'). To the data of the 'Yb-setup' a power law function $\dot{\bar{n}}(\omega_{\mathrm{rad}}) = a\omega_{\mathrm{rad}}^{b}$ is fitted, from which $b = \text{-}1.95(25)$ [114] is deduced, which agrees with the scaling found in other traps [189]. The heating rates measured here perfectly follow the fit of the 'Yb-setup'. Thus, it can be concluded that the two traps show very similar low heating rates with the same scaling and the trap manufacturing process seems to be well under control. For the 'Yb-setup' the heating rate is found to be stable over the course of the four years of its use.

Figure 4.16.: *Comparison of heating rates measured in this work, labeled as 'In-clock setup' and for the identical trap characterized in [22, 114] labeled as 'Yb-setup'. The data of the 'Yb-setup' is fitted with a power law function $\dot{\bar{n}}(\omega_{\mathrm{rad}}) = a\omega_{\mathrm{rad}}^{b}$ to extract the ω_{rad} scaling of $\dot{\bar{n}}$ which results in $b = \text{-}1.95(25)$ [114].*
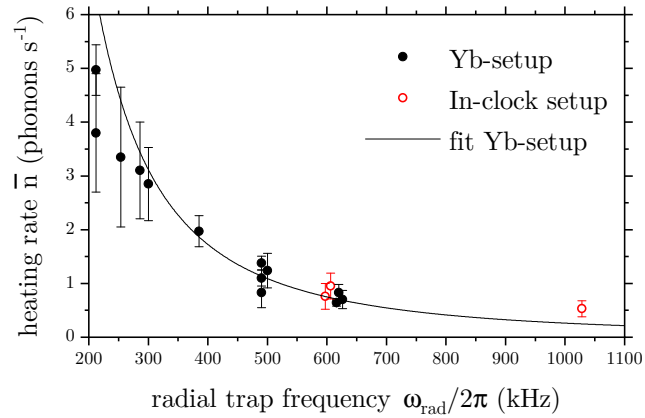
For the operation of a multi-ion clock, the effect of the heating rate of multiple ions and modes along all trap axes need to be considered. In [114], the analysis of single-ion heating in the identical trap is extended to radial and axial frequencies, as well as to linear single-species ion chains and 2D- and 3D-ion crystals.

4.4. Temperature of the trap

The content presented in section 4.4 is part of a publication by the author of this thesis [117].

The uncertainty associated with the ac Stark shift due to thermal radiation is a major contribution to the overall systematic uncertainty of state-of-the-art optical atomic clocks. The ion trap covers a significant portion of the solid angle that the ion sees, and earlier ion traps have warmed by several 10 K. For this reason a design focus for this trap has been to keep the rf induced heating low with thoroughly selected materials that have a high thermal conductance and low rf losses. Large cross sections and good thermal contacts between different constituents provide effective heat removal. The trap features two integrated Pt100 sensors, which have been calibrated and allow to deduce the trap-related temperature rise at the position of the ions with an uncertainty on the order of a few 100 mK maximum via

4. Ion trap characterization

a numerical model that has been confirmed with infrared camera measurements. All details about the material choice, the design optimization, the numerical model, all temperature measurements of three identical traps and a discussion about the uncertainty contributions to the temperature of the trap and at the position of the ion can be found in [117], where also the the resulting trap-related uncertainty of the blackbody radiation (BBR) shift for typical ion clock species in discussed. The trap of this setup is labeled with 'C' in the publication. This section only summarizes the most important results and relations to determine the BBR-induced ac Stark shift in this trap. The temperature uncertainty of the two integrated Pt100 sensors and the temperature derivation at the position of the ions is presented in section 4.4.1. The rf-induced heating of the trap, measured with these sensors, is characterized in section 4.4.2, where also the temperature increase at the positions of the ions for the trap confinement used for the clock spectroscopy, presented in section 6, is given.

4.4.1. Temperature uncertainty of the two integrated Pt100 sensors and temperature derivation at the position of the ions

The absolute temperature uncertainty of the two integrated Pt100 sensors on the rf voltage carrying chips 2 and 3 (compare Fig. 3.1 (b)) has been obtained from the calibration procedure explained in the appendix A. The result is shown in Fig. 4.17 and illustrates the linear temperature dependence of the uncertainty, which increases by about $3\,\mathrm{mK/K}$. At a typical lab temperature of $22\,°\mathrm{C}$ both sensors have an uncertainty below $60\,\mathrm{mK}$. The temperature resolution of the reading of the sensors is below $1\,\mathrm{mK}$, which allows the in-situ detection of very small temperature changes during trap operation.
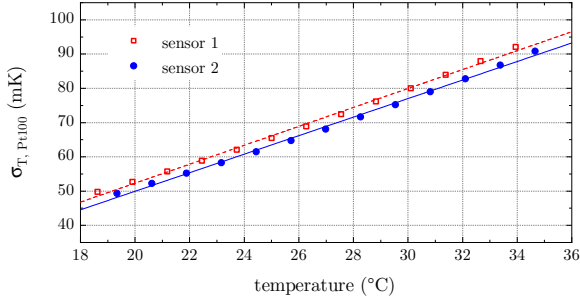
Figure 4.17.: *Absolute temperature uncertainty $\sigma_{\mathrm{T,Pt100}}$ for the two integrated and calibrated Pt100 sensors. The uncertainty is temperature dependent and increases with about $3\,\mathrm{mK/K}$.*

To specify the BBR-induced ac Stark shift with the smallest possible uncertainty, the temperature at the position of the ions T_{ions} needs to be known precisely. The trap experiences a temperature rise relative to the vacuum chamber T_{chamber} when an rf voltage is applied, which is characterized in section 4.4.2. The temperature increase of the trap leads to a higher temperature corresponding BBR radiation at the ion position ΔT_{ions} because a large part of the solid angle visible to the ions is covered by the ion trap. The effective BBR temperature at the position of the ions T_{ions} is therefore

$$T_{\mathrm{ions}} = T_{\mathrm{chamber}} + \Delta T_{\mathrm{ions}}. \tag{4.14}$$

The integrated Pt100 sensors allow the determination of the rf-induced temperature rise at the positions of the sensors $\Delta T_{\mathrm{sensor\ i}}$ (i=1,2) with respect to the temperature of the

vacuum chamber. With the numerical model described in [117] and its accuracy confirmed by temperature measurements with an IR camera and the integrated Pt100 sensors for an identical trap, the temperature at any position of the trap assembly can be inferred. Thus, the rise of the effective BBR temperature at the position of the ions ΔT_{ions} and the temperature rise at the location of the Pt100 sensors $\Delta T_{\text{sensor i}}$ can be compared and conversion factors (α and β) between those two temperatures can be derived as defined:

$$\Delta T_{\text{ions}} = \alpha \cdot \Delta T_{\text{sensor 1}} = \beta \cdot \Delta T_{\text{sensor 2}} \tag{4.15}$$
$$(\text{with } \alpha = 0.43 \pm 0.10 \text{ and } \beta = 0.32 \pm 0.10).$$

A smaller temperature uncertainty can be obtained by using the mean value derived from both sensors:

$$\Delta T_{\text{ions}} = \frac{\alpha \cdot \Delta T_{\text{sensor 1}} + \beta \cdot \Delta T_{\text{sensor 2}}}{2}. \tag{4.16}$$

With the temperature monitoring of the vacuum chamber described in section 3.2.4, this enables the in-situ monitoring of the effective BBR temperature at the location of the ions T_{ions} and the resulting ac Stark shift by measuring the temperature rise at the positions of the sensors $\Delta T_{\text{sensor i}}$ (i=1,2).

For the uncertainty $\sigma_{\Delta T \text{ions}}$, several contributions need to be considered, as discussed in detail in [117]. The first and obvious contributions are the temperature uncertainties $\sigma_{\text{T,Pt100}}$ of the sensors. The sensors only provide local temperature measurements. Temperature gradients on the trap chip can lead to additional errors in the temperature estimate and are investigated with IR camera measurements and compared to the model [117], so that also the uncertainty of the IR camera measurement and deviations between the model and the IR camera measurement enter the uncertainty $\sigma_{\Delta T \text{ions}}$. Another contribution is a deviation between the model and the Pt100 readings. The combined uncertainty for the deviation between model and experiment is given by $\sigma_{\text{T,FEM/Exp}} = 0.42 \text{ K} / \text{kV}^{-2}$. The lower bound of this uncertainty is given by the noise of the IR camera reading: $\sigma_{\text{T,cam}} = 0.2 \text{ K} + 0.05 \Delta T$, where ΔT is the observed temperature rise.

In summary, the uncertainty $\sigma_{\Delta T, \text{Trap}_{(i)}}$ on the trap temperature rise $\Delta T_{\text{sensor i}}$ measured with sensor i contains the absolute uncertainty of the Pt100 reading $\sigma_{\text{T,Pt100}}$ and the uncertainty for the deviation between the model and experiment $\sigma_{\text{T,FEM/Exp}}$, leading to the uncertainty $\sigma_{\Delta T, \text{Trap}_{(i)}} = \sqrt{\sigma_{\text{T,FEM/Exp}}^2 + \sigma_{\text{T,Pt100}_{(i)}}^2}$ with $\sigma_{\text{T,FEM/Exp}} \geq 0.25 \text{ K}$ for the typical temperature rises.

The temperature rise at the location of the sensors $\Delta T_{\text{sensor i}}$ is transferred from the Pt100 sensor measurements to the position of the ions ΔT_{ions} via the conversion factors α and β derived from the numerical model and introduced in Eq. 4.16. The uncertainty of those parameters $\sigma_\alpha = \sigma_\beta = 0.10$ has been deduced from simulations with varying input parameters in [117].

4. Ion trap characterization

Gaussian error propagation on Eq. (4.16) reveals the final uncertainty of the BBR induced temperature rise at the position of the ions $\sigma_{\Delta T\text{ions}}$ as

$$\sigma_{\Delta T\text{ions}}^2 = \sigma_\alpha^2 \cdot \frac{\Delta T_{\text{sensor 1}}^2}{4} + \sigma_{\Delta T,\text{Trap}_{(1)}}^2 \cdot \frac{\alpha^2}{4}$$
$$+ \sigma_\beta^2 \cdot \frac{\Delta T_{\text{sensor 2}}^2}{4} + \sigma_{\Delta T,\text{Trap}_{(2)}}^2 \cdot \frac{\beta^2}{4}. \tag{4.17}$$

4.4.2. rf-induced trap heating

The application of an rf voltage to the ion trap leads to a temperature rise which follows a quadratic behavior with respect to the amplitude [190], while the scaling with the frequency is more complex due to the different heating mechanisms in conductors and insulators. The frequency scaling of the heating is linear in dielectrics, quadratic in thin conductors and follows a power law with the exponent 2.5 in thick conductors

$$\Delta T(\Omega_{\text{rf}}) = \gamma_{\text{T}} \cdot U_{\text{rf}}^2 \cdot (\lambda_1 \cdot \frac{\Omega_{\text{rf}}}{\Omega_{\text{ref}}} + \lambda_2 \cdot \frac{\Omega_{\text{rf}}^2}{\Omega_{\text{ref}}^2} + \lambda_3 \cdot \frac{\Omega_{\text{rf}}^{2.5}}{\Omega_{\text{ref}}^{2.5}}). \tag{4.18}$$
$$\lambda_1 = 0.15 \qquad \lambda_2 = 0.50 \qquad \lambda_3 = 0.35$$

Here γ_{T} describes the dependence of the temperature rise on the rf voltage amplitude U_{rf} at a reference frequency Ω_{ref}, which can be slightly different even at the same Ω_{ref} for identical traps due to variations in the heat conductivity or the gold thickness of the electrodes originating from the manufacturing process. The coefficients λ_1, λ_2 and λ_3 are determined by the prevalence of the respective heating mechanism (λ_1: dielectrics, λ_2: thin conductors and λ_3: thick conductors) at a common reference rf frequency Ω_{ref}. Here $\Omega_{\text{rf}} = 2\pi \times 16.4\,\text{MHz}$. The values of the coefficients λ_1, λ_2 and λ_3 are derived from the heat distribution given by the numerical model described in [117].

The rf-induced temperature increase has been measured with the two integrated Pt100 sensors for several rf voltage amplitudes U_{rf} at $\Omega_{\text{rf}} = 2\pi \times 21.8\,\text{MHz}$ and $\Omega_{\text{rf}} = 2\pi \times 16.4\,\text{MHz}$, as shown in see Fig. 4.18. Equation 4.18 is used to rescale the voltage-dependent temperature rise ΔT measured at $\Omega_{\text{rf}} = 2\pi \times 21.8\,\text{MHz}$ to $\Omega_{\text{rf}} = 2\pi \times 16.4\,\text{MHz}$, to compare this with a measurement at $\Omega_{\text{rf}} = 2\pi \times 16.4\,\text{MHz}$. The temperature drift of the vacuum chamber over the course of the measurements has been monitored with the seven additional Pt100 sensors (see section 3.2.4). The respective drifts have been considered in all measurements. The trap only shows heating below $2\,\text{K}$ for the two tested rf drive frequencies. The temperature rise on sensor 1 (positioned on chip 2, open squares) is always lower than on sensor 2 (positioned on chip 3, filled circles) because its location is closer to the carrier board and thereby the heat sink. To determine the temperature rise the trap drive has first been switched on until the system reached thermal equilibrium and then switched off until thermal equilibrium has been reached again. This warming and cooling of the trap is then fitted and the difference between the two steady-state temperatures is taken as the temperature rise ΔT. The voltage dependent temperature rise ΔT has been fitted with a quadratic function. The measurement at $\Omega_{\text{rf}} = 2\pi \times 21.8\,\text{MHz}$ is additionally displayed after rescaling it to $\Omega_{\text{rf}} = 2\pi \times 16.4\,\text{MHz}$ with

Eq. 4.18 (black lines) in order to verify the numerical model. The temperature rise increases with frequency, as is expected from all contributions to Eq. 4.18. The measurements at the two rf drive frequencies overlap after the rescaling with Eq. 4.18, implying that the partial heating processes in the trap are well captured by the model. Thus, Eq. 4.18 can be used to estimate the trap temperature rise at an other rf drive frequency Ω_{rf} and amplitude U_{rf}.

Figure 4.18.: *Voltage dependent rf-induced temperature rise measured with the integrated Pt100 sensors for two different rf drive frequencies: 16.4 MHz (red) and 21.8 MHz (green) [117]. The open squares and closed circles correspond to sensor 1 and sensor 2, respectively. The dashed and solid lines are quadratic fits to the measured values. The values at 21.8 MHz have been rescaled to an rf frequency of 16.4 MHz (black lines). The error bars are dominated by the absolute uncertainty of the integrated Pt100 sensors, since the fitting errors of the warming and cooling of the trap are negligible.*
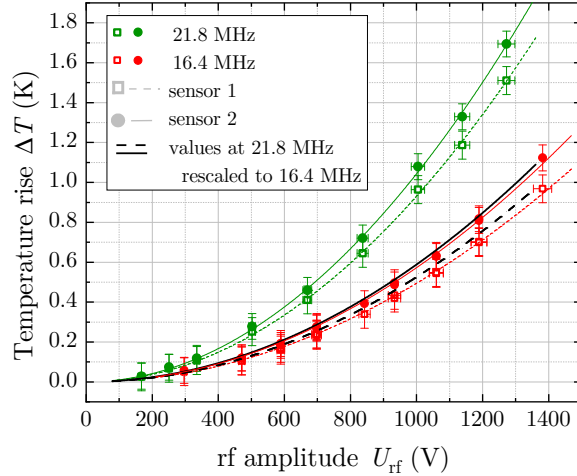
From the quadratic fits to the measurements in Fig. 4.18 the scaling factor $\gamma_{\mathrm{T, \, sensor \, i}}$ (i=1,2 for the two sensors) giving the relation between the temperature rise $\Delta T_{\mathrm{sensor \, i}}$ and applied rf voltage U_{rf} at the location of the sensors 1 and 2 has been extracted for the two rf drive frequencies. Table 4.4 lists these values (Ω_{ref} as explained previously).

Table 4.4.: *Scaling factors γ_{T} for the relation between temperature rise and rf voltage amplitude at the location of the sensors 1 and 2 for the two tested rf drive frequencies. The factors have been deduced from the measured rf voltage scaling of the temperature rise shown in Fig. 4.18.*

$\Omega_{\mathrm{ref}}/2\pi$ (MHz)	$\gamma_{\mathrm{T, \, sensor \, 1}}$ $(10^{-7} \mathrm{~K/V^2})$	$\gamma_{\mathrm{T, \, sensor \, 2}}$ $(10^{-7} \mathrm{~K/V^2})$
16.4	4.9 ±0.1	5.7 ±0.1
21.8	9.3 ±0.2	10.4 ±0.2

In [117], the measurement of the rf-induced heating of this trap is compared with the identical trap characterized in [22, 90, 114], which is labeled with 'B' in the publication, after rescaling to the same rf drive frequency via Eq. 4.18. For sensor 2 the voltage dependent

temperature rises in the two traps agree, while for sensor 1 they differ noticeably. While for this trap, the temperatures determined by the two sensors agree reasonably (deviation $\approx 12\,\%$ at $1.2\,\mathrm{kV}$, compare Fig. 4.18), the temperature sensor 1 in the second trap shows much colder temperatures than the sensor 2 ($\approx 35\,\%$ deviation at $1.2\,\mathrm{kV}$). It is suspected that this difference is due to better thermal sinking with the vacuum chamber in the set-up of the second trap and to a different geometry of the rf strips connecting the trap to the chamber rf feedthrough and the rf ground. FEM simulations showed qualitatively that the latter has an influence on the spread in temperature rise between the sensor 1 and 2. Nevertheless the agreement in sensor 2 between the two traps show that the trap fabrication works reproducibly with regard to the thermal properties.

In Table 4.5, the temperature rise at the position of the ions ΔT_{ion} for an rf drive amplitude $U_{\mathrm{rf}} = 1151\,\mathrm{V}$ is given for the two analyzed rf drive frequencies Ω_{rf} for this trap. For $\Omega_{\mathrm{rf}} = 2\pi \times 21.8\,\mathrm{MHz}$, this corresponds to the trap confinement used for the clock spectroscopy results of section 6, where $\omega_{\mathrm{rad}} = 2\pi \times 1.230\,\mathrm{MHz}$ for a single In$^+$ ion. For $\Omega_{\mathrm{rf}} = 2\pi \times 16.4\,\mathrm{MHz}$, this rf voltage amplitude corresponds to $\omega_{\mathrm{rad}} = 2\pi \times 1.630\,\mathrm{MHz}$.

Table 4.5.: *BBR temperature rise at the position of the ions ΔT_{ion} for an rf drive amplitude of 1151 V for the two analyzed rf drive frequencies Ω_{rf}. The values are deduced from the temperature readings of the integrated Pt100 sensors and transferred to the location of the ions with Eq. 4.16.*

	$\Omega_{\mathrm{rf}}/2\pi = 16.4\,\mathrm{MHz}$ ΔT_{ion} (K)	$\Omega_{\mathrm{rf}}/2\pi = 21.8\,\mathrm{MHz}$ ΔT_{ion} (K)
From sensor 1	0.28 ± 0.25	0.51 ± 0.27
From sensor 2	0.24 ± 0.20	0.44 ± 0.23
Both sensors (mean)	0.26 ± 0.16	0.47 ± 0.18

For both rf drive frequencies, the temperature uncertainty at the place of the ions due to the rf heating of the trap is below $200\,\mathrm{mK}$. This result is among the smallest reported trap-related BBR temperature uncertainties at the position of the ions and shows that the trap manufacturing process seems to be under control with regard to the thermal properties. The only trap showing a comparable temperature uncertainty at the position of the ions is the end-cap trap of NPL [191] with $140\,\mathrm{mK}$ at $\omega_{\mathrm{rad}} = 2\pi \times 1\,\mathrm{MHz}$ and $\Omega_{\mathrm{rf}} = 2\pi \times 14\,\mathrm{MHz}$. That uncertainty is derived from a IR measurement in combination with a FEM model.

4.5. Trap-related uncertainty budget

In this section, the trap-related uncertainty budget contributions for a multi-ion In$^+$ clock with a crystal length of $400\,\mu\mathrm{m}$, based on the trap characterization measurements shown in section 4.2-4.4, are assembled. All shifts and uncertainties are adjusted for the trap potential

used for the clock spectroscopy measurements presented in section 6.2, if they were measured for a different trap potential.

For clock spectroscopy, an rf drive frequency of $\Omega_{\text{rf}} = 2\pi \times 21.7\,\text{MHz}$ with an rf voltage amplitude $U_{\text{rf}} = 1151\,\text{V}$ has been used. The secular frequencies for a single Yb$^+$ (In$^+$) ion are $\omega_{\text{rad},1}/2\pi \approx 800\,\text{kHz}$ (1200 kHz), $\omega_{\text{rad},2}/2\pi \approx 820\,\text{kHz}$ (1230 kHz) and $\omega_{\text{ax}}/2\pi \approx 260\,\text{kHz}$ (318 kHz). The two principal axes have a projection of $\approx 60\,^\circ$ and $\approx 30\,^\circ$ with respect to the y-direction.

Second-order Doppler and ac Stark shift induced by EMM

The residual EMM results in a fractional second-order Doppler shift $\frac{\Delta\nu_{\text{D2,EMM}}}{\nu}$, which is described by Eq. 2.50. Because the 3D-EMM measurements presented in section 4.2 have been performed at a different rf drive frequency and trap potential, they need to be converted to the clock potential. For simplicity, the average frequency of the two radial modes is assumed for both modes. The relevant parameters of both potentials are summarized in Table 4.6.

Table 4.6.: *Trap potential parameters for the conversion of the 3D-EMM measurements of section 4.2 to the clock potential used in section 6.2.*

	$\Omega_{\text{rf}}/2\pi$ (MHz)	$\omega_{\text{rad}}/2\pi$ (kHz)	$E_{\text{rf,z}}$
EMM measurement potential	16.4	560	$E_{\text{rf,z,meas}}$
clock potential	21.7	810	$(810/560)^2\,E_{\text{rf,z,meas}}$

For the radial directions the same electric stray field E_{dc} is assumed to convert the measured rf field amplitudes E_{rf} to the clock potential. For the axial direction the $E_{\text{rf,z}}$ component needs to be scaled with the ratio of the squares of the respective radial secular frequencies ω_{rad}: $(810/560)^2 = 2.09$. For the estimate a $400\,\mu\text{m}$ sized linear crystal, which is trapped in segment 2 between the ion positions 4.72 mm and 5.12 mm is assumed (see Fig. 4.7). Across that region the spread of $|\vec{E_{\text{rf}}}|$ is only $(8.2 \pm 7.7)\,\text{V/m}$. The individual shifts at the positions of all In$^+$ ions will need to be averaged for a correct evaluation. For an upper bound, two In$^+$ ions are assumed at the positions with the largest difference of $|\vec{E_{\text{rf}}}|$ in the selected range and their average shift is taken as the EMM-induced second-order Doppler shift $\frac{\Delta\nu_{\text{D2,EMM}}}{\nu}$.

Table 4.7 summarizes the relevant information about the described conversion. The resulting average shift is $\frac{\Delta\nu_{\text{D2,EMM}}}{\nu} = (\text{-}1.32 \pm 0.15) \times 10^{-18}$ with a spread of $(0.15 \pm 0.29) \times 10^{-18}$ between the two extreme values.

The rf field not only induces a second-order Doppler shift, but also an ac Stark shift $\Delta\nu_S$, the fractional frequency shift of which is described by Eq. 2.51. The trap-related contribution arises from the rf field due to EMM. Taking the average of $|\vec{E_{\text{rf}}}| = (112.2 \pm 6.5)\,\text{V/m}$ of the two positions in table 4.7 this leads to a shift of $(\text{-}1.24 \pm 0.18) \times 10^{-19}$ and the spread between the two extreme values is $(1.3 \pm 3.3) \times 10^{-20}$.

4. Ion trap characterization

Table 4.7.: *EMM-induced second-order Doppler and ac Stark shift extrema within a 400 mum long region in segment 2. The results of the measurement presented in Fig. 4.7 are converted to the clock operating potential. The parameters which are relevant for the conversion are listed in Table 4.6.*

	5.02 mm (measurement)	4.72 mm (measurement)	5.02 mm (clock potential)	4.72 mm (clock potential)
$E_{\mathrm{rf,x}}$ (V/m)	-7.2 ± 13.5	14.5 ± 13.5	-6.7 ± 12.5	13.4 ± 12.5
$E_{\mathrm{rf,y}}$ (V/m)	-7.2 ± 6.7	-28.0 ± 6.5	-6.7 ± 6.2	25.9 ± 6.0
$E_{\mathrm{rf,z}}$ (V/m)	51.9 ± 4.6	52.3 ± 4.7	108.6 ± 9.2	111.5 ± 9.2
$|\vec{E}_{\mathrm{rf}}|$ (V/m)	52.9 ± 4.9	61.1 ± 5.9	109.0 ± 9.2	115.3 ± 9.1
$\frac{\Delta \nu_{\mathrm{D2,EMM}}}{\nu}$ (10^{-18})	-0.52 ± 0.10	-0.69 ± 0.13	-1.25 ± 0.21	-1.40 ± 0.22
$\frac{\Delta \nu_{\mathrm{S,EMM}}}{\nu}$ (10^{-19})	-0.27 ± 0.06	-0.37 ± 0.08	-1.17 ± 0.22	-1.30 ± 0.24

Influence of the heating rate

In section 4.3, the effect of the heating rate on the resulting second-order Doppler shift $\frac{\partial}{\partial t}\left(\frac{\Delta \nu_{\mathrm{D2,\dot{n}}}}{\nu}\right)$ for a single $^{115}\mathrm{In}^+$ ion and a single trap axis has been derived. For the clock spectroscopy results shown in this work, the smallest crystal consists of 1 In$^+$ ion and 3 Yb$^+$ ions, so that 12 modes need to be considered. The heating rates of higher-order modes α and their effect on the thermal second-order Doppler shift in a linear mixed-species crystal can be calculated according to Eq. 2.47 and Eq. 2.48, respectively. Only the COM modes heat significantly, as described in section 2.4.1. For the clock trap potential, the radial COM mode frequency of Yb$^+$ is at $\omega_{\mathrm{rad,Yb}} = 2\pi \times 810\,\mathrm{kHz}$, which according to Fig. 4.16 results in $\dot{n} \approx 0.5\,\mathrm{phonons/s}$ and is equivalent to $\frac{\partial}{\partial t}\left(\frac{\Delta \nu_{\mathrm{D2,\dot{n}}}}{\nu}\right) \approx 1.58 \times 10^{-20}\,\mathrm{s}^{-1}$, which corresponds to $\approx 3 \times 10^{-21}$ for a clock interrogation pulse duration of 200 ms. The radial COM mode frequency of In$^+$ is at $\omega_{\mathrm{rad,In}} = 2\pi \times 1215\,\mathrm{kHz}$, where $\dot{n} \approx 0.25\,\mathrm{phonons/s}$ and results in $\frac{\partial}{\partial t}\left(\frac{\Delta \nu_{\mathrm{D2,\dot{n}}}}{\nu}\right) \approx 7.9 \times 10^{-21}\,\mathrm{s}^{-1}$ and $\approx 2 \times 10^{-21}$ for the clock pulse. The resulting frequency shift contribution of the heating during the clock interrogation is therefore estimated to be $< 10^{-20}$, which is negligible compared to the other trap-related contributions and is not analyzed in more detail. The heating rates are so low that they have negligible impact on the equilibrium temperature reached by sympathetic cooling. Accordingly, the cooling process is here independent of the trap and thus the thermal second-order Doppler shift is not considered in the assembled trap-related uncertainty budget in Table 4.8.

ac stark shift induced by BBR

The uncertainty of the BBR shift stems from the uncertainty of the differential static polarizability of the trapped species, but also from the absolute temperature of the BBR at the position of the ions T_{ions}, which is defined by the temperature and emissivities of the

parts surrounding them. T_{ions} is dominated by the contribution from the trap because a large part of the solid angle is covered by the trap. But also the vacuum chamber with its viewports need to be considered. Even though the stabilization of the chamber is a technical challenge, a determination of the BBR temperature at the location of the atoms at the level of 5 mK uncertainty has already been demonstrated in neutral atom experiments [192]. The change in thermal radiation due to the temperature rise of the rf feedthrough has also to be taken into account. Its effect on the trap temperature is read out by the integrated Pt100 sensors. Here only the uncertainty of the trap temperature is considered, which heats up under electrical drive and is often dominating the overall temperature uncertainty in optical ion clocks. The rf-induced temperature rise of the trap with respect to the temperature of the vacuum chamber has been obtained from measurements of the Pt100 sensors integrated in the trap and transferred to the position of the ions with Eq. 4.16 as described in section 4.4. For the clock potential, the rf induced temperature increase at the position of the ions is $\Delta T_{\text{ions}} = (0.47 \pm 0.18)\,\text{K}$. Assuming $T_{\text{ions}} = 300\,\text{K}$, the resulting trap-related fractional frequency shift according to Eq. 2.53 is $\Delta \nu_{\text{BBR}}/\nu = (\text{-}13.60 \pm 0.031) \times 10^{-18}$. For a complete description, the effect of the vacuum chamber must also be considered. Furthermore, the uncertainty of the BBR-induced frequency shift is presently dominated by the uncertainty of the only theoretically determined polarizability, as described in section 2.4.2. This uncertainty can be reduced with a measurement and is not considered for the trap-related uncertainty budget.

Summary of the trap-related uncertainty budget
In table 4.8, the previously discussed contributions of the trap-related uncertainty budget for a linear $400\,\mu\text{m}$ long crystal are summarized. All uncertainties are well below 10^{-18}, the largest uncertainty being attributed to the second-order Doppler shift caused by EMM, which is in the low 10^{-19} regime and can likely be reduced with a better choice of the compensation voltages as described previously.

Table 4.8.: *Estimated trap-related partial uncertainty budget in fractional units for a linear $400\,\mu m$ long crystal trapped in the the trap potential used for the clock spectroscopy measurements, presented in section 6.*

Shift	value (10^{-18})	uncertainty (10^{-18})	max. spread (10^{-18})
Second-order Doppler (EMM)	-1.32	0.15	0.15(29)
rf field induced ac stark shift (EMM)	-0.124	0.018	0.013(33)
Second-order Doppler (heating rate)	< 0.01	< 0.01	-
BBR-induced ac stark shift	-13.60	0.031	-

In summary, the characterized ion trap enables In^+ clock spectroscopy across a $400\,\mu\text{m}$ long region with a fractional frequency uncertainty $< 1.6 \times 10^{-19}$. Of course this low uncertainty can only be maintained for the operation of clock if the contributions are stable over time. To keep the largest uncertainty from the EMM-induced second-order Doppler shift below 10^{-18},

radial EMM needs to be compensated every 6 h, as deduced conservatively from the highest observed drifts in the compensation voltages. In the long-term, in-situ EMM monitoring and compensation is planned to be implemented in the clock sequence.

5. Sympathetic cooling and permutation control in dual-species linear crystals

The content of this chapter is currently being prepared for a separate publication.

This chapter addresses sympathetic cooling in linear dual-species crystals and consequently considerations for the crystal permutation and its control. The efficiency of sympathetic cooling depends on the coupling between the ions and thereby only on the aspect ratio $\alpha = \omega_{\mathrm{rad}}/\omega_{\mathrm{ax}}$ of the trapping potential. With regard to clock operation, also the absolute value of ω_{rad} becomes relevant, because many systematic shifts benefit from a high radial confinement. The trade-offs related to systematic shifts are described in Keller et al. [90].

Technical considerations favor low rf-drive frequencies Ω_{rf}. rf voltage induced heating in dielectrics and conductors scales with Ω_{rf} (compare Eq. 4.18) and at the same time the voltage U_{rf} required to reach a given radial confinement ω_{rad} increases with Ω_{rf} (see Eq. 2.9 and 2.12). Unfortunately, lower rf-drive frequencies Ω_{rf} result in a higher Mathieu q parameter for a certain radial confinement ω_{rad} (see Eq. 2.12), and a potentially lower crystal stability, as described in section 2.2. To explore a suitable range for the Mathieu q parameter of dual-species linear crystals, measurements on the q dependent stability of a $^{115}\mathrm{In}^+/^{172}\mathrm{Yb}^+$ crystal at two rf drive frequencies are presented in section 5.1. Based on this, the radial confinement for the following analysis of sympathetic cooling is chosen.

The efficiency of sympathetic cooling in dual-species crystals not only depends on the aspect ratio of the trapping potential, but especially on the mass ratio of the two species [88, 98, 193] and the exact arrangement of the ion string, the permutation. In section 5.2, the influence of the crystal composition and permutation are analyzed systematically. Furthermore, calculations of the cooling efficiency for the specific permutation of interleaved ion arrangements are presented. Those permutations can be reordered reliably as shown by experimental results, presented in section 5.3.

In section 5.4 all findings of this chapter are summarized in relation to each other and implications for the operation of a multi-ion clock are discussed.

5. Sympathetic cooling and permutation control in dual-species linear crystals

5.1. Stability of linear dual-species crystals: Mathieu q dependent crystal to cloud transition

Already in the 1980s, a phase transition from an ordered, stable ion crystal to a chaotic ion cloud was observed when increasing the rf voltage amplitude, i.e. the radial confinement as quantified by the Mathieu q [95] and analyzed empirically [194, 195]. Discussion about the existence of a well defined order-chaos transitions took place and they were studied in two-ion crystals, as summarized in Hoffnagle et al. [196]. It was found that the ion crystal undergoes a phase transition to an ion cloud when increasing the Mathieu q factor above a critical value q_c, where $q_c < q_M$, with q_M being the point where trapping becomes unstable. But already before this critical value is reached, there are perturbation-induced chaotic transients whose lifetimes depend on q. Possible reasons for melting are collision-induced disruptions of the ion crystal, non-adiabatic changes in the trap control parameters a and q [197] and noise-induced heating. Blümel et al. describe that the occurrence of the cloud to crystal transition depends not only on the control parameters a and q but also on the laser power and detuning [198]. For multi-ion crystals, the critical value q_c is smaller compared to its single-ion value, as was shown by the experimental and analytical investigation of the crystal to cloud transition of two and three Ba$^+$ ion crystals in Hoffnagel et al. [194]. There is a region in the a - q single-ion stability region in which two-ion crystals are unstable [199]. For a two-ion crystal, the boundaries can be calculated analytically, but for larger crystals, this becomes impossible and has not been done for dual-species crystals. Only recently Xu et al. report about controlled melting of a linear ^{174}Yb$^+$ 22-ion crystal which is heated locally with a blue-detuned beam which is focused on one ion at q=0.3 and on the stabilization of large ion crystals [200].

In the following, it is investigated at which radial frequencies a 5 In$^+$/5 Yb$^+$ ion cloud can get crystallized immediately after intentional heating which simulates the effect of collision-induced melting. Since q is inversely proportional to the mass m and proportional to the radial trap frequency ω_{rad} (see Eq. 2.14) the largest and most critical q values arise for the lighter species In$^+$. For this reason the stability of the crystal is plotted against the radial trap frequency ω_{rad} or the corresponding Mathieu q given for a single In$^+$ ion. The crystal is stored at an axial trap frequency of 137 kHz (for a single In$^+$ ion) and only cooled via Yb$^+$ Doppler cooling with the beams H1 and V (compare Fig. 3.6). The saturation parameter is fixed to $s_{\text{H1}} = 1.6$ in H1 and $s_{\text{V}} = 0.5$ in V for all measurements.

In an automatized routine, visualized in Fig. 5.1, the crystal is melted by blue detuning the Yb$^+$ Doppler cooling laser by $+\Gamma/5$ from resonance for 100 ms. Afterwards, the cooling laser is repeatedly ramped from -2.5Γ to -$\Gamma/2$ within 3 s and between each cooling ramp the status of the crystal is detected with the EMCCD camera. After successful recrystallization, the number of required cooling ramps is noted. This routine has been repeated ≈ 500 times for all data points and a mean number of required cooling ramps has been determined for radial trap frequencies $\omega_{rad}/2\pi$ between 850 kHz and 1500 kHz for rf-trap drive frequencies of 16.34 MHz and 21.79 MHz.

5.1. Stability of linear dual-species crystals: Mathieu q dependent crystal to cloud transition
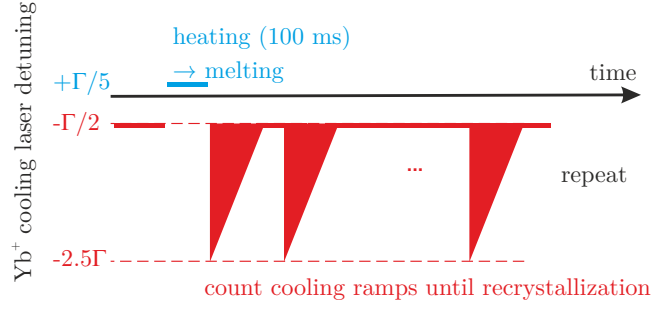
Figure 5.1.: *Routine to measure the stability of linear In^+/Yb^+ ion crystals. First the crystal is melted by blue detuning the Yb^+ Doppler cooling laser by $+\Gamma/5$ from resonance for 100 ms. Afterwards the cooling laser is repeatedly ramped from -2.5Γ to -$\Gamma/2$ within 3 s and between each cooling ramp the status of the crystal is detected and after successful recrystallization the number of required cooling ramps is noted.*

The result is presented in Fig. 5.2 (a). For the lower trap drive frequency, the number of required cooling ramps increases drastically at 1100 kHz and for the higher drive frequency this point is only reached at 1450 kHz. To exclude resonant heating at the mentioned frequencies, the routine was also tested at higher frequencies which are indicated with 0 needed cooling ramps in Fig. 5.2. Crystallization was not possible at all for these values.
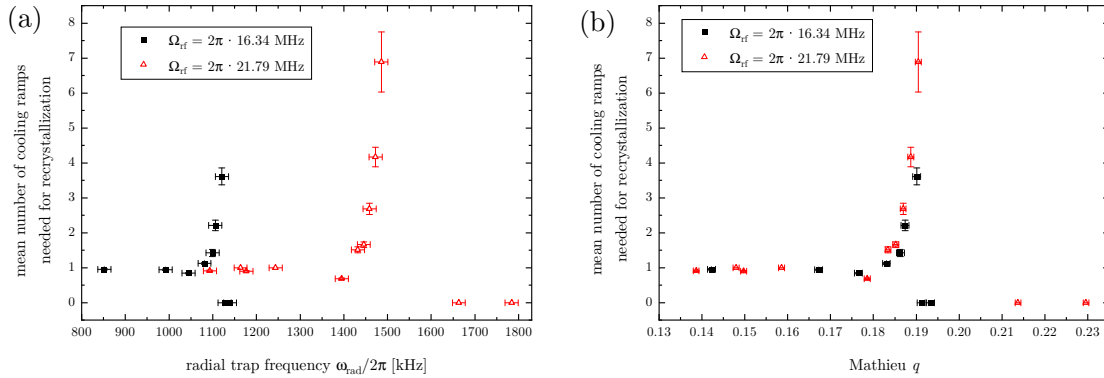
Figure 5.2.: *Mean number of low saturation cooling ramps on the Yb^+ ions needed for the recrystallization of a 5 In^+/5 Yb^+ ion cloud in dependence of the radial trap frequency $\omega_{rad}/2\pi$ (a) and the Mathieu q (b) for trap drive frequencies of 16.34 MHz and 21.79 MHz. The saturation parameter is fixed to $s_{H1} = 1.6$ and $s_V = 0.5$ for all measurements. To exclude that resonant heating leads to the increase in needed cooling ramps the measurement was repeated at the frequencies indicated with 0 needed cooling ramps, there no crystallization could be achieved.*

As Fig. 5.2 (b) shows, the instability occurs at $q \approx 0.19$ for both drive frequencies for the given cooling conditions. With this knowledge one can well estimate which rf-drive frequency is suitable for a given radial trap frequency. An increase of the power in the cooling beams

shifts the instability to higher frequencies. The effect is small, but clarifies that the observed $q \approx 0.19$ is smaller than the critical value for q_c at which only the cloud is stable. A likely reason for the failure of recrystallization is rf induced heating which is described and analyzed in detail by van Mourik et al [201]. In an ion cloud, energy from the rf-driven micromotion can be transferred to the secular motion. The heating rate of this process depends on the rf field strength and as soon as the heating rate is higher than the cooling rate, the ions will not crystallize.

In a sequence without continuous Doppler cooling, rf heating can heat up ion clouds to energies of several meV within a few ms and in order to recrystallize, Doppler cooling at a detuning $\delta \approx$ -6Γ and at least a coupling strength of 3Γ should be applied [201]. In many precision experiments, the ions are only cooled with a low saturation beam at a detuning of -$\Gamma/2$, in which case the radial confinement should be chosen a few ten kHz below the point where the crystal can not be recrystallized anymore.

5.2. Sympathetic cooling of dual-species linear crystals

The mass difference in dual-species crystals decouples motion of the two species to some degree, which reduces sympathetic cooling efficiency compared to the case of equal mass [98]. The mass-ratio dependence for the efficiency of sympathetic cooling in dual-species 2-ion crystals has been investigated in detail [88, 100, 111].

In the following, the influence of the ion numbers n_{cool} and n_{spec} of the cooling and spectroscopy species and the string permutation on the cooling efficiency is analyzed systematically. In section 2.3.1, the measure for sympathetic cooling efficiency via the value of C_α is described. Because the motional mode structure (see section 2.2.1), that depends on the masses of the involved species, is directly connected to C_α, an assumption for the masses of the cooling and spectroscopy ions m_{cool} and m_{spec} is required. The calculations are shown for a ratio of $m_{\mathrm{cool}}/m_{\mathrm{spec}} = 1.5$ between cooling and spectroscopy ion masses [as in, e.g., $m\left(^{172}\mathrm{Yb}^+\right)/m\left(^{115}\mathrm{In}^+\right)$ or $m\left(^{40}\mathrm{Ca}^+\right)/m\left(^{27}\mathrm{Al}^+\right)$]. The findings are not only valid for Doppler cooling, but also apply for electromagnetically-induced-transparency (EIT) cooling [202–204] and polarization-gradient cooling [205, 206]. Both techniques are so far used to cool long single-species ion strings and EIT cooling is also implemented for axial cooling of small dual-species chains.

Before the systematic study and favorable conditions for sympathetic cooling are presented in section 5.2.2, boundary conditions ensuring fair comparisons between different crystals are introduced in section 5.2.1. The calculations in section 5.2.3 focus on interleaved permutations, which can be produced reliably (as demonstrated in section 5.3 below).

5.2.1. Selection of parameters for comparisons between different crystals

Stronger axial confinement increases the coupling of ion motion in a linear chain and thus improves sympathetic cooling efficiency. This is accompanied by a reduction of the radial

mode frequencies, until, as the lowest frequency becomes zero, the phase transition to a two-dimensional crystal occurs (see, e.g., [207]). In practice, considerations like the radial mode Lamb-Dicke parameters or the second-order Doppler effect due to intrinsic micromotion are likely to favor a confinement aspect ratio with some distance to the phase transition [90]. Since the mode spectrum of a mixed-species crystal depends on its permutation, so does the optimal confinement aspect ratio under given constraints. To achieve comparable conditions, a fixed value for the lowest radial frequency is chosen and the axial confinement for each permutation is adjusted accordingly.

Figure 5.3.: *Mode spectrum and sympathetic cooling efficiencies of an interleaved crystal with 4 cooling and 10 spectroscopy ions. (a) axial and (b) radial mode frequencies and their cooling efficiencies C_α and time constants $t_{\mathrm{cool},\alpha}$. The inset in (a) shows the permutation, with spectroscopy (cooling) ions depicted as empty (solid) circles. The radial modes clearly separate into bands with predominant motion of an individual species, which is reflected in their cooling efficiency.*
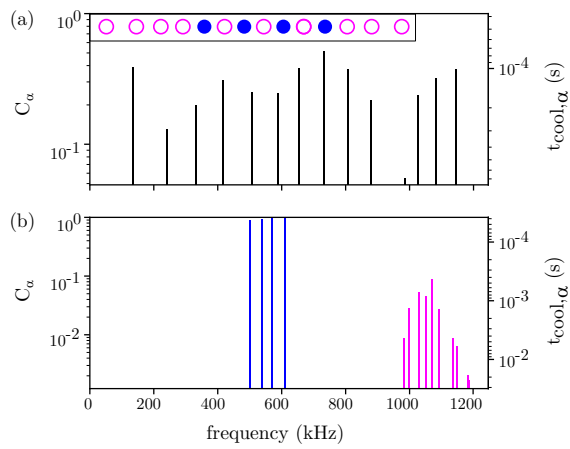
In the example in Fig. 5.3, a radial confinement corresponding to 800 kHz for a single cooling ion is assumed and the axial potential is adjusted to yield a lowest radial mode frequency of 500 kHz. Following this convention, Fig. 5.3 displays the frequencies of all axial (a) and radial (b) modes for the interleaved permutation of an $(n_{\mathrm{cool}}, n_{\mathrm{spec}}) = (4, 10)$ ion crystal and their values for C_α and $t_{\mathrm{cool},\alpha}$ (see section 2.3.1). The axial spectrum evenly covers a wide range, and, with one exception, shows relatively strong coupling between the species. The radial frequencies split up into two bands, with the motion of each dominated by one of the species. This is clearly reflected in the cooling efficiencies, which are close to 1 for modes associated with Yb^+ motion and significantly lower for those with high In^+ participation.

Figure 5.4 illustrates the distributions of C_α (and $t_{\mathrm{cool},\alpha}$) for all modes of all relevant permutations of the ion crystal of Fig. 5.3. Omitted are mirror images of already included permutations for clarity. The permutations are sorted by their lowest value C_α in descending order, i.e. from best to worst overall sympathetic cooling efficiency. While all permutations have some modes with C_α close to 1, the lowest efficiencies vary by almost four orders of magnitude across the set, emphasizing the relevance of the cooling ion positions. In the following, only the worst modes with the lowest values of C_α are analyzed, since they both limit the cooling efficiency of their permutation and have the highest spectroscopy ion participation.

5. Sympathetic cooling and permutation control in dual-species linear crystals
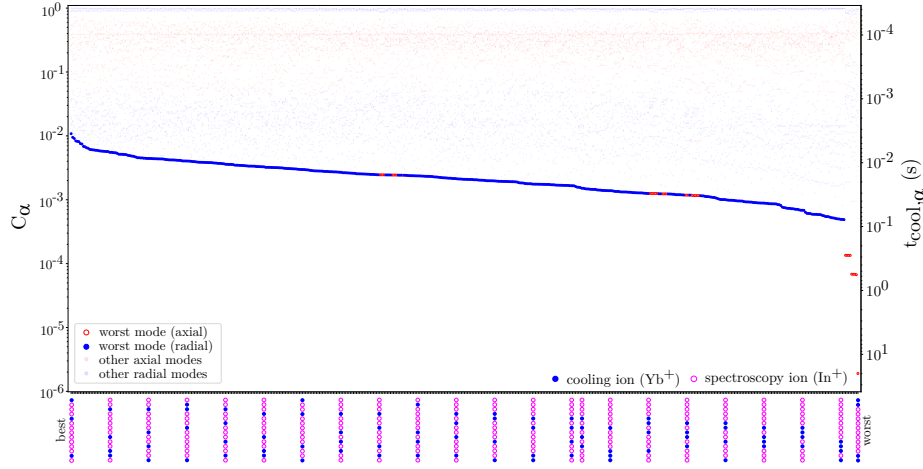
Figure 5.4.: *Cooling efficiency of all modes for all unique permutations of a crystal consisting of 4 cooling and 10 spectroscopy ions. The solid blue (empty red) circles represent radial (axial) modes. The permutations are sorted by their lowest values of C_α, which are indicated by larger symbols. The structure of the permutations is indicated on the x-axis.*

5.2.2. Influence of crystal composition and permutation

Using the above conventions, trends in sympathetic cooling efficiency in dependence on composition and permutation of a crystal are observed and guidelines for choosing suitable parameters are derived.

Figure 5.5 (a) shows the cooling efficiencies of crystals with a fixed ion number of $n_{\text{total}}=10$ and different ratios $n_{\text{cool}}/n_{\text{spec}}$. The horizontal scale is adjusted to cover the respective number of unique permutations for each composition. As intuitively expected, higher fractions of cooling ions improve cooling efficiency, but the results also reveal that their placement is crucial, i.e. fewer cooling ions in specific positions are preferable to random permutations with more cooling ions.

A similar analysis for a fixed ratio $n_{\text{cool}}/n_{\text{spec}}=1$ and a varying total number of ions n_{total} is shown in Fig. 5.5 (b) and reveals that higher total ion numbers n_{total} lead to an overall decrease in the cooling efficiency. In Fig. 5.5 (c), the number of spectroscopy ions n_{spec} is fixed to $n_{\text{spec}} = 5$ and different numbers of cooling ions n_{cool} are added, such that both the ratio $n_{\text{cool}}/n_{\text{spec}}$ and the total number of ions n_{total} are changing. Adding more cooling ions n_{cool} does not necessarily improve the cooling efficiency, but might only add modes which do not interact with the spectroscopy ions or even give rise to permutations with more decoupled motion of the species. For the permutations close to the optimum (on the left), the highest number of cooling ions is favorable, but a significant fraction of the non-optimal permutations with fewer cooling ions outperform those with the highest n_{cool}. Choosing the optimal composition thus requires a look at specific permutations.
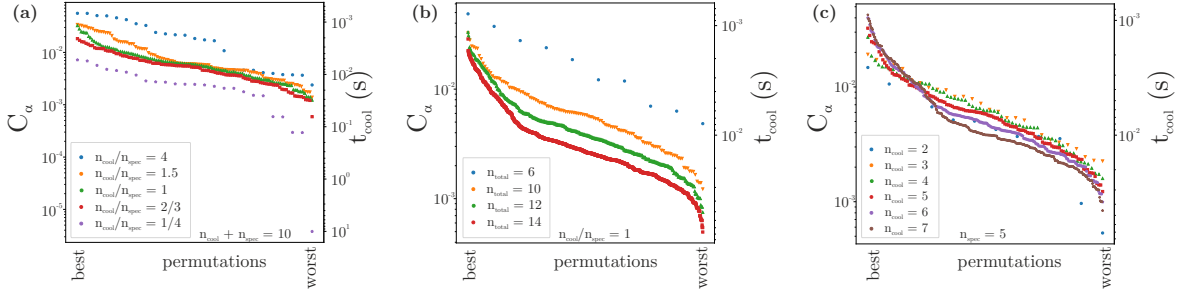
Figure 5.5.: *Sympathetic cooling efficiency dependence on crystal composition. (a) varied ratio of cooling to spectroscopy ions for a fixed total ion number of $n_{\mathrm{cool}} + n_{\mathrm{spec}} = 10$. (b) varied total ion number for a fixed ratio $n_{\mathrm{cool}}/n_{\mathrm{spec}} = 1$. (c) varied cooling ion number for a fixed amount of spectroscopy ions $n_{\mathrm{spec}} = 5$.*

Therefore the structure of more and less efficiently cooled permutations is investigated. As an example, Fig. 5.6 lists the six most and least efficiently cooled permutations of an $(n_{\mathrm{cool}}, n_{\mathrm{spec}}) = (4, 10)$ (a) and a $(5, 5)$ ion crystal (b). An asymmetric uniform distribution of the cooling ions over the crystal is advantageous for efficient cooling in both cases. For the larger crystal (a), the worst permutations are determined by axial modes and have the four cooling ions arranged at the edges of the chain. For the $(5, 5)$ crystal, the least efficiently cooled permutations are the ones where all cooling ions bunch in one half of the crystal and, in contrast to the larger crystal, the radial modes are responsible. Due to the higher total ion number and the lower fraction of cooling ions in crystal (a), its cooling efficiencies C_α (indicated next to the permutations) are significantly lower and span a wider range than those of crystal (b).
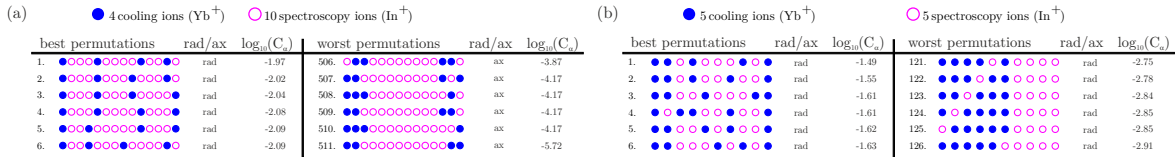
Figure 5.6.: *Ranking of crystal permutations by their lowest mode cooling efficiency. (a) crystal with 4 cooling and 10 spectroscopy ions. (b) 5 cooling and 5 spectroscopy ions. It is indicated whether the worst mode is a radial or an axial mode. Only the six best and worst ranked permutations are shown. The best permutations feature an asymmetric distribution of the cooling ions (blue) and spectroscopy ions (pink) across the whole chain. The worst permutations are in (a) the symmetric ones with cooling ions only at the edges of the crystal while for (b) all cooling ions are located in one half of the chain in case of the worst permutations.*

The two examples in Fig. 5.6 illustrate that the ratio between cooling and spectroscopy ions determines the responsible mode direction and structure of the badly cooled permuta-

tions. Investigating total ion numbers between four and fourteen, the following trends have been derived: For $n_{\mathrm{spec}} \leq n_{\mathrm{cool}}$, the badly cooled permutations are always dominated by a radial mode and the permutations show accumulation of all cooling ions on one side of the chain as shown in Fig. 5.6 b. In case of $n_{\mathrm{spec}} > n_{\mathrm{cool}}$, the worst permutations in terms of the radial modes feature the same one-sided accumulation of cooling ions as for $n_{\mathrm{spec}} \leq n_{\mathrm{cool}}$, but with increasing ratio $n_{\mathrm{spec}}/n_{\mathrm{cool}}$ more and more axial modes become even worse than the inefficiently cooled radial modes. The bad permutations dominated by axial modes show the in Fig. 5.6 (a) illustrated bunching of cooling ions at the edges of the chain and in case of an even n_{spec} the worst permutation features a mirror symmetric distribution of cooling ions.

Lin et al. [208] compare "edge cooling" with cooling ions only at the edges of the crystal and "periodic-node cooling" with a periodic arrangement of the cooling ions and conclude that the latter is more efficient. This agrees with the previous observations that the "edge cooling" permutations are in fact the worst possible choices and that a distribution of cooling ions across the entire crystal length is advantageous. However, care should be taken to avoid global symmetries, which can give rise to exceptionally badly cooled modes. The results presented here do not reproduce the increase in periodic-node cooling efficiency with chain length as described in Sosnova et al. [209]. Presumably, this is a consequence of different boundary conditions for the axial confinement: With an increased ion number in a fixed potential, cooling efficiencies benefit from the increase in coupling strength. Since in this work the potential is adjusted for equal coupling in each permutation, this effect is removed from the analysis and a trend towards better cooling efficiencies in shorter chains is revealed [cf. Fig. 5.5 (b)].

5.2.3. Influence of composition in interleaved arranged dual-species crystals

Now the analysis is restricted to the class of permutations with an interleaved order of species in the chain center, as these have the highest cooling efficiencies among those which can be reliably produced with the reordering techniques presented in section 5.3 below.

Only calculations of radial modes are presented, since the axial motion was well coupled for all considered crystals. Figure 5.7 (a) displays C_{α} for the worst mode of interleaved permutations with 1 to 30 spectroscopy ions and 1 to 20 cooling ions. As expected, the cooling efficiency decreases with increasing spectroscopy ion number n_{spec}. Branches with different power-law dependence can be identified. As Fig. 5.7 illustrates for the case of $n_{\mathrm{cool}} = 13$, each branch corresponds to a particular mode which appears when n_{spec} crosses a threshold. The lowest of these branches exists for $n_{\mathrm{spec}} \geq n_{\mathrm{cool}}$, where spectroscopy ions occupy positions at the edge of the chain and increasingly decouple from the cooled crystal center. The periodic drops in C_{α} for low n_{cool} are due to the higher likeliness of cooling ion positions coinciding with nodes of motion for odd crystal symmetries.

The same behavior can be observed in Fig 5.8, which shows C_{α} as a function of n_{cool}. Upward steps in cooling efficiency occur as cooling ions occupy positions further away from
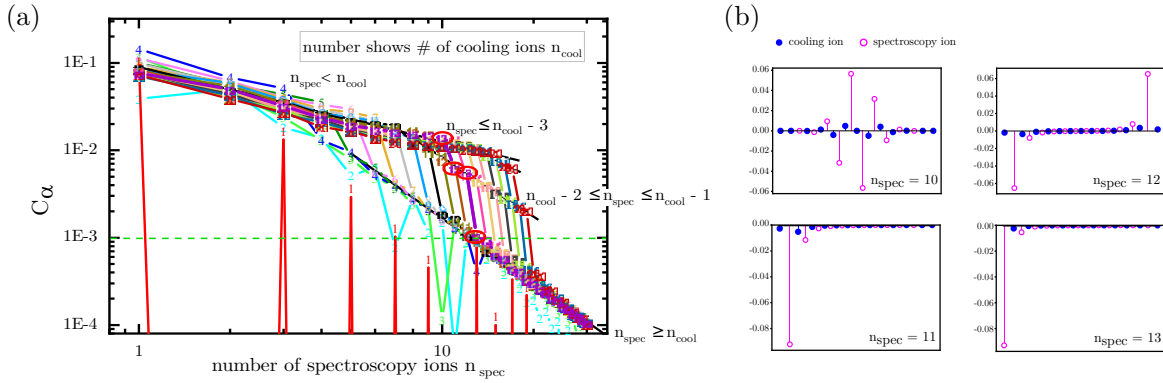
Figure 5.7.: *Cooling efficiency for worst modes of interleaved permutations as a function of spectroscopy ion number. (a) Cooling efficiency as a function of spectroscopy ion number. (b) Worst modes for a crystal with 13 cooling ions. The branches in (a) can be assigned to the occurrence of problematic modes as thresholds in spectroscopy ion number are crossed.*

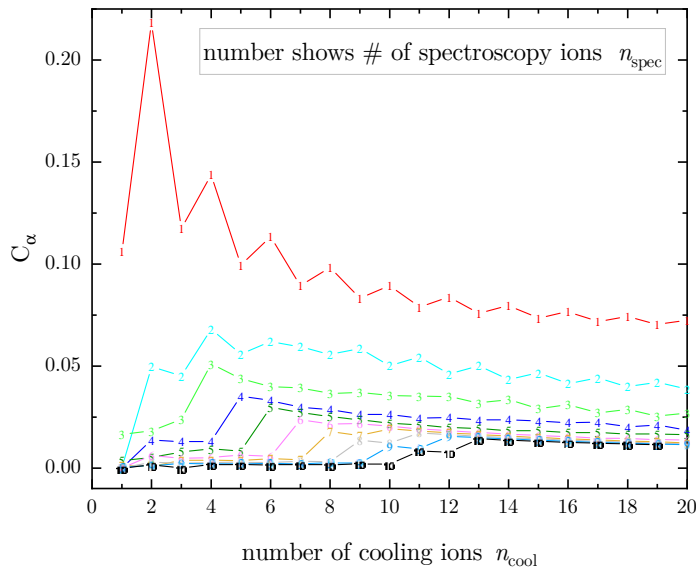the chain center, eliminating problematic motional modes. Beyond the last step, there is no benefit in adding additional cooling ions.

Figure 5.8.: *Cooling efficiency for worst modes of interleaved permutations as a function of cooling ion number.*

5.3. Reordering linear dual-species crystals

Reordering linear dual-species crystals to permutations with a high sympathetic cooling efficiency is crucial to avoid long cooling times, as presented in the previous section 5.2, and also ensures reproducible systematic shifts for precision spectroscopy. For small systems, stochastic reordering can be performed [193, 210]. With increasing ion number this approach becomes unfeasible and at the same time the need for reliable rearrangement becomes more important as the cross section for background gas collisions increases as well. One possibility is two-by-two reordering in micro-segmented ion traps [211]. A fast and simple approach is to make use of the mass-dependence of the total potential, which is also applicable in larger ion traps as used for (quantum) metrology, and is used in many experiments with up to 4 ions [211–213]. The routine used in this work, which is also applicable to larger ion crystals, is also based on the mass dependence of the trapping potential, with the additional application of an external electric field.

The methods presented here are restricted to traps with large ion-electrode distances used for precision spectroscopy and do not require differential forces on different crystal parts. While it is not possible to produce arbitrary permutations, very reproducible ones with acceptable cooling efficiencies can be obtained, as will be shown in the following. Three different types of dual-species ion arrangements have been generated: (I) an interleaved arrangement of the two species starting from the center, (II) permutations where the heavier (^{172}Yb$^+$) ions are in the center and (III) arrangements where the heavier ions are building pairs or triplets that alternate with single ions of the lighter species (^{115}In$^+$) in the center and have light ions at the edges. The three types are visualized in Fig. 5.9. The routine is explained in section 5.3.1 and an automatized study concerning the reliability of the reordering routine of In$^+$/Yb$^+$ crystals with 4 to 16 ions is presented in section 5.3.2.
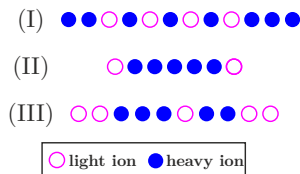
Figure 5.9.: *Types of dual-species ion arrangements: (I) - interleaved arrangement starting from the center, (II) - centered heavier ions and (III) - heavier ions build pairs or triplets that alternate with single ions of the lighter species and light ions at the edges.*

5.3.1. Routine

If both ion species are singly charged, the most straightforward property to make use of to rearrange the ions is the mass-dependence of the ponderomotive potential in the radial directions [214]. When lowering the radial confinement, the heavier species finds equilibrium positions away from the nodal line first, so that stable 2-dimensional zigzag crystals or even 3-dimensional crystals are formed. An additional DC-field in radial direction pushes the heavier ions further away from the nodal line. All these changes to the potential to achieve stable crystals in an intermediate stage are applied at the same time; afterwards the initial (default) trapping confinement is applied again and the ions slide to pre-determined positions

in the linear chain.
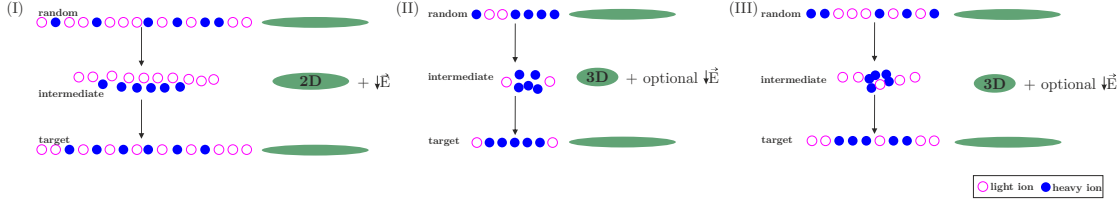
Figure 5.10.: *Scheme for reordering linear singly charged dual-species crystals. The lighter ions are shown as open pink circles while the heavier ions are represented by closed blue circles. The process for reordering starts for all three permutation types (I-III) in the linear phase, followed by an intermediate phase where the trap potential is changed such that 2- or 3D crystals are formed; in the end the linear target permutation is reached after the original potential is restored. Green ellipses illustrate the trap potential aspect ratios.*

Interleaved permutations with an alternating arrangement of the two ions species in the center of the chain (I) are achieved when the intermediate phase consists of two separate single-species chains. When applying the initial potential the heavier ions slide into the interstices between the lighter ions. Figure 5.10 (a) illustrates this process for 10 light and 6 heavy ions and the shape of the trap potential and the DC-field. Figure 5.11 shows a possible initial permutation, the intermediate stage and the final reordered crystal for 5 In$^+$ and 5 Yb$^+$ ions, recorded with the EMCCD camera.

Figure 5.11.: *Superimposed EMCCD images of both species illustrating the reordering process of 5 In$^+$/5 Yb$^+$ ions to an interleaved permutation. In$^+$ ions are colored in pink and Yb$^+$ ions in blue. The Yb$^+$ images are increased to the same magnification as the In$^+$ images and rotated by 1.2° to correct for the tilt in the imaging system. The exposure time is 200 ms.*
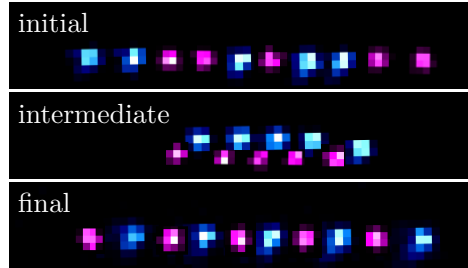
To access permutations where all heavy ions are in the center and all light ions on the edges (II), the ratio between the radial and axial secular frequency is smaller than for the interleaved permutations (compare green ellipses in Fig. 5.10), so the crystal is already in the 3-dimensional phase during the intermediate stage. The heavier ions preferentially occupy off-axis positions in the center of the crystal while the lighter ions stay on-axis positions at the edges as displayed in Fig. 5.10 (b). The axial squeezing has to be high enough that the radial displacement of the heavier ions is large enough that they can access this lowest energy configuration independent of the initial permutation. For larger crystals an additional DC-field is needed to allow all heavy ions to move to the center. When relaxing the radial confinement again, the heavy ions stay in the center. This method is used in several experiments with two-species linear ion crystals of up to 4 ions [212, 213] and a detailed description

5. Sympathetic cooling and permutation control in dual-species linear crystals

of the underlying physics can be found in [211].

Arrangements where the heavy ions build pairs or triplets that alternate with single light ions (III) are the result of the same trap potential change as for case (II), the difference is the larger number of light ions. In addition to the on-axis positions at the edges, the light ions also occupy positions in the center of the crystal that are close to the axis while the heavy ions arrange in 3D around as illustrated in Fig. 5.10 (c). With an additional DC-field in the intermediate stage, different final permutations can be obtained. For small ion numbers (≈ 5), these trapping parameters and a relatively large displacement lead to the interleaved configuration.

The parameters for a reproducible intermediate configuration are optimized by observing the crystal structure on the EMCCD camera. Afterwards the reliability of the reordering process is analyzed with an automated routine that takes 158 ms and is described in the following. Fine adjustment of the parameters, typically towards more stronger axial confinement and higher electric field values, is done by evaluating these automated measurements.

During the whole routine, the Yb$^+$ cooling laser beams H1 and V are switched on with a saturation parameter of $s_{H1} \approx s_V \approx 2$ and the In$^+$ ions are cooled sympathetically. The permutation of the crystal is detected with the EMCCD as described in section 3.2.3. The routine ensures an initial condition different from the target by conditional melting of the crystal using a blue detuned laser pulse. After each reordering attempt, the resulting permutation is determined.

The implementation of the reordering routine into the spectroscopy sequence is currently hardware limited to a minimum length of 158 ms. For this reason, the reliability tests of the routine for different compositions presented in the next section have been performed with this sequence length. With a hardware update, a sequence length of about 20 ms becomes possible, which is only limited by the resistance-capacitance filters on the trap which have a cutoff frequency of 113 Hz.

5.3.2. Reliability

The reordering routines have been repeated 200-1000 times for all compositions given in table 5.1. The study includes measurements at trap drive frequencies of 16.34 MHz and 21.79 MHz, but no influence of the drive frequency on the reliability has been found. The radial trap frequency f_{rad} in the decisive intermediate phase is about 610 kHz in most measurements, but for some compositions also higher or lower secular frequencies have been tested and reveal that only the aspect ratio of the trap $\alpha = \omega_{rad}/\omega_{ax}$ determines the reliability of the reordering. Table 5.1 lists the results and required parameters. The values for the displacement $d_{intermed}$ are deduced from theoretically calculated EMM slopes and the uncertainties result from a comparison of calculations and measurements, presented in section 4.2.5.

Table 5.1.: *Reliability of the reordering routine for linear In^+/Yb^+ crystals to the three different permutation types I (a), II (b) and III (c). For each tested crystal composition, the table lists the target permutation, the achieved success rate, the aspect ratio α between the radial and axial trap frequency $f_{\mathrm{rad,intermed}}/f_{\mathrm{ax,intermed}}$, the radial trap frequency $f_{\mathrm{rad,intermed}}$ and -if a DC-field is applied- the displacement d_{intermed}. The rf drive frequency is 16.34 MHz for the crystals marked with * and 21.79 MHz otherwise.*

Composition	Target permutation ○-In^+, ●-Yb^+	$f_{\mathrm{rad,intermed}}/$ $f_{\mathrm{ax,intermed}}$	$f_{\mathrm{rad,intermed}}$ (kHz)	d_{intermed} (μm)	Success rate in %
2 In^+ 2 Yb^+	○●○●	2.57	603 ± 5	9.6 ± 0.7	99^{+1}_{-6}
2 In^+ 3 Yb^+	●○●○●	2.57	603 ± 5	9.6 ± 0.7	97^{+3}_{-6}
2 In^+ 4 Yb^+	●○●○●●	2.55	576 ± 5	7.8 ± 0.6	96^{+4}_{-5}
2 In^+ 5 Yb^+	●●○●○●●	2.57	603 ± 5	6.1 ± 0.4	96^{+4}_{-5}
3 In^+ 5 Yb^+	●○●○●○●●	2.59	603 ± 5	7.7 ± 0.6	87 ± 6
4 In^+ 3 Yb^+	○●○●○●○	2.57	603 ± 5	7.7 ± 0.6	95 ± 5
4 In^+ 8 Yb^+	●●●○●○●○●○●●	4.61	437 ± 5	10.5 ± 0.8	92^{+8}_{-16}
5 In^+ 5 Yb^+	○●○●○●○●○●	3.10	607 ± 5	9.3 ± 0.7	95^{+5}_{-7}
7 In^+ 5 Yb^+	○○●○●○●○●○●○	3.10	607 ± 5	7.4 ± 0.5	97^{+3}_{-6}
8 In^+ 3 Yb^+ *	○○○●○●○●○○○	2.45	412 ± 5	7.4 ± 0.6	89 ± 4
8 In^+ 4 Yb^+	○○○●○●○●○●○○	3.21	556 ± 5	9.3 ± .7	93 ± 7
8 In^+ 6 Yb^+	○○●○●○●○●○●○●○	3.04	608 ± 5	7.7 ± 0.5	83 ± 5
9 In^+ 3 Yb^+ *	○○○○●○●○●○○○	2.45	412 ± 5	7.4 ± 0.6	91 ± 4
10 In^+ 4 Yb^+ *	○○○○●○●○●○●○○○	3.13	388 ± 5	11.8 ± 0.9	86 ± 4
10 In^+ 6 Yb^+ *	○○○●○●○●○●○●○●○○	3.13	388 ± 5	11.7 ± 0.9	72 ± 5

(a) *(I) Interleaved permutations (moderate axial squeezing + DC field)*

5. Sympathetic cooling and permutation control in dual-species linear crystals

Composition	Target permutation ○-In$^+$, ●-Yb$^+$	$f_{\mathrm{rad,intermed}}/f_{\mathrm{ax,intermed}}$	$f_{\mathrm{rad,intermed}}$ (kHz)	d_{intermed} (μm)	Success rate in %
2 In$^+$ 3 Yb$^+$	○●●●○	1.36	429 ± 5	-	99^{+1}_{-5}
2 In$^+$ 3 Yb$^+$ *	○●●●○	1.36	429 ± 5	-	93 ± 4
2 In$^+$ 5 Yb$^+$	○●●●●●○	1.35	422 ± 5	-	96^{+4}_{-6}
3 In$^+$ 2 Yb$^+$ *	○○●●○	1.36	429 ± 5	-	94^{+6}_{-14}
3 In$^+$ 3 Yb$^+$ *	○○●●●○	1.36	429 ± 5	-	93 ± 6
3 In$^+$ 5 Yb$^+$ *	○○●●●●●○	1.50	434 ± 5	6.6 ± 0.6	92 ± 4
4 In$^+$ 3 Yb$^+$	○○●●●○○	1.35	422 ± 5	2.9 ± 0.2	94 ± 6
4 In$^+$ 3 Yb$^+$ *	○○●●●○○	1.45	42 ± 5	7.0 ± 0.6	93 ± 4
4 In$^+$ 5 Yb$^+$ *	○○●●●●●○○	1.5	434 ± 5	6.6 ± 0.6	91 ± 6

(b) *(II) Permutations with all Yb$^+$ ions at center (high axial squeezing + DC field for larger crystals)*

Composition	Target permutation ○-In$^+$, ●-Yb$^+$	$f_{\mathrm{rad,intermed}}/f_{\mathrm{ax,intermed}}$	$f_{\mathrm{rad,intermed}}$ (kHz)	d_{intermed} (μm)	Success rate in %
4 In$^+$ 3 Yb$^+$	○○●○●●○	1.35	422 ± 5	-	96^{+4}_{-6}
5 In$^+$ 5 Yb$^+$	○○●●○●●●○○	1.90	458 ± 5	-	95 ± 3
5 In$^+$ 5 Yb$^+$ *	○○●○●●●○○	1.86	588 ± 5	-	90 ± 4
8 In$^+$ 6 Yb$^+$	○○○●○●●○●●○○	1.36	427 ± 5	-	60 ± 7
8 In$^+$ 6 Yb$^+$	○○○●●○●●●○●○○○	1.36	427 ± 5	-	22 ± 7
1 In$^+$ 3 Yb$^+$	●●○●	1.34	416 ± 5	18.9 ± 1.3	99^{+1}_{-6}
2 In$^+$ 3 Yb$^+$	●○●○●	1.37	419 ± 5	18.2 ± 1.5	96^{+4}_{-5}
4 In$^+$ 3 Yb$^+$	○○●●○●○	1.35	422 ± 5	6.7 ± 0.5	94 ± 6
5 In$^+$ 5 Yb$^+$ *	○○●●○●●○●○	1.86	375 ± 5	12.1 ± 1.0	64 ± 4
5 In$^+$ 5 Yb$^+$ *	○○●○●●○●●○	1.86	375 ± 5	12.1 ± 1.0	17 ± 4

(c) *(III) Permutations with Yb$^+$ ion pairs or triplets alternating with single In$^+$ ions and In$^+$ ions at the edges (high axial squeezing + DC field to achieve different permutations)*

The success rates for reordering to interleaved permutations (I) reach from $99\,^{+1}_{-6}\,\%$ for 4 ions to $72 \pm 5\%$ for 16 ions as presented in Table 5.2a. Larger crystals are more likely to end up in a permutation which differs slightly from the target permutation. But even with a reliability of only $72\,\%$, two reordering attempts guarantee the target permutation with a probability of more than $90\,\%$.

Permutation (II) could only be reached reproducibly for compositions with a maximum ion number $N \leq 9$ and a relatively small proportion of In^+ ions such that they occupy only the on-axis positions at the edges of the 3D-crystal in the intermediate phase, as explained in section 5.3.1. For ion numbers $N > 6$, squeezing the trap potential in axial direction alone is not enough to reliably push all Yb^+ ions to the center, but with an additional DC-field (radial displacement d) the high success rates around $95\,\%$ can be extended up to $4\,In^+/5\,Yb^+$ ions, as shown in table 5.2b (II). Additional In^+ ions occupy positions in the center of the intermediate crystal and thus lead to final permutations of type (III) as listed in table 5.2c. For the permutations where the Yb^+ ions build pairs or triplets that alternate with single In^+ ions in the center and have In^+ ions at the edges of the crystal (III), the reliabilities are presented in table 5.2c. Reliabilities around $95\,\%$ are obtained for $4\,In^+/3\,Yb^+$ ions as well as for $5\,In^+/5\,Yb^+$ ions. It can be seen that a small change in the displacement can lead to a different reliable permutation. Taking the example of $4\,In^+/3\,Yb^+$ ions: no displacement leads to a different position of the Yb^+ pair within the permutation than a displacement of $6.7\,\mu m$. A displacement of $2.9\,\mu m$ and maintaining all trap frequencies the same as before reliably produces a permutation with all Yb^+ ions in the center as listed in Table 5.2b. The arrangement of the ions in the intermediate phase is almost identical for these three different displacements, so it becomes less predictable from the intermediate phase which permutation will be achieved. For the compositions with $5\,In^+/5\,Yb^+$ ions and also with $8\,In^+/6\,Yb^+$ ions, instead of a single permutation two almost identical permutations occur for the same parameters: one with around 60% the other with around $20\,\%$ reliability. Due to their similarities, their cooling times will be comparable such that they could be considered for reliable reordering since their success rates add up to more than $80\,\%$.

5.4. Implications for multi-ion clocks

In this section, the results of section 5.1-5.3 are set in relation to each other and their impact on the operation of a multi-ion clock are discussed.

As mentioned in section 5.1, many systematic shifts benefit from a high radial confinement [90] and technical considerations favor low rf-drive frequencies. In view of the results on the rf-drive frequency dependent stability of a $5\,In^+/5\,Yb^+$ ion crystal, this frequency has to be chosen according to the targeted radial confinement such that $q < 0.19$. If operation at a higher Mathieu q is required, a Doppler cooling beam with a detuning $\delta \approx$ -6Γ and at least a coupling strength of 3Γ should be implemented [201], but this is no favorable regime for reliable high-accuracy clock operation.

5. Sympathetic cooling and permutation control in dual-species linear crystals

For low instabilities of optical clocks, a short cooling time is crucial to enable a duty cycle dominated by clock interrogation. The cooling efficiency ($\propto C_\alpha$) of the worst mode can vary over several orders of magnitude between the different permutations of a linear dual-species crystal. The influence of the permutation on motional shifts at a given temperature is comparatively low as analyzed in [215], thus the choice of the ion permutation for a multi-ion clock should predominantly be based on the cooling efficiency. Only ion permutations that can be reliably restored are applicable, because background gas collisions will require reordering. Traps with large ion-electrode distances, as typically used for precision spectroscopy which are lacking the possibility to apply differential forces on different crystal parts, do not allow to reorder arbitrary crystal permutations, e.g. the best cooled permutations with cooling ions asymmetrically uniformly distributed across the chain. But three permutation types can be reliably produced, depending on the crystal composition. In order to evaluate the different types with regard to their cooling efficiency Fig. 5.12 (a) displays C_α for the worst mode of all possible permutations of a linear 5 In^+/5 Yb^+ ion crystal and highlights the different types of produced permutations.
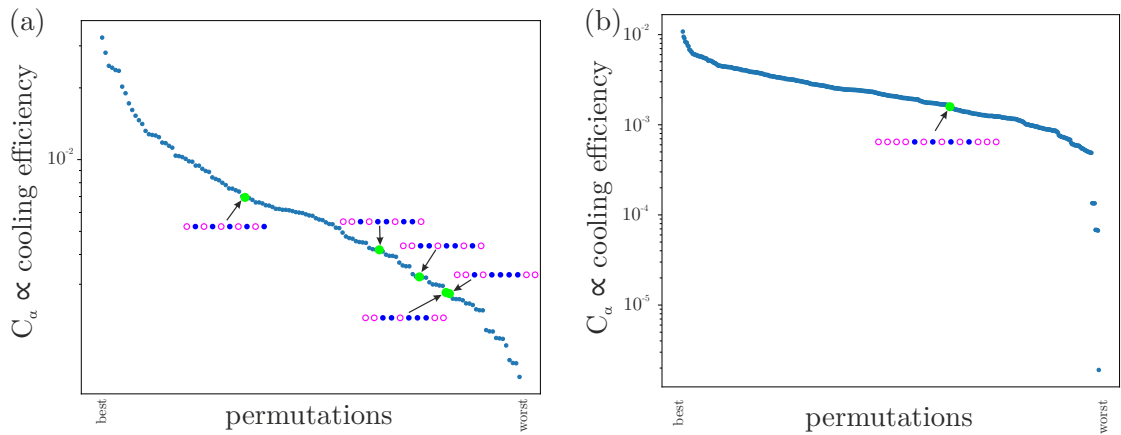
Figure 5.12.: *Cooling efficiency of the worst mode for all possible permutations of a 5 In^+/5 Yb^+ (a) and 10 In^+/4 Yb^+ (b) ion Coulomb crystal. The highlighted green permutations indicate the permutations that can deterministically be generated. The interleaved permutation has the highest cooling efficiency among those.*

By far the best experimentally realizable permutation is the interleaved one (type (I) in section 5.3), which can be achieved with a reliability of 95 %. Next come the permutations with Yb^+ ion pairs alternating with single In^+ ions (type (III)) followed by those where almost all heavy Yb^+ ions are in the center (type (II)). This assessment also applies to the other tested compositions. Fortunately, the interleaved permutation, in contrast to for example the permutation with all heavy ions in the center, can be reliably restored for all tested compositions and there is no obvious reason why this should not be achieved for even higher ion numbers. The reliability is above 90 % for up to 12 ions and degrades to about 72 % for 16 ions, but even this results in a probability of 90 % that at least one out of two reordering attempts is successful. Nonetheless, the relative rank of the interleaved permutation shifts

toward the worst-cooled permutation as the total ion number increases, as Fig. 5.12 (b) illustrates for a crystal with 10 In$^+$ and 4 Yb$^+$ ions. Still, comparing the cooling efficiency of the worst mode of the best permutation with the interleaved permutation, the latter is not even an order of magnitude worse, while the spread over all permutations is several orders of magnitude. In summary, the interleaved permutation type is a good choice for operating a dual-species multi-ion clock that is based on sympathetic cooling.

The optimum number of cooling ions n_{cool} for the interleaved permutation depends on the number of spectroscopy ions n_{spec}. For $n_{\mathrm{spec}} \leq 7$, the optimum is a cooling ion number $n_{\mathrm{cool}} = n_{\mathrm{spec}} + 1$. For $n_{\mathrm{spec}} > 7$, the optimum is $n_{\mathrm{cool}} = n_{\mathrm{spec}} + 3$. Adding more cooling ions decreases the cooling efficiency and would also increase the collision rate, which would then also increase the rate at which reordering is needed.

The current trap DC supply hardware limits the implementation of the reordering sequence into the spectroscopy sequence to a minimum length of 158 ms. With a hardware update, a sequence length that is only limited by the resistance-capacitance filters on the trap becomes possible. The cutoff frequency is 113 Hz, resulting in a technically possible sequence length around 20 ms. The effect of a reduced sequence length on the reliability still needs to be investigated. 158 ms are relatively long compared to the clock spectroscopy sequence with a duration around 260 ms (see section 6.2.1). The required reordering frequency, given by the respective collision rate $\bar{\Gamma}_{\mathrm{swap,ion}} = (0.0029 \pm 0.0003)\,\mathrm{s}^{-1}\mathrm{ion}^{-1}$, allows an estimation of the influence of reordering on the duty cycle of clock spectroscopy. For a 10-ion crystal the reordering increases the average sequence length by about 0.5 % to around 261.1 ms. Thus, the instability of a multi-ion clock would benefit significantly more from a reduction in cooling or detection time than from a shortened reordering sequence. Of course the effect of reordering can be different in other setups, as it depends on the background gas pressure in each experimental apparatus.

In principle, one could also consider to reorder the crystal only if the present permutation has a longer cooling time than the interleaved permutation. This has the drawback of regularly changing systematic uncertainties, even though the differences are marginal. Since reordering increases the average clock cycle by only 0.5 %, the conservative approach in terms of systematic shifts should be chosen and reordering should always be used to ensure constant conditions.

The narrow $^1S_0 \leftrightarrow\ ^3P_1$ intercombination line of the clock ion In$^+$ allows not only direct state detection but also the implementation of a second cooling stage. With this, temperatures $< 100\,\mu\mathrm{K}$ regime are reachable [89]. For other clock species which lack the possibility of direct cooling, more efficient sympathetic cooling in an ion string could potentially be realized by mode-mode coupling via the application of a parametric drive. Gorman et al. demonstrate this approach for a single ion by coupling to a mode that lacks optical access and briefly discuss its suitability for ion strings [216]. Parametric coupling is also applicable for larger frequency differences, as present in dual-species crystals, which is not the case for electromagnetically induced transparency cooling (EIT) which can only address modes within a certain bandwidth and has been used for cooling low number ion strings [202–204,

5. Sympathetic cooling and permutation control in dual-species linear crystals

217].

Based on the discussed findings, spectroscopy of In^+/Yb^+ crystals (presented in section 6) is performed at an rf-drive frequency of 21.73 MHz and radial trap frequencies of about 800 kHz (for a single Yb^+ ion) and an axial confinement which leads to the lowest radial frequency being at 500 kHz for the dual-species crystal. The orientation of the radial trap axes is chosen such that the In^+ spectroscopy laser has projections on both radial trap axes in order to derive bounds for the maximal temperature along both axes.

6. Spectroscopy of the ^{1}S$_0$ ↔ ^{3}P$_1$ and ^{1}S$_0$ ↔ ^{3}P$_0$ transition of ^{115}In$^+$ ions

This chapter describes the spectroscopy of a single In$^+$ ion which is sympathetically cooled with at least one Yb$^+$ ion as well as the spectroscopy of In$^+$/Yb$^+$ crystals with up to 12 ions. This includes results on two transitions in In$^+$. The ^{115}In$^+$ term scheme including the fine structure splitting is illustrated in the lower right bottom of Fig. 6.1. In the context of this work, the $5s^2$ ^{1}S$_0$ ↔ $5s5p$ ^{3}P$_1$ transition at 230.6 nm and the $5s^2$ ^{1}S$_0$ ↔ $5s5p$ ^{3}P$_0$ transition at 236.5 nm are used, for which Fig. 6.1 also shows the hyperfine structure splitting and indicates the used Zeeman transitions.

Figure 6.1.: _^{115}In$^+$ term scheme including the fine structure splitting (box in the lower right corner). For this work relevant are the transitions $5s^2$ ^{1}S$_0$ ↔ $5s5p$ ^{3}P$_1$ at 230.6 nm and $5s^2$ ^{1}S$_0$ ↔ $5s5p$ ^{3}P$_0$ at 236.5 nm for which the hyperfine structure splitting is shown and the used Zeeman components are indicated. The values given in brackets are the first-order Zeeman shifts per m_F._
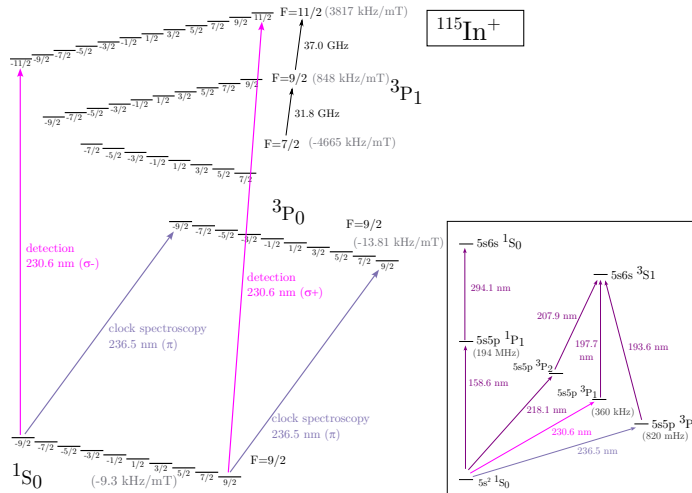
In section 6.1, the influence of sympathetic cooling in spectroscopy of the $5s^2$ ^{1}S$_0$ ↔ $5s5p$ ^{3}P$_1$ intercombination line of a single In$^+$ ion sympathetically cooled with one Yb$^+$ is studied and a frequency measurement versus the H-maser at PTB is presented. The experimental sequence employed for spectroscopy of the narrow $5s^2$ ^{1}S$_0$ ↔ $5p$ ^{3}P$_0$ line is explained in section 6.2.1. Section 6.2.2 contains frequency scans of the clock transition and the optimization of sympathetic cooling via the observation of Rabi oscillations for a single In$^+$ ion which is either cooled with one or three Yb$^+$ ions. The first evaluation of an In$^+$/Yb$^+$ optical clock is presented in section 6.2.3. Finally, the spectroscopy is extended to larger mixed crystals in section 6.2.4 and first results on the instability for the use of multiple In$^+$ ions are presented in section 6.2.5.

6. Spectroscopy of the $^1\mathrm{S}_0 \leftrightarrow ^3\mathrm{P}_1$ and $^1\mathrm{S}_0 \leftrightarrow ^3\mathrm{P}_0$ transition of $^{115}\mathrm{In}^+$ ions

6.1. $^1\mathrm{S}_0 \leftrightarrow ^3\mathrm{P}_1$ intercombination line

6.1.1. First observation and influence of sympathetic cooling

For the initial search of the $^1\mathrm{S}_0$ ($F = 9/2$) $\leftrightarrow ^3\mathrm{P}_1$ ($F = 11/2$) transition, three In$^+$ ions and one Yb$^+$ ion have been trapped at $\omega_{\mathrm{rad},1}/2\pi \approx 785\,\mathrm{kHz}$, $\omega_{\mathrm{rad},2}/2\pi \approx 815\,\mathrm{kHz}$ and $\omega_{\mathrm{ax}}/2\pi \approx 116\,\mathrm{kHz}$ (In$^+$ COM mode frequencies) and approximately equal projection of both radial trap axes on the y-direction. A magnetic field of $0.03\,\mathrm{mT}$ has been applied along the z-direction to ensure that all Zeeman components overlap within the saturation-broadened linewidth and no population is trapped in substates with off-resonant transitions. The $230.6\,\mathrm{nm}$ beam, propagating along the z-direction as well, as shown in Fig. 3.6, has been overlapped with a temporary axial $370\,\mathrm{nm}$ beam for alignment via Yb$^+$ fluorescence. A power of $\approx 6\,\mu\mathrm{W}$, which is equivalent to a saturation parameter $s \approx 10$, has been used for the $230.6\,\mathrm{nm}$ beam. The Yb$^+$ ion has been cooled with the $370\,\mathrm{nm}$ beam H1 at a power of $7\,\mu\mathrm{W}$ ($s_{\mathrm{H1}} = 1$).

The dipole transition $^2\mathrm{S}_{1/2} \leftrightarrow ^2\mathrm{P}_{1/2}$ in Yb$^+$ at $370\,\mathrm{nm}$, used for Doppler cooling, has a linewidth $\Gamma_{\mathrm{Yb}} = 2\pi \times 19.6\,\mathrm{MHz}$ [163]. With $\Gamma_{\mathrm{Yb}} \gg \omega_{\mathrm{sec}}$, the transition is in the so called weak binding regime and the Doppler temperature $T_{\mathrm{D}} = 0.47\,\mathrm{mK}$. The $^1\mathrm{S}_0 \leftrightarrow ^3\mathrm{P}_1$ line in $^{115}\mathrm{In}^+$ has a linewidth $\Gamma_{\mathrm{In}} = 2\pi \times 360\,\mathrm{kHz}$, which is interesting because it corresponds to neither of the two typical regimes of resolved sideband cooling (strong binding regime) and Doppler cooling (weak binding regime) (see section 2.3) for our trapping parameters, where in the axial direction $\Gamma_{\mathrm{In}} \approx \omega_{\mathrm{sec}}$ and for the radial direction ω_{sec} is only slightly higher than Γ_{In}. For a single In$^+$ ion, a temperature below $100\,\mu\mathrm{K}$ has been demonstrated [89]. If both lasers interact with In$^+$/Yb$^+$ crystals, interesting cooling dynamics can be observed which highly depend on the saturation parameters of both lasers and manifest in the observed lineshapes via the corresponding Doppler shifts. In thermal equilibrium, the ions feature a Maxwell-Boltzmann velocity distribution and the spectral line resembles a Gaussian line profile with the FWHM ω_G [218]:

$$\omega_G = \frac{\omega_0}{c}\sqrt{\frac{8k_B T \ln 2}{m}} \tag{6.1}$$

with the transition frequency ω_0. The Doppler temperature of Yb$^+$ $T_{\mathrm{D}} = 0.47\,\mathrm{mK}$ leads to a line broadening of $\omega_G = 2\pi \times 1.94\,\mathrm{MHz}$ on the In$^+$ transition at $230.6\,\mathrm{nm}$ which is 5 times larger than the natural linewidth. Correspondingly, a low saturation in the Yb$^+$ cooling beam is crucial to reach a low temperature of both ions to keep the temperature associated broadening of the $^1\mathrm{S}_0 \leftrightarrow ^3\mathrm{P}_1$ transition low. For the first observation the In$^+$ fluorescence has been sent to the PMT to be less sensitive on the focus position of the detection system. The $922\,\mathrm{nm}$ laser has been sent to a frequency comb that allows the conversion to the absolute frequency via a H-maser that is referenced to primary Cs clocks and UTC(PTB). The frequency of the $230.6\,\mathrm{nm}$ beam is scanned with a double pass AOM before the frequency is quadrupled. The scan range around the literature value [219] has been $\pm 4\,\mathrm{MHz}$ in the UV. For the further optimizations of the beam alignment, the polarization of the beam and the sympathetic cooling a 1 In$^+$/1 Yb$^+$ crystal has been used.

The Yb$^+$ Doppler cooling parameters influence the ^{1}S$_0 \leftrightarrow\ ^3$P$_1$ intercombination line in In$^+$, which is analyzed systematically in the following for one ^{115}In$^+$ ion, sympathetically cooled with one ^{172}Yb$^+$ ion.

The 230.6 nm beam to drive the ^{1}S$_0 \leftrightarrow\ ^3$P$_1$ transition is always propagating along the trap axis (z-direction), in parallel with the magnetic field. To drive the ^{2}S$_{1/2} \leftrightarrow\ ^2P_{1/2}$ transition in Yb$^+$ at 370 nm, either the horizontal beam H1 only or the V beam with a highly attenuated H1 beam is used (compare Fig. 3.6) at a detuning of -$\Gamma_{\text{Yb}}/2$. The In$^+$ fluorescence is collected on the PMT.

Figure 6.2 shows frequency scans across the two stretched states with a saturation parameter $s_{230} = 2$ while continuously cooling the Yb$^+$ ion with H1 at $s_{\text{H1}} = 0.4$. The two-ion crystal is confined at $\omega_{\text{rad},1}/2\pi \approx 875$ kHz, $\omega_{\text{rad},2}/2\pi \approx 897$ kHz and $\omega_{\text{ax}}/2\pi \approx 135$ kHz (In$^+$ COM mode frequencies) and approximately equal projection of both radial trap axes on the y-direction. The polarization has been controlled with an EOM which enable fast polarization switching between $\sigma+$ and $\sigma-$ for the clock cycle. The typical line shape of the cooling transition of a bound particle is a Lorentzian on the red side of the resonance with an abrupt breakdown of the signal at resonance because the ion is heated and not crystallized at the blue side of the resonance. Here the red side of both stretched states features the typical Lorentzian line shape, but the signal continues after the resonance because the In$^+$ ion is sympathetically cooled by the Yb$^+$ ion. Presumably, one sees different temperature regimes in which heating and cooling effects on the two species produce different equilibria, respectively. The intensity of the Yb$^+$ cooling beam has a high impact on the line shape of the ^{1}S$_0 \leftrightarrow\ ^3$P$_1$ transition. In Fig. 6.3 (a), scans across the $m_F = +9/2 \rightarrow +11/2$ ($\sigma+$) at $s_{230} = 2$ with varied saturation parameter s_{H1} of the Yb$^+$ cooling beam H1 are compared.

Figure 6.2.: *Frequency scans of the two stretched states of the $^1S_0 \leftrightarrow\ ^3P_1$ transition in $^{115}In^+$. The recorded PMT signal shows the frequency dependent fluorescence of a single In$^+$ ion interacting with the axial 230.6 nm beam at $s_{230} = 2$ that is sympathetically cooled with one Yb$^+$ ion in parallel via the horizontal cooling beam H1 at $s_{H1} = 0.4$ and a detuning -$\Gamma_{\text{Yb}}/2$.*
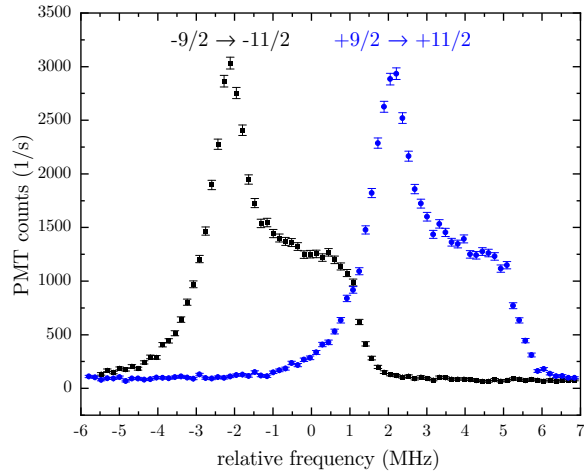
With increasing s_{H1}, the linewidth increases and the fluorescence at resonance reduces. At high saturation parameter in H1 s_{H1} the temperature of the crystal is dominated by the photon scattering of the Yb$^+$ ion and the lineshape is more symmetric to the resonance across a larger range because the heating on In$^+$ is low compared to the cooling on Yb$^+$. But the

generally larger temperature due to the higher saturation parameter s_{H1} leads to a significant broadening of the $^1S_0 \leftrightarrow {}^3P_1$ signal. If, instead of a two-ion crystal, 2 In$^+$ ions and 1 Yb$^+$ ion are used, the scans only show the described shape if the Yb$^+$ ion is occupying one of the outer positions in the linear chain. If it is located in the center, the In$^+$ fluorescence drops to the background level immediately after crossing the resonance because there is an axial mode in which the Yb$^+$ ion is not moving but the In$^+$ ions do thus they are not cooled via the Yb$^+$ ion.

Figure 6.3 (b) illustrates scans across the $m_F = +9/2 \rightarrow +11/2$ at $s_{230} = 2$ with varied saturation parameter s_V of the Yb$^+$ cooling beam V and a highly attenuated H1 beam. For these scans, the confinement is changed such that the strong radial trap axis is aligned almost parallel to the y-direction, the respective trap frequencies are $\omega_{rad,1}/2\pi \approx 838$ kHz, $\omega_{rad,2}/2\pi \approx 927$ kHz and $\omega_{ax}/2\pi \approx 1471$ kHz (In$^+$ COM mode frequencies). In this case, the signal breaks off at resonance because the V beam has no projection on the axis of the 230-6 nm beam and thus cannot prevent axial heating caused by the interaction of the In$^+$ ion with the blue detuned laser. The signal height reduces to similar values as for cooling with the H1 beam at similar intensity because the emission is isotropic.
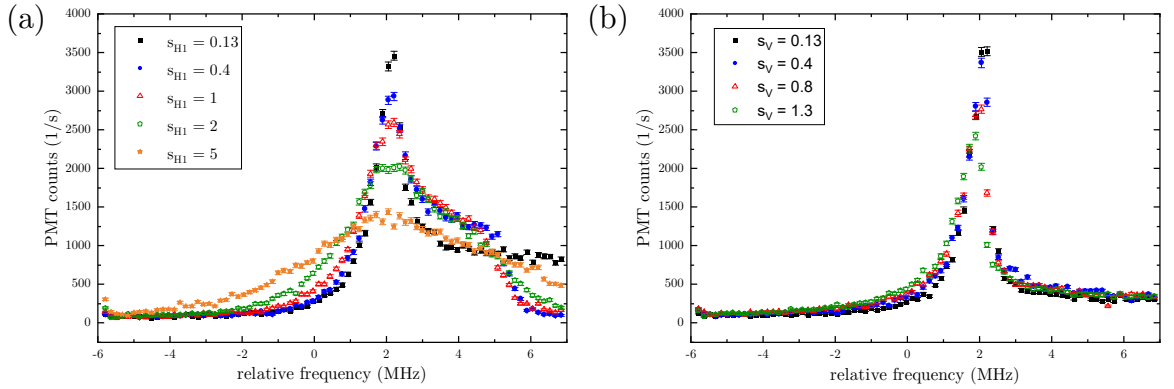
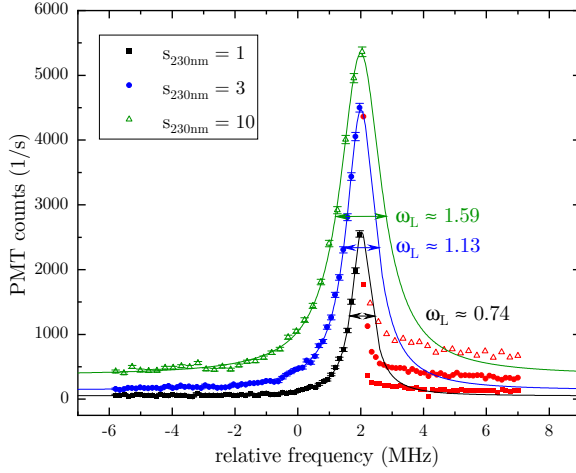**Figure 6.3.:** *Frequency scans of the $m_F = +9/2 \rightarrow +11/2$ ($\sigma+$) $^1S_0 \leftrightarrow {}^3P_1$ transition with the axial 230.6 nm beam at $s_{230} = 2$. (a) Variation of the saturation parameter s_{H1} of the Yb$^+$ cooling beam H1. (b) Variation of the saturation parameter s_V of the Yb$^+$ cooling beam V.*

If the 230.6 nm and the 370 nm laser are not applied at the same time but alternating, the influence of the Yb$^+$ cooling laser reduces drastically. In Fig. 6.4 (a), the $m_F = -9/2 \rightarrow -11/2$ transition at $s_{230} = 6$ with varied saturation parameter s_{H1} of the Yb$^+$ cooling beam H1 is shown. Both lasers have been applied for a pulse length $t_{pulse} = 0.5$ s each. With the alternating application of the pulses, the intensity of the 370 nm cooling beam (H1) has no noticeable influence on the line shape of the $^1S_0 \leftrightarrow {}^3P_1$ transition. The temperature during the 230.6 nm pulse seems to be dominated by the 230.6 nm laser. In Fig. 6.4 (b), the influence of the pulse length t_{pulse} is analyzed, where the t_{pulse} is identical for both lasers and has been varied between 10 ms and 500 ms. The number of repetitions has been adjusted such that an integration time of 1 s has been reached for all scans. Indeed the pulse length has an
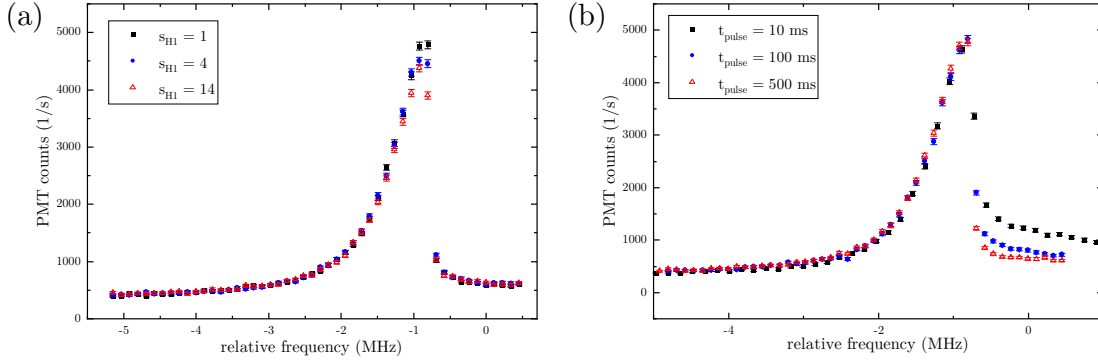
Figure 6.4.: *Frequency scans of the $m_F = -9/2 \rightarrow -11/2$ (σ-) $^1S_0 \leftrightarrow {}^3P_1$ transition with the axial 230.6 nm beam at $s_{230} = 6$ with alternating application oft the 230.6 nm and 370 nm lasers. (a) Variation of the saturation parameter s_{H1} of the Yb$^+$ cooling beam H1. The pulse length t_{pulse} for the application of each laser is 500 ms. (b) Variation of the pulse length t_{pulse}. The intensity of the 370 nm cooling beam is fixed at $s_{H1} = 1$.*

influence on the line shape, not so much on the red detuned side of the resonance but for short pulses the fluorescence stays on a plateau after the resonance while for 500 ms pulses it immediately drops to the background level. While the 500 ms pulses seem to be enough to get into the equilibrium of the temperature determined by the In$^+$ ion, the short pulses seem to be too short, so that the In$^+$ ion is not yet completely heated.

In Fig. 6.5, the $m_F = +9/2 \rightarrow +11/2$ transition for saturation parameters s_{230} between 1 and 10 and a fixed saturation parameter $s_V = 0.4$ of the Yb$^+$ cooling beam and a highly attenuated H1 beam is shown. The two lasers have been applied in an alternating sequence, each for a pulse length $t_{\text{pulse}} = 0.5$ s. The data on the red detuned side of the resonance has been fitted with a Lorentzian function and shows an increase of the FWHM ω_L scaling with $\sqrt{s_{230} + 1}$. At a saturation parameter $s_{230} = 1$, $\omega_L > \sqrt{2}\,\Gamma_{\text{In}}$, indicating that a Lorentzian function is not the correct model to describe the lineshape. Presumably the temperature changes over the scan and thus changes the line shape. The line centers agree within their uncertainties. Furthermore, Fig. 6.5 demonstrates the high signal-to-noise ratio for the detection of In$^+$. At saturation a count rate of 7000 c/s is achieved for a single In$^+$ ion.

Frequency scans with parallel interrogation of both lasers at adapted parameters would allow to reduce the uncertainty of the temperature and resulting second-order Doppler shift for the frequency comparisons of the clock transition frequency, presented in section 6.2. Its contribution is currently the largest for the total uncertainty budget. Therefore, the temperature of the crystal has to be determined by the Yb$^+$ scattering rate. At low secular frequencies and under consideration of the Lamb-Dicke factors the scans can be treated conceptually similar to the determination of the transition frequency outside the strong-binding regime presented in [220]. The lowest achievable temperature is $T_D = 0.47$ mK which leads to a line broadening of $\omega_G = 1.94$ MHz on the 360 kHz wide $^1S_0 \leftrightarrow {}^3P_1$ transition in In$^+$, as discussed in section 6.1.1. An ion temperature of 1 mK results in a Gaussian width $\omega_G \approx 2\pi \times 2.75$ MHz

6. Spectroscopy of the $^1S_0 \leftrightarrow {}^3P_1$ and $^1S_0 \leftrightarrow {}^3P_0$ transition of ^{115}In$^+$ ions

Figure 6.5.: *Frequency scans of the $m_F = +9/2 \rightarrow +11/2$ $(\sigma+)$ $^1S_0 \leftrightarrow {}^3P_1$ transition of a single $^{115}In^+$, sympathetically cooled with one Yb^+ ion at $s_V = 0.4$ for different saturation parameters s_{230}. The 230.6 nm and 370 nm laser have been applied alternating with a pulse length $t_{pulse} = 0.5\,s$. The data on the red detuned side of the resonance has been fitted with a Lorentz function to extract the FWHM ω_L.*

(see Eq. 6.1), so the achievable temperature resolution is very promising to put tight bounds on the temperature of the In$^+$ ion and the method can easily be implemented along the axial and radial direction.

6.1.2. Frequency measurement

In this section, the frequency of the $^1S_0$ $(F = 9/2) \leftrightarrow {}^3P_1$ $(F = 11/2)$ transition, determined from frequency scans of the two stretched states, is measured versus one of the H-maser that is referenced to primary Cs clocks and UTC(PTB).

Figure 6.6 shows the scans of the $m_F = -9/2 \rightarrow -11/2$ $(\sigma-)$ and $m_F = +9/2 \rightarrow +11/2$ $(\sigma+)$ transitions, which have been recorded with a 1 In$^+$/1 Yb$^+$ crystal with the PMT. The ions are confined at $\omega_{rad,1}/2\pi \approx 778$ kHz, $\omega_{rad,2}/2\pi \approx 808$ kHz and $\omega_{ax}/2\pi \approx 177$ kHz (In$^+$ COM mode frequencies) and approximately equal projection of both radial trap axes on the y-direction. The magnetic field along the z-axis is 0.03 mT. The power of the 230.6 nm beam at the position of the ions is $0.5\,\mu$W $(s_{230} = 1)$ and the Yb$^+$ ion is cooled with H1 $(s_{H1} = 0.7)$. The scans have been recorded with alternating pulses of the two lasers with a pulse length $t_{pulse} = 0.5$ s. The polarization of the 230.6 nm beam has been controlled with an EOM.

The connection to the frequency comb allows to convert the measured relative frequency to a frequency versus a H-maser that is referenced to primary Cs clocks and UTC(PTB). The line centers of the two transitions are extracted from Lorentzian fits and reveal $f_{\sigma-} = (1299648953766 \pm 18)$ kHz and $f_{\sigma+} = (1299648955051 \pm 14)$ kHz. The resulting center frequency

$$f_0 = (1299648954409 \pm 86)\,\text{kHz} \tag{6.2}$$

is the average of the frequencies $f_{\sigma-}$ and $f_{\sigma+}$. The calculation of the uncertainty of f_0 is explained below. f_0 agrees within the uncertainties with the previously published values of (1299648954.54 ± 0.10) MHz [219] and (1299648955.7 ± 1.9) MHz [221]. The here determined
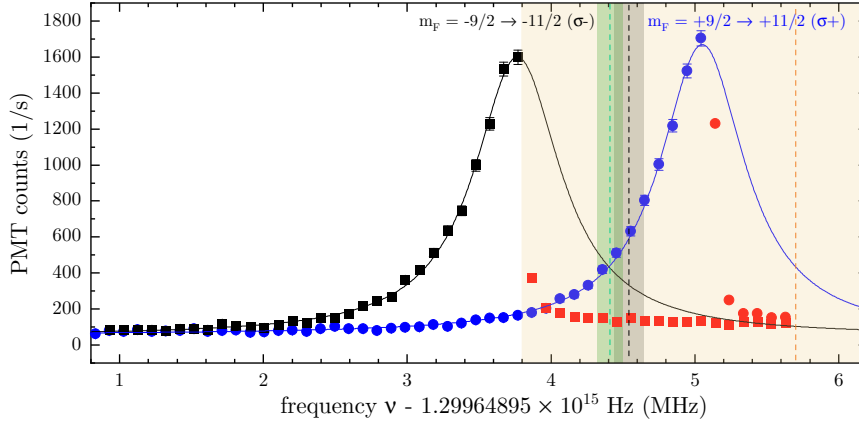
Figure 6.6.: *Frequency measurement of the $^1S_0$ (F = 9/2) $\leftrightarrow {}^3P_1$ (F = 11/2) transition in $^{115}In^+$ versus a H-maser that is referenced to primary Cs clocks and UTC(PTB). Shown are frequency scans of the two stretched states for a 1 In^+/1 Yb^+ crystal. The two transitions are fitted with a Lorentz function which neglects the data points on the blue side of the resonance (red points). The center frequency $f_0 = (1299648954409 \pm 86)\,kHz$ (indicated with the dashed green line, uncertainty in green) results from the average of the two line centers and agrees within the uncertainties with the previously published values in [219] (indicated with the dashed black line, uncertainty in grey) and [221] (indicated with the dashed orange line, uncertainty in orange).*

value and the two literature values are indicated in Fig. 6.6.

The frequency determination via the shown scans, that have been recorded with an alternating application of the Yb^+ cooling and the 230.6 nm laser, has a drawback. First, only the half of the line red-detuned to resonance can be used for the fit. Second, the temperature of the In^+ ion for this scan parameters is determined by the In^+ 230.6 nm laser itself, as described in section 6.1.1. As the frequency and thus the detuning to resonance shifts during the scan, the temperature of the In^+ ion changes over the scan, which can lead to a deformation of the line and a shift of the observed line center with respect to the actual resonance frequency.

Better suited would be a frequency measurement with alternating long pulses with the 230.6 nm laser at a detuning $\Delta = -\Gamma/2$ and then short pulses at low intensity with variable 230.6 nm frequency, conceptually similar to the method described in [222]. Then the temperature would be given by the long pulses, which means an over the scan constant and above all much lower temperature than in the case of sympathetic cooling with Yb^+. The result would be a scan symmetrical to resonance across the entire line, which could be fitted accurately to extract the center. It may be necessary to insert sympathetic cooling pulses on Yb^+ in between, to avoid decrystallization. In this case, it must be ensured that the next long 230.6 nm pulse at $\Delta = -\Gamma/2$ determines the temperature of the ions.

Symmetric frequency scans of the 230.6 nm resonance with the ideal parameters are not

available. The systematic series in Fig. 6.3 (a) can, however, be used to constrain the possible line center shift due to the above reasons. If only the points on the red-tuned half to resonance are used for the fit, the resulting center frequency is shifted to higher values. If additional points on the blue side of the resonance are considered, the central frequency shifts to lower values and the shift converges with the addition of more points. The frequency of the data shown in Fig. 6.6 has been corrected by the resulting difference of 83 kHz and the full shift is assumed for the uncertainty contribution. In addition, the recoil shift has to be considered. Due to the low axial trap frequency of $\omega_{ax}/2\pi \approx 135$ kHz, the In$^+$ ion is not in the Lamb-Dicke regime. While the carrier transition is recoil free, the sidebands experience a frequency shift ranging in value from ≈ 32.6 kHz of a free particle to 0 kHz, which affects the shape of the envelope of the carrier transition and the sidebands. For the evaluation half of the shift for a free particle (≈ 16.3 kHz) was used and again the entire shift is assumed to be the uncertainty contribution. But, the recoil shift and its uncertainty are negligible compared to the shift considered due to the above discussion, so this approximation is made here. The fit uncertainties of $f_{\sigma+}$ and $f_{\sigma-}$ result in a fit uncertainty of 16 kHz for the central frequency f_0. All three contributions are included in the total uncertainty for f_0 and result in 86 kHz. The H-maser used for the measurement has a much lower uncertainty at the level of 20 Hz and is completely negligible.

6.2. $^1S_0 \leftrightarrow {}^3P_0$ clock transition

The narrow $^1S_0 \leftrightarrow {}^3P_0$ transition in ^{115}In$^+$ at 236.5 nm is highly suitable for the operation of an optical clock based on single or multiple In$^+$ ions as discussed in section 2.5. In this work, the $m_{F,g} = +9/2 \rightarrow m_{F,e} = +9/2$ and $m_{F,g} = \text{-}9/2 \rightarrow m_{F,e} = \text{-}9/2$ Zeeman components are analyzed and used to lock the ultra-stable 946 nm laser to the atomic resonance.

Figure 6.1 gives an overview of the Zeeman substates and the magnetic sensitivity of the transition. The two extremal Zeeman states $m_{F,g} = \pm 9/2$ can cleanly be prepared with optical pumping via the $^1S_0 \leftrightarrow {}^3P_1$ transition at 230.6 nm. Starting from there, the ions can either be transferred to the $m_{F,e} = \pm 9/2$ state with π polarized light or to the $m_{F,e} = \pm 7/2$ state with $\sigma-/\sigma+$ polarized light. The Zeeman splitting is 6.45 kHz/mT for the σ transitions and 20.19 kHz/mT for the π transitions, so the σ transitions are less sensitive to magnetic field noise. Nevertheless, for this work the π transitions are chosen because then fast polarization switching is only required for the 230.6 nm laser while the polarization of the 236.5 nm laser stays linear. Hence the 230.6 nm detection laser beam with left/right-handed circular polarization needs to be aligned parallel to the magnetic field vector and the linearly polarized 236.5 nm clock laser beam perpendicular to the magnetic field vector. For the direction of the clock laser, the high confinement of the radial directions is desired and it therefore points in the vertical direction y (see Fig. 3.6), while the k vector of the 230.6 nm laser and the magnetic field are pointing along the trap axis z. This has the further advantages that also large linear crystals can be illuminated with a 230.6 nm beam with a low waist and low power and an axial beam typically leads to fewer stray light induced charges on the trap chips.

6.2.1. Clock spectroscopy sequence

The experimental sequence for spectroscopy of the $5s^2\ ^1S_0 \leftrightarrow 5s5p\ ^3P_0$ line is visualized in Fig. 6.7. The sequence is used both to measure frequency scans and Rabi oscillations and to lock the ultra-stable 946 nm clock laser to the atomic resonance. Depending on the type of measurement, different parameters are varied, as explained later in the chapter. The temporal sequence of various blocks is divided into four branches which depend on specific decisions in the sequence and is shown in Fig. 6.7 (a). Note that Fig. 6.7 (b) contains information about lasers and their saturation parameter in the individual blocks. Hereby the table in (b) is not meant as a temporal sequence, but gives an overview about the relevant laser parameters.
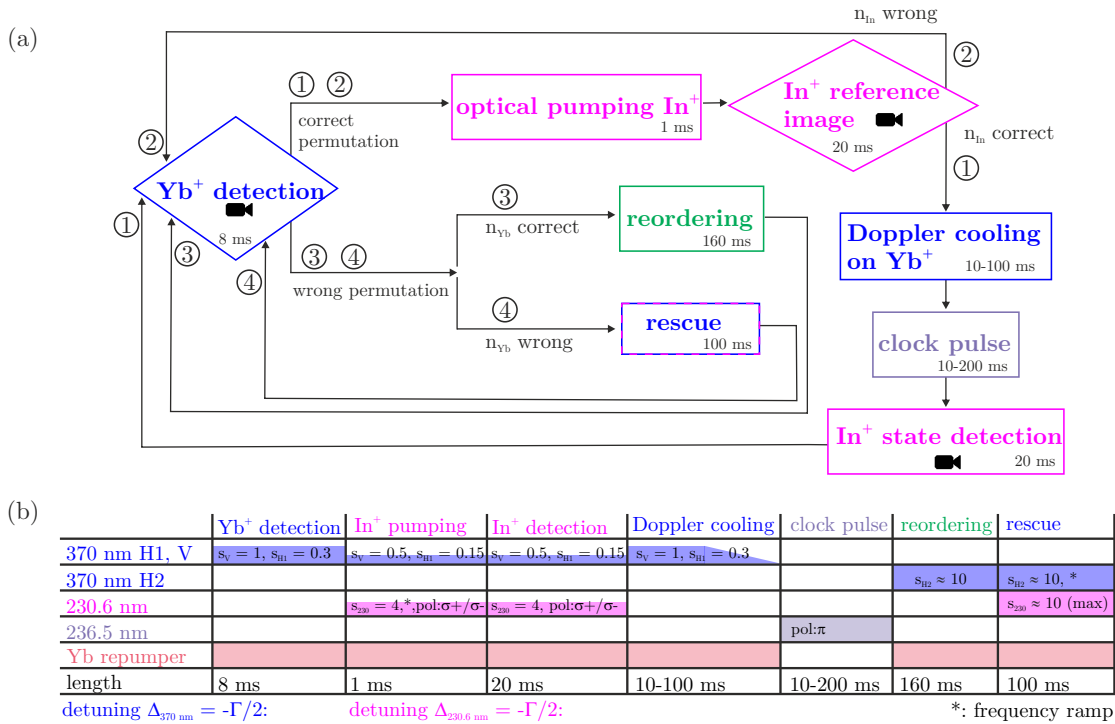
Figure 6.7.: *Clock spectroscopy sequence. (a) The temporal sequence of the different blocks is divided into four branches, which depend on specific decisions in the sequence. (b) Overview about the lasers and their typical parameters in the individual blocks shown in (a).*

The sequence is based on spatially resolved state detection of the In$^+$ ions via electron shelving (described in section 3.3) and status monitoring of the linear In$^+$/Yb$^+$ crystal via Yb$^+$ ion fluorescence. Status monitoring involves determining the number of Yb$^+$ ions and the permutation (the arrangement of the In$^+$ and Yb$^+$ ions) of the crystal. For these two tasks, regions of interest (ROIs) are placed above all ion positions, each in the In$^+$ and Yb$^+$ image. Threshold detection with different threshold values for the In$^+$ and Yb$^+$ ROIs is used for both tasks.

Every clock interrogation of an In$^+$ ion and the following detection yields a binary infor-

mation, if the ion has been excited to the $^3P_0$ state ($|e\rangle$) the ion is detected as "dark", if it remains in the $^1S_0$ ground state ($|g\rangle$) it is detected as "bright". To evaluate the excitation probability $p \equiv |c_e|^2$, the sequence is repeated multiple times and p is approximated by the fraction

$$p \approx \frac{n_{dark}}{N_{total}}, \tag{6.3}$$

with n_{dark} being the number of measurements where the indium ion is detected in $|e\rangle$ and N_{total} the total number of measurements. If n_{In} In$^+$ ions are interrogated in parallel, each clock interrogation reveals the binary information for each ion and hence the number of measurements per clock cycle is increased by a factor n_{In} compared to the interrogation of a single In$^+$ ion. p is then evaluated for all In$^+$ ions together when locking the clock laser, but post processing of the data allows to evaluate p for the individual ions. When locking the clock laser to the atomic resonance N_{total} is typically on the order of 10. For frequency scans and Rabi oscillations N_{total} is typically set to 100-200.

The clock spectroscopy sequence starts with *Yb$^+$ detection*, for which the Yb$^+$ lasers are switched on and the fluorescence in the Yb$^+$ ROIs is recorded with the EMCCD camera. Via the previously described threshold detection, the number of Yb$^+$ ions and the permutation of the crystal is determined. In case of the correct permutation or its mirror image (mirror images of a permutation yield the same mode structure and hence efficiency in terms of sympathetic cooling) the next step is *optical pumping*. With this the In$^+$ ions are prepared in either of the extremal Zeeman states $m_{F,g} = \pm 9/2$ using the indium detection transition ($^1S_0 \leftrightarrow {}^3P_1$) at 230.6 nm with circularly polarized light ($\sigma+/\sigma$-). To account for the Zeeman shift of the $m_{F,g/e}$ substates of the detection transition, the laser frequency is ramped. This is followed by *In$^+$ reference detection*, which includes the fluorescence collection in the In$^+$ ROIs via the camera, with subsequent threshold evaluation whether the In$^+$ ions are "bright" and hence in the ground state $|g\rangle$. If all In$^+$ ions are bright (number of In$^+$ ions n_{In} correct), they are prepared in $|g\rangle$ and the next step on branch 1 is *Doppler cooling on Yb$^+$*. The length of this phase t_{cool} depends on the composition of the crystal and consists of two sub-phases with the length $t_{\text{cool}}/2$. In the first, the saturation parameter of the cooling beams is held constant and in the second the saturation parameter is ramped down linearly to 0. The ramp ensures a further reduction of the temperature due to the intensity dependence of the end temperature of the cooling process. Subsequently, the *clock pulse* at 236.5 nm with π-polarized light to drive the $^1S_0 \leftrightarrow {}^3P_0$ transition is applied. The length of this pulse depends on the type of measurement and during this pulse all other lasers except for the clock laser (236.5 nm) are blocked with mechanical shutters to avoid ac-Stark shifts. The residual ac-Stark shift due to the clock laser itself is calculated in [116]. The low heating rate of the trap (see section 4.3) allows clock laser interrogation without parallel cooling. The *clock pulse* is followed by *In$^+$ state detection* which determines the state of the In$^+$ ions analogue to the *In$^+$ reference detection*. If the evaluation of the threshold reveals "dark", the ions have been excited by the clock pulse, otherwise not. This completes branch 1 and the sequence starts again. The parameters in both In$^+$ detection phases are identical and are therefore only listed once in Fig. 6.7 (b).

To save time, the next step of branch 1 is already started during the evaluation of the detection images and is aborted again in case of a wrong permutation or too low In$^+$ ion number n_{In}.

In case that the evaluation of the *In$^+$ reference detection* reveals that less than the expected number of In$^+$ ions are "bright" (n_{In} wrong) branch 2 is taken which returns to the start of the sequence without clock interrogation. A "dark" In$^+$ ion means that either the ion has not decayed from the excited state $|e\rangle$ yet or it formed a molecular ion with a background gas particle.

When the evaluation of the *Yb$^+$ detection* in the beginning of the sequence results in a wrong permutation of the crystal, branch 3 or 4 are taken. When all Yb$^+$ ions are "bright"(number of Yb$^+$ ions n_{Yb} correct), but in the wrong positions, a collision with a background gas particle has changed the arrangement of the ion, and the desired permutation is restored by *reordering* the crystal as described in section 5.3[1]. In addition to the initialization of *reordering*, the result of the previous clock interrogation will be neglected in the evaluation of p because the collision could have happened during the clock interrogation inducing a frequency shift or the present permutation could be less advantageous in terms of sympathetic cooling (see section 5.2 for details on the permutation dependent efficiency of sympathetic cooling) resulting in a higher ion temperature during clock interrogation. After the *reordering* attempt, branch 3 returns to the start of the sequence.

If the evaluation of the *Yb$^+$ detection* detects a reduced number of "bright" Yb$^+$ ions (n_{Yb} wrong), *rescue* of the crystal is initialized. The crystal is either melted or a molecular ion has formed. A high intensity Yb$^+$ cooling laser beam (H2) is switched on and its frequency is ramped to account for high ion temperatures and hence high 1st order Doppler shifts. Additionally, the indium detection beam is switched on at maximum saturation parameter s_{230} because the photons of the deep UV light can dissociate molecular bonds. For details about molecule formation and dissociation the reader is referred to section 3.2.3. After the *rescue* pulse, branch 4 is completed and returns to the beginning of the sequence.

The simplest crystal used for clock spectroscopy in this work consists of 1 In$^+$ and 3 Yb$^+$ ions and the used permutation is Yb$^+$-In$^+$-Yb$^+$-Yb$^+$/Yb$^+$-Yb$^+$-In$^+$-Yb$^+$. For this crystal, the Doppler cooling time is 50 ms and for the instability measurement shown in section 6.2.3, a clock pulse with a length of $t_{\text{clock}} = 150$ ms has been used. In that case branch 1 consumes a total time $t_{\text{branch 1}} = t_{\text{d}} + t_{\text{clock}} = 249$ ms with a dead time $t_{\text{d}} = 99$ ms which results in a duty cycle of $t_{\text{clock}}/t_{\text{branch 1}} \approx 0.6$. This is of course a lower limit, since the other branches lack a clock laser interrogation and therefore add dead time to the average cycle time t_{c}. The sequence has been modeled and optimized regarding the In$^+$ ion temperature for this 4-ion

---

[1]In contrast to the description in section 5.3, where the Yb$^+$ cooling beams H1 and V are used, in the clock sequence H2 is switched on. The reason is the lower saturation parameter s_{H1} compared to s_V, which is required for Doppler cooling but unfavorable for efficient *reordering* because of its low axial cooling power. The beams H1 and V are controlled with the same AOM and their saturation parameter ratio can only slowly be adjusted with a PBS and motorized waveplate as shown in Fig. A.8.

6. Spectroscopy of the $^1S_0 \leftrightarrow {}^3P_1$ and $^1S_0 \leftrightarrow {}^3P_0$ transition of $^{115}In^+$ ions

crystal in [116].

Almost the entire clock spectroscopy sequence runs on the FPGA introduced in section 3.7 to ensure precise timing of the pulses and avoid delays in signal processing. Only the *reordering* of the ions requires the change of the trap voltages, which currently can only be controlled via the PC. Therefore a "Remote Procedure Call" is issued by the FPGA to execute code on the experiment PC. Gradually, all resources necessary for *reordering* will be moved to hardware controlled by the FPGA to avoid the associated communication delays. Details about the programming of the clock-cycle and its optimization with regard on time consumption can be found in [184].

6.2.2. Spectroscopy with a 1 In$^+$/1 Yb$^+$ and 1 In$^+$/3 Yb$^+$ ion crystal

In the following, results on the spectroscopy of a single In$^+$ ion which is sympathetically cooled with either one or three Yb$^+$ ions are presented. The used permutation in case of three Yb$^+$ ions is Yb$^+$-In$^+$-Yb$^+$-Yb$^+$/Yb$^+$-Yb$^+$-In$^+$-Yb$^+$ which can be restored with a reliability of $99\,^{+1}_{-6}\,\%$, as presented in Table 5.1.

For all measurements with these two crystals, an rf drive frequency of $\Omega_{\mathrm{rf}} = 2\pi \times 21.7\,\mathrm{MHz}$ with an rf voltage amplitude $U_{\mathrm{rf}} = 1151\,\mathrm{V}$ has been used. The secular frequencies for a single Yb$^+$ ion are $\omega_{\mathrm{rad},1}/2\pi \approx 800\,\mathrm{kHz}$, $\omega_{\mathrm{rad},2}/2\pi \approx 820\,\mathrm{kHz}$ and $\omega_{\mathrm{ax}}/2\pi \approx 260\,\mathrm{kHz}$ which corresponds to $\omega_{\mathrm{rad},1}/2\pi \approx 1200\,\mathrm{kHz}$, $\omega_{\mathrm{rad},2}/2\pi \approx 1230\,\mathrm{kHz}$ and $\omega_{\mathrm{ax}}/2\pi \approx 318\,\mathrm{kHz}$ for a single In$^+$ ion. The two principal axes have a projection of $\approx 60\,^\circ$ and $\approx 30\,^\circ$ with respect to the clock laser (y-direction).
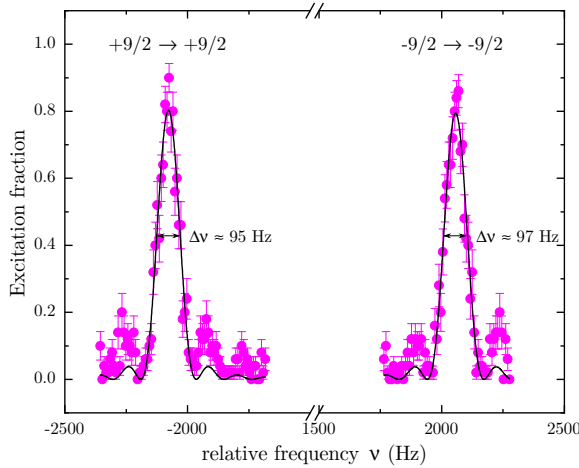
Figure 6.8.: *Frequency scan across the two Zeeman components $m_{F,g} = \pm 9/2 \rightarrow m_{F,e} = \pm 9/2$ of the $^1S_0 \leftrightarrow {}^3P_0$ transition. The single In$^+$ ion is cooled with one Yb$^+$ ion and the clock pulse length is $t_{\mathrm{clock}} = 10\,ms$. The data is fitted with a squared Sinc function and reveals a Fourier limited linewidth $\Delta\nu_+ \approx \Delta\nu_- \approx 96\,Hz$.*

In Fig. 6.8, a frequency scan across the two Zeeman components $m_{F,g} = \pm 9/2 \rightarrow m_{F,e} = \pm 9/2$ with a clock pulse length $t_{\mathrm{clock}} = 10\,\mathrm{ms}$ is shown for a 1 In$^+$/1 Yb$^+$ crystal. The saturation parameter of the 230.6 nm beam during optical pumping and In$^+$ detection is $s_{230} = 6$. The saturation parameters of the cooling beams H1 and V for Yb$^+$ detection and Doppler cooling are $s_V = 2$, $s_{H1} = 0.6$ and the Doppler cooling time $t_{\mathrm{cool}} = 100\,\mathrm{ms}$. All other parameter are

as given in Fig. 6.7 (b). The two components reach an excitation of almost 90 % and have a Fourier limited linewidths $\Delta\nu_+ \approx \Delta\nu_- \approx 96$ Hz.

For the locking of the ultra-stable laser to the atomic resonance, described in section 6.2.3, the clock pulse length is increased to $t_{\text{clock}} = 150$ ms. A frequency scan across the $m_{F,g} = +9/2 \rightarrow m_{F,e} = +9/2$ Zeeman component at this pulse length, and otherwise the same parameters as for the scans in Fig. 6.8, is shown in Fig. 6.9 and reveals a Fourier limited linewidth $\Delta\nu \approx 6.2$ Hz. The reason for the reduced contrast of ≈ 58 % is mainly the excited state lifetime $\tau_e = 1/(2\pi\gamma) = 195(8)$ ms [79], from theory one would expect ≈ 65 % contrast.

Figure 6.9.: *High resolution frequency scan across the $m_{F,g} = +9/2 \rightarrow m_{F,e} = +9/2$ Zeeman component of the $^1S_0 \leftrightarrow {}^3P_0$ transition. The single In$^+$ ion is cooled with one Yb$^+$ ion and the clock pulse length is $t_{\text{clock}} = 150$ ms. The fit with a squared Sinc function reveals a Fourier limited linewidth $\Delta\nu \approx 6.2$ Hz.*
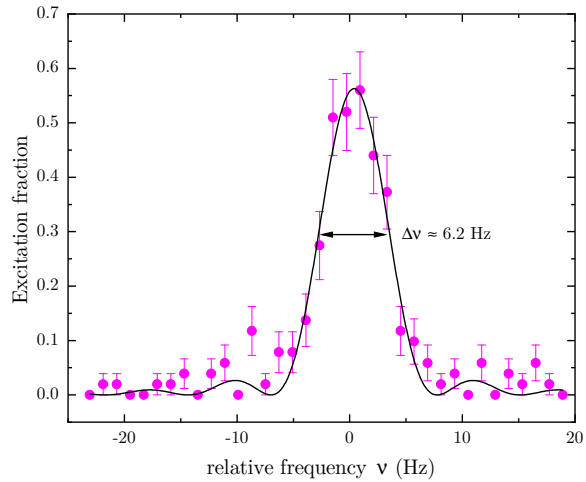
The optimization of the parameters for the Doppler cooling has been done by the evaluation of Rabi oscillations. Apart from the saturation parameters s_{H1} and s_V of the 370 nm cooling beams H1 and V and their relative ratio, the time spent for Doppler cooling t_{cool} is relevant to achieve low temperatures of the ions. With regard to the duty cycle, a compromise must be found for the cooling time. While the saturation parameters of the cooling beams and their relative ratio stay constant for different crystals, the cooling time t_{cool} needs to be adjusted to the number of ions and the ratio between In$^+$ and Yb$^+$ ions. The dependence of the efficiency of sympathetic cooling in dual-species crystals on the composition and permutation has been analyzed in section 5.2.

Figure 6.10 presents measurements of Rabi oscillations on the $m_{F,g} = -9/2 \rightarrow m_{F,e} = -9/2$ Zeeman component recorded with different cooling durations t_{cool}. The trapping potential is the same as for the previously shown frequency scans, but the single In$^+$ ion is sympathetically cooled with three Yb$^+$ ions instead of one. The use of three cooling ions leads to a better cooling efficiency ($\propto C_\alpha$, see section 5.2) and thus shorter cooling time. In principle the same cooling efficiency can also be reached with a single cooling ion, but this would require axial confinement voltages beyond the 12 V range available at the time. In addition to the use of two more cooling ions, the saturation parameter of the cooling laser beams H1, V and the In$^+$ detection laser been have slightly been reduced and are as stated in Fig. 6.7 (b). For $t_{\text{cool}} = 8$ ms, the Rabi frequency is smaller than for $t_{\text{cool}} = 50$ ms, the maximum contrast

6. Spectroscopy of the $^1S_0 \leftrightarrow ^3P_1$ and $^1S_0 \leftrightarrow ^3P_0$ transition of ^{115}In$^+$ ions

is lower and faster dephasing is observed. Increasing $t_{\mathrm{cool}} > 50\,\mathrm{ms}$ does not change the oscillation compared to $t_{\mathrm{cool}} = 50\,\mathrm{ms}$.
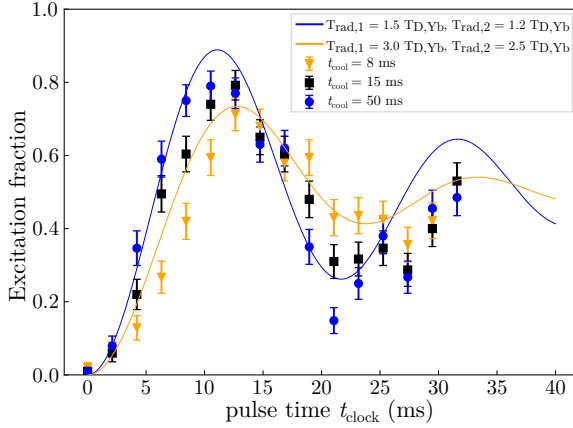
Figure 6.10.: *Rabi oscillations on the $m_{F,g} = $ -9/2 $\rightarrow m_{F,e} = $ -9/2 Zeeman component of the $^1S_0 \leftrightarrow ^3P_0$ transition for different cooling times t_{cool}. For the measurements, a 1 In$^+$/3 Yb$^+$ ion crystal with the permutation Yb$^+$-In$^+$-Yb$^+$-Yb$^+$ or its mirrored permutation Yb$^+$-Yb$^+$-In$^+$-Yb$^+$ has been used. The shown theoretical calculations assume different multiples of the Doppler temperature of Yb$^+$ $(T_{D,Yb} = 0.47\,mK)$ for the two radial mode temperatures $T_{\mathrm{rad},1}$ and $T_{\mathrm{rad},2}$.*

To estimate the temperature reached for the In$^+$ ion, a Rabi oscillation of the 1 In$^+$/3 Yb$^+$ ion crystal with $t_{\mathrm{cool}} = 50\,\mathrm{ms}$ is compared with theoretical calculations in Fig. 6.11. The red line indicates the theoretical course for the oscillation with a Rabi frequency $\Omega_0/2\pi = 53\,\mathrm{Hz}$ and assuming the Doppler temperature of Yb$^+$ $T_{D,Yb} = 0.47\,\mathrm{mK}$ for both radial modes. The other lines show the course for the assumption that either both mode temperatures $T_{\mathrm{rad},1} = T_{\mathrm{rad},2} = 2\,T_{D,Yb}$ or one being at $2\,T_{D,Yb}$ and the other at $T_{D,Yb}$. The experimental data agree with the assumption that both modes are at the Doppler temperature of Yb$^+$.
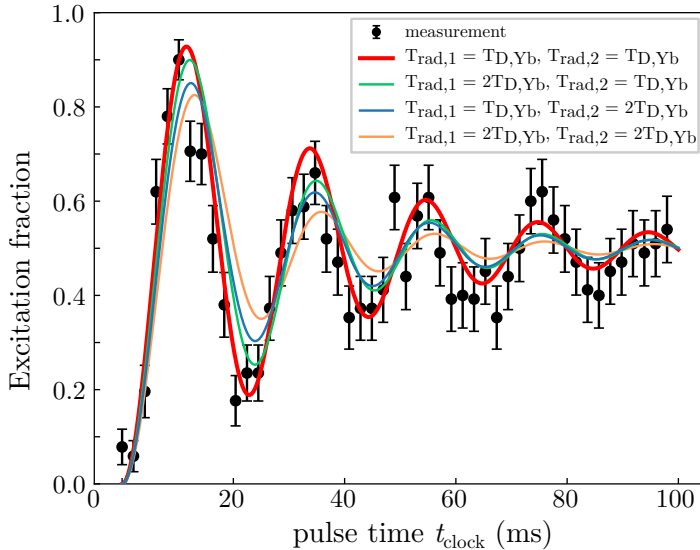
Figure 6.11.: *Temperature estimation for the In$^+$ ion in a sympathetically cooled 1 In$^+$/3 Yb$^+$ ion crystal. The permutation of the crystal is Yb$^+$-In$^+$-Yb$^+$-Yb$^+$ or its mirrored permutation Yb$^+$-Yb$^+$-In$^+$-Yb$^+$. The measured Rabi oscillation for $t_{\mathrm{cool}} = 50\,ms$ is compared with theoretical calculations assuming different multiples of the Doppler temperature of Yb$^+$ $(T_{D,Yb} = 0.47\,mK)$ for the two radial mode temperatures $T_{\mathrm{rad},1}$ and $T_{\mathrm{rad},2}$.*

6.2.3. Operation of the first In^+/Yb^+ clock

This section contains results about the operation of the first dual species In^+/Yb^+ optical clock. The results are limited to the evaluation of the statistical uncertainty, i.e. instability of the clock (see section 2.3). The analysis of the systematic uncertainty will be published elsewhere. A preliminary estimate is given in the outlook in section 7.

Figure 6.12 presents the instability measured with a 1 $In^+/3$ Yb^+ crystal versus the single-ion $^{171}Yb^+$(E3) clock [19] (a) and the ^{87}Sr lattice clock [223] (b) at PTB. The trap confinement and operating parameters are similar to the measurement of the Rabi oscillation in Fig. 6.11 and thus the parameters given in the overview in Fig. 6.7 (b). The clock pulse length $t_{\mathrm{clock}} = 150\,\mathrm{ms}$ results in a linewidth $\Delta\nu \approx 6.5\,\mathrm{Hz}$ as shown for a comparable frequency scan in Fig. 6.9. To lock the ultra-stable laser to the atomic resonance, the excitation is probed on the $m_{F,g} = \text{-}9/2 \rightarrow m_{F,e} = \text{-}9/2$ and $m_{F,g} = +9/2 \rightarrow m_{F,e} = +9/2$ Zeeman component on in total four locking points (an example for one component is shown in Fig. 2.2). Each point is probed 10 times and after the 40 measurements the frequency correction is derived and applied to the laser.
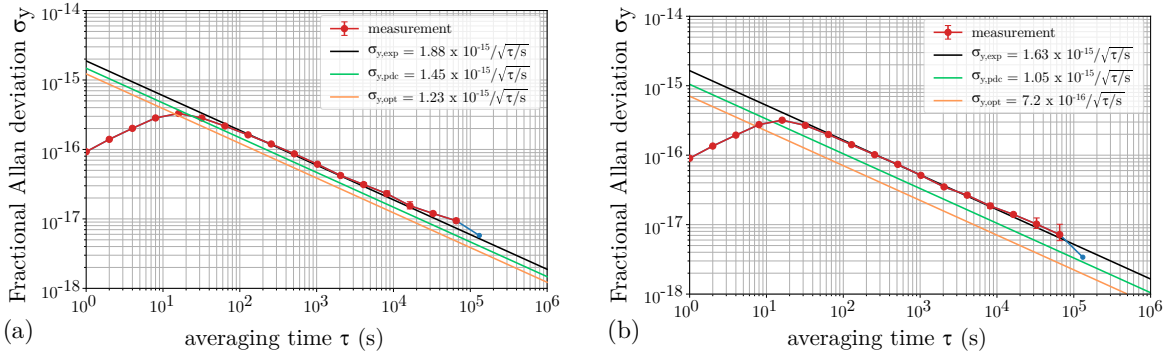
Figure 6.12.: *Instability measured with a 1 $In^+/3$ Yb^+ crystal versus the single-ion $^{171}Yb^+$(E3) clock [19] (a) and the ^{87}Sr lattice clock [223] (b) at PTB. The measured combined instabilities agree with the according to Eq. 2.4 expected $\sigma_{\mathrm{y,exp}}$ (black line). In addition the theoretical instability for the perfect case of a duty cycle of 100% $\sigma_{\mathrm{y,pdc}}$ (green line) and the theoretical optimal instability for Ramsey interrogation with a phase evolution time of the length of the excited state lifetime $\sigma_{\mathrm{y,opt}}$ (orange line), according to [75], are indicated. For the single-ion $^{171}Yb^+$(E3) clock its typical instability of $1.0 \times 10^{-15}/\sqrt{\tau/s}$ is assumed.*

The data shown in Fig. 6.12 has been taken during an optical clock comparison campaign within the frame of the European Metrology project 18SIB05 ROCIT[2]. The time period used for the evaluation extends over 13 days during which (apart from the weekends) only the nights are considered because strong vibrations due to construction work in the immediate vicinity of all three clocks disrupted measurements during the day. The instability is expressed as the fractional Allan deviation σ_{y}. In addition to the measured σ_{y}, the according

---

[2]Robust optical clocks for international timescales, http://empir.npl.co.uk/rocit/

6. Spectroscopy of the $^1\mathrm{S}_0 \leftrightarrow {}^3\mathrm{P}_1$ and $^1\mathrm{S}_0 \leftrightarrow {}^3\mathrm{P}_0$ transition of $^{115}\mathrm{In}^+$ ions

to Eq. 2.4 expected $\sigma_{\mathrm{y,exp}}$, the theoretical instability for the perfect case of a duty cycle of 100% $\sigma_{\mathrm{y,pdc}}$ and the theoretical optimal instability for Ramsey interrogation with a phase evolution time of the length of the excited state lifetime $\sigma_{\mathrm{y,opt}}$, according to [75], are indicated in Fig. 6.12. The basis for the calculation of the $^{115}\mathrm{In}^+$ contribution of $\sigma_{\mathrm{y,exp}}$ and $\sigma_{\mathrm{y,pdc}}$ is the frequency scan shown in Fig. 6.9. For the expected combined instability (Eq. 2.5) versus the single-ion $^{171}\mathrm{Yb}^+$(E3) clock in Fig. 6.12 (a) its instability contribution is assumed to be at its typical value of $1.0 \times 10^{-15}/\sqrt{\tau/s}$. The instability of the $^{87}\mathrm{Sr}$ lattice clock is negligible in relation to the instability of the In$^+$ ion, thus the combined expected instability in Fig. 6.12 (b) is completely dominated by the In$^+$ contribution. In both comparisons, the measurement perfectly agrees with the expected $\sigma_{\mathrm{y,exp}}$ and reveals $\sigma_{\mathrm{y}}(^{115}\mathrm{In}^+/^{171}\mathrm{Yb}^+) = 1.88 \times 10^{-15}/\sqrt{\tau/s}$ and $\sigma_{\mathrm{y}}(^{115}\mathrm{In}^+/^{87}\mathrm{Sr}) = 1.6 \times 10^{-15}/\sqrt{\tau/s}$. The best reported instability of an optical clock based on one $^{115}\mathrm{In}^+$ ion, sympathetically cooled with $^{40}\mathrm{Ca}^+$, is $\sigma_{\mathrm{y}} = 1.7 \times 10^{-13}/\sqrt{\tau/s}$ [224] so this work demonstrates an improvement of two orders of magnitude.

The main reasons for the improvement are a much shorter state detection time of the In$^+$ ions in this setup due to the detection system, presented in section 3.15, and a more stable clock laser. Here a duty cycle of $\approx 60\%$ is achieved as described in section 6.2.1, and in [224] only $\approx 20\%$. Possibly there are further reasons for this, which are not specified in more detail in the publication.

The frequency ratios $f_{\mathrm{In}+}/f_{\mathrm{Yb}+(\mathrm{E3})}$ and $f_{\mathrm{In}+}/f_{\mathrm{Yb}}$ ($^{171}\mathrm{Yb}$ lattice clock [225]) measured during the campaign have never been determined before and the preliminary evaluation, which is still ongoing, results in an improvement of at least two orders of magnitude for $f_{\mathrm{In}+}/f_{\mathrm{Sr}}$ compared to the previously best published value [224].

6.2.4. Multi-ion spectroscopy

In this section, the spectroscopy of the $^1\mathrm{S}_0 \leftrightarrow {}^3\mathrm{P}_0$ in $^{115}\mathrm{In}^+$ is extended to a linear crystal comprised of 4 In$^+$ ions and 8 Yb$^+$ ions arranged in the interleaved permutation. The achieved reliability to restore this permutation is $92\,^{+8}_{-16}\%$ (see Table 5.1).

As for the measurements with a single In$^+$ ion, an rf drive frequency of $\Omega_{\mathrm{rf}} = 2\pi \times 21.7\,\mathrm{MHz}$ and an rf voltage amplitude $U_{\mathrm{rf}}, = 1151\,\mathrm{V}$ have been used. The axial confinement needed to be reduced to maintain a linear arrangement of the ion crystal: the secular frequencies for a single Yb$^+$ ion are $\omega_{\mathrm{rad,1}}/2\pi \approx 821\,\mathrm{kHz}$, $\omega_{\mathrm{rad,2}}/2\pi \approx 833\,\mathrm{kHz}$ and $\omega_{\mathrm{ax}}/2\pi \approx 110\,\mathrm{kHz}$ which corresponds to $\omega_{\mathrm{rad,1}}/2\pi \approx 1200\,\mathrm{kHz}$, $\omega_{\mathrm{rad,2}}/2\pi \approx 1230\,\mathrm{kHz}$ and $\omega_{\mathrm{ax}}/2\pi \approx 135\,\mathrm{kHz}$ for a single In$^+$ ion. The two principal axes have a projection of $\approx 60°$ and $\approx 30°$ with respect to the clock laser (y-direction).

Figure 6.13.: *Multi-ion frequency scan across the $m_{F,g} = +9/2 \rightarrow m_{F,e} = +9/2$ Zeeman component of the $^1S_0 \leftrightarrow {}^3P_0$ transition. The 4 In$^+$/8 Yb$^+$ ion crystal is arranged in the interleaved permutation and the clock pulse duration is $t_{\mathrm{clock}} = 150\,ms$. The fit with a squared Sinc function reveals a Fourier limited linewidth $\Delta\nu \approx 6.4\,Hz$, which agrees with the 1 In$^+$/1 Yb$^+$ measurement with the same clock pulse duration.*
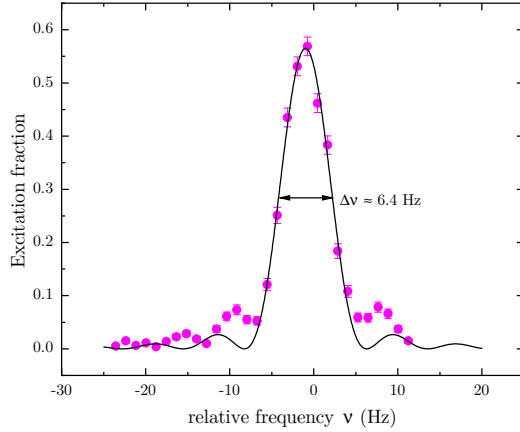
Figure 6.13 shows a frequency scan of the $m_{F,g} = \text{-}9/2 \rightarrow m_{F,e} = \text{-}9/2$ Zeeman component of a linear 4 In$^+$/8 Yb$^+$ ion crystal for a clock pulse duration $t_{\mathrm{clock}} = 150\,\mathrm{ms}$. As for the 1 In$^+$/3 Yb$^+$ ion crystal, $t_{\mathrm{cool}} = 50\,\mathrm{ms}$ and the other parameters are also the same and as summarized in Fig. 6.7 (b). A fit with a squared Sinc function results in a Fourier limited linewidth with $\Delta\nu \approx 6.4\,\mathrm{Hz}$, which agrees with the corresponding linewidth $\Delta\nu$ of the 1 In$^+$/1 Yb$^+$ crystal shown in Fig. 6.9.

To identify whether all four In$^+$ ions contribute equally to the signal, the frequency scan shown in Fig. 6.13 is evaluated for each ion individually, which is presented in Fig. 6.14. The individual signals feature the same maximum excitation and the fits of the individual signals agree with each other.

Figure 6.14.: *Ion-resolved multi-ion frequency scan across the $m_{F,g} = +9/2 \rightarrow m_{F,e} = +9/2$ Zeeman component of the $^1S_0 \leftrightarrow {}^3P_0$ transition with a clock pulse duration $t_{\mathrm{clock}} = 150\,ms$. The four In$^+$ ions of the shown 4 In$^+$/8 Yb$^+$ ion crystal contribute equally to the averaged signal shown in Fig. 6.13.*
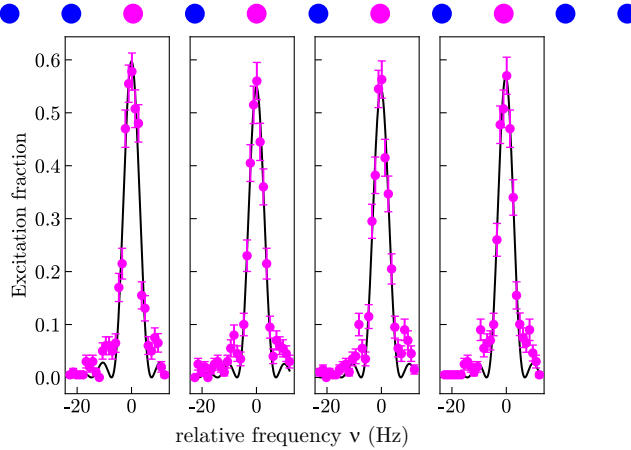
In Fig. 6.15 (a), multi-ion Rabi oscillations of the $m_{F,g} = \text{-}9/2 \rightarrow m_{F,e} = \text{-}9/2$ component are shown, which have been recorded for the same crystal and with the same parameters as the frequency scan shown in Fig. 6.13 an Fig. 6.14. As for the scans, the averaged signals and the signals of the individual ions are presented. In Fig. 6.15 (b), ion-resolved theory calculations with a Rabi frequency $\Omega_0/2\pi = 53\,\mathrm{Hz}$ and assuming twice the Doppler temperature

6. Spectroscopy of the $^1S_0 \leftrightarrow {}^3P_1$ and $^1S_0 \leftrightarrow {}^3P_0$ transition of ^{115}In$^+$ ions

of Yb$^+$ $2 \times T_{\mathrm{D,Yb}} = 0.94$ mK for both radial modes are depicted. The theoretical calculation in (b) and the measurement in (a) show great agreement. For the assumption that both radial modes are at $T_{\mathrm{D,Yb}}$, the contrast reaches 90% which is not the case in the measurement so that a more realistic assumption is $2\,T_{\mathrm{D,Yb}}$. According to the comparison between measurement and calculation the ions are equally cooled and thus all relevant modes at the estimated temperature of $\approx 2\,T_{\mathrm{D,Yb}}$. The reason for the faster oscillation of ion 10 compared to the other ions (see Fig. 6.15 (b)) is an on average lower Lamb-Dicke parameter of that ion.
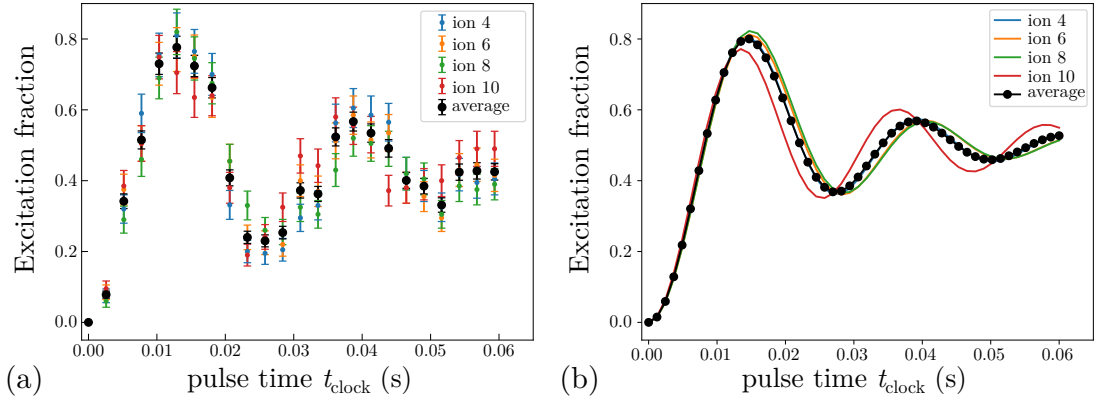
Figure 6.15.: *Multi-ion Rabi oscillations of the $m_{F,g} = \textit{-9/2} \rightarrow m_{F,e} = \textit{-9/2}$ component for a 4 In$^+$/8 Yb$^+$ ion crystal. (a) shows an ion resolved measurement and (b) a theoretical calculation assuming twice the Doppler temperature of Yb$^+$ $T_{\mathrm{D,Yb}} = 0.47$ mK for both radial modes.*

6.2.5. Multi-ion clock operation

In the following, the first clock operation with more than one In$^+$ ion is analyzed. As in section 6.2.3, the results are limited to the evaluation of the statistical uncertainty and the analysis of the systematic uncertainty will be published elsewhere.

In the later stages of the optical clock comparison campaign, mentioned in section 6.2.3, the clock operation has been extended from a 1 In$^+$/3 Yb$^+$ ion crystal to a 2 In$^+$/4 Yb$^+$ and 4 In$^+$/8 Yb$^+$ ion crystal. The rf confinement has been identical for the three crystals; only the axial confinement needed to be adjusted to the crystal length to ensure a linear arrangement of the ions. The laser parameters and pulse lengths t_{cool} and t_{clock} are identical for all crystals and as specified for the single ion instability measurement in section 6.2.3. As before, 10 measurements per locking point have been performed, counting each ion separately, such that with increasing In$^+$ ion number $N_{\mathrm{In+}}$ the cycle number to reach 10 data points reduces by $1/N_{\mathrm{In+}}$. The clock cycle was repeated until a minimum of 10 data points had accumulated, meaning that the 4-In$^+$ configuration used 12 interrogations per locking point.
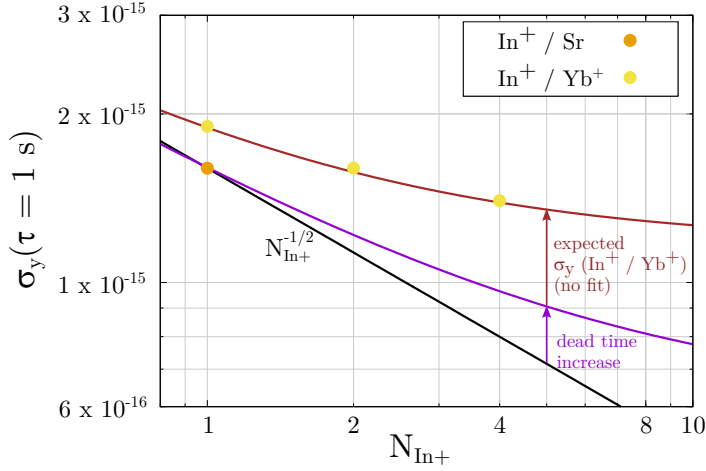
Figure 6.16.: *Scaling of the instability measured with different linear multi-ion In^+/Yb^+ crystals versus the single-ion $^{171}Yb^+$ (E3) clock [19]. The instability $\sigma_y(^{115}In^+/^{87}Sr)$ has only be measured for $N_{In+}=1$. To estimate if the instability contribution of the In^+ clock scales with $1/\sqrt{N_{In+}}$, the value of $\sigma_y(^{115}In^+/^{87}Sr)$ has been extrapolated to larger N_{In+} and ideally results in the black line. Consideration of the increased (measured) dead time results in the purple line. With the assumption of the instability $\sigma_y(^{171}Yb^+) = 1.0 \times 10^{-15}/\sqrt{\tau/s}$ used as before, the combined instability $\sigma_y(^{115}In^+/^{171}Yb^+)$ results in the brown line.*

During the clock operation with with the longer crystals, only the single-ion ^{171}Yb$^+$(E3) clock [19] but not the ^{87}Sr lattice clock [223] was operated. In Fig. 6.16, the combined instability $\sigma_y(^{115}\text{In}^+/^{171}\text{Yb}^+)$ at $\tau = 1\,$s is shown in dependence of the In$^+$ ion number $N_{\text{In+}}$. The combined instability $\sigma_y(^{115}\text{In}^+/^{171}\text{Yb}^+)$ is limited by both clocks and therefore does not decrease as much as the instability $\sigma_y(^{115}\text{In}^+)$. In addition to the measured values of $\sigma_y(^{115}\text{In}^+/^{171}\text{Yb}^+)$ at $\tau = 1\,$s the value for the combined, In$^+$ dominated instability $\sigma_y(^{115}\text{In}^+/^{87}\text{Sr})$ at $\tau = 1\,$s for $N_{\text{In+}} = 1$ is indicated.

To analyze whether the instability scales inversely with $\sqrt{N_{\text{In+}}}$, as one would expect from Eq. 2.4, the instability $\sigma_y(^{115}\text{In}^+/^{87}\text{Sr}, \tau = 1\,\text{s})$ (orange dot) from the single-ion measurement in section 6.2.3 is assumed to be the instability $\sigma_y(^{115}\text{In}^+)$. Ideally, one would expect the black line for extrapolating to larger ion numbers $N_{\text{In+}}$. The dead time of the clock cycle as a function of $N_{\text{In+}}$ is known from the measurements and increases with $N_{\text{In+}}$ (purple line). A small fraction of this is attributed to more frequent reordering since the collision rate directly scales with the total ion number, as described in section 3.2.3. The remaining increase is caused by the increased average time required for all clock ions to decay back to the ground state, due to the lack of a repumper, and some technical overhead which is currently being investigated. With the assumption of the instability $\sigma_y(^{171}\text{Yb}^+) = 1.0 \times 10^{-15}/\sqrt{\tau/s}$ used as before, the combined instability $\sigma_y(^{115}\text{In}^+/^{171}\text{Yb}^+)$ results in the brown line, which fits very well with the actual measured values (yellow dots).

Accordingly, the scaling of the instability $\sigma_y(^{115}\text{In}^+)$ with $N_{\text{In+}}$ is understood and scales

taking into account the dead time, as one would expect. Therefore, to really observe the $\sqrt{N_{\text{In+}}}$ scaling, a suitable repumper must be used and the technical additional dead time must be removed.

7. Summary and outlook

Summary

The main objective of this thesis was the setup and commissioning of an optical clock based on the simultaneous interrogation of multiple ^{115}In$^+$ ions, which are sympathetically cooled with ^{172}Yb$^+$ ions in a linear Coulomb crystal.

This work builds upon and for the first time brings together many previously developed components from colleagues, such as the ultra-stable lasers [165, 168], the ion trap [20–22], the doubling cavities for the indium detection laser, the deep UV fibers [169], the stabilization of all lasers via a wavemeter [102] and the control software, as well as measurement methods and experimental techniques which have been implemented and characterized [22, 185]. The vacuum system developed and built within the scope of this work and the bichromatic detection system for the state detection of both species together with all other components resulted in the construction of an optical frequency standard, and with the help of the frequency comb infrastructure at PTB finally in the first operation as an optical atomic clock.

The developed compact titanium vacuum system is optimized for low systematic uncertainties, high optical access, low background pressure, and exhibits a collision rate of $(0.0029 \pm 0.0003)\,\mathrm{s}^{-1}\,\mathrm{ion}^{-1}$ of collisions that lead to a rearrangement of the crystal. The chamber is equipped with temperature sensors to measure the BBR environment of the ions and magnetic field coils which have been optimized for low gradients to prevent Zeeman shift associated line broadening in extended crystals. In addition, a two-layer μ-metal shield protecting against disturbing magnetic fields is provided and the setup is mostly prepared for its installation.

For spatially-resolved state detection of both species via electron shelving, the fluorescence light of the ions is collected with an aspherical lens doublet, then the two wavelengths are split and for the Yb$^+$ ions the image is corrected with another lens doublet. Subsequently, the fluorescence of both species is recombined and imaged on a common EMCCD camera. For In$^+$ detection on the comparatively narrow line (360 kHz), a solid angle of $\approx 7\,\%$ is collected with an $NA = 0.45$. For both species, detection via a photomultiplier tube is also possible and Yb$^+$ fluorescence is divided between both detection devices during clock operation to allow simultaneous spatially-resolved state detection and in-situ micromotion measurements.

The systematic uncertainties associated with the trap are at a similar level as for the identical trap characterized in [22, 90], indicating that the trap fabrication process is well controlled and understood. For the trap potential ($f_{\mathrm{rad,In+}} \approx 1200\,\mathrm{kHz}$) used for the presented clock measurements and a $400\,\mu$m long crystal, the total uncertainty of the fractional frequency shifts associated with the trap is $< 1.6 \times 10^{-19}$. The main contribution with a

7. Summary and outlook

frequency shift of -1.32(15) $\times 10^{-18}$ is due to the second-order Doppler shift caused by EMM. The rf field-induced ac Stark shift is -0.124(18) $\times 10^{-18}$ and the ac Stark shift induced by the BBR radiation of the trap corresponds to -13.600(31) $\times 10^{-18}$. The overall heating rate $\dot{n} \approx 0.5$ phonons/s and is completely negligible for the second-order Doppler shift. Thus, the trap does not initially represent a limitation of the achievable uncertainty, since the trap-independent contributions, especially those associated with the temperature of the many-body system, are currently in the 10^{-18} range.

The experiments on the influence of the radial trapping frequency on the stability of a linear $5\,\mathrm{In}^+/5\,\mathrm{Yb}^+$ crystal for the two tested rf drive frequencies of 16.34 MHz and 21.79 MHz have shown that above a Mathieu $q_{\mathrm{In}} > 0.19$ with the cooling parameters used, cooling of the decrystallized ion cloud no longer leads to recrystallization. Accordingly, this point is already reached at lower radial confinement for the lower drive frequency than for the higher drive frequency. For this reason, the higher drive frequency was used for the clock operation and a radial confinement well below $q_{\mathrm{In}} = 0.19$ was selected.

The systematic analysis of the efficiency of sympathetic cooling in linear dual-species crystals has revealed a strong dependence on the exact arrangement of the ions, the permutation. A distribution of cooling ions over the entire chain without symmetries is advantageous. The worst cooling efficiencies are found in permutations where all the cooling ions are together in one half of the crystal or where the cooling ions are symmetrically arranged at the edges of the chain. In the first case the poor cooling is caused by a radial mode and in the second case by an axial one. The cooling efficiencies of different permutations of a crystal composition vary over up to 5 orders of magnitude (depending on the size of the crystal), thus control of the permutation is necessary to prevent long cooling times in clock operation and to allow reproducible temperatures. The experimental study on reordering dual-species ion chains has revealed three reliably producible permutation types. The one with the best cooling efficiency (Type I) has an alternating arrangement of the two species in the center and can be produced for up to 12 ions with a reliability of over 90 %. The analysis of the cooling efficiency of this interleaved permutation has shown that the optimal number of cooling ions n_{cool} to cool n_{spec} spectroscopy ions for $n_{\mathrm{spec}} \leq 7$ is $n_{\mathrm{cool}} = n_{\mathrm{spec}} + 1$. For $n_{\mathrm{spec}} > 7$ the optimum is $n_{\mathrm{cool}} = n_{\mathrm{spec}} + 3$. Adding more cooling ions only adds modes where the spectroscopy ions are hardly involved and therefore no additional cooling effect is induced.

The method used in this work for reordering linear crystals is based on the mass dependence of the trap potential and is already used in a similar form for crystals with up to 4 ions in other experiments [211–213]. Linear crystals with up to 16 ions are sorted. The method is restricted to ion traps with a large ion-electrode distance and does not require differential forces on different crystal parts. Instead, the aspect ratio of the trap potential is varied to deform the crystal from a linear chain into a 2D- or 3D-configuration. In addition, an electric field can be applied in the radial direction that affects the less strongly bound heavy ions (Yb$^+$) more than the light ones. Three stable types of target permutation have been identified. Besides the already mentioned alternating arrangement (type I), all heavy ions (Yb$^+$) can be localized in the middle of the chain (type II) or a permutation in which pairs of heavy ions (Yb$^+$) alternate with single light ions (In$^+$) in the middle (type III). The

last two types cannot be produced for all crystal compositions, but for crystals with up to 10 ions, reliabilities above 90 % have been achieved. Type I is the most relevant due to the best cooling efficiency and has been tested for up to 16 ions. There is no fundamental limit for a reliable realization with even longer crystals.

The findings on sympathetic cooling and sorting obtained in this work can be transferred phenomenological to other species. For the ^{27}Al$^+$/^{40}Ca$^+$ system, the results are directly transferable, since only the mass ratio is relevant, which is identical to ^{115}In$^+$/^{172}Yb$^+$ ($n_{\mathrm{cool}}/n_{\mathrm{spec}} = 1.5$). It is also important to mention that the findings on sympathetic cooling apply not only to Doppler cooling but also have relevance for other cooling techniques.

Spectroscopy of the ^{1}S$_0 \leftrightarrow {}^3$P$_1$ transition ($\Gamma_{\mathrm{In}} = 2\pi \times 0.36\,\mathrm{MHz}$), used for state detection in this work, shows for a single In$^+$ ion that is sympathetically cooled with one Yb$^+$ ion ($\Gamma_{\mathrm{Yb}} = 2\pi \times 19.6\,\mathrm{MHz}$) a clear influence of the Doppler cooling parameters on the line shape and width as expected. In particular, the cooling parameters for the direction parallel to the In$^+$ detection laser beam are crucial for the magnitude of the indium signal. Therefore, too large intensity in the Yb$^+$ cooling beam can negatively affect the indium detection signal. The result of the frequency measurement of the ^{1}S$_0$ ($F = 9/2$) $\leftrightarrow {}^3$P$_1$ ($F = 11/2$) transition versus a H-maser that is referenced to primary Cs clocks and UTC(PTB) is $f_0 = (1299648954409 \pm 86)\,\mathrm{kHz}$, which is compatible with previously published values [219, 221].

The results of spectroscopy on the ^{1}S$_0 \leftrightarrow {}^3$P$_0$ clock transition with a single ^{115}In$^+$ ion cooled with one or three ^{172}Yb$^+$ ions show a Fourier limited linewidth. Rabi oscillations with a radial probe beam direction are compatible with the Doppler temperature of Yb$^+$ ($T_{\mathrm{D,Yb}} = 0.47\,\mathrm{mK}$). In the frequency comparisons against the single-ion ^{171}Yb$^+$(E3) clock [19] and the ^{87}Sr lattice clock [223] at PTB, instabilities of $\sigma_{\mathrm{y}}(^{115}\mathrm{In}^+/^{171}\mathrm{Yb}^+) = 1.88 \times 10^{-15}/\sqrt{\tau/s}$ and $\sigma_{\mathrm{y}}(^{115}\mathrm{In}^+/^{87}\mathrm{Sr}) = 1.6 \times 10^{-15}/\sqrt{\tau/s}$ have been found. $\sigma_{\mathrm{y}}(^{115}\mathrm{In}^+/^{87}\mathrm{Sr})$ is almost entirely determined by the indium clock. These values are exactly in line with those expected from the observed contrast and duty cycle and represent an improvement of two orders of magnitude over the previously most stable optical clock based on a single ^{115}In$^+$ ion [224], which was operated with an instability $\sigma_{\mathrm{y}} = 1.7 \times 10^{-13}/\sqrt{\tau/s}$. The analysis of the overall systematic uncertainty is beyond the scope of this thesis and will be published elsewhere. A preliminary estimate is given in the outlook.

Spectroscopy of a $4\,\mathrm{In}^+/8\,\mathrm{Yb}^+$ crystal in the interleaved permutation also yields a Fourier limited linewidth and, after evaluation of the individual ion signals, shows that all ions contribute with equal contrast to the signal. According to Rabi oscillations, all ions have the same temperature of $\approx 2\,T_{\mathrm{D,Yb}}$ in the radial direction.

The frequency comparison against the single-ion ^{171}Yb$^+$(E3) clock [19] has been extended to crystals with up to four In$^+$ ions and shows a decreasing instability with increasing In$^+$ ion number $N_{\mathrm{In+}}$. A direct frequency comparison against the ^{87}Sr lattice clock, where the resulting instability would also for $N_{\mathrm{In+}} > 1$ still have been dominated by the indium clock, has not yet been performed. To analyze whether the instability scales inversely with $\sqrt{N_{\mathrm{In+}}}$,

7. Summary and outlook

the instability $\sigma_{\mathrm{y}}(^{115}\mathrm{In}^+/^{87}\mathrm{Sr}, \tau = 1\,\mathrm{s})$ from the single-ion measurement is assumed to be the instability $\sigma_{\mathrm{y}}(^{115}\mathrm{In}^+)$. Its extrapolation with $\sqrt{N_{\mathrm{In}+}}$ under consideration of the measured dead time increase of the clock cycle with increasing $N_{\mathrm{In}+}$ results for the combined instability $\sigma_{\mathrm{y}}(^{115}\mathrm{In}^+/^{171}\mathrm{Yb}^+)$ with the assumption $\sigma_{\mathrm{y}}(^{171}\mathrm{Yb}^+) = 1.0 \times 10^{-15}/\sqrt{\tau/s}$ exactly in the course shown by the direct measurement against the single-ion $^{171}\mathrm{Yb}^+(\mathrm{E3})$ clock. The dead time increase is caused by the increased average time required for all clock ions to decay back to the ground state, due to the lack of a repumper, and some technical overhead which is currently being investigated.

Accordingly, the scaling of the instability $\sigma_{\mathrm{y}}(^{115}\mathrm{In}^+)$ with $N_{\mathrm{In}+}$ is understood and to really observe the $\sqrt{N_{\mathrm{In}+}}$ scaling, a suitable repumper must be used and the technical additional dead time must be removed. Afterwards, the simultaneous interrogation of $N_{\mathrm{In}+}$ In$^+$ ions reduces the averaging time to resolve a given systematic uncertainty by a factor $1/N_{\mathrm{In}+}$.

Outlook

In April 2022, the indium ion clock was involved in an international measurement campaign on frequency comparisons of optical clocks (European Metrology project 18SIB05 ROCIT[1]). The data for the instabilities of the frequency measurements against the single-ion $^{171}\mathrm{Yb}^+(\mathrm{E3})$ clock [19] and the $^{87}\mathrm{Sr}$ lattice clock [223] at PTB, presented in this work, have been acquired during this campaign. After completion of the still ongoing evaluation, the campaign will result in previously unknown frequency ratios involving $^{115}\mathrm{In}^+$ and clocks from all over Europe. The already achieved instability of the indium ion clock with $1.6 \times 10^{-15}/\sqrt{\tau/s}$ is very promising and will be improved for a single ion as well as by using a larger number of clock ions. As the third optical frequency standard at PTB, the indium ion clock is an important part of PTB's optical clock ensemble and can contribute to further development of optical frequency measurements.

The planned near-time improvements to the experiment are described below. Some are already very concrete and are about to be implemented, others will take more time. The actions described will not necessarily be implemented in this order. In particular, the improvements to the systematic uncertainty will occur in parallel with the further scaling of the In$^+$ ion number.

The preliminary estimated systematic uncertainty for the presented frequency comparisons with a 1 In$^+$/3 Yb$^+$ crystal, which is currently evaluated and to be published elsewhere, is $\approx 2.1 \times 10^{-18}$ with an additional contribution of $\approx 2.6 \times 10^{-18}$ originating from the clock servo algorithm, which can be reduced to a negligible level for the next measurements with the implementation of an improved clock laser drift correction. The largest contribution is the thermal second-order Doppler shift. This is partly due to the need for a more precise estimate of the axial temperature. However, a significantly larger positive effect would be achieved by reducing the ion temperature in all directions. Therefore, after the new frequency doubling cavity for the In$^+$ detection and cooling laser with a higher output power has been put into operation, a second cooling stage on the In$^+$ ions will be implemented. For this

---

[1]Robust optical clocks for international timescales, http://empir.npl.co.uk/rocit/

purpose, a radial beam will be set up in addition to the existing axial beam. Temperatures below $100\,\mu\text{K}$ were realized for a single and two In^+ ions [89]. Similar temperatures should then be achievable in the mixed In^+/Yb^+ crystals, which will reduce the thermal second-order Doppler shift to the low 10^{-19} regime.

A preliminary systematic uncertainty estimate for the frequency comparison measured with $4\ \text{In}^+/8\ \text{Yb}^+$ ions showed no deviation from the single In^+ ion measurement at the 10^{-17} level. The detailed evaluation is in progress and will be published elsewhere.

The uncertainty of the BBR-induced ac Stark shift is currently not dominated by temperature measurements, but by the uncertainty of the differential static polarizability $\Delta\,a_{\text{stat}}$, which is only known theoretically [85]. For a precise measurement, the light shift induced by an IR laser ($1650\,\text{nm}$ used for Yb^+ repuming) with well-known intensity, which could be calibrated by its effect on an Yb^+ ion, could be measured. Comparable experiments with other species have already been done [19, 132].

To improve the frequency uncertainties associated with the magnetic field, the In^+ g factors will be measured more precisely and the magnetic field gradients of the Helmholtz-coils are going to be determined with a $^{172}\text{Yb}^+$ ion moved along the trap axis. $^{172}\text{Yb}^+$ has a much higher magnetic field sensitivity, enabling a precise in-situ characterization. In addition, the closing of the μ-metal shield will also help to reduce the uncertainty.

An already prepared hardware upgrade of the FPGA system will cause a further optimization of the clock cycle and clock operation. Currently, the clock operation is interrupted about every 6 hours and a micromotion measurement and compensation is performed via the experiment PC. In the future, this can be run on the FPGA and run without interrupting the cycle, for example, during crystal state detection on Yb^+ or in parallel with existing dead times. Another part of the clock cycle which currently requires communication via the experiment PC is the reordering. Although this only happens relatively rarely and leads to an average increase of the average clock cycle duration by $0.5\,\%$ for a 10-ion crystal, this procedure can also run completely on the FPGA with reduced dead-time after the upgrade.

In parallel, the In^+ ion number will be increased even further and frequency comparisons with the longer crystals will be performed to evaluate the instability and uncertainty for these crystals as well. With the already described improvements an uncertainty in the low 10^{-18} regime should be realizable also for the longer crystals which would significantly reduce the needed averaging time in upcoming frequency comparisons. To fully exploit the potential of the larger In^+ ion numbers, an efficient repumping scheme must be found to bring the ions from the excited clock state to the ground state. Currently, the decay is being waited for, which wastes valuable time.

Another step to improve the instability is to switch from the Rabi scheme to a Ramsey interrogation [75].

Further efforts will focus on making the clock operation more robust and requiring less

7. Summary and outlook

human intervention. During the measurement campaign described before, an uptime of 75 % was achieved over a stretch of two days where external disturbances due to heavy construction were paused. This can likely be increased significantly, already with some of the planned near-term improvements. For this purpose, for example some of the Yb$^+$ lasers still have to be equipped with automatic relocks and an automatic reloading of ions in case of ion loss is desirable. This would already be possible with the automated loading procedures currently in use, but the loading process involves some risks, so that additional safeguards are necessary.

On a much longer time horizon, the potential of the segmented ion trap design and scalability can be exploited with integrated optics. This refers to both the delivery of the corresponding lasers through photonic waveguides and grating couplers and the integration of state detection optics into the trap. While this has already been demonstrated at the Yb$^+$ wavelengths and for other species with wavelengths exclusively in the visible an IR-range [226–234], this becomes technically much more difficult for the deep UV wavelengths of the In$^+$ ion. Successful implementation of these concepts would allow ion chains in several segments to be manipulated simultaneously and, for example, one ensemble to be cooled or reordered while clock interrogation takes place in another ensemble. Also reloading of new ions could happen in parallel. The result would be a dead-time free clock operation, which significantly improves the instability and the robustness of the system. Apart from exploiting scalability, integrated optics would also significantly reduce the size of the experimental setup around the vacuum chamber.

A. Appendix

A.1. Calibration of temperature sensors

Integrated Pt100 sensors on trap chip

The uncertainty of the Pt100 sensors is specified by the manufacturer to be $300\,\mathrm{mK}$. For a more precise temperature estimate a smaller uncertainty is necessary. The calibration of bare sensors is commonly carried out with an oil-bath. When calibrating the sensors integrated into the trap, it is necessary to include the additional conductive paths on the trap and the electrical contacts between sensors and trap. The calibration must therefore be done with the complete trap. To maintain the UHV suitability a complex calibration procedure avoiding the use of the common oil-bath has been developed for this type of calibration. It is described in the following. The sensors make use of the temperature dependent electrical resistance $R(T)$ which can be approximated with a second-order polynomial (T in $^\circ$C):

$$R(T) = R_0 \cdot (1 + c_1 \cdot T + c_2 \cdot T^2). \tag{A.1}$$

For temperatures above $0\,^\circ$ C the inverse relation is given by:

$$T(R) = \frac{-R_0 \cdot c_1 \sqrt{(R_0 \cdot c_1)^2 - 4R_0 \cdot c_2 \cdot (R_0 - R)}}{2R_0 \cdot c_2}. \tag{A.2}$$

To achieve a low uncertainty for the temperature measurement, the coefficients c_1, c_2 and R_0 have been determined for both sensors.

Calibration procedure
For this calibration the trap is installed inside a copper cuboid with a wall thickness of $10\,\mathrm{mm}$. Four reference sensors, calibrated at PTB to an uncertainty of $7\,\mathrm{mK}$[1], are placed on the inside and outside of the cuboid. The cuboid is wrapped in several layers of bubble wrap and is placed inside a Styrofoam box. This box is positioned inside a refrigerator box with an integrated Peltier element, which is used to heat and cool the box to different temperatures (figure A.1). The resistance measurements of the six sensors, the two on the trap and the four reference sensors, is performed with a calibrated precision digital multimeter[2] and the four-wire sensing method. In total the trap in its thermal shield has been cooled and heated to eight different temperatures between $20\,^\circ$C and $32\,^\circ$C.

Before measuring the resistances of the six sensors for the respective temperatures the system was allowed to equilibrate for two days. The resistance value of each sensor at each

---

[1]Cleverlab
[2]Agilent 34401A

A. Appendix
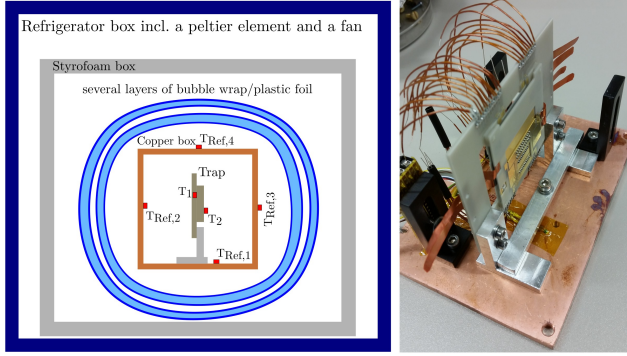
Figure A.1.: *Set-up for the absolute temperature calibration of the integrated Pt100 sensors. Left: side view of the trap placed inside a refrigerator box including a Peltier module. Right: Picture of the trap placed on the copper base plate. The rest of the box is then placed on top of it.*

temperature is the mean of 25 equidistant measurements over a time interval of two minutes while its standard deviation gives a statistical uncertainty for that value. The resistance measurement is performed twice for one of the reference sensors, at the beginning and at the end of each measurement series, in order to quantify the temperature drift over the time elapsed during the measurement procedure for all sensors. The mean value of the four calibrated reference sensors is taken as the equilibrated temperature inside the box. The reading of the Pt100 sensors is done with a current of $1\,\mathrm{mA}$ leading to a resistive heating, which needs to be considered for precise temperature measurements. This so called self-heating is characterized for all sensors and considered for the temperature and uncertainty determination. Therefore small dc currents between $0.5\,\mathrm{mA}$ and $10\,\mathrm{mA}$ are applied to the sensors and the current and voltage drop across the sensor is measured with two calibrated precision digital multimeters[3]. With Ohm's law the respective resistance and thereby the temperature can be calculated and the quadratic behavior between measurement current and temperature can be fitted.
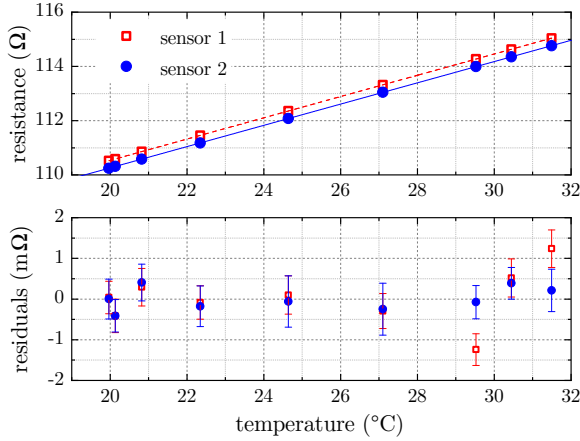
Figure A.2.: *Top: Temperature dependency of the resistance of the integrated Pt100 sensors. The open symbols correspond to sensor 1 and the closed to sensor 2. The error bars are below $0.5\,\mathrm{m\Omega}$ and thereby smaller than the plotted points. Bottom: Residuals of the fitted measurement. The temperature uncertainties across the temperature range of $20\text{-}32\,^{\circ}C$ are between $4\text{-}31\,\mathrm{mK}$.*

Result

Figure A.2 shows the result of the calibration of the integrated sensors and the fit of the data using equation (A.1). Table A.1 lists the respective fit results of the parameters c_1, c_2 and R_0.

---

[3]Agilent 34401A

148

Table A.1.: *Calibration coefficients for the two integrated Pt100 sensors on the trap.*

Trap	R_0 (Ω)	c_1 ($10^{-3}\,\Omega/°C$)	c_2 ($10^{-7}\,\Omega/°C$)
Sensor 1	102.658±0.0101	3.850±0.008	-6.1±1.6
Sensor 2	102.376±0.010	3.864±0.008	-7.1±1.6

Table A.2 lists all accounted uncertainties for the temperature determinations that are used for the calibration of the two integrated Pt100 sensors. The dominant uncertainty source at $22\,°C$ (as a typical lab temperature) are the temperature gradients across the copper cuboid which increase with the temperature at a rate of $3\,mK/°C$.

Table A.2.: *Uncertainty contributions for the temperature determination at T=22°C within the Pt100 sensor calibration. The resulting absolute uncertainty of the temperature determination $\sigma_{T,Pt100}$ is obtained with Gaussian error propagation on equation (A.2)*

Source	Uncertainty (mK)
Reference Pt100 sensors	<8
Digital multimeter	<1
Self-heating per sensor	<1
Temperature drift during measurements	<4
Temperature gradients over copper box	<10

Less dominant are the temperature uncertainties of the individual reference sensors and the temperature drift during the measurement. The uncertainties of the digital multimeter and the self-heating of all sensors are almost negligible. Table A.2 lists only the uncertainty of a resistance measurement at a single temperature. The temperature dependency of the sensor resistance is then fitted using equation (A.1). The fit errors on the parameters c_1, c_2 and R_0 add to the total temperature uncertainty of the sensors.

With Gaussian error propagation on equation (A.2) and the calibration coefficients from table A.1 the absolute temperature uncertainty $\sigma_{T,Pt100}$ can be derived. The resulting absolute temperature uncertainty $\sigma_{T,Pt100}$ for both integrated sensors is shown in Fig. 4.17 in section 4.4.1. For a typical lab temperature of $22\,°C$ the absolute temperature uncertainty of both sensors is below $60\,mK$.

Pt100 sensors on vacuum chamber

The Pt100 sensors that are glued to the vacuum chamber to monitor the thermal environment of the ions have been calibrated before they were attached to the chamber to improve

A. Appendix

the temperature uncertainty of $\pm 1\,\mathrm{K}$ stated by the vendor.

The sensors make use of the temperature dependent electrical resistance $R(T)$ which can be approximated with the second-order polynomial already given in Eq. A.1 in section A.1. Typically, the second-order polynomial is only used if precise calibration over a large temperature range in required. For temperatures constant within a few K, the simple linear approximation

$$R(T) = R_0 \cdot (1 + 3.85 \cdot 10^{-3} K^{-1} \cdot T) \iff T(R) = \frac{R - R_0}{3.85 \cdot 10^{-3} K^{-1} \cdot R_0} \tag{A.3}$$

is often used.
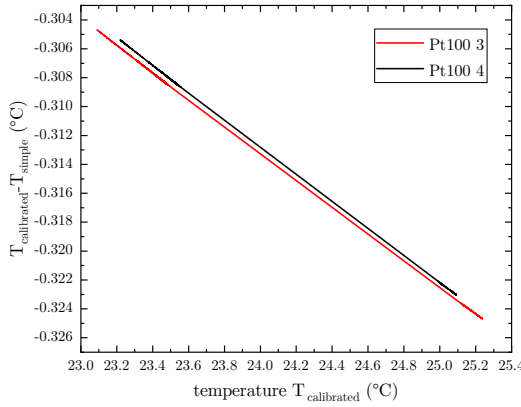
Figure A.3.: *Temperature dependency of the difference between the calibrated temperature evaluation via a 2nd order polynomial and the simple linear evaluation for the two calibrated sensors Pt100-3 and Pt100-4.*

To test whether a calibration with a 2nd order polynomial is necessary for the monitoring of the temperature of the vacuum chamber, which should always be at room temperature, the difference between the two evaluations has been determined over a range of $2\,^{\circ}\mathrm{C}$ with the help of two precisely calibrated Pt100 sensors, labeled Pt100-3 and Pt100-4, that have an uncertainty of $7.4\,\mathrm{mK}$. The two sensors have been placed on an aluminium plate that was heated from 23-25 $^{\circ}\mathrm{C}$ and the resistance was measured. Figure A.3 shows for both sensors the temperature $T_{\mathrm{calibrated}}$ determined with the calibration coefficients and the 2nd order polynomial versus the difference between this temperature and the temperature derived with the simple linear relation T_{simple}. Over the range of $2\,^{\circ}\mathrm{C}$ the temperature difference derived from the two evaluations changes about $0.02\,^{\circ}\mathrm{C}$ ($20\,\mathrm{mK}$). According to that the eight sensors for monitoring the vacuum chamber temperature can be calibrated with the linear relation (Eq. A.3) and an additional offset T_{off} if the calibration is carried out at room temperature.

For the calibration the eight sensors (labeled with Ch3 to Ch10) have been taped in a row in between the two calibrated sensors Pt100-3 and Pt100-4 on the aluminium plate. The plate was placed on a table covered by a card board box to protect it from air flow and the system was left to get to thermal equilibrium while recording the resistances of all sensors. The corresponding temperature profiles are shown in Fig.A.4, here the resistances of the two calibrated sensors Pt100-3 and Pt100-4 are evaluated with the 2nd order polynomial (Eq.A.1) and the ones of the sensors Ch3 to Ch10 with the simple linear relation

(Eq.A.3). To determine the offset T_{off} for the eight sensors the temperatures at the time of 7.5 h are evaluated (this point is indicated with a dashed line in Fig.A.4). At this point sensor Pt100-3 and Pt100-4 show temperatures of $(23.114\pm0.007)\,°C$ and $(23.136\pm0.007)\,°C$, respectively, so they agree within $(22\pm10)\,mK$ and the average temperature of the two sensors is $(23.125\pm0.007)\,°C$. Assuming that the aluminium plate was in thermal equilibrium after 7.5 h, the offset T_{off} for the sensors Ch3 to Ch10, given in Table A.3 (and also in Table 3.5), are deduced from the difference between the temperature of the respective sensor at 7.5 h and the average temperature of Pt100-3 and Pt100-4. With this offsets the temperatures measured by the sensors Ch3 to Ch10 can be evaluated with the relation given in Eq.A.4.

Figure A.4.: *Calibration of the Pt100 sensors Ch3 to Ch10. The temperature values for the calibration are deduced at a measurement time of 7.5 h, which is indicated with the dashed line. The two precisely calibrated sensors Pt100-3 and Pt100-4 agree within $(22\pm10)\,mK$ and have and reveal an average temperature of $(23.125\pm0.007)°C$. The offsets T_{off} for the sensors Ch3 to Ch10 are deduced from the difference between their temperature and the average temperature.*
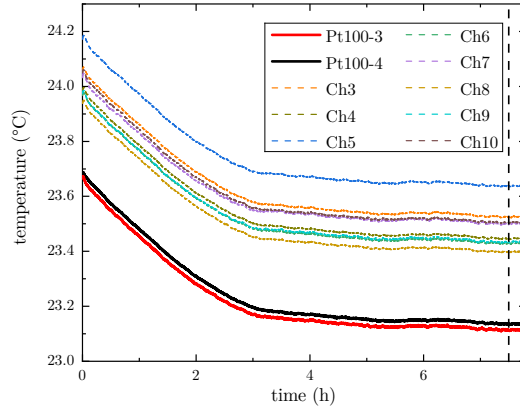
Table A.3.: *Temperature offset correction T_{off} for the Pt100 sensors Ch3 to Ch10.*

Sensor	T_{off} [mK]
Ch3	-400
Ch4	-321
Ch5	-511
Ch6	-304
Ch7	-375
Ch8	-273
Ch9	-308
Ch10	-378

Because the temperature of the aluminium plate was only measured precisely at the two points of Pt100-3 and Pt100-4 the maximal temperature spread within the plate is conservatively assumed to be 100 mK. Considering that the temperature difference between the temperatures $T_{\text{calibrated}}$ and T_{simple} over a range of 2 °C only changed about 0.02 °C (20 mK)

and the calibration of the sensors has been done at the temperature at which they will be used the overall uncertainty for the temperatures measured with the sensors Ch3 to Ch10 is assumed to be $0.2\,^{\circ}\mathrm{C}$ $(200\,\mathrm{mK})$.

$$T(R) = \frac{R - R_0}{3.85 \cdot 10^{-3} K^{-1} \cdot R_0} + T_{\text{off}} \tag{A.4}$$

A.2. Laser setup

Laser beam paths

This section provides schematic drawings of the relevant laser setups and the laser distribution on the experimental table. In Fig. A.5 the symbols used throughout this section are introduced.
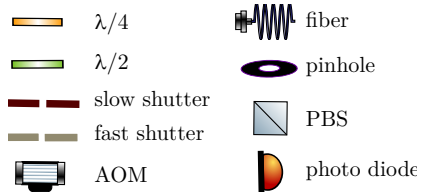
Figure A.5.: *Symbols for the drawings of the laser beam paths.*

The breadboard illustrated in Fig. A.6 is the basis for all laser beams entering the trap in the horizontal plane and is mounted around the vacuum chamber.
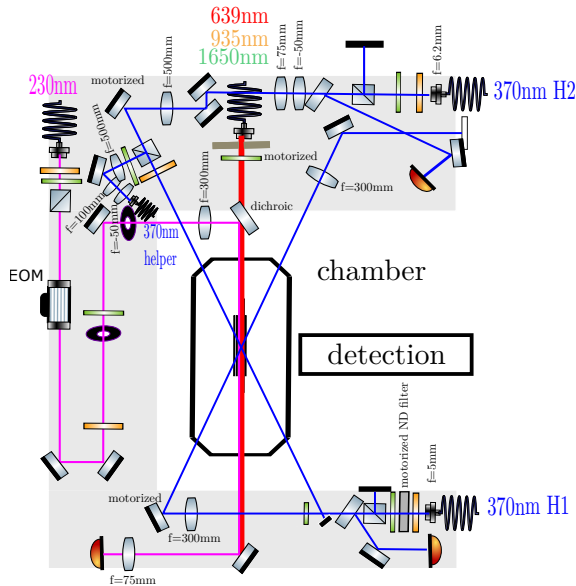
Figure A.6.: *Breadboard for laser delivery at the horizontal plane around the vacuum chamber. It contains the 370 nm cooling beams H1, H2 and the helper and the axial repumpers for Yb^+ and the 230 nm detection beam for In^+. All beams are guided to the breadboard via fibers.*

The optical table that holds the vacuum chamber is also used for the delivery of all vertical laser beams, which are guided on three different heights. Figure A.7 illustrated a scheme of the table. The ionization lasers go 55 mm above the table, the vertical 370 nm cooling laser
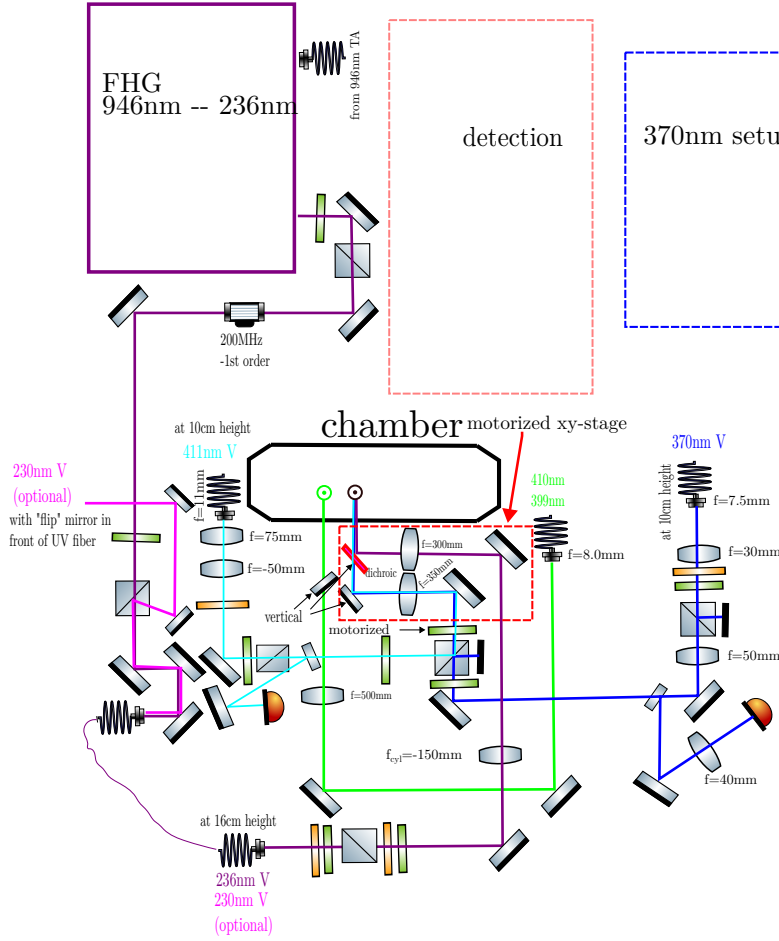
Figure A.7.: *Laser beam paths on the experiment table to guide the vertical laser beams to the ions. The beams are guided at three different heights to allow simultaneous delivery of all vertical beams. The optics in the dashed red box are mounted on a motorized 2-dimensional translation stage to steer them to all trap segments.*

and the 411 nm laser at 100 mm above the table and the 236 nm laser (+ optional 230 nm laser) at 160 mm above the table. The reason for the height differences is the delivery to the ions. The photoionization lasers are guided via a fixed mirror to the loading segment. The last two mirrors and the focusing lens for the other lasers are mounted on a motorized 2-dimensional translation stage (red box in Fig. A.7), which enables the laser delivery to all trap segments with the same beam size. The 236 nm (and optional 230 nm) laser goes on top of the two Yb$^+$ lasers and they are overlapped with a dichroic mirror which is transmittive for wavelengths above 250 nm and was optimized for the used wavelengths. Apart from the mentioned vertical laser beams and the chamber the optical table contains the fourth harmonic generation cavities for the clock laser (946 nm $\rightarrow$ 236 nm), the detection setup, the 370 nm laser setup and the second SHG stage (461 nm $\rightarrow$ 230 nm) for the In$^+$ detection laser.

A. Appendix

The 370 nm laser is divided into four beams as shown in Fig. A.8. The double pass AOM is used to control the frequency of all beams. Because the diffraction efficiency in the UV is highly polarization dependent the typical double-pass setup based on polarization switching before the second pass to separate the incoming and out-coming beams with a polarizing beam splitter cube is inefficient. Instead a cat eye style mirror is used which separates the incoming and outgoing beam vertically. It consists of two mirrors which are glued on a right-angled aluminium piece mounted in a mirror holder. The two single-pass AOMs are used to control the cooling beams (H1 and V) independently from the optical pumping beam H2. The helper beam has a frequency offset of -85 MHz to the other beams and is not used during the spectroscopy sequences. The four beams are coupled into fibers.
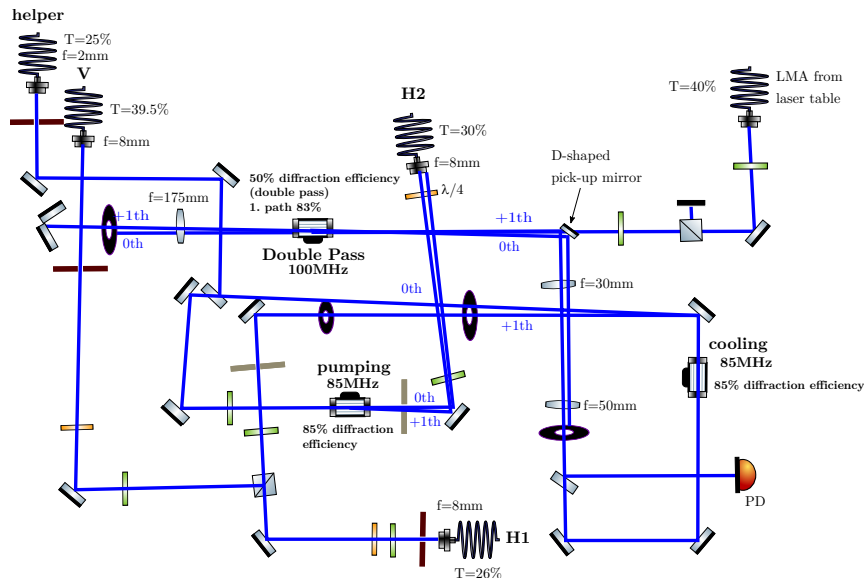
Figure A.8.: *Beam paths of the Doppler cooling laser. The power is distributed in four beams and can be controlled in frequency by a shared double pass AOM and in power by two single-pass AOMs.*

The principle of the overlapping box for all axial beams is shown in Fig. A.9. The four individual lasers beams are coupled to the box via individual fibers and guided and overlapped in a shared LMA fiber with dichroic beamsplitters. To reach high coupling efficiencies through the LMA fiber all beam path contain a telescope which was adjusted to the wavelength dependent mode-field diameter (MFD) of the LMA at the respective wavelength after measuring the beam size of the collimated beams behind the outcouplers of the individual fibers. Moreover, the polarization of all paths is adjusted to the axis of the LMA fiber. The power in all individual beam paths is monitored with photodiodes. For more details see [164].

The photoionization lasers for indium and ytterbium are overlapped with polarizing beam splitter cubes as shown in Fig. A.10 and then coupled into a fiber.
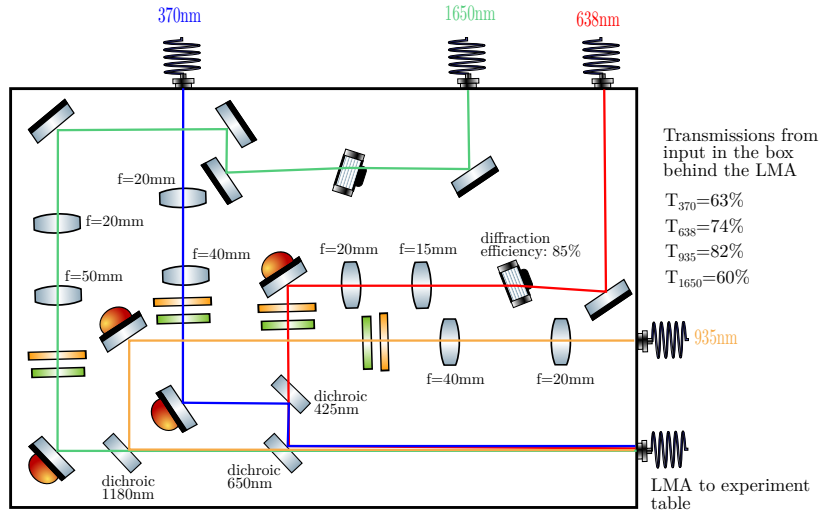
Figure A.9.: *Scheme of the box for overlapping the four axial beams and coupling them in a shared LMA fiber. The wavelengths indicated at the dichroics are the cut-on wavelength, i.e. the wavelength above which they are transmittive. Next to the drawing the transmission from the input in the box behind the LMA fiber are given for all wavelengths.*
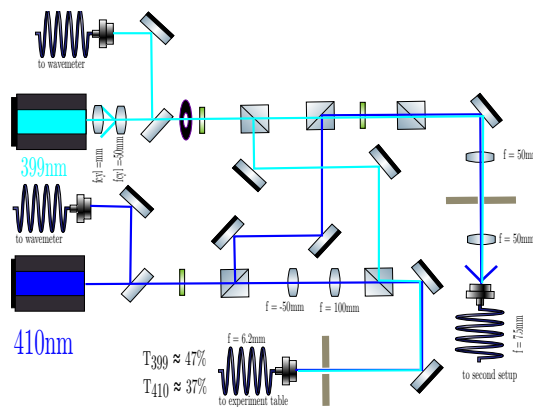
Figure A.10.: *Overlapping of the ionization lasers for indium and ytterbium.*

A. Appendix

The setup of the ultra stable 822 nm laser is described in detail in [102]. In Fig. A.11 only the part behind the SHG cavity going to this setup is drawn.
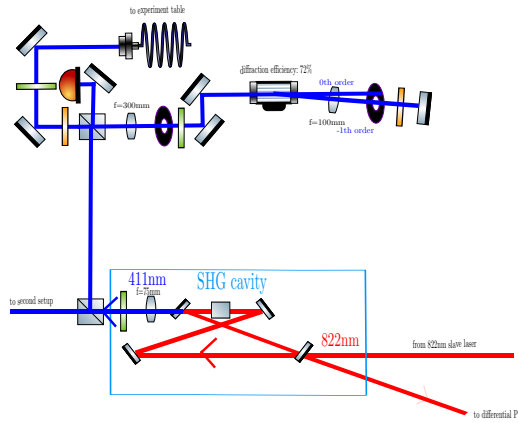
Figure A.11.: *Schematic drawing of the 411 nm beam line going to the indium clock setup. After the SHG cavity the power is divided between two experiments, a double pass AOM is used for frequency control and power stabilization.*

Achromatic fiber outcoupler for the axial beams

The achromatic fiber outcoupler for the axial beams with wavelengths between 370 nm and 1650 nm, shown in Fig. A.12, consists of four lenses. The distance between the fiber tip and the first lens is adjustable, the other distances are fixed.
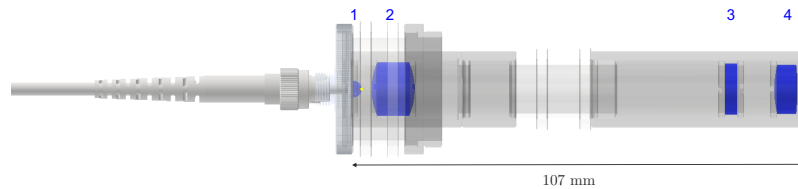
Figure A.12.: *Drawing of the achromatic fiber outcoupler for the axial beams. It consists of four lenses and has a length of 107 mm. The distance between the fiber tip and the first lens is adjustable, all other distances are fixed.*

Table A.4 lists the properties of the four lenses. The coating of the lenses 1 and 3 is customized and has been optimized for lowest reflection at 370 nm as this wavelength is most critical to induce charging of the ion trap. The resulting reflection at the four used wavelengths is: $R_{370\,\mathrm{nm}} \approx 1\,\%$, $R_{638\,\mathrm{nm}} \approx 5\,\%$, $R_{935\,\mathrm{nm}} \approx 12\,\%$ and $R_{1650\,\mathrm{nm}} \approx 10\,\%$.

The system has been optimized with a ray tracing software[4]. The last surface of the 4th lens has a distance of 307 mm to the trap center. In between there are two optical elements that need to be considered in the optimization: a 6.35 mm thick dichroic beam combiner that overlaps the beams coming out of the coupler with the In$^+$ detection laser beam at 230 nm

---

[4]Optics Software for Layout and Optimization (OSLO)

Table A.4.: *Properties of the lenses of the achromatic fiber outcoupler. * On the half-ball lens the customized coating has only been applied to the plane surface.*

lens	material	diameter	EFL	coating
		d (mm)	(mm)	coating
1-half-ball	fused silica	4.0	-4	customized*
2-achromatic Hastingtriplett	N-F2/N-BK7/N-F2	12.5	20	MgF$_2$: 400-700 nm
3-plano-concave	fused silica	12.0	-50	customized
4-achromatic doublet	N-FK5/N-F2	12.5	40	AR: 345-700 nm

and the 2.16 mm thick vacuum window.
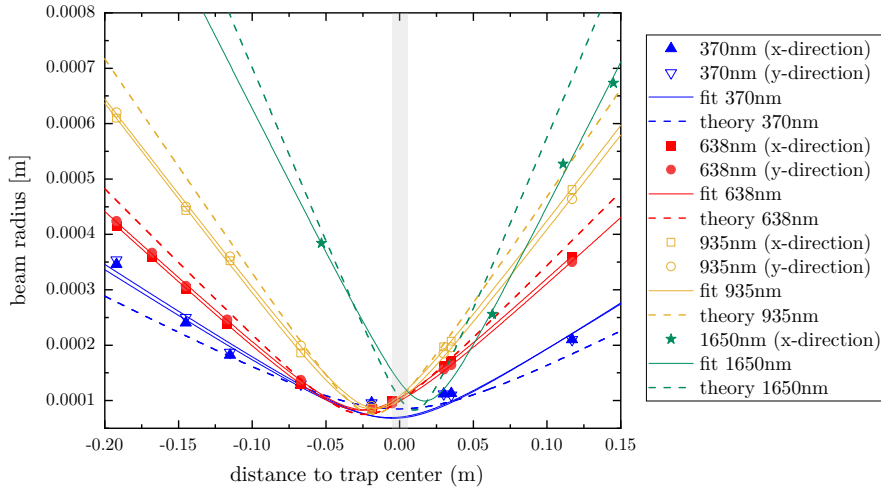
Figure A.13.: *Measurements and calculations of the beam radius of the axial beams behind the achromatic outcoupler without the vacuum window and the beam combiner. The grey area indicates the trapping region of the trap. For all wavelengths except the 1650 nm the beam size was measured in two directions with a camera but for the 1650 nm laser the size was determined with a knife edge and a photodiode and only one direction was measured.*

Figure A.13 and Table A.5 show the result of waists measurements of all four wavelengths and the theoretical calculations performed with the ray tracing software. The measurements have been done without the vacuum window and the beam combiner and this is also considered in the theoretical values. The two additional components only increase the waist positions on the z-axis by 3 mm. For all wavelength except the 1650 nm the beam size was measured in two directions with a camera but for the 1650 nm laser the size was determined with a knife edge and a photodiode and only one direction has been measured. The gray area indicates the trapping region of the trap. The theoretical waists of all wavelengths lay

A. Appendix

Table A.5.: *Measurements and calculations of the beam radius of the axial beams behind the achromatic outcoupler without the vacuum window and the beam combiner. Apart from the measured waists ω_x and ω_y in two directions, the waist positions relative to the trap center and the beam radius ω_{center} at the center the respective simulated values ω_{theo} and $\omega_{\mathrm{center,theo}}$ are listed for all wavelengths. In addition the wavelength dependent mode field diameter MFD of the fiber is listed.*

λ (nm)	MFD (μm)	ω_x /ω_y (μm)	position of ω_x /ω_y	ω_{center} (μm)
370	8.3	$68 \pm 3/69 \pm 3$	$-4.5 \pm 5.3/-6.3 \pm 5.3$	70
638	8.5	$83 \pm 1/83 \pm 1$	$-26.3 \pm 0.1/-22.7 \pm 0.3$	103
935	8.7	$85 \pm 1/86 \pm 1$	$-19.2 \pm 0.5/-15.5 \pm 0.5$	105
1650	9.2	99 ± 3	17.0 ± 2.0	134

λ (nm)		ω_{theo} (μm)	position of ω_{theo}	$\omega_{\mathrm{center,theo}}$ (μm)
370		85	-1	85
638		75	-24	98
935		76	-18	104
1650		83	10	105

between $75\,\mu$m and $85\,\mu$m but the waist positions are at slightly different positions (between -24 mm and 10 mm) on the z-axis. The measured waists ω of the wavelengths λ show a larger variation than theory predicts and lay between $70\,\mu$m and $100\,\mu$m and also the waist positions spread over a larger span (from -26 mm to 17 mm). Nevertheless the beam radii of all wavelengths are with $70\,\mu$m to $150\,\mu$m within the complete trapping region in a convenient range. A better agreement with the theory can most likely be achieved by slightly changing the distance between the first lens and the fiber tip as the resulting beam shape is very sensitive to this distance.

The achromatic lens triplet (lens 2) and doublet (lens 4) both feature a coating, optimized for the visible wavelength range. The reflectivity for the two IR wavelengths is not specified and has been estimated from the course of the coating curves, which are steep in that wavelength range so the estimates have a large uncertainty. Table A.6 summarizes the (estimated) transmission through each lens for the four involved wavelength considering the coating of both surfaces. The transmission through the complete achromatic outcoupler has also been measured and agrees well with the total transmission calculated from the estimated individual transmissions.

Compared to the system characterized in [164] lacking the customized coating optimized for 370 nm the transmission at 935 nm and 1650 nm is lower, which has been unavoidable

Table A.6.: *Transmission through the individual lenses of the achromatic fiber outcoupler for the four involved wavelength. The measured transmissions agree well with the estimated individual transmissions from the coating curves.*

lens	$T_{370\,nm}$	$T_{638\,nm}$	$T_{935\,nm}$	$T_{1650\,nm}$
1	0.90	0.90	0.80	0.81
2	$\approx$0.86	0.97	$\approx$0.95	$\approx$0.9
3	1.0	0.84	0.78	0.81
4	0.98	0.71	<0.94	<0.90
total	0.75	0.71	$\approx$0.55	$\approx$0.53
measured	0.70	0.78	0.54	0.46

when keeping the reflectivity at 370 nm minimal. The transmission at 370 nm has not been characterized for the system without the customized lens coating.

Beam size of the clock laser at the ions position

The collimated beam behind the fiber outcoupler has a $1/e^2$ waist of $\approx$410 μm which should result in a waist of 55 μm at the position of the ions with the 300 mm focussing lens for the radial direction. For the axial direction an additional -150 mm cylindrical lens is implemented which should lead to a waist of $\approx$820 μm to illuminate even larger linear ion chains uniformly. To align the clock laser to the ions the only 6 nm detuned In$^+$ detection laser is sent through the same fiber as the clock laser. The coupling is achieved with a self-built flip mirror in front of the fiber that normally guides the light to the horizontal plane of the trap (see Fig.A.7). Figure A.14 shows an EMCCD image of the the vertical (radial) illumination of a linear 8 In$^+$/5 Yb$^+$ crystal with the In$^+$ detection laser and the line profile along the horizontal direction summed over three pixels (indicated in red). The line profile shows a decreasing brightness of the In$^+$ ions at both edges while the spread of the two outer In$^+$ ions is 100 μm only which is far less than the estimated beam waist of $\approx$820 μm. Checking the beam size with a paper in front of and behind the vacuum chamber reveals a distinct elongated beam shape. Before performing spectroscopy on longer ion chains the beam shape has to be measured and adapted if necessary.

A. Appendix
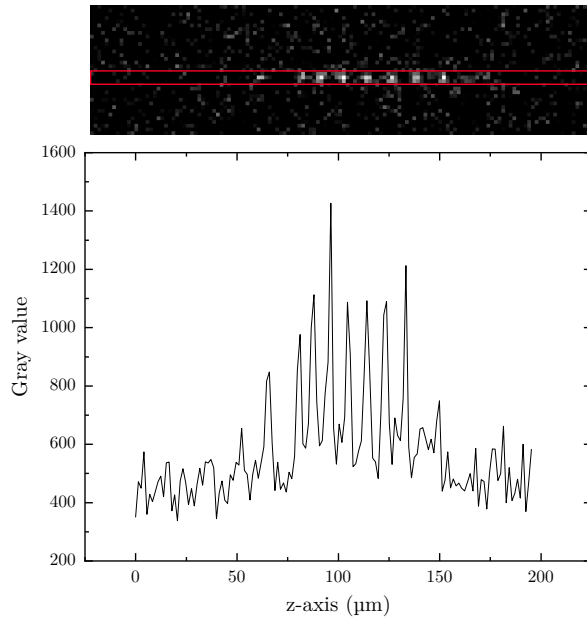
Figure A.14.: *EMCCD image of the vertical illumination of a linear 8 In$^+$/5 Yb$^+$ crystal with the In$^+$ detection laser through the beam path of the clock laser. The lower graph is the horizontal line profile summed over three pixels in the vertical direction (indicated by the red rectangle in the EMCCD image). The brightness of the outer In$^+$ ions decreases at both sides, indicating that the beam radius is distinctly smaller than the estimated $\approx 820\,\mu m$.*

A.3. Homogeneity of the magnetic field coils

The calculated spatial variation of the magnetic field coils can be seen in Fig. A.15.
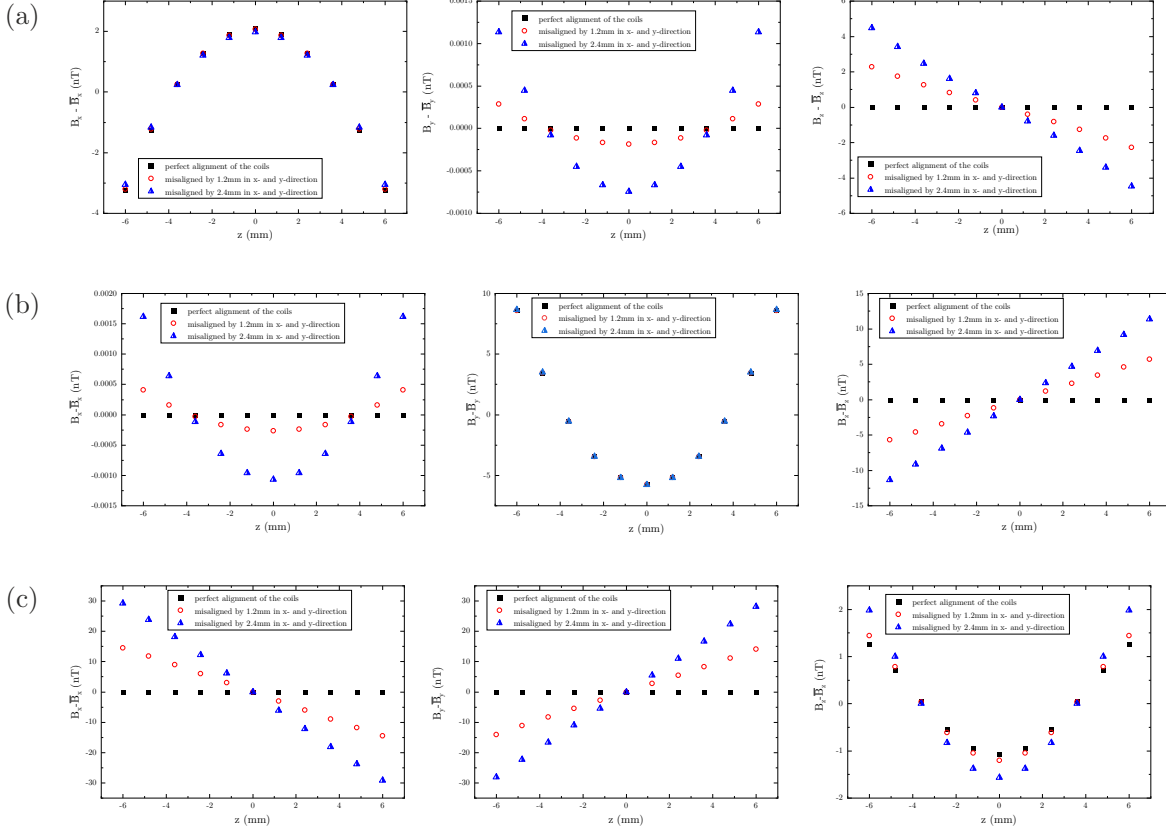
Figure A.15.: *Calculated spatial variation of the magnetic field components B_x, B_y and B_z along the z direction for all three coil pairs: (a) B_x coils, (b) B_y coils and (c) B_z coils. The graphs show the difference between the magnetic field component B and the average $\overline{B}$ component of the respective direction along the z-direction. In addition to an optimal alignment, a displacement of both coils by 1.2 mm (2.4 mm) in x- and y-direction is assumed.*

A.4. Tolerances of the detection system

In the following all components apart from the two doublets are assumed to be perfect. Table A.7 summarizes realistic tolerances for the center thickness and the radius of the front and back side of the four lenses, given by the manufacturer. With these tolerances the encircled energy reduces slightly to $f_{ee}(r_c = 8\,\mu m) = 0.95$ for both wavelengths.

The four lenses form two doublets (S1+AS1 and S2 and AS2), each set in its own mount. More details about the mounting of the lenses are given in section 3.6.4. In Tab. A.8 tolerances for the mounting of the lenses are given, which already represent the limits of manufacturing

A. Appendix

Table A.7.: *Tolerances for center thickness and radii of the lenses. The specified values refer to a reference wavelength of 546 nm, so 1 fringe (fr) = 273 nm. For the curved back sides of the lenses an absolute radius tolerance is given in addition to the power tolerance.*

Lens	Power tolerance front side (fr)	Power tolerance back side (fr)	Center thickness tolerance (μm)
S1	1	1 (1μm)	±50
AS1	1	1 (3μm)	±50
S2	1	1 (3μm)	±50
AS2	1	1 (3μm)	±20

feasibility.

Table A.8.: *Tolerances for tilts and decentering of the lenses.*

Tolerance	Value
Distance of the plane surfaces within one mount	$\pm\,30\,\mu$m
Decentering of mount S1+AS1	$\pm50\,\mu$m
Decentering of mount S2+AS2	$\pm50\,\mu$m
Tilt of mount S1+AS1	$\pm2\,$arcmin
Tilt of mount S2+AS2	$\pm1\,$arcmin
Tilting of the plan support for S1	$\pm2\,$arcmin
Tilting of the plan support for AS1	$\pm2\,$arcmin
Tilting of the plan support for S2	$\pm2\,$arcmin
Tilting of the plan support for AS2	$\pm2\,$arcmin
Tilting front to back S1	$\pm2\,$arcmin
Tilting front to back AS1	$\pm2\,$arcmin
Tilting front to back S2	$\pm2\,$arcmin
Tilting front to back AS2	$\pm2\,$arcmin

With these tolerances $f_{ee}(r_c = 8\,\mu\text{m}) = 0.8$ for the 230.6 nm path and $f_{ee}(r_c = 8\,\mu\text{m}) = 0.7$ for the 369.5 nm path in worst case as shown in Fig. 3.17. Hereby worst case means the worst

result out of 4000 combinations of all mentioned tolerances. This means the expected fluorescence yield on one pixel is reduced to 80% and 70 % at 230.6 nm and 369.5 nm, respectively.

In addition to the tolerances mentioned above, surface form tolerances must also be taken into account. These are given in Tab.A.9 and reduce the fluorescence enclosed in a radius $r_\mathrm{c} = 8\,\mu\mathrm{m}$ by another 8 %, resulting in $f_\mathrm{ee,tol}(r_\mathrm{c,tol} = 8\,\mu\mathrm{m}) \approx 0.7$ and $f_\mathrm{ee,tol}(r_\mathrm{c,tol} = 8\,\mu\mathrm{m}) \approx 0.6$ for the 230.6 nm and 369.5 nm, respectively. As mentioned in section 3.6.2 the beamsplitter (BS) and wedged substrate (WS) in the 369.5 nm path, as well as the vacuum window (W), are not considered in the tolerancing process. However, transmitting elements exhibit a large influence on aberrations, so the actual performance will probably be worse.

Table A.9.: *Surface form tolerances of the lenses. The specified values refer to a reference wavelength of 546 nm, so 1 fringe (fr) = 273 nm.*

Lens	Irregularity front side (fr)	RMSi front side (nm)	Irregularity back side (fr)	RMSi back side (nm)
S1	0.5	<20	0.7	<30
AS1	0.5	<25	0.5	<25
S2	0.7	<30	0.8	<35
AS1	1.0	<40	0.8	<35

Acronyms

AOM acousto-optic modulator

BBO beta-barium borate

BBR black-body radiation

COM center of mass

ECDL external-cavity diode laser

EMCCD electron-multiplying CCD

EMM excess micromotion

EOM electro-optic modulator

FEM finite-element method

FPGA field-programmable gate array

LMA large mode area

OHFC oxygen-free high conductivity

PDH Pound-Drever-Hall[235]

PMT photomultiplier tube

PPKTP periodically poled potassium titanyl phosphate

PTB Physikalisch-Technische Bundesanstalt, national metrology institute of Germany

rf radio-frequency

ROI region of interest

SBC sideband cooling

SHG second-harmonic generation

FHG fourth-harmonic generation

SNR signal-to-noise ratio

SSC sine-to-square converter

Acronyms

TA tapered amplifier

TDC time-to-digital converter

Bibliography

[1]   F. L. Walls and J. R. Vig, "Fundamental limits on the frequency stabilities of crystal oscillators", *IEEE Transactions on Ultrasonics, Ferroelectrics, and Frequency Control* **42**, 576–589 (1995) (cit. on p. 1).

[2]   J. Terrien, "News from the International Bureau of Weights and Measures", *Metrologia* **4**, 41–45 (1968) (cit. on p. 1).

[3]   J. C. Maxwell, *The scientific papers of James Clerk Maxwell*, ed. by W. D. Niven, vol. II, Cambridge University Press, 1890 (cit. on p. 1).

[4]   A. L. Schawlow and C. H. Townes, "Infrared and Optical Masers", *Phys. Rev.* **112**, 1940–1949 (1958) (cit. on p. 1).

[5]   T. H. Maiman, "Stimulated Optical Radiation in Ruby", *Nature* **187**, 493–494 (1960) (cit. on p. 1).

[6]   T. W. Hänsch and A. L. Schawlow, "Cooling of gases by laser radiation", *Opt. Commun.* **13**, 68 (1975) (cit. on p. 1).

[7]   D. J. Wineland and H. Dehmelt, "Proposed $10^{14} \delta\nu/\nu$ laser fluorescence spectroscopy on Tl^+ mono-ion oscillator III (sideband cooling)", *Bull. Am. Phys. Soc.* **20**, 637 (1975) (cit. on pp. 1, 21).

[8]   D. J. Wineland, R. E. Drullinger, and F. L. Walls, "Radiation-Pressure Cooling of Bound Resonant Absorbers", *Phys. Rev. Lett.* **40**, 1639–1642 (1978) (cit. on p. 1).

[9]   D. J. Wineland and W. M. Itano, "Laser cooling of atoms", *Phys. Rev. A* **20**, 1521–1540 (1979) (cit. on pp. 1, 15, 16, 21).

[10] J. Guéna et al., "First international comparison of fountain primary frequency standards via a long distance optical fiber link", *Metrologia* **54**, 348–354 (2017) (cit. on p. 1).

[11] B. C. Young et al., "Visible Lasers with Subhertz Linewidths", *Phys. Rev. Lett.* **82**, 3799–3802 (1999) (cit. on p. 1).

[12] T. Udem, R. Holzwarth, and T. W. Hänsch, "Optical frequency metrology", *Nature* **416**, 233–237 (2002) (cit. on pp. 1, 5).

[13] B. J. Bloom et al., "An optical lattice clock with accuracy and stability at the 10^{-18} level", *Nature* **506**, 71–75 (2014) (cit. on p. 1).

[14] W. F. McGrew et al., "Atomic clock performance enabling geodesy below the centimetre level", *Nature* **564**, 87–90 (2018) (cit. on p. 1).

[15] T. Bothwell et al., "JILA SrI optical lattice clock with uncertainty of 2.0×10^{-18}", *Metrologia* **56**, 065004 (2019) (cit. on p. 1).

Bibliography

[16]   M. Takamoto et al., "Test of general relativity by a pair of transportable optical lattice clocks", *Nature Photonics* , 1–5 (2020) (cit. on pp. 1, 2).

[17]   N. Ohmae et al., "Transportable Strontium Optical Lattice Clocks Operated Outside Laboratory at the Level of 10^{-18} Uncertainty", *Advanced Quantum Technologies* **4**, 2100015 (2021) (cit. on p. 1).

[18]   S. M. Brewer et al., "^{27}Al^{+} Quantum-Logic Clock with a Systematic Uncertainty below 10^{-18}", *Phys. Rev. Lett.* **123**, 033201 (2019) (cit. on pp. 1, 6, 8, 22, 28).

[19]   N. Huntemann et al., "Single-Ion Atomic Clock with 3×10^{-18} Systematic Uncertainty", *Phys. Rev. Lett.* **116**, 063001 (2016) (cit. on pp. 1, 8, 22, 28, 135, 139, 143–145).

[20]   N. Herschbach et al., "Linear Paul trap design for an optical clock with Coulomb crystals", *Appl. Phys. B* **107**, 891–906 (2012) (cit. on pp. 1, 10, 26, 32, 80, 141).

[21]   K. Pyka et al., "A high-precision segmented Paul trap with minimized micromotion for an optical multiple-ion clock", *Appl. Phys. B* **114**, 231–241 (2014) (cit. on pp. 1, 32, 141).

[22]   T. Burgermeister, "Development and characterization of a linear ion trap for an improved optical clock performance", PhD thesis, Gottfried Wilhelm Leibniz Universität Hannover, QUEST-Leibniz-Forschungsschule, 2019 (cit. on pp. 1, 11, 12, 32, 35–37, 73, 74, 76, 80–83, 88, 91, 93, 97, 141).

[23]   J. Keller et al., "Probing Time Dilation in Coulomb Crystals in a High-Precision Ion Trap", *Phys. Rev. Applied* **11**, 011002 (2019) (cit. on pp. 1, 31, 79).

[24]   Kyle Arnold et al., "Prospects for atomic clocks based on large ion crystals", *Phys. Rev. A* **92**, 032108 (2015) (cit. on pp. 2, 29).

[25]   Nati Aharon et al., "Robust optical clock transitions in trapped ions using dynamical decoupling", *New Journal of Physics* **21**, 083040 (2019) (cit. on pp. 2, 29).

[26]   L. Pelzer et al., "Tailored optical clock transition in ^{40}Ca^{+}", *Measurement: Sensors* **18**, 100326 (2021) (cit. on pp. 2, 29).

[27]   T. Rosenband and D. R. Leibrandt, "Exponential scaling of clock stability with atom number", arXiv:1303.6357 (2013) (cit. on pp. 2, 8, 29).

[28]   J. Borregaard and A. S. Sørensen, "Efficient Atomic Clocks Operated with Several Atomic Ensembles", *Phys. Rev. Lett.* **111**, 090802 (2013) (cit. on pp. 2, 8, 29).

[29]   D. B. Hume and D. R. Leibrandt, "Probing beyond the laser coherence time in optical clock comparisons", *Phys. Rev. A* **93**, 032138 (2016) (cit. on pp. 2, 29).

[30]   D. J. Wineland et al., "Spin squeezing and reduced quantum noise in spectroscopy", *Phys. Rev. A* **46**, R6797–R6800 (1992) (cit. on pp. 2, 7, 9).

[31]   D. J. Wineland et al., "Squeezed atomic states and projection noise in spectroscopy", *Phys. Rev. A* **50**, 67–88 (1994) (cit. on pp. 2, 7, 9).

[32]   A. André, A. S. Sørensen, and M. D. Lukin, "Stability of Atomic Clocks Based on Entangled Atoms", *Phys. Rev. Lett.* **92**, 230801 (2004) (cit. on pp. 2, 7, 9).

[33] J. J . Bollinger et al., "Optimal frequency measurements with maximally correlated states", *Phys. Rev. A* **54**, R4649–R4652 (1996) (cit. on pp. 2, 7, 9).

[34] Dietrich Leibfried et al., "Toward Heisenberg-limited spectroscopy with multiparticle entangled states", *Science* **304**, 1476–1478 (2004) (cit. on pp. 2, 7, 9).

[35] R. Shaniv et al., "Toward Heisenberg-Limited Rabi Spectroscopy", *Phys. Rev. Lett.* **120**, 243603 (2018) (cit. on pp. 2, 7, 9).

[36] M. Vermeer, *Chronometric Levelling*, Reports of the Finnish Geodetic Institute, Geodeettinen Laitos, Geodetiska Institutet, 1983 (cit. on p. 2).

[37] A. Bjerhammar, "On a relativistic geodesy", *Bulletin géodésique* **59**, 207–220 (1985) (cit. on p. 2).

[38] J. Müller et al., "High performance clocks and gravity field determination", *Space Science Reviews* **214**, 1–31 (2018) (cit. on p. 2).

[39] T. E Mehlstäubler et al., "Atomic clocks for geodesy", *Reports on Progress in Physics* **81**, 064401 (2018) (cit. on p. 2).

[40] C. W. Chou et al., "Optical Clocks and Relativity", *Science* **329**, 1630–1633 (2010) (cit. on p. 2).

[41] N. Poli et al., "A transportable strontium optical lattice clock", *Applied Physics B* **117**, 1107–1116 (2014) (cit. on p. 2).

[42] J. Cao et al., "A compact, transportable optical clock with 1×10^{-17} uncertainty and its absolute frequency measurement", *Applied Physics Letters* **120**, 054003 (2022) (cit. on p. 2).

[43] R. M. Godun et al., "Frequency Ratio of Two Optical Clock Transitions in ^{171}Yb$^+$ and Constraints on the Time Variation of Fundamental Constants", *Phys. Rev. Lett.* **113**, 210801 (2014) (cit. on p. 2).

[44] N. Huntemann et al., "Improved Limit on a Temporal Variation of m_p/m_e from Comparisons of Yb$^+$ and Cs Atomic Clocks", *Phys. Rev. Lett.* **113**, 210802 (2014) (cit. on p. 2).

[45] M. S. Safronova et al., "Search for new physics with atoms and molecules", *Rev. Mod. Phys.* **90**, 025008 (2018) (cit. on p. 2).

[46] C. Sanner et al., "Optical clock comparison for Lorentz symmetry testing", *Nature* **567**, 204–208 (2019) (cit. on p. 2).

[47] R. Lange et al., "Improved Limits for Violations of Local Position Invariance from Atomic Clock Comparisons", *Phys. Rev. Lett.* **126**, 011102 (2021) (cit. on p. 2).

[48] K. Beloy et al., "Frequency ratio measurements at 18-digit accuracy using an optical clock network", *Nature* **591**, 564–569 (2021) (cit. on p. 2).

[49] E. Peik and C. Tamm, "Nuclear laser spectroscopy of the 3.5 eV transition in Th-229", *Europhysics Letters* **61**, 181 (2003) (cit. on p. 2).

[50] C. J. Campbell et al., "Single-Ion Nuclear Clock for Metrology at the 19th Decimal Place", *Phys. Rev. Lett.* **108**, 120802 (2012) (cit. on p. 2).

Bibliography

[51] B. Seiferle et al., "Energy of the 229Th nuclear clock transition", *Nature* **573**, 243–246 (2019) (cit. on p. 2).

[52] S. Kraemer et al., "Observation of the radiative decay of the ^{229}Th nuclear clock isomer", arXiv:2209.10276 (2022) (cit. on p. 2).

[53] K. Beloy, V. A. Dzuba, and S. M. Brewer, "Quadruply Ionized Barium as a Candidate for a High-Accuracy Optical Clock", *Phys. Rev. Lett.* **125**, 173002 (2020) (cit. on p. 2).

[54] P. Micke et al., "Coherent laser spectroscopy of highly charged ions using quantum logic", *Nature* **578**, 60–65 (2020) (cit. on p. 2).

[55] S. A. King et al., "Algorithmic Ground-State Cooling of Weakly Coupled Oscillators Using Quantum Logic", *Phys. Rev. X* **11**, 041049 (2021) (cit. on p. 2).

[56] J. R. Crespo López-Urrutia, "Frequency metrology using highly charged ions", *Journal of Physics: Conference Series* **723**, 012052 (2016) (cit. on p. 2).

[57] M. G. Kozlov et al., "Highly charged ions: Optical clocks and applications in fundamental physics", *Rev. Mod. Phys.* **90**, 045005 (2018) (cit. on p. 2).

[58] E Peik et al., "Nuclear clocks for testing fundamental physics", *Quantum Science and Technology* **6**, 034002 (2021) (cit. on p. 2).

[59] A. W. Young et al., "Half-minute-scale atomic coherence and high relative stability in a tweezer clock", *Nature* **588**, 408–413 (2020) (cit. on p. 2).

[60] Fritz Riehle, "Towards a redefinition of the second based on optical atomic clocks", *Comptes Rendus Physique* **16**, 506–515 (2015) (cit. on p. 2).

[61] Patrick Gill, "Is the time right for a redefinition of the second by optical atomic clocks?", *Journal of Physics: Conference Series* **723**, 012053 (2016) (cit. on p. 2).

[62] CCTF (Consultative Committee for Time and Frequency), *Strategy Document*, 2016, `https://www.bipm.org/documents/20126/35554894/CCTF+Strategy/7cf0f648-2afe-d15c-0909-1f03406bbb8f`, (accessed: 2022-12-04) (cit. on p. 2).

[63] Bureau International des Poids et Mesures, *The International System of Units(SI)*, 2019, `https://www.bipm.org/documents/20126/41483022/SI-Brochure-9-EN.pdf`, (accessed: 2022-12-04) (cit. on p. 2).

[64] J. L. Hall, "Nobel Lecture: Defining and measuring optical frequencies", *Rev. Mod. Phys.* **78**, 1279–1295 (2006) (cit. on p. 5).

[65] Theodor W. Hänsch, "Nobel Lecture: Passion for precision", *Rev. Mod. Phys.* **78**, 1297–1309 (2006) (cit. on p. 5).

[66] S. Dörscher et al., "Optical frequency ratio of a ^{171}Yb^{+} single-ion clock and a ^{87}Sr lattice clock", *Metrologia* **58**, 015005 (2021) (cit. on p. 6).

[67] Andrew D. Ludlow et al., "Optical atomic clocks", *Rev. Mod. Phys.* **87**, 637–701 (2015) (cit. on pp. 6, 22, 26).

[68] D.W. Allan, "Statistics of atomic frequency standards", *Proceedings of the IEEE* **54**, 221–230 (1966) (cit. on p. 6).

[69]   F. Riehle, *Frequency standards: basics and applications*, John Wiley & Sons, 2006 (cit. on pp. 6, 17, 18).

[70]   N. F. Ramsey, "A Molecular Beam Resonance Method with Separated Oscillating Fields", *Phys. Rev.* **78**, 695–699 (1950) (cit. on p. 7).

[71]   W. Nagourney, J. Sandberg, and H. Dehmelt, "Shelved optical electron amplifier: Observation of quantum jumps", *Phys. Rev. Lett.* **56**, 2797–2799 (1986) (cit. on pp. 7, 9, 46, 89).

[72]   W. M. Itano et al., "Quantum projection noise: Population fluctuations in two-level systems", *Phys. Rev. A* **47**, 3554–3570 (1993) (cit. on p. 7).

[73]   C. Champenois et al., "Evaluation of the ultimate performances of a Ca^+ single-ion frequency standard", *Physics Letters A* **331**, 298–311 (2004) (cit. on p. 7).

[74]   E. Riis and A. G. Sinclair, "Optimum measurement strategies for trapped ion optical frequency standards", *Journal of Physics B: Atomic, Molecular and Optical Physics* **37**, 4719 (2004) (cit. on p. 7).

[75]   E. Peik, T. Schneider, and C. Tamm, "Laser frequency stabilization to a single ion", *J. Phys. B* **39**, 145–158 (2006) (cit. on pp. 7, 135, 136, 145).

[76]   N. Yu, H. Dehmelt, and W. Nagourney, "The 31S0-33P0 transition in the aluminum isotope ion 26A1+: a potentially superior passive laser frequency standard and spectrum analyzer.", *Proceedings of the National Academy of Sciences* **89**, 7289 (1992) (cit. on p. 8).

[77]   E. Peik, G. Hollemann, and H. Walther, "Laser cooling and quantum jumps of a single indium ion", *Phys. Rev. A* **49**, 402–408 (1994) (cit. on pp. 8, 9).

[78]   H. G. Dehmelt, "Monoion oscillator as potential ultimate laser frequency standard", *IEEE Transactions on Instrumentation and Measurement* **IM-31**, 83–87 (1982) (cit. on p. 8).

[79]   T. Becker et al., "High-resolution spectroscopy of a single In^+ ion: Progress towards an optical frequency standard", *Phys. Rev. A* **63**, 051802 (2001) (cit. on pp. 9, 25, 28, 57, 133).

[80]   P. O. Schmidt et al., "Spectroscopy Using Quantum Logic", *Science* **309**, 749–752 (2005) (cit. on pp. 9, 28).

[81]   D. B. Hume et al., "Trapped-Ion State Detection through Coherent Motion", *Phys. Rev. Lett.* **107**, 243902 (2011) (cit. on p. 9).

[82]   M. Schulte et al., "Quantum Algorithmic Readout in Multi-Ion Clocks", *Phys. Rev. Lett.* **116**, 013002 (2016) (cit. on p. 9).

[83]   E. R. Clements et al., "Lifetime-Limited Interrogation of Two Independent $^{27}Al^+$ Clocks Using Correlation Spectroscopy", *Phys. Rev. Lett.* **125**, 243602 (2020) (cit. on p. 9).

[84]   S. G. Porsev and A. Derevianko, "Multipolar theory of blackbody radiation shift of atomic energy levels and its implications for optical lattice clocks", *Phys. Rev. A* **74**, 020502 (2006) (cit. on pp. 9, 24).

Bibliography

[85] M. S. Safronova, M. G. Kozlov, and Charles W. Clark, "Precision Calculation of Blackbody Radiation Shifts for Optical Frequency Metrology", *Phys. Rev. Lett.* **107**, 143006 (2011) (cit. on pp. 9, 24, 25, 28, 145).

[86] K. Beloy, D. R. Leibrandt, and W. M. Itano, "Hyperfine-mediated electric quadrupole shifts in Al$^+$ and In$^+$ ion clocks", *Phys. Rev. A* **95**, 043405 (2017) (cit. on pp. 9, 26, 28).

[87] K. Wakui, K. Hayasaka, and T. Ido, "Generation of vacuum ultraviolet radiation by intracavity high-harmonic generation toward state detection of single trapped ions", *Applied Physics B* **117** (2014) (cit. on p. 9).

[88] J. Wübbena et al., "Sympathetic Cooling of Mixed Species Two-Ion Crystals for Precision Spectroscopy", *Physical Review A* **85** (2012) (cit. on pp. 10, 19, 103, 106).

[89] E. Peik et al., "Sideband cooling of ions in radio-frequency traps", *Phys. Rev. A* **60**, 439–449 (1999) (cit. on pp. 10, 119, 122, 145).

[90] J. Keller et al., "Controlling systematic frequency uncertainties at the 10^{-19} level in linear Coulomb crystals", *Phys. Rev. A* **99**, 013405 (2019) (cit. on pp. 10, 22, 24, 26, 32, 61, 91, 97, 103, 107, 117, 141).

[91] P. K. Ghosh, *Ion traps*, Oxford Univeristy Press, 1995 (cit. on p. 10).

[92] F. G. Major, V. N. Gheorghe, and G. Werth, *Charged Particle Traps*, Springer-Verlag, 2005 (cit. on pp. 10, 11).

[93] S. Earnshaw, "On the nature of the molecular forces which regulate the constitution of the luminiferous ether", *Transactions of the Cambridge Philosophical Society* **7**, 97 (1848) (cit. on p. 10).

[94] W. J. Paul, H. P. Reinhard, and U. von Zahn, "Das elektrische Massenfilter als Massenspektrometer und Isotopentrenner", *Zeitschrift für Physik* **152**, 143–182 (1958) (cit. on p. 10).

[95] Wolfgang Paul, "Electromagnetic traps for charged and neutral particles", *Rev. Mod. Phys.* **62**, 531–540 (1990) (cit. on pp. 10, 104).

[96] F. Diedrich et al., "Observation of a Phase Transition of Stored Laser-Cooled Ions", *Phys. Rev. Lett.* **59**, 2931–2934 (1987) (cit. on p. 13).

[97] D. J. Wineland et al., "Atomic-Ion Coulomb Clusters in an Ion Trap", *Phys. Rev. Lett.* **59**, 2935–2938 (1987) (cit. on p. 13).

[98] G. Morigi and H. Walther, "Two-species Coulomb chains for quantum information", *European Physical Journal D* **13**, 261–269 (2001) (cit. on pp. 13, 15, 16, 19, 103, 106).

[99] D. F. V. James, "Quantum dynamics of cold trapped ions with application to quantum computation", *Appl. Phys. B* **66**, 181–190 (1998) (cit. on pp. 13, 88).

[100] D. Kielpinski et al., "Sympathetic cooling of trapped ions for quantum logic", *Phys. Rev. A* **61**, 032310 (2000) (cit. on pp. 13, 19, 23, 106).

[101] D. Leibfried et al., "Quantum dynamics of single trapped ions", *Rev. Mod. Phys.* **75**, 281–324 (2003) (cit. on pp. 15, 18, 19).

[102] J. Keller, "Spectroscopic characterization of ion motion for an optical clock based on Coulomb crystals", PhD thesis, Gottfried Wilhelm Leibniz Universität Hannover, QUEST-Leibniz-Forschungsschule, 2015 (cit. on pp. 15, 47, 48, 50, 76–78, 90, 91, 141, 156).

[103] C. Cohen-Tannoudji, *Atoms In Electromagnetic Fields (2nd edition)*, World Scientific Publishing Company, 2004 (cit. on p. 15).

[104] R. H. Dicke, "The Effect of Collisions upon the Doppler Width of Spectral Lines", *Phys. Rev.* **89**, 472–473 (1953) (cit. on p. 16).

[105] I. Lizuain, J. G. Muga, and J. Eschner, "Motional frequency shifts of trapped ions in the Lamb-Dicke regime", *Phys. Rev. A* **76**, 033808 (2007) (cit. on p. 16).

[106] H. J. Lipkin, *Quantum mechanics*, North-Holland Publishing, Amsterdam, 1973 (cit. on p. 17).

[107] D. A. Steck, *Quantum and atom optics*, 2007, `http://steck.us/teaching` (cit. on p. 17).

[108] J. Eschner et al., "Laser cooling of trapped ions", *J. Opt. Soc. Am. B* **20**, 1003–1015 (2003) (cit. on pp. 18, 21).

[109] W. M. Itano and D. J. Wineland, "Laser cooling of ions stored in harmonic and Penning traps", *Phys. Rev. A* **25**, 35–54 (1982) (cit. on p. 18).

[110] J. Javanainen, "Light-pressure cooling of trapped ions in three dimensions", *Applied physics* **23** (1980) (cit. on p. 19).

[111] M. D. Barrett et al., "Sympathetic cooling of ^{9}Be$^+$ and ^{24}Mg$^+$ for quantum logic", *Phys. Rev. A* **68**, 042302 (2003) (cit. on pp. 19, 106).

[112] I. Marzoli et al., "Laser cooling of trapped three-level ions: Designing two-level systems for sideband cooling", *Phys. Rev. A* **49**, 2771–2779 (1994) (cit. on pp. 21, 47).

[113] Q. A. Turchette et al., "Heating of trapped ions from the quantum ground state", *Phys. Rev. A* **61**, 063418 (2000) (cit. on pp. 23, 91).

[114] D Kalincev et al., "Motional heating of spatially extended ion crystals", *Quantum Science and Technology* **6**, 034003 (2021) (cit. on pp. 23, 88, 91, 93, 97).

[115] D. J. Berkeland et al., "Minimization of ion micromotion in a Paul trap", *J. Appl. Phys.* **83**, 5025–5033 (1998) (cit. on pp. 23, 28, 76).

[116] M. von Boehn, "Modelling of symathetic Doppler cooling and analysis of probe field induced ac-Stark shifts in an ^{115}In$^+$ optical clock", Master thesis, Gottfried Wilhelm Leibniz Universität Hannover, 2022 (cit. on pp. 24, 130, 132).

[117] T. Nordmann et al., "Sub-kelvin temperature management in ion traps for optical clocks", *Review of Scientific Instruments* **91**, 111301 (2020) (cit. on pp. 25, 32, 93–97).

[118] Y. Ting and D. Williams, "Nuclear Gyromagnetic Ratios. IV", *Phys. Rev.* **89**, 595–596 (1953) (cit. on pp. 25, 28, 57).

[119] W. M. Itano, "External-Field Shifts of the ^{199}Hg$^+$ Optical Frequency Standard", *J. Res. Natl. Inst. Stand. Technol.* **105**, 829–837 (2000) (cit. on pp. 26, 29).

Bibliography

[120] T. R. Tan et al., "Suppressing Inhomogeneous Broadening in a Lutetium Multi-ion Optical Clock", *Phys. Rev. Lett.* **123**, 063201 (2019) (cit. on pp. 26, 29).

[121] A. M. Hankin et al., "Systematic uncertainty due to background-gas collisions in trapped-ion optical clocks", *Phys. Rev. A* **100**, 033419 (2019) (cit. on p. 27).

[122] A. Vutha, T. Kirchner, and P. Dub, "Doppler and collisional frequency shifts in trapped-atom clocks", arXiv:1812.00973 (2018) (cit. on p. 27).

[123] T. Rosenband et al., "Frequency Ratio of Al^+ and Hg^+ Single-Ion Optical Clocks; Metrology at the 17th Decimal Place", *Science* **319**, 1808– (2008) (cit. on p. 27).

[124] A. C. Vutha, T. Kirchner, and P. Dubé, "Collisional frequency shift of a trapped-ion optical clock", *Phys. Rev. A* **96**, 022704 (2017) (cit. on p. 27).

[125] T. Rosenband et al., "Observation of the $^1S_0 \rightarrow ^3P_0$ Clock Transition in $^{27}Al^+$", *Phys. Rev. Lett.* **98**, 220801 (2007) (cit. on p. 28).

[126] C. F. Roos et al., "Designer atoms for quantum metrology", *Nature* **443**, 316–319 (2006) (cit. on pp. 28, 29).

[127] G. Tommaseo et al., "The gJ-factor in the ground state of Ca^+", *The European Physical Journal D-Atomic, Molecular, Optical and Plasma Physics* **25**, 113–121 (2003) (cit. on p. 28).

[128] M. Chwalla, "Precision spectroscopy with $^{40}Ca^+$ ions in a Paul trap", PhD thesis, Innsbruck: Leopold-Franzens-Universitt Innsbruck, 2009 (cit. on p. 28).

[129] Y. Huang et al., "$^{40}Ca^+$ ion optical clock with micromotion-induced shifts below 1×10^{-18}", *Phys. Rev. A* **99**, 011401 (2019) (cit. on p. 28).

[130] A. Kreuter et al., "Experimental and theoretical study of the $3d$ ^2D–level lifetimes of $^{40}Ca^+$", *Phys. Rev. A* **71**, 032504 (2005) (cit. on p. 28).

[131] G. P. Barwood et al., "Measurement of the Electric Quadrupole Moment of the $4d$ $^2D_{5/2}$ Level in $^{88}Sr^+$", *Phys. Rev. Lett.* **93**, 133001 (2004) (cit. on p. 28).

[132] P. Dubé et al., "High-Accuracy Measurement of the Differential Scalar Polarizability of a $^{88}Sr^+$ Clock Using the Time-Dilation Effect", *Phys. Rev. Lett.* **112**, 173002 (2014) (cit. on pp. 28, 145).

[133] V. Letchumanan et al., "Lifetime measurement of the metastable $4d$ $^2D_{52}$ state in $^{88}Sr^+$ using a single trapped ion", *Phys. Rev. A* **72**, 012509 (2005) (cit. on p. 28).

[134] R. Lange et al., "Coherent Suppression of Tensor Frequency Shifts through Magnetic Field Rotation", *Phys. Rev. Lett.* **125**, 143201 (2020) (cit. on pp. 28, 29).

[135] C. Tamm et al., "Cs-based optical frequency measurement using cross-linked optical and microwave oscillators", *Phys. Rev. A* **89**, 023820 (2014) (cit. on p. 28).

[136] T. Schneider, "Optical Frequency Standard with a single $^{171}Yb^+$ Ion", PhD thesis, Leibniz-Universität Hannover, 2005 (cit. on p. 28).

[137] N. Yu and L. Maleki, "Lifetime measurements of the $4f^{14}5d$ metastable states in single ytterbium ions", *Phys. Rev. A* **61**, 022507 (2000) (cit. on p. 28).

[138]   William F. Meggers, "The second spectrum of Ytterbium (Yb II)", *J. Res. Nat. Bureau Stand. A* **71A**, 396 (1967) (cit. on p. 28).

[139]   R. Lange et al., "Lifetime of the $^2F_{7/2}$ Level in Yb$^+$ for Spontaneous Emission of Electric Octupole Radiation", *Phys. Rev. Lett.* **127**, 213001 (2021) (cit. on pp. 28, 47).

[140]   R. Kaewuam et al., "Precision measurement of the $^3D_1$ and $^3D_2$ quadrupole moments in Lu$^+$", *Phys. Rev. A* **102**, 042819 (2020) (cit. on p. 28).

[141]   Z. Zhiqiang et al., "Hyperfine-mediated effects in a Lu$^+$ optical clock", *Phys. Rev. A* **102**, 052834 (2020) (cit. on p. 28).

[142]   K. J. Arnold et al., "Blackbody radiation shift assessment for a lutetium ion clock", *Nature communications* **9**, 1–6 (2018) (cit. on p. 28).

[143]   K. J. Arnold et al., "Observation of the $^1S_0$ to $^3D_1$ clock transition in ^{175}Lu$^+$", *Phys. Rev. A* **94**, 052512 (2016) (cit. on p. 28).

[144]   E. Paez et al., "Atomic properties of Lu$^+$", *Phys. Rev. A* **93**, 042112 (2016) (cit. on p. 28).

[145]   K. Cui et al., "Scalable quantum logic spectroscopy", *Phys. Rev. Lett.* **129**, 193603 (2022) (cit. on p. 29).

[146]   "Hyper-Ramsey spectroscopy of optical clock transitions", *Phys. Rev. A* **82**, 011804 (2010) (cit. on p. 29).

[147]   N. Huntemann et al., "High-Accuracy Optical Clock Based on the Octupole Transition in ^{171}Yb$^+$", *Phys. Rev. Lett.* **108**, 090801 (2012) (cit. on p. 29).

[148]   P. Dubé et al., "Evaluation of systematic shifts of the ^{88}Sr$^+$ single-ion optical frequency standard at the 10^{-17} level", *Phys. Rev. A* **87**, 023806 (2013) (cit. on p. 29).

[149]   P. Dubé et al., "Electric Quadrupole Shift Cancellation in Single-Ion Optical Frequency Standards", *Phys. Rev. Lett.* **95**, 033001 (2005) (cit. on p. 29).

[150]   G. P. Barwood et al., "Automatic laser control for a ^{88}Sr$^+$ optical frequency standard", *Measurement Science and Technology* **23**, 055201 (2012) (cit. on p. 29).

[151]   M. D. Barrett, "Developing a field independent frequency reference", *New Journal of Physics* **17**, 053024 (2015) (cit. on p. 29).

[152]   R. Shaniv, N. Akerman, and R. Ozeri, "Atomic Quadrupole Moment Measurement Using Dynamic Decoupling", *Phys. Rev. Lett.* **116**, 140801 (2016) (cit. on p. 29).

[153]   R. Shaniv et al., "Quadrupole Shift Cancellation Using Dynamic Decoupling", *Phys. Rev. Lett.* **122**, 223204 (2019) (cit. on p. 29).

[154]   R. Kaewuam et al., "Hyperfine Averaging by Dynamic Decoupling in a Multi-Ion Lutetium Clock", *Phys. Rev. Lett.* **124**, 083202 (2020) (cit. on p. 29).

[155]   M. D. Barrett, K. J. Arnold, and M. S. Safronova, "Polarizability assessments of ion-based optical clocks", *Phys. Rev. A* **100**, 043418 (2019) (cit. on p. 29).

[156]   David R. Leibrandt et al., "Prospects of a thousand-ion Sn^{2+} Coulomb-crystal clock with sub-10^{-19} inaccuracy", arXiv:2205.15484 (2022) (cit. on p. 30).

Bibliography

[157] K. Pyka, "High-precision ion trap for spectroscopy of Coulomb crystals", PhD thesis, Gottfried Wilhelm Leibniz Universität Hannover, Fakultät für Mathematik und Physik, 2013 (cit. on pp. 32, 36, 49).

[158] W. W. Macalpine and R. O. Schildknecht, "Coaxial Resonators with Helical Inner Conductor", *Proceedings of the IRE* **47**, 2099–2105 (1959) (cit. on p. 32).

[159] J. D. Siverns et al., "On the application of radio frequency voltages to ion traps via helical resonators", *Applied Physics B* **107**, 921–934 (2012) (cit. on p. 33).

[160] K. Deng et al., "A modified model of helical resonator with predictable loaded resonant frequency and Q-factor", *Review of Scientific Instruments* **85**, 104706 (2014) (cit. on pp. 33–35).

[161] Vacom GmbH, *White paper: Outgassing Rates of Aluminum compared to Stainless Steel*, https://www.vacom.net/fileadmin/user_upload/5.Downloads/5.5White_Paper/White_Paper_AluVaC_Ausgasverhalten_Web_EN.pdf, (accessed: 2022-10-10) (cit. on p. 39).

[162] T. M. Hoang et al., "YbH$^+$ formation in an ytterbium ion trap", *Phys. Rev. A* **101**, 022705 (2020) (cit. on p. 43).

[163] E. Bimont et al., "Lifetime calculations in Yb II", *Journal of Physics B: Atomic, Molecular and Optical Physics* **31**, 3321 (1998) (cit. on pp. 46, 122).

[164] C. Hu, "Design and set-up of optical system for optical multi-ion clock", Studienarbeit, 2020 (cit. on pp. 48, 154, 158).

[165] J. Keller et al., "Simple vibration insensitive cavity for laser stabilization at the 10^{-16} level", *Appl. Phys. B* **116**, 203–210 (2014) (cit. on pp. 48, 50, 141).

[166] T. Kessler, T. Legero, and U. Sterr, "Thermal noise in optical cavities revisited", *J. Opt. Soc. Am. B* **29**, 178 (2012) (cit. on p. 49).

[167] D. G. Matei et al., "1.5 μm Lasers with Sub-10 mHz Linewidth", *Phys. Rev. Lett.* **118**, 263202 (2017) (cit. on p. 49).

[168] Alexandre Didier et al., "946-nm Nd:YAG digital-locked laser at 1.1×10^{-16} in 1 s and transfer-locked to a cryogenic silicon cavity", *Opt. Lett.* **44**, 1781–1784 (2019) (cit. on pp. 49, 141).

[169] N. H. Hausser, "Bereitstellung von UV-Laserlicht zur direkten Khlung und Detektion von ^{115}In$^+$", Master thesis, Gottfried Wilhelm Leibniz Universität Hannover, 2019 (cit. on pp. 50, 141).

[170] Yves Colombe et al., "Single-mode optical fiber for high-power, low-loss UV transmission", *Opt. Express* **22**, 19783–19793 (2014) (cit. on p. 50).

[171] L. Skuja, H. Hosono, and M. Hirano, "Laser-induced color centers in silica", *Laser-Induced Damage in Optical Materials: 2000*, ed. by Gregory J. Exarhos et al., vol. 4347, International Society for Optics and Photonics, SPIE, 2001, pp. 155 –168 (cit. on p. 50).

[172] P. Karlitschek, G. Hillrichs, and K.-F. Klein, "Influence of hydrogen on the colour center formation in optical fibers induced by pulsed UV-laser radiation. Part 1: all silica fibers with high-OH undoped core", *Optics Communications* **155**, 376–385 (1998), ISSN: 0030-4018 (cit. on p. 50).

[173] P. Karlitschek, G. Hillrichs, and K.-F. Klein, "Influence of hydrogen on the colour center formation in optical fibers induced by pulsed UV-laser radiation.: Part 2: All-silica fibers with low-OH undoped core", *Optics Communications* **155**, 386–397 (1998), ISSN: 0030-4018 (cit. on p. 50).

[174] Y. Coulombe, "Making a LMA-10-UV patch cord", *Personal communication* (June 2013) (cit. on p. 50).

[175] D. H. Slichter, *UV fiber patch cord recipe*, 2014, `https://www.nist.gov/system/files/documents/2017/05/09/UV-fiber-patch-cord-recipe-10-2014-v2-3.pdf`, (accessed: 2022-12-04) (cit. on p. 50).

[176] DFV James, "Quantum dynamics of cold trapped ions with application", *Quantum Computation and Quantum Information Theory: Reprint Volume with Introductory Notes for ISI TMR Network School, 12-23 July 1999, Villa Gualino, Torino, Italy* **66**, 345 (2000) (cit. on p. 53).

[177] M. Roberts et al., "Observation of an Electric Octupole Transition in a Single Ion", *Phys. Rev. Lett.* **78**, 1876–1879 (1997) (cit. on p. 57).

[178] P. Taylor, "Observation of an ultra-high Q resonance in a single ion of ^{172}Yb$^+$.", PhD thesis, University of London, 1996 (cit. on p. 57).

[179] Lord Rayleigh F.R.S., "XXXI. Investigations in optics, with special reference to the spectroscope", *The London, Edinburgh, and Dublin Philosophical Magazine and Journal of Science* **8**, 261–274 (1879) (cit. on p. 60).

[180] R. T. Borlinghaus, *Super-Resolution - On a Heuristic Point of View About the Resolution of a Light Microscope*, 2014, `https://research.ninds.nih.gov/sites/default/files/documents/Super-Resolution.pdf`, (accessed: 2022-10-11) (cit. on p. 60).

[181] Laseroptik GmbH, `https://www.laseroptik.com/en/coating-guide/thin-film-basics/tips-and-tricks`, (accessed: 2022-10-25) (cit. on p. 62).

[182] M-Labs, *ARTIQ*, `https://m-labs.hk/experiment-control/artiq/`, (accessed: 2022-10-11) (cit. on p. 71).

[183] Sebastien Bourdeauducq, *Timing control in ARTIQ*, `https://m-labs.hk/docs/artiq/slides_timing.pdf`, (accessed: 2022-10-11) (cit. on p. 71).

[184] E. Surzhikova, "Autonome Steuerung einer optischen Atomuhr mit Zustandserkennung und -korrektur", Bachelor thesis, Universität Leipzig, 2020 (cit. on pp. 71, 132).

[185] J. Keller et al., "Precise determination of micromotion for trapped-ion optical clocks", *J. Appl. Phys.* **118**, 104501 (2015) (cit. on pp. 76–78, 141).

[186] L. Deslauriers et al., "Scaling and Suppression of Anomalous Heating in Ion Traps", *Phys. Rev. Lett.* **97**, 103007 (2006) (cit. on p. 91).

Bibliography

[187] J. Labaziewicz et al., "Temperature Dependence of Electric Field Noise above Gold Surfaces", *Phys. Rev. Lett.* **101**, 180602 (2008) (cit. on p. 91).

[188] M. Brownnutt et al., "Ion-trap measurements of electric-field noise near surfaces", *Rev. Mod. Phys.* **87**, 1419–1482 (2015) (cit. on p. 91).

[189] I. A. Boldin, A. Kraft, and C. Wunderlich, "Measuring Anomalous Heating in a Planar Ion Trap with Variable Ion-Surface Separation", *Phys. Rev. Lett.* **120**, 023201 (2018) (cit. on p. 93).

[190] M. Doležal et al., "Analysis of thermal radiation in ion traps for optical frequency standards", English, *Metrologia* **52**, 842–856 (2015) (cit. on p. 96).

[191] P. B. R. Nisbet-Jones et al., "A single-ion trap with minimized ionenvironment interactions", *Applied Physics B* **122**, 1432–0649 (2016) (cit. on p. 98).

[192] A. D. Ludlow and J. Ye, "Progress on the optical lattice clock", *Comptes Rendus Physique* **16**, 499–505 (2015) (cit. on p. 101).

[193] T. Sakrejda, L. Zhukas, and B. Blinov, "Efficient sympathetic cooling in mixed barium and ytterbium ion chains", *Quantum Information Processing* **20** (2021) (cit. on pp. 103, 112).

[194] J. Hoffnagle et al., "Order-Chaos Transition of Two Trapped Ions", *Phys. Rev. Lett.* **61**, 255–258 (1988) (cit. on p. 104).

[195] R. Blümel et al., "Phase transitions of stored laser-cooled ions", *Nature* **334**, 309–313 (1988) (cit. on p. 104).

[196] J. A. Hoffnagle and R. G. Brewer, "Two-ion chaos", *Physica Scripta* **1995**, 380 (1995) (cit. on p. 104).

[197] R. G. Brewer, J. Hoffnagle, and R. G. DeVoe, "Transient two-ion chaos", *Phys. Rev. Lett.* **65**, 2619–2622 (1990) (cit. on p. 104).

[198] R. Blümel et al., "Chaos and order of laser-cooled ions in a Paul trap", *Phys. Rev. A* **40**, 808–823 (1989) (cit. on p. 104).

[199] J. W. Emmert, M. Moore, and R. Blümel, "Prediction of a deterministic melting transition of two-ion crystals in a Paul trap", *Phys. Rev. A* **48**, R1757–R1760 (1993) (cit. on p. 104).

[200] Y.-Z. Xu et al., "Controlled melting of a Wigner ion crystal with atomic resolution", *Phys. Rev. A* **102**, 063121 (2020) (cit. on p. 104).

[201] M. W. van Mourik et al., "rf-induced heating dynamics of noncrystallized trapped ions", *Phys. Rev. A* **105**, 033101 (2022) (cit. on pp. 106, 117).

[202] R. Lechner et al., "Electromagnetically-induced-transparency ground-state cooling of long ion strings", *Phys. Rev. A* **93**, 053401 (2016) (cit. on pp. 106, 119).

[203] L. Feng et al., "Efficient Ground-State Cooling of Large Trapped-Ion Chains with an Electromagnetically-Induced-Transparency Tripod Scheme", *Phys. Rev. Lett.* **125**, 053001 (2020) (cit. on pp. 106, 119).

[204] Y. Lin et al., "Sympathetic Electromagnetically-Induced-Transparency Laser Cooling of Motional Modes in an Ion Chain", *Phys. Rev. Lett.* **110**, 153002 (2013) (cit. on pp. 106, 119).

[205] S. Ejtemaee and P. C. Haljan, "3D Sisyphus Cooling of Trapped Ions", *Phys. Rev. Lett.* **119**, 043001 (2017) (cit. on p. 106).

[206] M. K. Joshi et al., "Polarization-gradient cooling of 1D and 2D ion Coulomb crystals", *New Journal of Physics* **22**, 103013 (2020) (cit. on p. 106).

[207] D. H. E. Dubin, "Theory of structural phase transitions in a trapped Coulomb crystal", *Phys. Rev. Lett.* **71**, 2753–2756 (1993) (cit. on p. 107).

[208] G. Lin and L. M. Duan, "Sympathetic cooling in a large ion crystal", *Quantum information processing* **15**, 5299–5313 (2016) (cit. on p. 110).

[209] K. Sosnova, A. Carter, and C. Monroe, "Character of motional modes for entanglement and sympathetic cooling of mixed-species trapped-ion chains", *Phys. Rev. A* **103**, 012610 (2021) (cit. on p. 110).

[210] J. Wright et al., "Scalable quantum computing architecture with mixed species ion chains", *Quantum Information and Computation XIII*, ed. by Eric Donkor, Andrew R. Pirich, and Michael Hayduk, vol. 9500, Society of Photo-Optical Instrumentation Engineers (SPIE) Conference Series, 2015, 95000K, 95000K (cit. on p. 112).

[211] J. P. Home, "Chapter 4 - Quantum Science and Metrology with Mixed-Species Ion Chains", *Advances in Atomic, Molecular, and Optical Physics*, ed. by Ennio Arimondo, Paul R. Berman, and Chun C. Lin, vol. 62, Advances In Atomic, Molecular, and Optical Physics, Academic Press, 2013, pp. 231–277 (cit. on pp. 112, 114, 142).

[212] J. D. Jost et al., "Entangled mechanical oscillators", *Nature* **459**, 683–685 (2009) (cit. on pp. 112, 113, 142).

[213] N. Ohtsubo et al., "Frequency measurement of the clock transition of an indium ion sympathetically-cooled in a linear trap", *Opt. Express* **25**, 11725–11735 (2017) (cit. on pp. 112, 113, 142).

[214] H. L. Partner et al., "Dynamics of topological defects in ion Coulomb crystals", *New J. Phys.* **15**, 103013 (2013) (cit. on p. 112).

[215] L. Schomburg, "Controlling mixed-species ion Coulomb crystals for optimal cooling and mitigating micromotion induced non-thermal heating", Master thesis, Gottfried Wilhelm Leibniz Universität Hannover, 2021 (cit. on p. 118).

[216] D. J Gorman et al., "Two-mode coupling in a single-ion oscillator via parametric resonance", *Phys. Rev. A* **89**, 062332 (2014) (cit. on p. 119).

[217] N. Scharnhorst et al., "Experimental and theoretical investigation of a multimode cooling scheme using multiple electromagnetically-induced-transparency resonances", *Phys. Rev. A* **98**, 023424 (2018) (cit. on p. 119).

[218] W. Demtröder, *Laserspektroskopie: Grundlagen und Techniken*, Springer-Verlag, 2007 (cit. on p. 122).

Bibliography

[219] Y. H. Wang et al., "Absolute frequency and isotope shift measurements of the cooling transition in singly ionized indium", *The European Physical Journal D* **44**, 307–311 (2007) (cit. on pp. 122, 126, 127, 143).

[220] M. Herrmann et al., "Frequency Metrology on Single Trapped Ions in the Weak Binding Limit: The $3s_{1/2}-3p_{3/2}$ Transition in $^{24}Mg^+$", *Phys. Rev. Lett.* **102**, 013006 (2009) (cit. on p. 125).

[221] K. König et al., "Transition frequencies and hyperfine structure in $^{113,115}In^+$: Application of a liquid-metal ion source for collinear laser spectroscopy", *Phys. Rev. A* **102**, 042802 (2020) (cit. on pp. 126, 127, 143).

[222] Thaned Pruttivarasin, Michael Ramm, and Hartmut Hffner, "Direct spectroscopy of the 2S1/2 2P1/2 and 2D3/2 2P1/2 transitions and observation of micromotion modulated spectra in trapped 40Ca+", *Journal of Physics B: Atomic, Molecular and Optical Physics* **47**, 135002 (2014) (cit. on p. 127).

[223] S. Dörscher, arXiv: () publication in preparation (cit. on pp. 135, 139, 143, 144).

[224] N. Ohtsubo et al., "Frequency ratio of an 115In+ ion clock and a 87Sr optical lattice clock", *Opt. Lett.* **45**, 5950–5953 (2020) (cit. on pp. 136, 143).

[225] M. Pizzocaro et al., "Absolute frequency measurement of the 1S03P0 transition of 171Yb with a link to international atomic time", *Metrologia* **57**, 035007 (2020) (cit. on p. 136).

[226] J. T. Merrill et al., "Demonstration of integrated microscale optics in surface-electrode ion traps", *New Journal of Physics* **13**, 103005 (2011) (cit. on p. 146).

[227] K. K. Mehta et al., "Integrated optical addressing of an ion qubit", *Nature nanotechnology* **11**, 1066–1070 (2016) (cit. on p. 146).

[228] C. Sorace-Agaskar et al., "Versatile Silicon Nitride and Alumina Integrated Photonic Platforms for the Ultraviolet to Short-Wave Infrared", *IEEE Journal of Selected Topics in Quantum Electronics* **25**, 1–15 (2019) (cit. on p. 146).

[229] R. J. Niffenegger et al., "Integrated multi-wavelength control of an ion qubit", *Nature* **586**, 538–542 (2020) (cit. on p. 146).

[230] K. K. Mehta et al., "Integrated optical multi-ion quantum logic", *Nature* **586**, 533–537 (2020) (cit. on p. 146).

[231] W. J. Setzer et al., "Fluorescence detection of a trapped ion with a monolithically integrated single-photon-counting avalanche diode", *Applied Physics Letters* **119**, 154002 (2021) (cit. on p. 146).

[232] M. Ivory et al., "Integrated Optical Addressing of a Trapped Ytterbium Ion", *Phys. Rev. X* **11**, 041033 (2021) (cit. on p. 146).

[233] S. L. Todaro et al., "State Readout of a Trapped Ion Qubit Using a Trap-Integrated Superconducting Photon Detector", *Phys. Rev. Lett.* **126**, 010501 (2021) (cit. on p. 146).

[234] D. Reens et al., "High-Fidelity Ion State Detection Using Trap-Integrated Avalanche Photodiodes", *Phys. Rev. Lett.* **129**, 100502 (2022) (cit. on p. 146).

[235] R. W. P. Drever et al., "Laser phase and frequency stabilization using an optical resonator", *Applied Physics B* **31**, 97–105 (1983) (cit. on p. 165).

Acknowledgments

List of publications

- J. Keller, T. Burgermeister, D. Kalincev, A. Didier, A. P. Kulosa, T. Nordmann, J. Kiethe and T. E. Mehlstäubler, "Controlling systematic frequency uncertainties at the 10^{-19} level in linear Coulomb crystals", *Phys. Rev. A* **99**, 013405 (2019)

- J. Keller, D. Kalincev, T. Burgermeister, A. P. Kulosa, A. Didier, T. Nordmann, J. Kiethe and T. E. Mehlstäubler, "Probing Time Dilation in Coulomb Crystals in a High-Precision Ion Trap", *Phys. Rev. Applied* **11**, 0110002 (2019)

- T. Nordmann, A. Didier, M. Doležal, P. Balling, T. Burgermeister and T. E. Mehlstäubler, "Sub-kelvin temperature management in ion traps for optical clocks", *Review of Scientific Instruments* **91**, 111301 (2020)

- T. Nordmann, S. Wickenhagen, M. Doležal and T. E. Mehlstäubler, "Bichromatic UV detection system for atomically-resolved imaging of ions", currently under review at Review of Scientific Instruments

- T. Nordmann, J. Keller, L. Schomburg, J. Kiethe, N. H. Hausser and T. E. Mehlstäubler, "Sympathetic cooling and permutation control in dual-species linear crystals", in preparation